UNIVERSITÀ DI PARMA

Università degli Studi di Parma

Dottorato di ricerca in
Scienza e Tecnologia dei Materiali

Ciclo XXXIII

Cavitand-based polymers for the detection and removal of organic analytes in water

Coordinatore:
Prof. Enrico Dalcanale
Tutore:
Prof. Enrico Dalcanale

Dottorando: Mattia Amorini

Anni Accademici 2017/2018 – 2019/2020

Contents

Chapter 1

Supramolecular receptors – Resorcinarene based Cavitands

Chapter 2

Benzoquinoxaline-bridged Cavitand

Chapter 3

Surface activation of 3d-printed membranes

Chapter 4

Tetraphosphonate cavitand as receptor in QCM sensors

Chapter 5

Cavitand-based Polythiophenes for Impedance sensors

Chapter 1

Supramolecular receptors – Resorcinarene based Cavitands

1.1 Supramolecular Chemistry

In which direction is society moving? And then towards which horizons is Chemistry now tracing the next paths?
Considering these questions and their possible answers, it is clear to us that we are living in a new era, full of present and future challenges, all aimed at an increasingly pressing metamorphosis of modern society and the vision of the future. The need for new, coherent and environmentally sustainable technologies, the development of new high-performance materials and systems capable of effective actions to fight climate change and pollution is shaping the horizons and perspectives of future research scientific. The progressive abandonment of a traditional economy has allowed a whirlwind twist of Science in the direction of a new global green deal, able to pave the way for a profound change in the society itself.
Chemistry itself, with a role that has always been central, is more and more involved in exploring and developing new fields of transversal research, able to introduce features and concepts not typical of the Chemistry of the last century but can be traced back to systems typical of the natural world. Their complexity and the mechanisms that regulate it prove to be an exceptional opportunity for the development of new advanced technologies and smart materials, bringing the concept of Chemistry towards a real engineering of molecules.
Here, emerges the fundamental role of a new branch called Supramolecular Chemistry, a new field that involved the development of complex highly ordered and functional systems obtained by non-covalent interactions between several molecular building blocks under equilibrium conditions.[1] It represents a new interdisciplinary field that has grown with an unpredictable rate in the last years. The origins are to be traced back to Paul Ehrlich's research on receptors, the studies of Alfred Werner on the coordinating chemistry and the intuitions of Emil Fischer who originally described the concept of molecular recognition with the lock-key model.[2–4] Only in the 1970s, following the introduction of self-assembly and the self-organization concepts, the Supramolecular Chemistry started to become a relevant and fundamental field.[5,6] These principles, essential both for the understanding of the biological systems and for the development of artificial

molecular receptors, become a real extension of the key-lock theory over the structural and energetics molecular features.

In concomitance with an increasing interest in the biological systems and their mechanisms, the accidental discovery of crown ethers by C. Pedersen in the sixties disclosed the horizons of this new Chemistry branch.[7,8] Inspired by this research Lehn and Cram started to explore the potential of the Supramolecular Chemistry working on the development of new molecular receptors for the binding of small and charged molecules.[9,10] For their pioneering researches they were awarded with the Nobel Prize in the 1987. But chemists had just begun to explore this new world. During the 90s researchers such as Balzani, Feringa, Stoddard and Sauvage prompted the Supramolecular Chemistry to even more sophisticated levels, in order to develop molecular machinery with highly complex self-assembled structures and giving new impetus to the nanotechnology era.[11–13] Their works were awarded with a new Nobel Price for the Supramolecular Chemistry advancements in 2016, after 30 years the first one dedicated to this field. Based on these innovation different definitions of Supramolecular Chemistry has emerged over the years like “chemistry of molecular assemblies and of the intermolecular bond” and also “non-molecular chemistry”, but the most famous definition and perhaps the one that in a few words encloses all the potential of this branch was given by Lehn in his Nobel Lecture, the “Chemistry beyond the molecule”.[1,14]

Supramolecular Chemistry relies on the existence of a selective molecular recognition, defined by the identification and the simultaneous binding of guest molecules by highly specific molecular host systems. This phenomenon is driven by the synergic combination between a defined structure of intermolecular interactions and a high shape complementary.[15] The building of supramolecular structure trough self-organization requires finely programmed molecular elements and a precise control on the weak interactions involved in the final systems. Through a fine tune molecular design it is possible to generate supramolecular assemblies with high complexity degree such as helix, grids, capsules or polyhedral and to create new materials with outstanding properties.[16–18] Inspired by nature and his complexity, the Supramolecular Chemistry highlighted the power of a fine tune on weak interactions in order to create new materials, becoming in the last decades a central Science for the

generation of structure with advanced tasks in several field like catalysis, drug delivery, functional materials and sensors.

1.2 Molecular Receptors

A key role in the field of advanced molecular receptors was played by a series of macrocyclic compounds called cavitands and discovered in 1982 by Cram.[19] Using the cavitand word, originally Cram defined all the compounds with a constrained structure that generates a large cavity able to host other molecules. In agreement with this definition, several macrocyclic compounds like cyclodextrins, calixarenes, pillararenes and cucurbiturils can be classified as cavitands.[20–23] However, in recent years the term cavitand was associated to resorcinarene and their derivatives.

The name resorcinarene identify a class of macrocyclic hosts that are generally synthesized through an acid-catalyzed condensation between resorcinol and either aliphatic or aromatic aldehydes (**Figure 1.1**).[24] In the resorcinarene structure it is possible to identify a wide upper rim characterized by the presence of eight hydroxy group and a narrow lower rim with four pendant chains, essential to control the macrocyclic solubility.

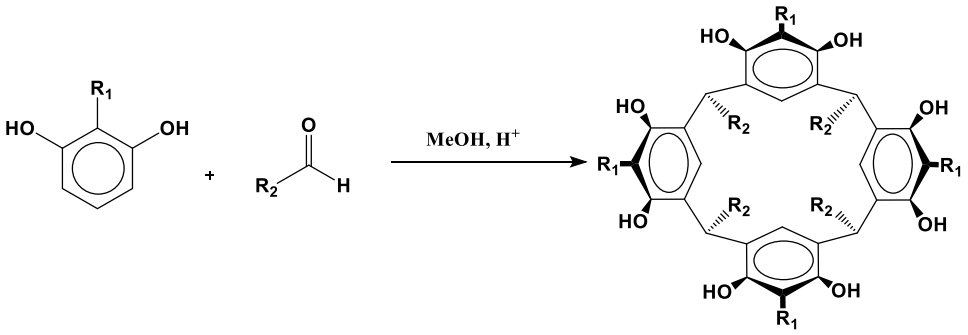

Figure 1.1 *General procedure for resorcin[4]arene synthesis.*

This peculiar structure organized over two different rims provide several entry points for subsequent modifications. Functional groups placed in different

position on the resorcinarene scaffold can play an essential role in the design of new performant and innovative molecular receptors affording new properties and behaviors to the final material.

The conformational flexibility of the resorcinarene structure makes these macrocycles unsuitable as host. To overcome this limitation and improving the complexation abilities of the molecule is essential to bridge the phenolic oxygens with the proper agents in order to generate a rigid cavity large enough to host and complex and complementary organic molecules or metal ions. In the design of new resorcinarene-based molecular receptors the choice of the bridging groups on the upper rim of the macrocyclic scaffold is pivotal in order to customize the cavity features as the shape, depth and the electronic charge distribution and the subsequent complexation ability of the final cavitand.

Over the last 20 years, many research groups synthesized several classes of cavitands, exploring their potential and introducing new functionalities in these macrocyclic structures.[25–27]

Among all these compounds, the two classes of cavitands that showed more potential and disclosed the horizons of wide applications are the quinoxaline and phosphonate cavitands

1.2.1 Tetraquinoxaline Cavitands

Tetraquinoxaline cavitands are synthesized through a nucleophilic aromatic substitution, bridging the resorcinarene phenolic hydroxyl groups in the upper rim with four quinoxaline walls. [19]

This particular scaffold functionalization provides the formation of a deep and rigid cavity. The four electron-rich walls lead to a highly hydrophobic cavity. A remarkable feature of the tetraquinoxaline cavitand and its derivates is the ability of the four quinoxaline walls to occupy either axial or equatorial positions.[28] As consequence of specific perturbations, the macrocyclic structure is able to switch the conformation between two equivalent form (free energy minima) and modify the total symmetry (**Figure 1.2**).[29] The total axial conformation (aaaa), called vase form, shows a closer organization with an interior cavity open in the upper section and locked on the bottom by the cavitand itself.

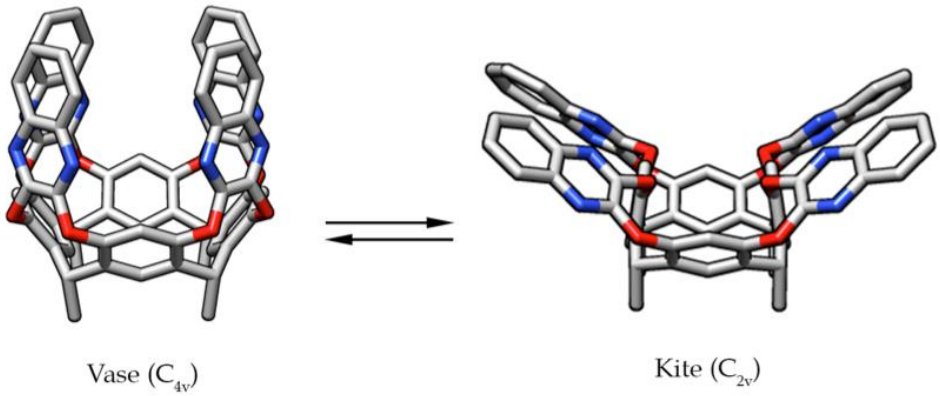

Figure 1.2 *Structure of quinoxaline cavitand vase (left) and kite (right) conformer.*[30]

In the vase conformer each quinoxaline wall interacts with the neighbor *via* α-hydrogens generating a cavity with C_{4v} symmetry which is approximately 7 Å wide and 8.3 Å deep. The total equatorial conformation (eeee), called kite conformation or velcrand by Cram, led to a more open structure with a flat and extended surface of 19.3 Å x 15.6 Å.[28,31]

The conformational equilibrium between vase and kite forms is influenced by several factors, such as structural variations or external stimuli. Methyl groups in the apical position in the resorcinarene scaffold stabilize the structure in the kite form, promoting the velcrand dimerization in solution through solvophobic interactions.

In absence of bulky groups in the apical position of the resorcinarene scaffold, vase and kite conformations co-exist in equilibrium and they can be monitored through NMR spectroscopy or spectrophotometry techniques.

Vase conformation of the tetraquinoxaline cavitand become dominant at room temperature and in apolar solvents, meanwhile at low temperatures we can observe a progressive conversion of vase form in the kite one.[32] Total conversion from the vase to the kite conformation is reached below 230 K. This relevant behavior is related to the different solvation grade of the two structural organizations. Kite form guarantee a more accessible surface to the solvent than

in the vase one, so more solvent molecules can stabilize the structure by non-covalent interactions.

This solvent-driven stabilization is effective only at low temperatures below 230 K, with the cavitand exposing a larger surface to the solvent, meanwhile the solvation entropic term become unfavorable at higher temperature, leading to the interconversion kite-vase.

Another strategy developed to perturbate the vase-kite conformational dynamic equilibrium in the quinoxaline cavitands involved pH variations of the media.[30] The mildly basic behavior (pKa = 0.56) of the N-atoms of quinoxaline walls, make possible their protonation by a strong acid such CF_3COOH or HCl. The cationic form of the quinoxaline walls leads to a mutual electrostatic repulsion and the consequent opening of the cavitand from the vase to the kite form. The pH perturbation becomes effective only in apolar solvents, and decreases with the increasing of the medium polarity.

Zn^{2+} coordination by the N-atoms of quinoxaline walls is an alternative method to perturbate and control the vase-kite equilibrium in the tetraquinoxaline cavitand.[33] Simulations proved that only in the kite form, the C_{2v} symmetry pushed the walls far enough to allow the zinc-coordination over the nitrogen atoms in two adjacent quinoxaline walls.

Beyond the vase-kite equilibrium, quinoxaline-based cavitands show an additional interesting feature; vase conformation, thanks to the rigidity and depth of its cavity, promotes the selective complexation of aromatic guest through CH-π, π- π interactions and H-bonds.

Dalcanale and co-workers, in 1992 demonstrated the ability of the tetraquinoxaline cavitand to remove pollutant dispersed in water.[34] Authors showed the extraction power of the macrocyclic compound in the removal of several chlorinated hydrocarbons, aromatic hydrocarbons and aromatic amine in ppb concentrations. The research highlighted the hydrophobicity of the pollutant molecules as real driving force in the sequestration process, pushing the contaminants to prefer the lipophilic cavity of the quinoxaline cavitand over the water solvation. For what concern both structural and interactive aspects of pollutant removal, the relevance of the $K_{o/w}$ of the pollutants became clear, together with the host-guest complementarity.

The potential of the quinoxaline based cavitand in detection and removal of suitable species is proved by several researches that widely explored new methods to modify or functionalize the quinoxaline cavitand in order to improve its performances.[27,35,36]
In this thesis we explored the performances of a new quinoxaline based cavitand in the removal of polycyclic aromatic hydrocarbons (PAH) in water. Moreover, we used the quinoxaline cavitand in order to develop new conductive polymers for the application in impedance and magneto sensors.

1.2.2 Tetraphosphonate Cavitands

Among the several bridging groups explored in the last years, phosponates became one of the most impacting moieties for sensing applications. The tetraphosphonate cavitands are effective molecular receptor toward positively charged species such as alkaline-earth cations, *N*-methylammonium or *N*-methylpyridinium species.[37,38]
The peculiarity of this specific cavitand is the presence of four P(V) stereogenic centers in the cavity that generates six possible diastereomeric isomers, differing from each other for the orientation of the PO groups, inward or outward the cavity (**Figure 1.3**).[39]

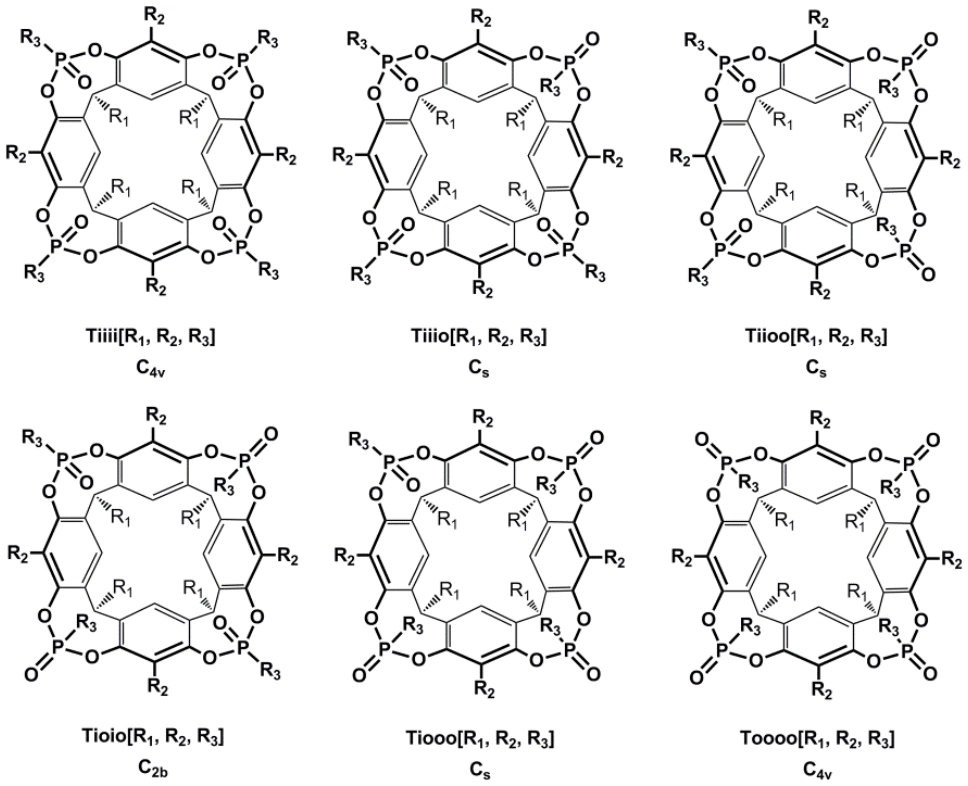

Figure 1.3 *Isomers of tetraphosphonate bridged cavitands*[40]

The distinction between these several possible orientations is relevant for what concern the complexation ability of the cavitand. Increasing the number of P=O groups oriented inward the cavity makes the cavity more appealing for the complexation of suitable guest molecules.[40–43] Therefore, the isomer with all the four P=O groups oriented inward the cavity is the most performing tetraphosphonate receptor.

It is necessity to follow a selective synthetic procedure in order to obtain the phosphonate cavitand with all the P=O groups oriented inward as the major product. This goal has been achieved through a highly selective synthetic procedure in two steps and widely explored in our research group (**Figure 1.4**).[44]

In the first step, the bridging functionalization of the resorcinarene scaffold with a dichlorophosphine derivative in pyridine affords the formation of an intermediate with four P(III) atoms with all the electrons lone pairs point inside the cavity.[45] The following step is the in situ oxidation of the P(III) atom using hydrogen peroxide, obtaining the Tiiii stereoisomer in high yield.

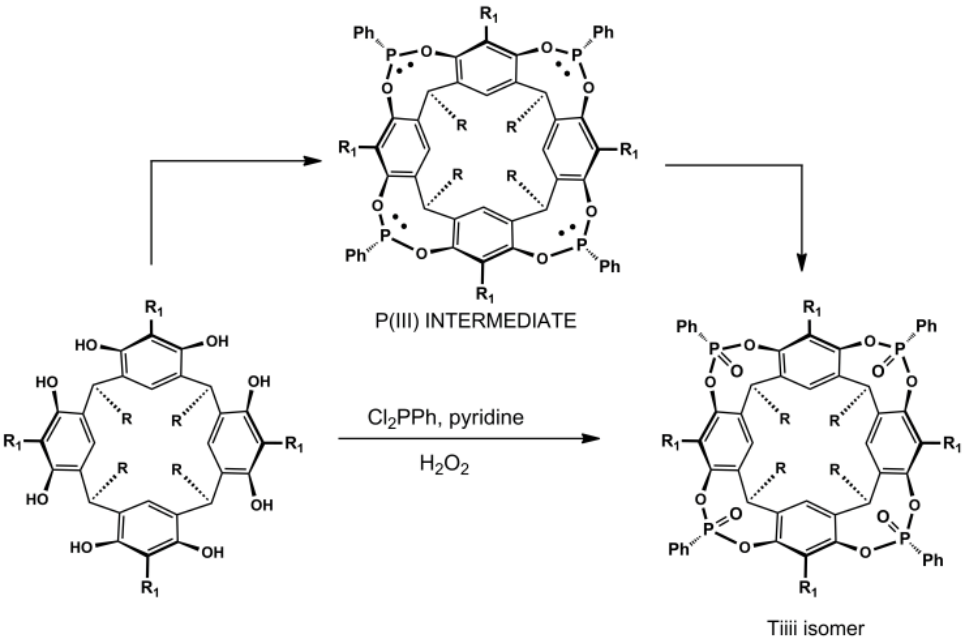

Figure 1.4 *Tiiii isomer synthesis*[46]

As discussed above, the tetraphosphonate cavitand ability to complex suitable guest is strongly related to its stereochemistry, reaching the best performances in presence of the Tiiii cavity organization. The preorganized P=O decorated cavity interacts with suitable guests through specific interactions like H-bonding, cation-π and cation-dipole interactions. The presence of these synergic interactions plays a key role in the definition of the cavitand versatility as molecular receptor and its application in performant sensoristic systems.

Positively charged species such as *N*-methylammonium and *N*-methylpyridinium salts, metal cations are optimal guests for tetraphenylphonate cavitands (**Figure**

1.5). The interactions involved in the complexation of *N*-methylammonium by tetraphenylphosphonate cavitand are: i) H-bonds between P=O groups and the nitrogen protons, ii) cation-π interactions between the charged *N*-methyl group of the guest and the π-basic cavity in the host, iii) $N^{+}\cdots O=P$ cation-dipole interactions.[47] With *N*-methylpyridinium salts only cation-π and cation-dipole interactions are involved.

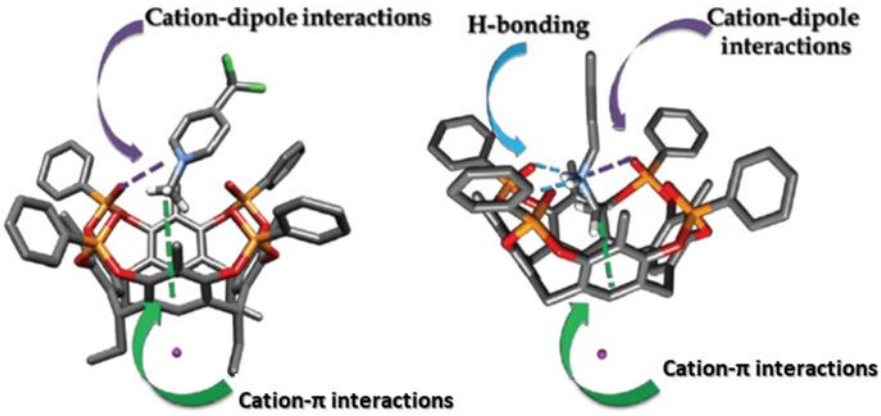

Figure 1.5 *Complexation of tetraphenylphosphonate cavitands towards N-methylpyridinium and N-methylammonium salts.*[48]

ITC measurements, performed over the ammonium salt series with increasing methyl groups, provide important information such as association constants of the host-guest complexes.[37] Monomethylated ammonium ions shows the highest K_a values, meanwhile the trimethylated ammonium species provided the lower K_a (not measurable with this technique).

Complexation properties of phosphonate cavitands towards suitable guest molecules in solid state, in solution and in the gas phase were extensively investigated by our group.[48–51]

After a deep investigation of the molecular recognition properties of the tetraphosphonate cavitands towards the detection of sarcosine, in 2012 Dionisio *et al.* developed a chemiresistive receptor based on single-walled carbon nanotubes (SWCNT's) covalently functionalized with Tiiii receptors for the detection of sarcosine and its ethyl ester hydrochloride in water, showing high selectivity at concentrations above 0.02 mM.[52] In the same year BIavardi *et al.*

developed a device for the detection in water of the whole class of methamphetamine drugs and related designer drugs through the covalent functionalization of silicon microcantilevers with the Tiiii cavitand.[48] The interesting feature of this new detector relies on the cavitand ability to selective detect the methylammonium psychoactive site of these psychotropic drugs. This remarkable property disclosed the opportunity to detect not only methylamphetamine but all the derived stimulants and new designer drugs.

In this thesis, two different synthetic strategies are reported to obtain new thiophene-based polymers functionalized with tetraphenylphosphonate cavitands with the aim to prepare new QCM and EIS sensors working in water.

1.3 References

1. J.-M. Lehn. Supramolecular Chemistry-Scope and Perspectives Molecules, Supermolecules, and Molecular Devices (Nobel Lecture). *Angew. Chemie Int. Ed.* **27**, 89–112 (1988).
2. Limbird, L. E. The Receptor Concept : A continuing evolution. *Mol. Interv.* **4**, 326–336 (2004).
3. Bowman-james, K. Alfred Werner Revisited : The Coordination Chemistry of Anions. *Acc. Chem. Res.* **38**, 671–678 (2005).
4. Lemieux, U. R. & Spohr, U. How emil fischer was led to the lock and key concept for enzyme specificity. *Adv. Carbohydr. Chem. Biochem.* **50**, 1–19 (1994).
5. Whitesides, G. M. & Boncheva, M. Beyond molecules : Self-assembly of mesoscopic and macroscopic components. *PNAS* **99**, 4769–4774 (2002).
6. Whitesides, G. M., Mathias, J. P. & Seto, C. T. Molecular Self-Assembly and Nanochemistry : A Chemical Strategy for the Synthesis Nanostructures. *Science (80).* **254**, 1312–1319 (1991).
7. Pedersen, C. J. Cyclic Polyethers and Their Complexes with Metal Salts. *J. Am. Chem. Soc.* **89**, 2495–2496 (1967).
8. Pedersen, C. J. & Frensdorff, H. K. Macrocyclic Polyethers and Their Complexes. *Angew. Chem. Int. Ed.* **11**, 16–25 (1972).
9. Cram, D. J., Stewart, K. D., Goldberg, I. & Trueblood, K. N. Complementary Solutes Enter Nonpolar Preorganized Cavities in Lipophilic Noncomplementary Media. *J. Am. Chem. Soc.* **107**, 2574–2575 (1985).
10. Cram, D. J. The Design of Molecular Hosts, Guests, and Their Complexes. *Angew. Chem. Int. Ed.* **27**, 1009–1020 (1988).
11. Balzani, V., Pez, Ä. & Stoddart, J. F. Molecular Machines. *Acc. Chem. Res.* **31**, 405–414 (1998).
12. Cesario, M., Dietrich-Buchecker, C. O., Guilhem, J., Pascard, C. & Sauvage, J. P. Molecular Structure of a Catenand and its Copper(I) Catenate: Complete Rearrangement of the Interlocked Macrocyclic Ligands by Complexation. *J. Chem. Soc. Chem. Commun.* 244–247 (1985).

13. Feringa, B. L. The Art of Building Small : From Molecular Switches to Motors (Nobel Lecture) *Angew. Chem. Int. Ed.* **56**, 11060–11078 (2017).

14. Lehn, J. M. Cryptates: inclusion complexes of macropolycyclic receptor molecules. *Pure Appl. Chem.* **50**, 871–892 (1978).

15. Lehn, J. Supramolecular Chemistry - Molecular Information and the Design of Supramolecular Materials. *Makromol. Chem.* 1–17 (1993).

16. Yashima, E. *et al.* Supramolecular Helical Systems : Helical Assemblies of Small Molecules , Foldamers , and Polymers with Chiral Amplification and Their Functions. *Chem. Rev.* **116**, 13752–13990 (2016).

17. Wu, J., Zhao, L., Guo, M. & Tang, J. Constructing supramolecular grids : from 4f square to 3d–4f grid. *Chem. Commun.* **51**, 17317–17320 (2015).

18. He, Y. *et al.* Hierarchical self-assembly of DNA into symmetric supramolecular polyhedra. *Nature* **452**, 198–202 (2008).

19. Moran, R. J., Karbach, S. & Cram, J. D. Cavitands: Synthetic Molecular Vessels. *J. Am. Chem. Soc.* **104**, 5826–5828 (1982).

20. Barrow, S. J., Kasera, S., Rowland, M. J. & Scherman, O. A. Cucurbituril-Based Molecular Recognition. *Chem. Rev.* **115**, 12320–12406 (2015).

21. Ogoshi, T., Yamagishi, T. & Nakamoto, Y. Pillar-Shaped Macrocyclic Hosts Pillar[n]arenes : New Key Players for Supramolecular Chemistry. *Chem. Rev.* **116**, 7937–8002 (2016).

22. Crini, G. Review : A History of Cyclodextrins. *Chem. Rev.* **114**, 10940–10975 (2014).

23. Acharya, A., Samanta, K. & Rao, C. P. Conjugates of calixarenes emerging as molecular entities of nanoscience. *Coord. Chem. Rev.* **256**, 2096–2125 (2012).

24. Tunstad, L. M. *et al.* Host-Guest Complexation. 48. Octol Building Blocks for Cavitands and Carcerands. *J. Org. Chem.* **54**, 1305–1312 (1989).

25. Tucci, F. C., Rudkevich, D. M. & Rebek, J. Deeper cavitands. *J. Org. Chem.* **64**, 4555–4559 (1999).

26. Dumele, O., Trapp, N. & Diederich, F. Halogen Bonding Molecular Capsules. *Angew. Chemie Int. Ed.* **54**, 12339–12344 (2015).

27. Trzcinski, W. J. *et al.* In Search of the Ultimate Benzene Sensor: The

EtQxBox Solution. *ACS Sensors* **2**, 590–598 (2017).

28. Roncucci, P. *et al.* Conformational Behavior of Pyrazine-Bridged and Mixed-Bridged Cavitands: A General Model for Solvent Effects on Thermal "Vase–Kite" Switching. *Chem. - A Eur. J.* **12**, 4775–4784 (2006).

29. Moran, J. R. *et al.* Vases and Kites as Cavitands. *J. Am. Chem. Soc.* **113**, 5707–5714 (1991).

30. Skinner, P. J., Cheetham, A. G., Beeby, A., Gramlich, V. & Diederich, F. Conformational switching of resorcin[4]arene cavitands by protonation: Preliminary communication. *Helv. Chim. Acta* **84**, 2146–2153 (2001).

31. Moran, J. R. *et al.* Vases and Kites as Cavitands. *J. Am. Chem. Soc.* **113**, 5707–5714 (1991).

32. Azov, V. A., Jaun, B. & Diederich, F. NMR Investigations into the Vase-Kite Conformational Switching of Resorcin[4]arene Cavitands. *Helv. Chim. Acta* **87**, 449–462 (2004).

33. Frei, M., Marotti, F., Chemie, O. & Ch-, Z. Zn[II]-induced conformational control of amphiphilic cavitands in Langmuir monolayers. *Chem. Commun.* **1**, 1362–1363 (2004).

34. Dalcanale, E., Costantini, G. & Soncini, P. Removal of Organic Pollutants from Water via Molecular Inclusion within a Cavitand. *J. Incl. Phenom. Mol. Recognit. Chem.* **13**, 87–92 (1992).

35. Bertani, F. *et al.* Triptycene-Roofed Quinoxaline Cavitands for the Supramolecular Detection of BTEX in Air. *Chem. - A Eur. J.* **22**, 3312–3319 (2016).

36. Riboni, N. *et al.* Conformationally blocked quinoxaline cavitand as solid-phase microextraction coating for the selective detection of BTEX in air. *Anal. Chim. Acta* **905**, 79–84 (2016).

37. Dionisio, M. *et al.* Nanomechanical Recognition of N -Methylammonium Salts. *J. Am. Chem. Soc.* **134**, 1–7 (2012).

38. Pinalli, R. *et al.* Metal ion complexation by tetraphosphonate cavitands : The influence of the ionic radius. *Inorganica Chim. Acta* **470**, 250–253 (2018).

39. Pinalli, R., Suman, M. & Dalcanale, E. Cavitands at Work : From Molecular Recognition to Supramolecular Sensors. *European J. Org. Chem.* 451–462

(2004).

40. Melegari, M., Suman, M., Pirondini, L. & Moiani, D. Supramolecular Sensing with Phosphonate Cavitands. *Chem. - A Eur. J.* **14**, 5772–5779 (2008).

41. Delangle, P., Mulatier, J., Tinant, B., Declercq, J. & Dutasta, J. Synthesis and Binding Properties of iiii (4i) Stereoisomers of Phosphonato Cavitands - Cooperative Effects in Cation Complexation in Organic Solvents. *European J. Org. Chem.* 3695–3704 (2001).

42. Dutasta, J. New Phosphorylated Hosts for the Design of New Supramolecular Assemblies. *Top Curr Chem* **232**, 55–91 (2004).

43. Pinalli, R., Nachtigall, F. F., Ugozzoli, F. & Dalcanale, E. Supramolecular Sensors for the Detection of Alcohols. *Angew. Chem. Int. Ed.* **38**, 2377–2380 (1999).

44. Nifantyev, E. E., Maslennikova, V. I. & Merkulov, R. V. Design and Study of Phosphocavitands s A New Family of Cavity Systems. *Acc. Chem. Res.* **38**, 108–116 (2005).

45. Xu, W., Rourke, J. P., Vittai, J. J. & Puddephatt, R. J. Anion Inclusion by a Calix[4]arene Complex : a Contrast Between Tetranuclear Gold (I) and Copper (I) Complexes. *J. Chem Soc., Chem. Commun.* **8**, 145–147 (1993).

46. Menozzi, D., Pinalli, R., Massera, C., Maffei, F. & Dalcanale, E. The Effect of Number and Position of P=O/P=S Bridging Units on Cavitand Selectivity toward Methyl Ammonium Salts. *Molecules* **20**, 4460–4472 (2015).

47. Menozzi, D., Biavardi, E., Massera, C., Schmidtchen, F. & Dalcanale, E. Thermodynamics of host – guest interactions between methylpyridinium salts and phosphonate cavitands. *Supramol. Chem.* **22**, 37–41 (2010).

48. Biavardi, E. *et al.* Cavitand-Grafted Silicon Microcantilevers as a Universal Probe for Illicit and Designer Drugs in Water. *Angew. Chemie Int. Ed.* **53**, 9183–9188 (2014).

49. Kalenius, E., Moiani, D., Dalcanale, E. & Vainiotalo, P. Measuring H-bonding in supramolecular complexes by gas phase ion – molecule reactions. *Chem. Commun.* 3865–3867 (2007)

50. Biavardi, E. *et al.* Fully reversible guest exchange in tetraphosphonate cavitand complexes probed by fluorescence spectroscopy. *Chem.*

Commun. 1638–1640 (2008).

51. Pinalli, R. *et al.* The origin of selectivity in the complexation of N- methyl amino acids by tetraphosphonate cavitands. *J. Am. Chem. Soc.* **138**, 8569–8580 (2016).

52. Dionisio, M. *et al.* Cavitand-Functionalized SWCNTs for N-Methylammonium Detection. *J. Am. Chem. Soc.* **134**, 5–8 (2012).

Chapter 2

Benzoquinoxaline-bridged Cavitand

2.1 Introduction

Water pollution and the shortage of clean water are general global issues that are becoming relevant in concomitance with the incoming climate change. Among the several pollutants present in water, polycyclic aromatic hydrocarbons (PAHs) have received particular attention in the last years.[1] PAHs are a class of hazardous organic compounds made by two or more aromatic rings, bonded together in linear, angular or cluster arrangements. They are byproducts of several anthropogenic activities related to industrial and mobility activities, and also from natural phenomena.[2] Currently, over 400 kinds of PAHs and their derivatives have been identified and classified, but most regulations, analyses and data are focused on only 14 to 20 PAH compounds.[3,4]

Most of the PAH pollutants are toxic, mutagenic and carcinogenic; their aromatic and delocalized structure confers them hydrophobicity and good lipid solubility.[5] PAH absorption and bioaccumulation in several tissue, in particular in the gastrointestinal tract of mammals, pushed USEPA (United States Environmental Agency) and EEA (European Environment Agency) to identify 16 PAH compounds as priority-contaminants and to introduce strict regulations.[6,7] The 16 PAHs monitored are acenaphthene, benzo[ghi]perylene, chrysene, acenaphthylene, benz[a]anthracene, benzo[b]fluoranthene, anthracene, fluorene, pyrene benzo[k]fluoranthene, benzo[a]pyrene, fluoranthene, indeno[1,2,3-cd]pyrene, naphthalene, phenanthrene, dibenz[a,h]anthracene. (**Figure 2.1**)

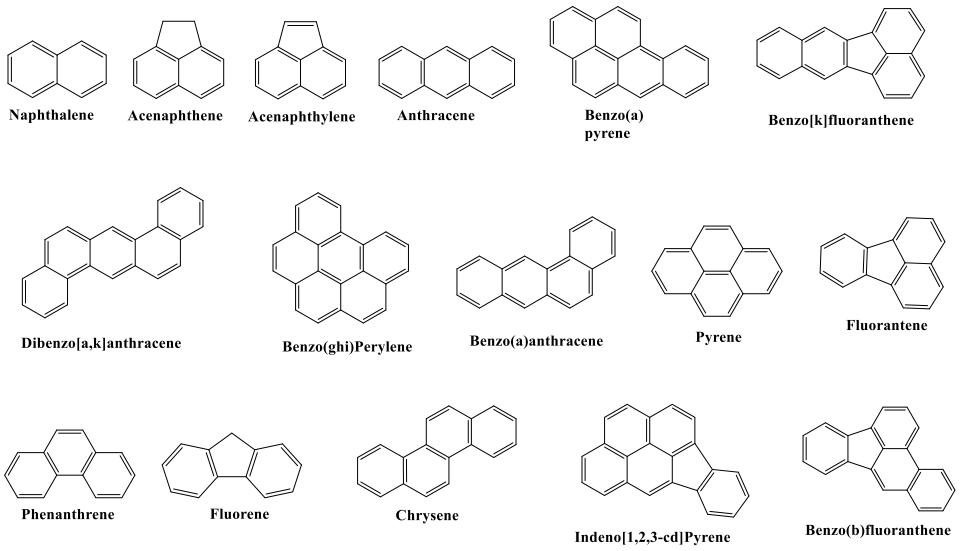

Figure 2.1. The *16 most regulated and monitored Polycyclic Aromatic Hydrocarbons.*

The European Union set the maximum limits in water of every single PAHs to 0.1 µg/L, with a particular attention to benzo[a]pyrene limited to 0.01 µg/L. Moreover, the EU set a limit of 0.1 µg/L for the sum of benzo[b]fluoranthene, benzo[k]fluoranthene, benzo[ghi]perylene and indenol[1,2,3-cd] pyrene.[8]

The removal of these pollutants from aqueous media represents a challenge. Current treatments involve advanced oxidation and ozonation processes, techniques that are affected in several cases by the formation of partial oxidized by-product more toxic than the starting molecules.[9] For what concern their detection, the most used technologies are based on the application of expensive and advanced laboratory equipment.[10]

In order to develop a molecular receptor selective for PAHs in water, we took inspiration from our previous research works on the detection and removal of aromatic pollutants using a tetraquinoxaline (QxCav) cavitand as molecular receptor.[11–13]

The QxCav is able to selectively bind geometrically suitable aromatic compounds inside the deep and electron-rich cavity through the formation of specific interactions such as multiple CH-π and π-π interactions. Moreover, in water the

lipophilicity of the cavity boosts the trapping of the hydrophobic aromatic compounds, which prefer to stay into the cavity of the quinoxaline cavitand with respect to water solvation.

The PAH compounds, as multiple fused aromatic rings, are characterized by the same electronic properties but they show a huge chemical structure variability, with several and different geometries. Their detection in water through cavitands requires the synthesis of compounds with an optimum balance between rigidity and flexibility, able to form suitable non-covalent interactions. More in details, structures equipped with deep and electron-rich hydrophobic cavities, large enough to host bulky guest molecules, become essential to reach the goal.

In this context, we decided to design and synthetize a new deep cavitand **5** (**Scheme 2.1**), extending the length of the QxCav aromatic walls through the functionalization of a resorcinarene scaffold with four benzoquinoxaline walls at the upper rim.

The extension of the classical quinoxaline walls using benzoquinoxaline groups led to a deeper and electron-rich hydrophobic cavity, a more suitable bowl for poly aromatic compounds such as PAHs. Moreover, the choice of deeper walls on the resorcinarene cavity do not affect the *vase-kite* conformational equilibrium (see *Chapter 1*) of the QxCav, essential for the decomplexation and subsequent regeneration of the hosting cavitand properties.[14]

2.2 Results and discussion

2.2.1 Synthesis of the Benzoquinoxaline Cavitand

The receptor was prepared following a convergent synthetic approach: i) synthesis of the benzoquinoxaline bridging unit **3**, and ii) synthesis of the deep cavitand **5** (**Scheme 2.1**). The synthetic pathway started with the preparation of the 2,3-dichlorobenzoquinoxaline as bridging wall. 2,3-diaminonaphtalene was condensed with oxalic acid under acidic conditions in order to obtain product **2** in quantitative yield. Target 2,3-dichlorobenzoquinoxaline **3** was synthesized through a chlorination reaction of **2** using thionyl chloride and DMF as catalyst in refluxing 1,2-dichloroethane. Product **3** was obtained as a pure yellow solid after precipitation in methanol in quantitative yield.[15]

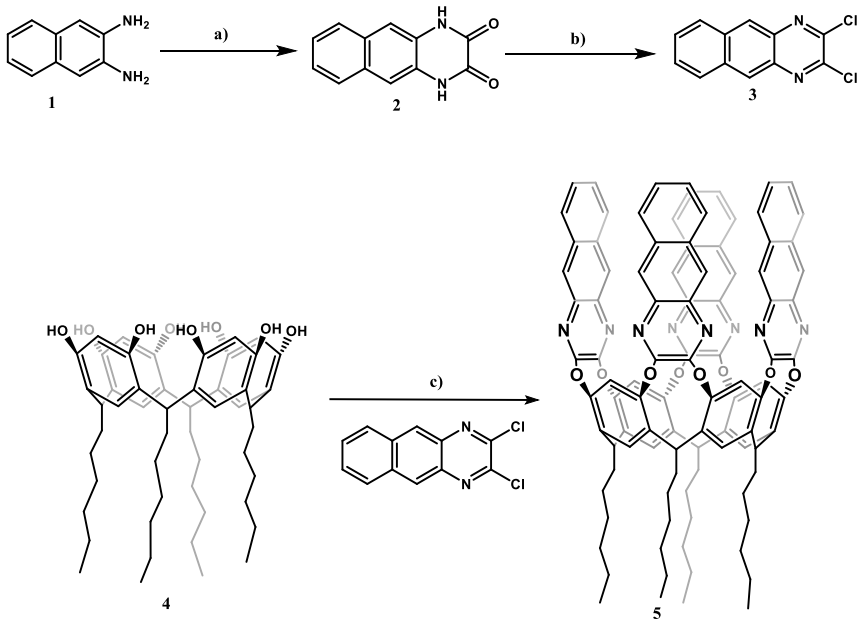

Scheme 2.1 *Synthesis of **3** and **5**: a) Oxalic Acid, HCl 4N, 105 °C, 15 h, quantitative yield; b) Thionyl Chloride, 1,2-dichloroethane, dimethylformamide, 85 °C, 12 h, quantitative yield; c) 2,3-dichlorobenzoquinoxaline, potassium carbonate, dimethylformamide, 80 °C, 12 h, 83% yield.*

As resorcinarene scaffold, we decided to use resorcinarene **4** equipped with four hexyl feet to guarantee the solubility of the partial-bridged intermediates in the reaction medium thus to complete the bridging reaction.

In the final step, **3** and **4** were reacted in presence of potassium carbonate in DMF as solvent. The product was obtained as a pure bright yellow solid after crystallization in ethyl acetate in 86% yield. Product **5** was characterized by MALDI-TOF and NMR.

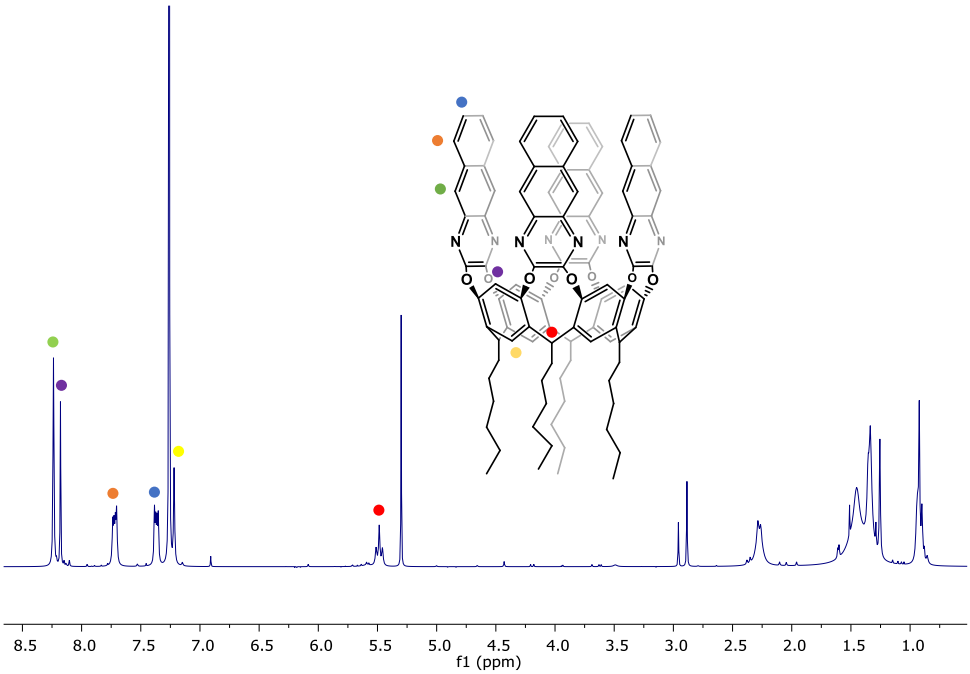

Figure 2.2 *^{1}H-NMR spectrum of **5** in $CDCl_3$ (300 MHz).*

The ^{1}H-NMR spectra of the target tetrabenzoquinoxaline cavitand **5** is reported above (**Figure 2.2**). The high field signals are related to the alkyl chains at the lower rim. The two singlet signals at 8.18 and 7.23 ppm belong to the protons on the resorcinarene scaffold (*purple* and *yellow* spots). The protons of the benzoquinoxaline walls are identified by the singlet signal at 8.24 ppm and the two multiplet signals at 7.72 and 7.36 ppm (*green*, *orange* and *blue* spots,

respectively). The diagnostic triplet of CH bridge signal at 5.49 ppm (*red* spot) confirms that in $CDCl_3$ the cavitand is in the *vase* conformation, thus in a C_{4v} symmetry in solution.

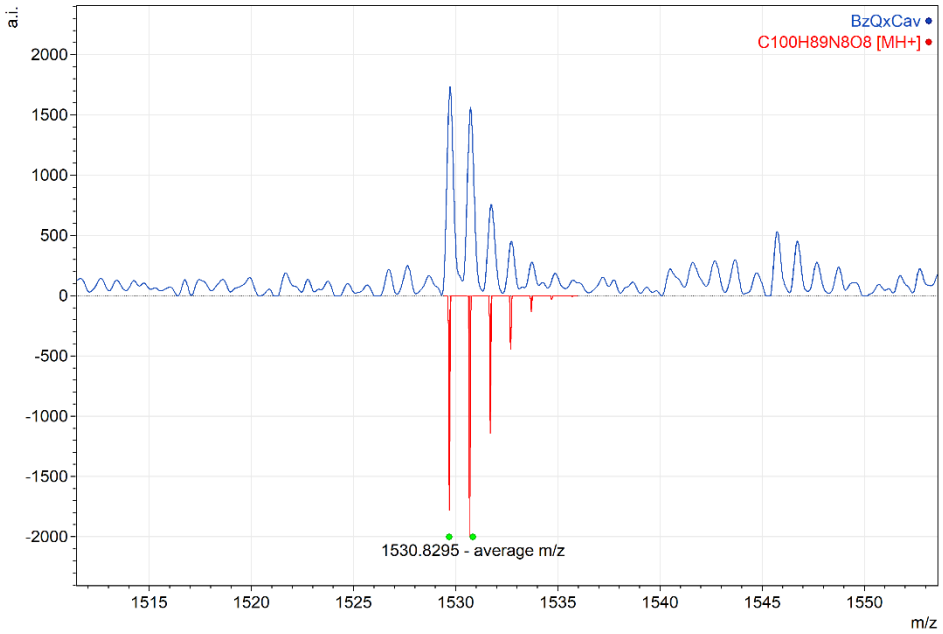

Figure 2.3 *High-resolution MALDI-TOF spectrum of **5**, with experimental (blue profile) versus flipped theoretical (red) isotopic distribution pattern*.

The MALDI spectrum confirms the presence of cavitand **5.** with the experimental isotopic distribution of the protonated molecular ion in agreement with the calculated one (**Figure 2.3**).

2.2.2 X-ray data collection and crystal structure determination

The structure of the new benzoquinoxaline cavitand was investigated with X-ray crystallographic and computational studies. Several trials of crystallization were performed dissolving cavitand **5** in different solvents such as chloroform, dichloromethane, dimethylformamide, tetrahydrofuran and dimethylsulfoxide. Suitable crystals for X-ray diffraction were obtained only in dimethylformamide (**Figure 2.4** *a*).

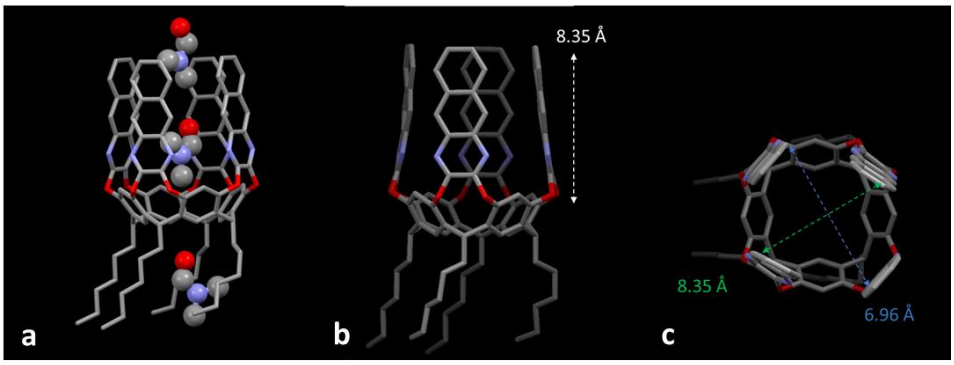

Figure 2.4*: a) Molecular structure of Cavitand* ***5*** *crystallized from DMF. The receptor hydrogens have been omitted for clarity. Solvent molecules are represented as spheres. c) Top and b) side view of Cavitand* ***5****, with dimensions highlighted in different colors.*

The molecular structure obtained *via* X-ray diffraction on single crystals showed that the cavitand adopts the closed *vase* conformation also in the solid state. The introduction of an additional ring fused at the upper rim provided a deeper cavity with a depth of 8.35 Å and an entrance of *ca*. 8.35 Å x 6.96 Å (**Figure 2.4** *b* and *c*). Taking as reference the tetraquinoxaline cavitand, which is 5.8 Å deep with an entrance of 10.0 Å x 7.1 Å, the introduction of the benzoquinoxaline walls led to an increment in depth of the cavity but also to a slight closure of the bowl mouth.

The crystallographic data were used as starting point to analyze the dimension of the cavity through computational software. The molecule surface was evaluated

with Yasara computational software, allowing the estimate of the cavity size (**Figure 2.5**).[16]

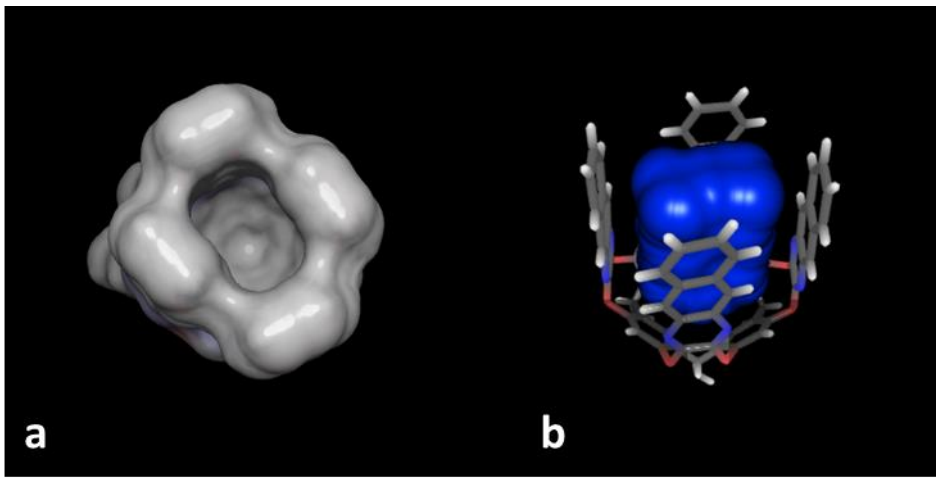

Figure 2.5 *Computations carried out on the crystal structure of **5.** a) Yasara computation of the molecule surface; b) Depth calculation of the free accessible volume.*

The accessible free volume inside the cavity was calculated using Caver software and Depth web server, obtaining an internal volume of 247 $Å^3$ against the 166 $Å^3$ of the parent tetraquinoxaline cavitand.[17,18]
These results show that replacing "standard" quinoxaline walls with benzoquinoxaline ones leads to the formation of a deeper and electron-richer cavity, suitable to host larger aromatic compounds.

2.2.3 Exploring the Vase-Kite Equilibrium

As already discussed in Chapter 1, quinoxaline-based cavitands are characterized by the ability to change their conformation between a closed *vase* conformation, having a C_{4v} symmetry, and an open *kite* structure featured by a C_{2v} symmetry and a flat extended surface.

The conformation adopted by a QxCav is solvent, pH and temperature dependent. The conformational dynamics can be monitored using either ^{1}H-NMR or UV/VIS-spectroscopy.[19,20]

In the case of cavitand **5**, we decided to monitor the *vase-kite* conformational equilibrium induced by pH perturbation using both techniques. Trifluoroacetic acid (TFA) was used to protonate the pyrazine nitrogen atoms of the benzoquinoxaline walls. Their protonation leads to an electrostatic repulsion of the resulting cationic cavitand walls causing the opening of the walls and the switch from *vase* to *kite* conformation.

At the ^{1}H NMR, the addition of different aliquots of TFA to the NMR tube containing a solution in $CDCl_3$ of cavitand **5** caused the shift of the methine signal at 5.49 ppm to higher fields (**Figure 2.6**). This is due to the protonation of the pyrazine nitrogen atoms of the benzoquinoxaline walls and the subsequent switching to the *kite* conformation.

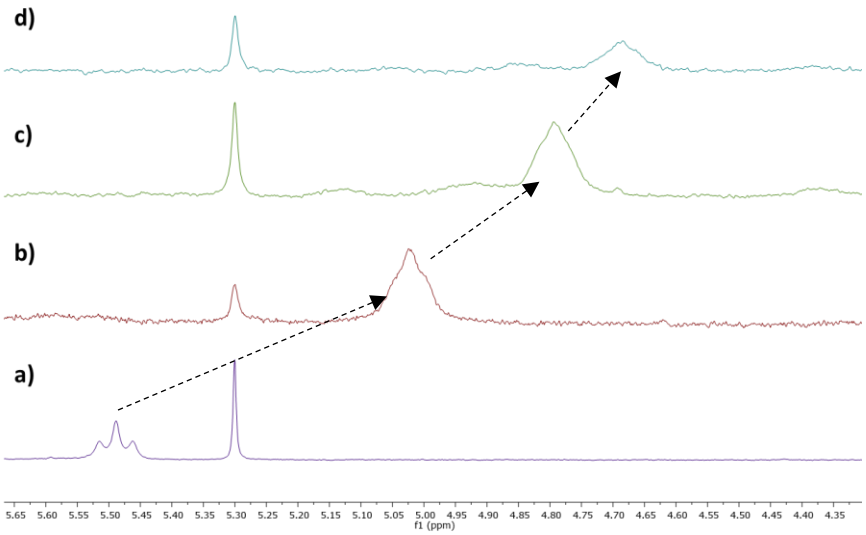

Figure 2.6 *Methine shift over pH perturbations in $CDCl_3$ at 298K a) ^{1}H-NMR of **5** in $CDCl_3$, b) ^{1}H-NMR of **5** + 10 eq. TFA, c) ^{1}H-NMR of **5** + 20 eq. TFA, c) ^{1}H-NMR of **5** + 30 eq. TFA in $CDCl_3$, d) ^{1}H-NMR of **5** + 40 eq. TFA.*

We decided to evaluate this pH-driven conformational switch through UV spectroscopy as well (**Figure 2.7**). We started to collect the UV absorption spectrum of a solution of **5** ([**5**] = $1 \cdot 10^{-5}$ M) in dichloromethane at 298K (*red line*). The UV profile shows two absorption peaks at 367 and 349 nm. The progressive additions of TFA (50 µL aliquots of a 0.8 M solution in dichloromethane) to the solution of **5** led to changes in the UV/Vis spectrum similar to those observed with the tetraquinoxaline cavitand and reported in literature.[19]

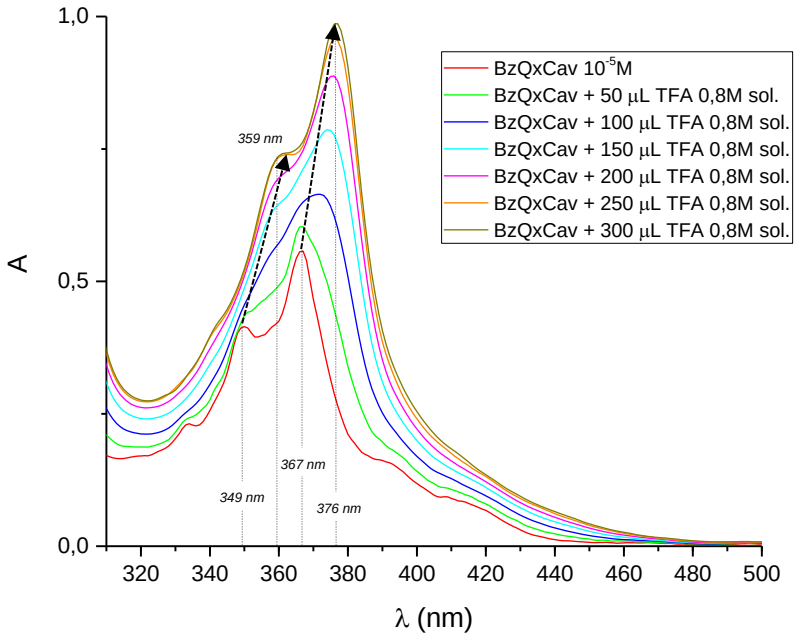

Figure 2.7 *Changes of the UV absorptions of **5** ([**5**] = $1.9 \cdot 10^{-5}$ M) in DCM upon addition of TFA (0 - 0.23 M). T = 298 K.*

The addition of TFA caused a red-shift of the maximum of absorption from 367 nm to 376 nm with an increase of the molar extinction coefficient ε from 28479 to 56752 $M^{-1} \cdot cm^{-1}$. The absorption peak at 349 nm was affected by a similar bathochromic shift (ε_{349} =21230; ε_{359} = 42413). Saturation was achieved at concentration of 0.23 M of TFA in DCM.

To confirm that the observed red shift is not due to a simple pH change but to the *vase*-to-*kite* conformational switch of the benzoquinoxaline cavitand upon the protonation of the pyrazinic nitrogens, two control experiments were performed. The first one was carried out to exclude that the mere pH change can cause such a shift in the UV spectrum. To this purpose, acetic acid was used to induce a pH change. Acetic acid was chosen since it is too weak to protonate the benzopyrazine nitrogens. As shown in **Figure 2.8** the addition of acetic acid to a solution containing cavitand **5** did not cause any shift in the UV spectrum, thus confirming that the previously observed bathochromic shift was related to the conformational switching of cavitand **5** upon protonation of the benzoquinoxaline walls rather than to a change in the solvent pH.

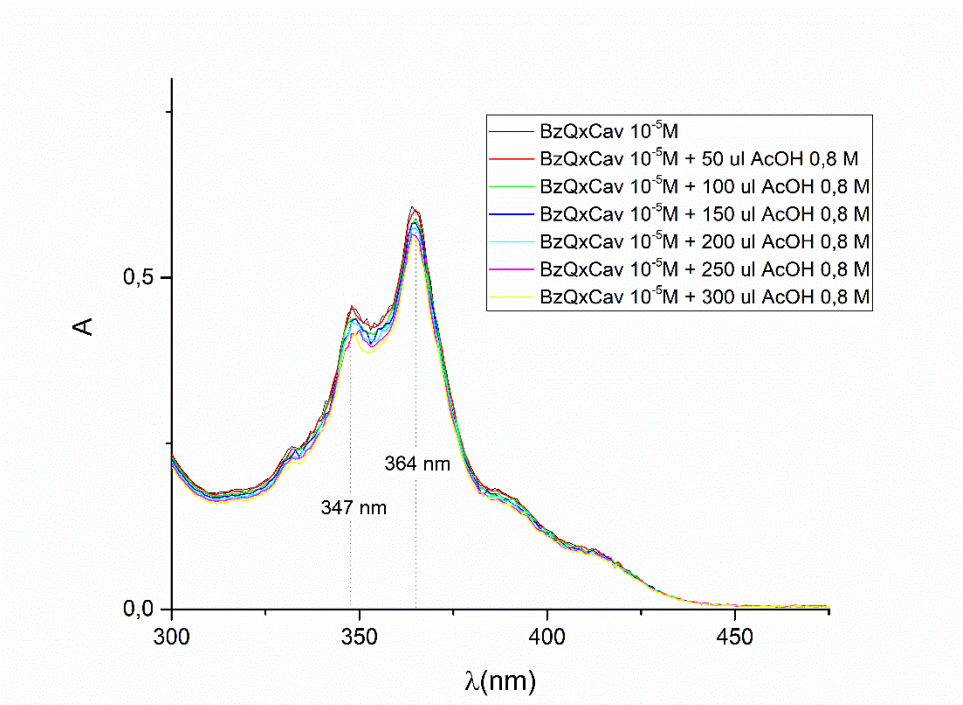

Figure 2.8 *Changes of the UV absorptions of **5** ([**5**] = 1·10^{-5} M) in DCM upon addition of AcOH (0 - 0.23 M). T = 298 K.*

The second control experiment was performed to confirm that the red shift is due to the conformational switching of the cavitand and not just to the protonation of the pyrazinic nitrogen. To this purpose, we added different aliquots of TFA to the single 2,3-dichlorobenzoquinoxaline bridging unit and we recorded the UV spectra. Also, in control experiment, the protonation of the nitrogen atoms of **3** did not give any shift of the absorption peaks (**Figure 2.9**), thus confirming than the red-shift recorded in the UV spectrum of cavitand **5** upon addition of TFA is related to *vase*-to-*kite* switch in the cavitand conformation.

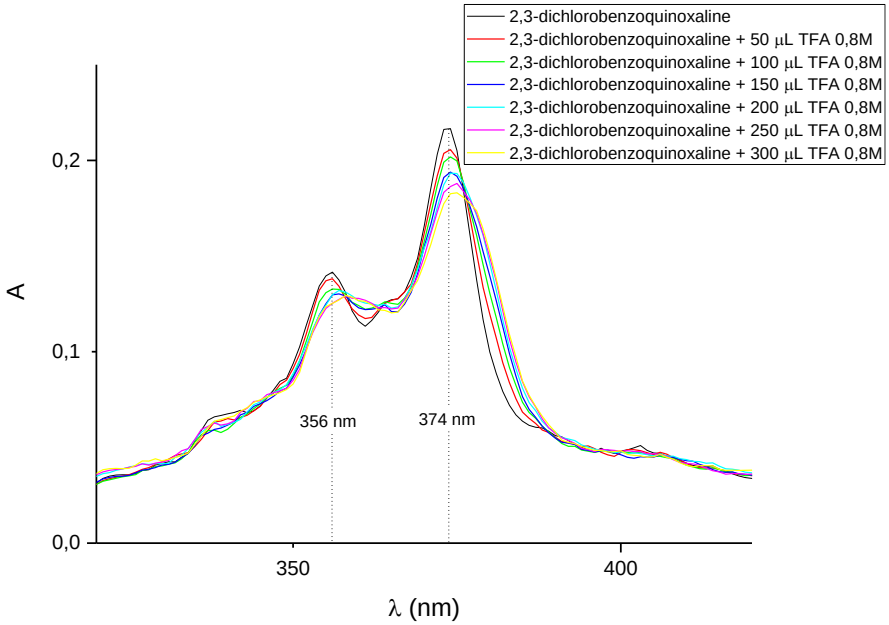

Figure 2.9 *Changes of the UV absorptions of **3** ([**3**] = 1·10^{-5} M) in DCM upon addition of TFA (0 - 0.23 M). T = 298 K.*

The behavior of cavitand **5** in presence of TFA was monitored by fluorescence spectroscopy as well. (**Figure 2.10**).

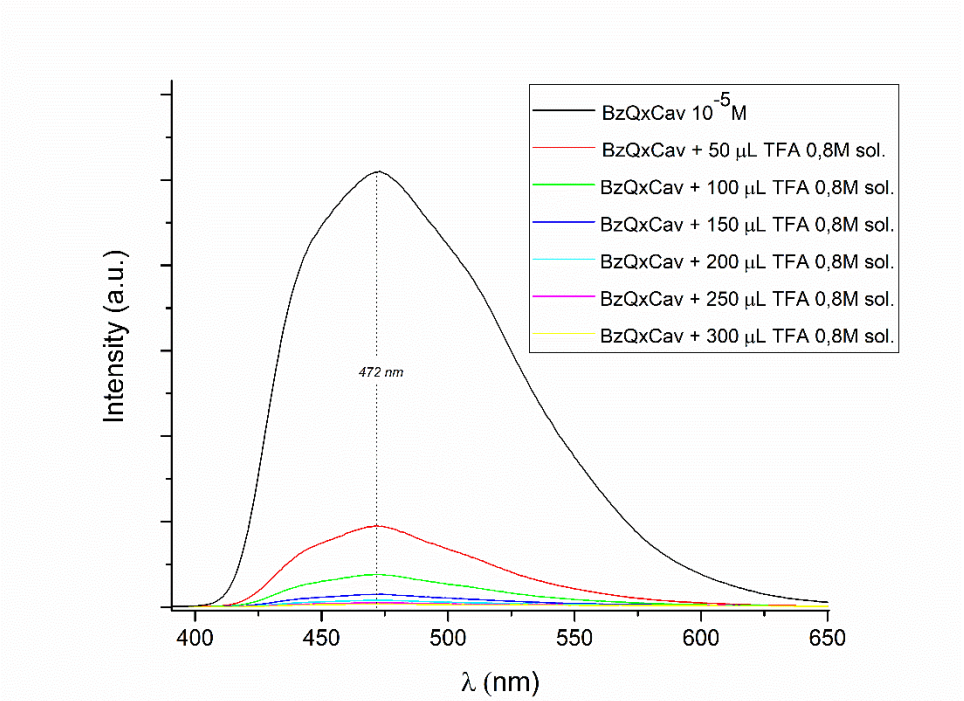

Figure 2.10 *Changes of the Fluorescence emission of **5** ([**5**] = 1·10^{-5} M) in DCM upon addition of TFA (0 - 0.23 M). T = 298 K.*

The fluorescence emission spectra of a solution of **5** ([**5**] = 1·10^{-5} M) in dichloromethane at 298 K showed a maximum of emission at 472 nm. The effect of the first addition of 50 µL of TFA (0.8 M in DCM) led to a drastic quench of the fluorescence emission, without any shift of the maximum emission peak. The subsequent additions of TFA aliquots led to a further quenching of the fluorescence without any shift. In the quinoxaline cavitand instead, the conformational switch from *vase* to *kite* form leads to a red-shift of the fluorescence emission and to an increase of the intensity.[21].

The reversibility of the conformation switch from *kite* to *vase* was demonstrated after addition of Et_3N through both UV-Vis and Fluorescence spectroscopy, and ^{1}H-NMR (**Figure 2.11** and **Figure 2.12,** respectively). These experiments show that the pH-driven *vase-kite* interconversion is easily triggered in solution in a reversible manner, allowing for controllable guest uptake and release.

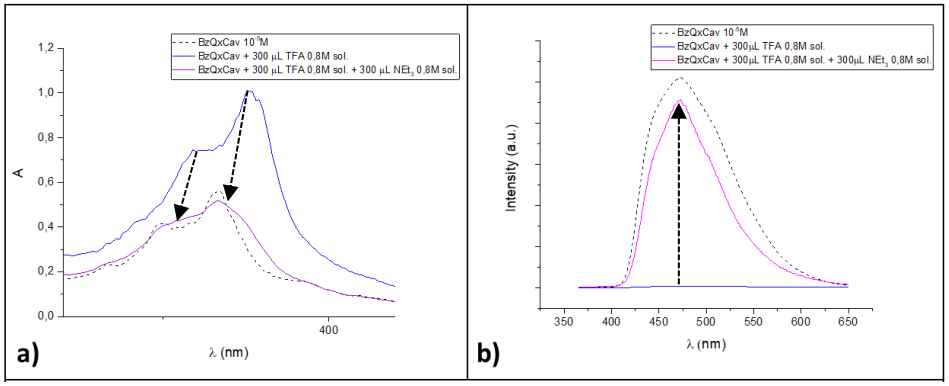

Figure 2.11 *Changes of the UV absorption and Fluorescence emission of **5** ([**5**] = $1 \cdot 10^{-5}$ M) in DCM upon addition of TFA and NEt_3. T = 298 K.*

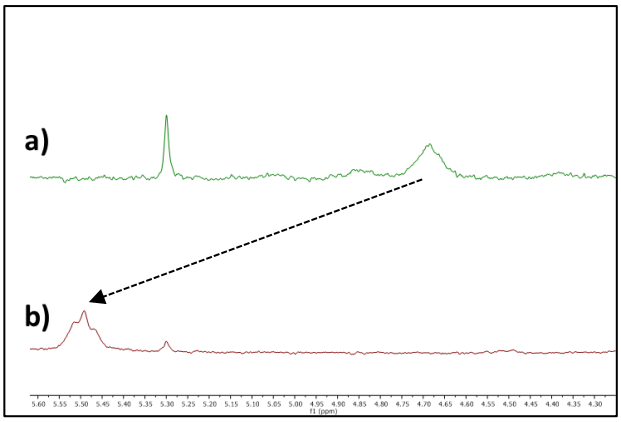

Figure 2.12 *Methine shift over pH perturbations at 298K a) ^{1}H-NMR of **5** + 40 eq. TFA in $CDCl_3$, b) ^{1}H-NMR of **5** + 40 eq. TFA + 60 eq. NEt_3 in $CDCl_3$ at 298K.*

2.2.4 PAH removal ability of cavitand 5

- *SPME Extractions*

Solid phase micro extractions (SPME) were performed in order to evaluate the PAH removal ability of cavitand **5** in water. Commercial silica fibers were coated with fine powdered benzoquinoxaline cavitand **5**, using an epoxy resin as glue. The same protocol was used to functionalize the commercial silica fibers with a quinoxaline cavitand to be used as comparison in the subsequent analyses. Once the fiber surface coating was completed, the fibers were closed in a sealed vial and soaked into a laboratory sample of contaminated water containing 20 ng/L of all the 16 most monitored PAH pollutants: acenaphthene, benzo[ghi]perylene, chrysene, acenaphthylene, benz[a]anthracene, benzo[b]fluoranthene, anthracene, fluorene, pyrene benzo[k]fluoranthene, benzo[a]pyrene, fluoranthene, indeno[1,2,3-cd]pyrene, naphthalene, phenanthrene, dibenz[a,h]anthracene.

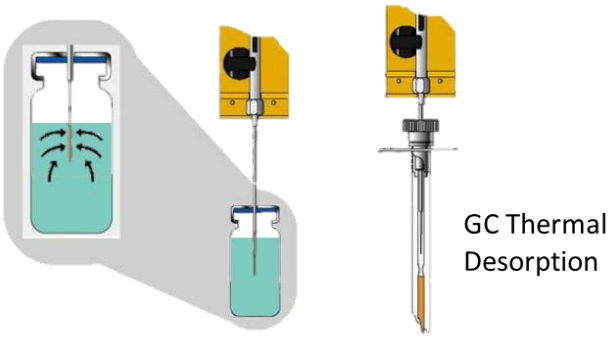

Figure 2.13 *SPME procedure followed in the PAH uptake analysis.*[22]

The incubation was performed for 30 minutes at room temperature, and then the fibers were treated at 300 °C in a GC inlet to provide thermal desorption of the adsorbed pollutants (**Figure 2.13**). The performances of cavitand **5** were compared with those of QxCav and PDMS 30, the commercial polymer currently used for the detection of PAH in water. Three replicated measurements for each substrate were performed.

The obtained response factors were used to correct the obtained GC data, in order to verify the efficiency of **5** in removing PHAs from water, and the obtained results reported in **Figure 2.14**. Each bar represents the amount of pollutants removed from water.

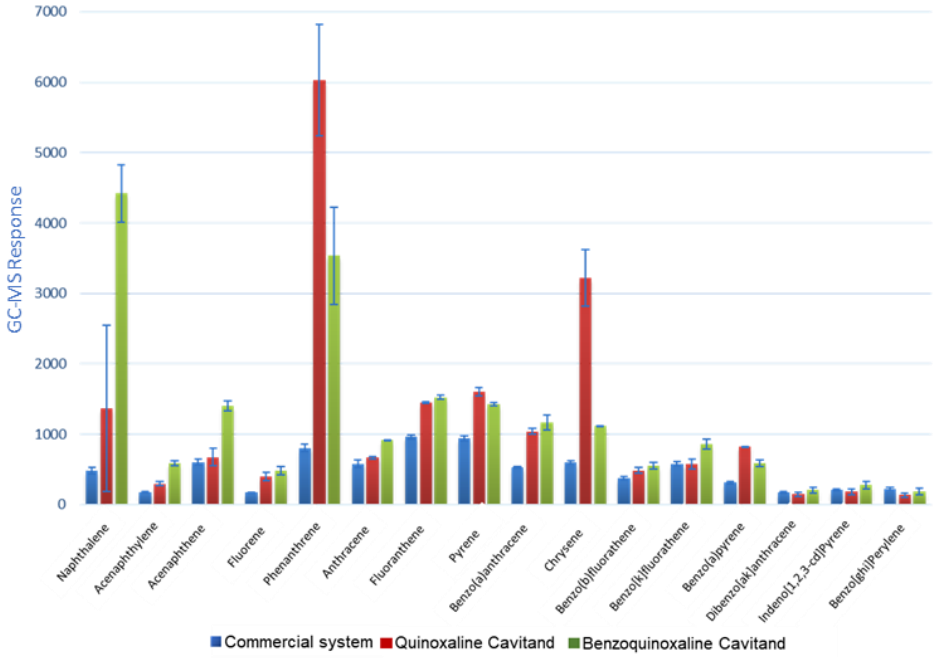

Figure 2.14 *Desorption profile of **5** (green bar), **QxBox** (red bar) and PDMS 30 (blue bar) SPME fibers performed at 300°C.*

As shown in **Figure 2.14** it is evident the better performances of cavitand **5** and QxCav over the commercial material in the PAHs' removal from water.
In particular, cavitand **5** showed a remarkable higher selectivity towards naphthalene, acenaphthylene acenaphthene, anthracene and benzo[k]fluorathene, meanwhile tetraQxCav was more selective towards phenanthrene, chrysene and benzo(a)pyrene.
Performances of the three coatings are comparable for the bulkiest polycyclic aromatic hydrocarbons such as dibenzo[a,k]anthracene, indeno[1,2,3-cd]pyrene, and benzo[ghi]perylene. Probably, the bulkiness of these compounds limits their uptake in the hydrophobic cavity, thus levelling out the performances of the two molecular receptors with those of the commercial fiber.

The deep benzoquinoxaline-based cavity showed a higher affinity towards the PAHs presenting almost linear structures in the first three aromatic rings. As for the QxCav, a higher selectivity towards phenantrene, chrysene and benzo(a)pyrene, which present an angular structure starting in the second aromatic ring, is observed. This is probably due to the larger entrance of the QxCav cavity respect to the cavity of receptor 5 (see paragraph 2.2.2).

- *Electrospun Fibers as Filtering Materials*

The positive results obtained with the SPME experiments prompted us to develop and test new polymeric membranes functionalized with receptor **5** able to remove in an efficient way PHAs from contaminated water.
Important features of a good absorbent material are a large porous structure and a high surface area, necessary to guarantee efficient absorption and high flow rate. In addition, water filtration on polymeric membranes represents a challenge for what concern the material mechanical properties; mechanical resistance and elasticity are pivotal to retain the capability and to avoid material leak or fragmentation in the filter.
Nonwoven materials made by micrometric fibers obtained by the electrospinning technology exhibit remarkable properties such as high area surfaces induced by a complex porous architecture, high flexibility and optimal mechanical strength.[23,24]
In this context, we turned our attention to electrospinning technology, which plays a central role in the design and development of new filtrating materials for pollutant removal.
Electrospinning is a relatively simple technique to produce very thin fibers. It is based on the application a high voltage electric field between a polymer solution coming out from a capillary or a nozzle and a collector. Once the electric field intensity increases, the hemispherical surface of the liquid at the end of the capillary extends and forms a conical shape known as Taylor cone. (**Figure 2.15**). By increasing the electric field further, the critical value at which the repulsive electrostatic force overcomes the surface tension is reached, and a flying jet of charged filament spurts out at the end of the Taylor cone. The strand of polymer solution starts a process of instability and lengthening, during which solvent evaporates. The fibers are then deposited on the collector and a non-woven mats is produced. .[25]

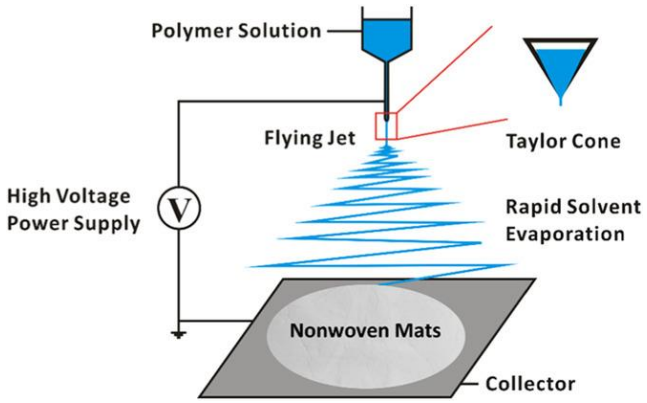

Figure 2.15 *Scheme of the Electrospinning process technique.*[26]

In collaboration with Prof. Chiara Gualandi from the Chemistry Department of the University of Bologna, we prepared a series of new filtrating materials via electrospinning of a solution of DMF containing the 10% m/V of a mixture of polyacrylonitrile/cavitand **5** (97:3 w/w or 94:6 w/w) (see *Experimental Section* for fibers preparation).
The electrospun fibers both unfunctionalized and functionalized were used in a frit-type filter as membranes to filter 10 mL of a water solution contaminated with 16 PAHs (acenaphthene, benzo[ghi]perylene, chrysene, acenaphthylene, benz[a]anthracene, benzo[b]fluoranthene, anthracene, fluorene, pyrene benzo[k]fluoranthene, benzo[a]pyrene, fluoranthene, indeno[1,2,3-cd]pyrene, naphthalene, phenanthrene, dibenz[a,h]anthracene) in concentration of 100 ppt each. A constant filtration flux (0.16 mL/s) was used to guarantee a proficient filtrating action towards the target pollutants. Three replicated measurements for each electrospun material were performed. PDMS-30 solid-phase micro extractions were performed to analyze the PAHs residual concentration in the filtered waters. Incubation was conducted by soaking the PDMS-30 fibers into the residual water for 45 minutes at room temperature. Subsequently, the fibers were desorbed at 270-300 °C and the resulting volatiles analyzed by GC-MS.
In **Figure 2.16** the analyses results are reported as % of pollutant removed from the water.

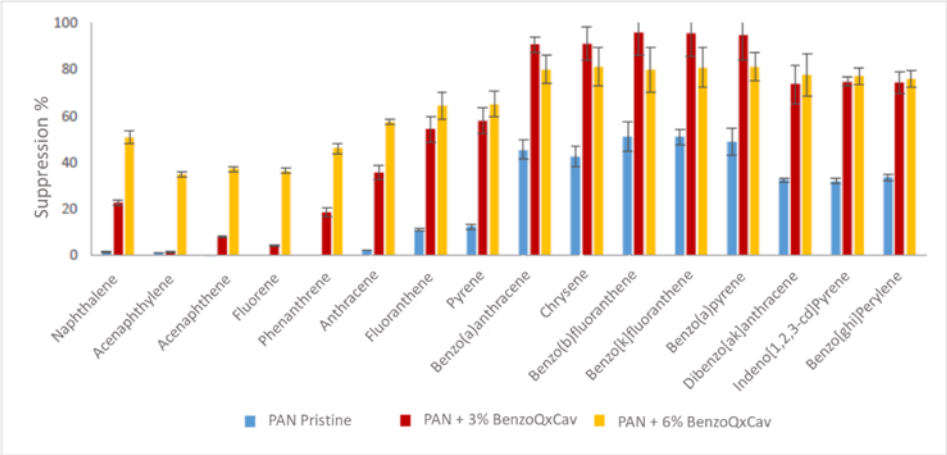

Figure 2.16 *Suppression profile of PAN Electrospun Fibers (blue bar), PAN Electrospun Fibers@3% BzQxCav (red bar) and PAN Electrospun Fibers@6% BzQxCav (yellow bar).*

As shown in Figure 2.17, the unfunctionalized PAN mats (*blue bar*) exhibited the worst performances. In particular, the lighter polycyclic aromatic pollutants (128 – 202 Da) were not absorbed by the PAN, while some effect was observed towards the high M_W PAHs, which were removed from water up to 50%. PAN fibers containing 6% of **5** (*yellow bar*) showed the best performance in the removal of the lighter PAHs, much better than PAN fibers charged with the 3% of the receptor in (*red bar*). As reported in **Figure 2.16**, 6% charged material absorbed up to 60% of lower molecular weight PAHs. It is interesting to note that both the functionalized PAN fibers removed in a very efficient way, up to 95%, the heaviest PAHs. This trend, observed for the heavier and bulky aromatic pollutants, clearly shows the occurrence of an additional absorption process. The concomitant drop of differences between the two functionalized PANs with the progressive increment in the absorbing abilities of the unfunctionalized PAN indicates the existence of a physisorption process that favors the absorption of the heavier pollutants. Therefore, not all the PAHs' removal can be attributed exclusively to cavity inclusion, particularly for the high M_W PAHs. For these PHAs, the sum of the chemisorption and physisorption process leads to their almost complete removal.

2.3 Conclusions

In this Chapter we reported the synthesis, the crystal structure and the the complexing abilities studies of a new deep benzoquinoxaline-bridged cavitand (cavitand **5**). Cavitand **5** was prepared in a single step by bridging resorcinarene **4** with four 2,3-dichlorobenzoquinoxaline walls (compound **3**). Solution and solid-state studies revealed that cavitand **5** is in the *vase* conformation at room temperature. The obtained crystal structure allowed to calculate the cavity dimensions, which resulted to be 8.3 Å deep, thus 2.3 Å deeper than the cavity of the standard QxCav. Using the computational software YASARA, Depth and Caver, an accessible internal volume of the cavity of 247 $Å^3$ was estimated, a free-volume suitable to host bulky guests. The pH driven *vase-kite* equilibrium of **5** and its reversibility was determined independently via ^{1}H-NMR, UV-Vis and fluorescence spectroscopy. Fluorescence analysis showed a decreasing of the fluorescence emission intensity during the conformational switch of the cavitand from the *vase* to the *kite* form, without any wavelength shift of the emission maximum, in contrast with the behavior of the tetraquinoxaline cavitand.

The PAHs' removal ability in water of cavitand **5** was evaluated and tested through SPME experiments, comparing the performances of **5** with the less deep QxCav and the commercial fiber PDMS 30. The obtained results highlighted that the performances of **5** were better respect to the commercial SPME fibers and showed the high selectivity of cavitand **5** towards polycyclic aromatic hydrocarbons with a linear structure in the first three aromatic ring and an angular evolution in the following ones. Lower selectivity was observed for PAHs having an angular structure starting in the second aromatic ring and towards bulkier species.

Given the promising results obtained with SPME extractions, cavitand **5** was embedded in PAN electrospun fibers. Electrospun PAN fibers were functionalized during the electrospinning process with 3% w/v and 6% w/v of cavitand **5**. Taking advantages of the high surface area provided by the electroctrospinning technique, we tested the PAN-based materials as filters in the purification of PAHs contaminated waters. The tests were performed comparing the removal properties of the unfunctionalized material with the functionalized PAN-fibers. The analytes removal was evaluated by GC-MS analysis, and the results demonstrated the molecular recognition ability of **5** towards lighter PAHs. As

expected, the 6% loaded fiber collected more PAHs than the 3% one, allowing the removal of almost the 60% of the lower molecular weight pollutants. Upon increase in the molecular weight and bulkiness of the aromatic pollutants, physisorption became dominant. The combined effects of molecular inclusion and polymer physisorption led to an efficient removal of the entire class of PAHs micropollutants.
Further tests and studies are now in progress to evaluate the influence of morphology and the porous architecture of the PAN fibers on the PAH removal efficiency.

2.4 Acknowledgments

Special thanks to Prof. Chiara Massera from Parma University for the crystal structure determination, to Prof. Chiara Gualandi from Bologna University for the production of the electrospun fibers, to Dr. Nicolò Riboni and Prof. Federica Bianchi from Parma University for SPME analysis.

2.5 Experimental Section

1,4-dihydrobenzo[g]quinoxaline-2,3-dione (*2*)[15,31]

A solution of oxalic acid (315 mg, 3.05 mmol) in 4N HCl (5 mL) was added to a solution of 2,3-diamino naphthalene **1** (500 mg, 3.2 mmol) in 4N HCl (5 ml), and the resulting mixture was refluxed for 15 hours. The reaction mixture was cooled to room temperature, and the resulting precipitate was filtered and washed with water until the complete pH neutralization. The precipitate was dried over vacuum. Product **2** was obtained as a light brown solid in quantitative yield (670.7 mg, 3.16 mmol).

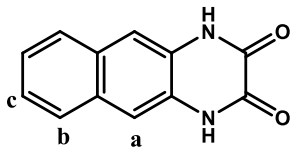

^{1}H NMR (300 MHz, DMSO-d_6): δ = 12.07 (s, 2H, **NH**), 7.83 (dd, *J* = 6.3, 3.3 Hz, 2H, $\mathbf{H_b}$), 7.54 (s, 2H, $\mathbf{H_a}$), 7.40 (dd, *J* = 6.3, 3.3 Hz, 2H, $\mathbf{H_c}$).

ESI-MS: m/z: calculated for $C_{12}H_9N_2O_2$ $[M+H]^+$ = 213.2
found = 213.5

2,3-dichlorobenzo[g]quinoxaline (*3*) [15,31]

To a suspension of **2** (670 mg, 3.16 mmol) in 1,2-dichloroethane (20 mL), thionyl chloride (1.13 mL, 16 mmol) and a catalytic amount of dimethylformamide were added. The mixture was heated to reflux for 12 hours. The reaction was quenched with methanol (50 mL) and the resulting precipitate was collected by filtration. Product **3** was recovered as a bright yellow solid in quantitative yield (382 mg, 3.16 mmol).

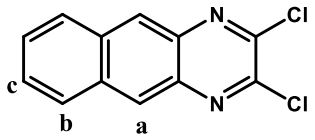

^{1}H NMR (300 MHz, $CDCl_3$): δ = 8.59 (s, 2H, **H_a**), 8.12 (dd, *J* = 6.5, 3.3 Hz, 2H, **H_b**), 7.65 (dd, *J* = 6.6, 3.2 Hz, 2H, **H_c**).

ESI-MS: m/z: calculated for $C_{12}H_7N_2Cl_2$ $[M+H]^+$ = 250.1
found = 250.7

Resorcinarene [C_6H_{13}; H] (*4*)[32]

To a solution of resorcinol (10 g, 90.8 mmol) and n-heptaldehyde (12.2 mL, 90.2 mmol) in MeOH (75 ml), a 37% solution of HCl (18 mL) was added dropwise over 30 min at 0°C. After the addition, the reaction mixture was stirred at 55°C for 5 days. The reaction was quenched with water, filtered and dried under vacuum, obtaining an orange powder. The crude product was used in the subsequent reaction without further purification.

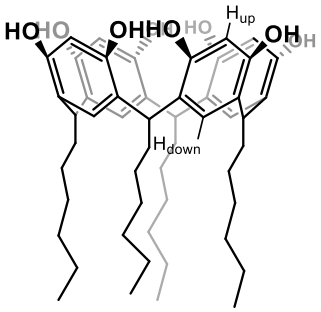

^{1}H-NMR (400 MHz Acetone-d_6,): δ = 8.41 (s, 8H, ArO**H**), 7.53 (s, 4H, Ar**H_{up}**), 6.20 (s, 4H, Ar**H_{down}**), 4.27 (t, 4H, J=7.8 Hz, ArC**H**), 2.26 (q, 8H, J=7.8 Hz, CHC**H_2**CH_2), 1.31- 1.24 (m, 32H, C**H_2**), 0.85 (t, 12H, J=6.9 Hz, CH_2CH_2**CH_3**);

ESI-MS: m/z: calculated for $C_{52}H_{72}O_8Na$ = 847.5 $[M+Na]^+$
found = 847.5

Benzoquinoxaline Cavitand (*5*)

To a solution of resorcinarene **4** (242 mg, 0.293 mmol) dissolved in dry DMF (12 mL), potassium carbonate (405 mg, 2.93 mmol) and **3** (321 mg, 1.29 mmol) were added. The mixture was stirred for 12 hours at 80°C. The reaction was quenched in water (50 mL). The obtained light brown precipitate was recovered by filtration and subsequently purified by crystallization from ethyl acetate. Product **5** was recovered as a light-yellow solid powder in 83% yield (372 mg, 0.243 mmol).

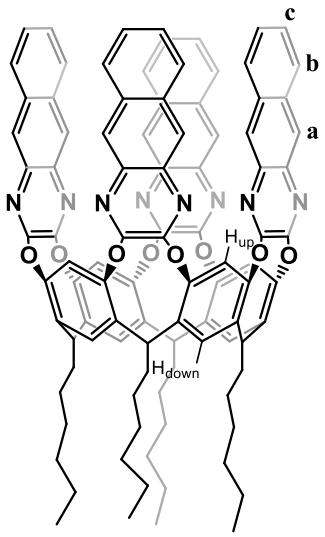

^{1}H NMR (300 MHz, $CDCl_3$): δ = 8.24 (s, 8H, **H_a**), 8.18 (s, 4H, Ar**H_{up}**), 7.72 (dd, *J* = 6.5, 3.3 Hz, 8H, **H_b**), 7.37 (dd, *J* = 6.6, 3.2 Hz, 8H, **H_c**), 7.22 (s, 4H, Ar**H_{down}**) 5.49 (t, *J* = 8.0 Hz, 4H, ArC**H**), 2.35 – 2.20 (m, 8H, CHC**H_2**CH_2), 1.54 – 1.21 (m, 32H, C**H_2**), 0.98 – 0.85 (m, 12H, CH_2C**H_3**).

^{13}C NMR (101 MHz, CD_2Cl_2) δ 152.29, 136.47, 135.72, 133.82, 133.06, 127.96, 126.57, 125.79, 72.54, 34.71, 32.28, 31.88, 29.39, 27.91, 22.70, 13.87.

MALDI-TOF : m/z: calculated for $C_{100}H_{89}N_8O_8$ $[M+H]^+$ = 1530.8295
found = 1530.8303

X-Ray Data Collection

The crystal structure of the benzoquinoxaline cavitand **5** was determined by X-ray diffraction methods. Crystal data and experimental details for data collection and structure refinement are reported in **Table 2.1**.

Intensity data and cell parameters were recorded at 190(2) K on a Bruker ApexII diffractometer equipped with a CCD area detector, using the MoKα radiation (λ = 0.71073). The raw frame data were processed using the programs SAINT and SADABS[27]. The structure was solved by Direct Methods using the SIR97 program[28] and refined on F_o^2 by full-matrix least-squares procedures, using the SHELXL-2014/7 program[29] in the WinGX suite v.2014.1.[30] All non-hydrogen atoms were refined with anisotropic atomic displacements, with the exception of some atoms belonging to the disordered DMF solvent molecules. The carbon-bound H atoms were placed in calculated positions and refined isotropically using a riding model with C-H ranging from 0.95 to 0.99 Å and Uiso(H) set to 1.2/1.5Ueq(C). The weighting scheme used in the last cycle of refinement was $w = 1/ [\sigma^2 F_o^2 + (0.20000P)^2]$ where $P = (F_o^2 + 2F_c^2)/3$.

Compound	Cavitand 5
empirical formula	$C_{106}H_{102}N_{10}O_{10}$
M	1675.97
crys syst	Monoclinic
space group	$P2_1/n$
a/Å	12.654(2)
b/Å	18.061(2)
c/Å	40.271(5)
□/°	98.366(7)
V/Å^3	9106(2)
Z	4
T/K	190(2)
ρ /g cm^{-3}	1.223
□ /mm^{-1}	0.079
F(000)	3552
total reflections	73502
unique reflections (R_{int})	14232 (0.2085)
observed reflections $[F_o>4\sigma(F_o)]$	5641
GOF on F^{2a}	1.000
R indices $[F_o>4\sigma(F_o)]^b R_1$, wR_2	0.1120, 0.2833
largest diff. peak and hole (eÅ^{-3})	1.197, -0.398

Table 2.1 Crystal data and structure refinement information for cavitand **5**.

[a]Goodness-of-fit S = $[\Sigma w(F_o^2-F_c^2)^2/ (n-p)]1/2$, where n is the number of reflections and p the number of parameters. [b]$R_1 = \Sigma \| F_o | - | F_c \| / \Sigma | F_o |$, $wR_2 = [\Sigma[w(F_o^2-F_c^2)^2]/\Sigma[w(F_o^2)^2]]^{1/2}$.

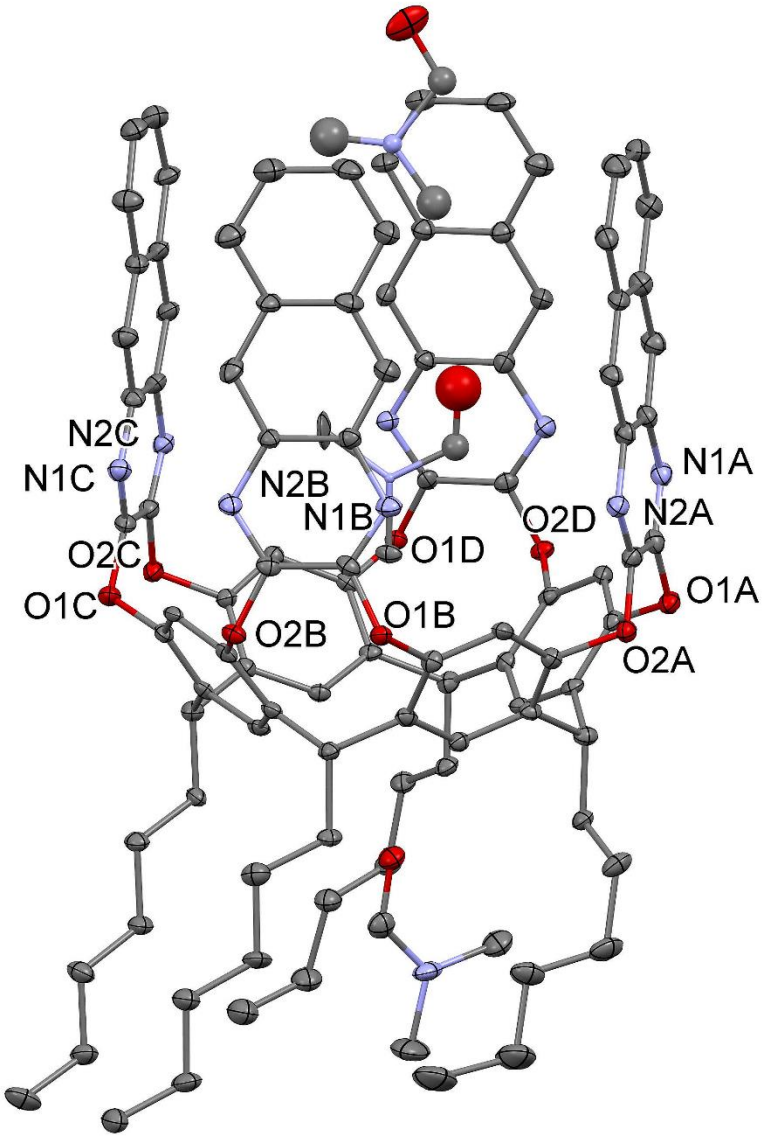

Figure 2.17. *Ortep view of cavitand* ***5*** *with ellipsoids drawn at the 20% level. H atoms have been omitted for clarity. The two DMF molecules inside the cavity have occupancy 0f 0.5 each.*

SPME Procedure using Cavitand 5

Preparation of the fibers: cavitand **5**, in the form of fine powder, was placed on a silicon support with the help of an epoxy resin resistant at high temperature.
Before use fibers were conditionated at 270°C in the GC inlet for 2h under helium flow to remove any trace of impurities.
Experiments were carried out by direct immersion technique in 10 mL glass vial containing 9.5 mL of the sample solution spiked with internal standard at the concentration of 20 ng/L.
Desorption was performed at 300 °C for 5 minutes.

GC-MS analysis
Gas-chromatograph HP 6890 Series Plus, Agilent Technologies (Milan, Italy) supplied with a PAL Combi Xt autosampler (Agilent Technologies):
- Column: RXi-17Sil MS (l=30 m, i.d.=0.25 mm, d.f.=0.25 µm) (Restek, Bellefonte, PA, USA);
- Carrier gas: helium
- Carrier gas flux: 1 mL/min
- Carrier gas pressure: 70 KPa.
- Injector Temp: 270-300°C
- Injection mode: splitless
-Temperature program: initial temperature 110° (15°C/min until 220°C) and then 4°C/min until 320°C. Isothermal for 5 min.

Mass Spectrometer MSD 5973, Agilent Technologies:
- Source Temperature: 150°C;
- Transfer Line temperature: 280°C;
- Ionization: E.I. (70 eV);
-Voltage: 2200 V;
-Acquisition modality: Time scheduled monitoring;
-Monitored ions: Range from 40 to 400 m/z

- Monitored ions PAHs (SIM):
from 2 to 5 min: 128, *m/z* for Naphthalene;
from 5 to 8.50 min: 152, 153 and 166 *m/z* for Acenaphthylene, Acenaphthene, Fluorene;
from 8.50 to 11 min: 178 *m/z* for Phenanthrene, Anthracene;
from 11 to 17 min: 202 m/z for Fluoranthene, Pyrene;

from 17 to 22 min: 228 m/z for Benzo[a]anthracene, Chrysene;
from 22 to 30 min: 252 m/z for Benzo[b]fluoranthene, Benzo[k]fluoranthene, Benzo[a]pyrene;
from 30 to 37.33 min: 276, 278 m/z for Indeno[1,2,3-c,d]pyrene, Dibenzo[a,h]anthracene, Benzo[g,h,i]perylene.

Fabrication of Polyacrylonitrile Electrospun fibers charged with Tetrabenzoquinoxaline cavitand 5

Instrumentation

The home-made electrospinning apparatus is composed of a SL 50 P10/CE/230 high voltage power supplier (Spellman, New York, USA), a KDS-200 syringe pump (KD Scientific Inc., Massachusetts, USA), a glass syringe containing the polymer solution, a stainless-steel blunt-ended needle (Hamilton, Bonaduz, Switzerland) connected with the power supply electrode and a grounded cylindrical aluminum collector (length = 10 cm, diameter = 5 cm, rotating at 50 rpm).

a) Electrospun fibers charged with 3% *w/v* Tetrabenzoquinoxaline cavitand 5

The polymer solution was dispensed through a Teflon tube to the needle that was orthogonally placed on the rotating cylindrical collector. To fabricate PAN mats the starting polymeric solution was prepared by dissolving a mixture polyacrylonitrile/Tetrabenzoquinoxaline cavitand **5** (97:3 w/w) in DMF (10% m/V), by using a G24 needle and by applying a voltage of 13 kV, a needle-to-collector distance of 20 cm and a flow rate of 1.2 mL/h. The obtained electrospun mats had a final dimension of about 15 × 15 cm^2 and a thickness in the range 70–100 μm.

b) Electrospun fibers charged with 6% *w/v* Tetrabenzoquinoxaline cavitand 5

The polymer solution was dispensed through a Teflon tube to the needle that was orthogonally placed on the rotating cylindrical collector. To fabricate PAN mats

the starting polymeric solution was prepared by dissolving a mixture polyacrylonitrile/Tetrabenzoquinoxaline cavitand **5** (94:6 w/w) in DMF (10% m/V), by using a G24 needle and by applying a voltage of 13 kV, a needle-to-collector distance of 20 cm and a flow rate of 1.2 mL/h. The obtained electrospun mats had a final dimension of about 15 × 15 cm^2 and a thickness in the range 70–100 μm.

2.6 References

1. Lawal, A. T. Polycyclic aromatic hydrocarbons. A review. *Cogent Environ. Sci.* **3**, 1–89 (2017).

2. Qiao, M. *et al.* Chemosphere Impact of secondary ef fl uent from wastewater treatment plants on urban rivers : Polycyclic aromatic hydrocarbons and derivatives. *Chemosphere* **211**, 185–191 (2018).

3. Fan, Z. & Lin, L. Exposure Science : Contaminant Mixtures. *Encycl. Environ. Heal.* 645–656 (2011).

4. Abdel-shafy, H. I. & Mansour, M. S. M. A review on polycyclic aromatic hydrocarbons : Source , environmental impact , effect on human health and remediation. *Egypt. J. Pet.* **25**, 107–123 (2016).

5. Gehle, K., MD & MPH. Toxicity of Polycyclic Aromatic Hydrocarbons. *Agency Toxic Subst. Dis. Regist.* 1–68 (2012).

6. Lestingi, C., Tavoloni, T., Bardeggia, V. & Perugini, M. Food Additives & Contaminants : Part A A fit-for-purpose method to monitor 16-EU-PAHs in food - results of five years official food control in two Italian regions. *Food Addit. Contam. Part A* **0**, (2017).

7. Keith, L. H. The Source of U.S. EPA's Sixteen PAH Priority Pollutants. *Polycycl. Aromat. Compd.* 37–41 (2014).

8. Union, C. of the E. COUNCIL DIRECTIVE 98/83/EC of 3 November 1998 on the quality of water intended for human consumption. *Off. J. Eur. Communities* 32–54 (1998).

9. Rodriguez-Narvaez, O. M., Peralta-Hernandez, J. M., Goonetilleke, A. & Bandala, E. R. Treatment technologies for emerging contaminants in water: A review. *Chem. Eng. J.* **323**, 361–380 (2017).

10. Locatelli, M. *et al.* Extraction and Detection Techniques for PAHs Determination in Beverages : A Review. *Curr. Chromatogr.* **1**, 122–138 (2014).

11. Dalcanale, E., Costantini, G. & Soncini, P. Removal of Organic Pollutants from Water via Molecular Inclusion within a Cavitand. *J. Incl. Phenom. Mol.*

Recognit. Chem. **13**, 87–92 (1992).

12. Bertani, F. *et al.* Triptycene-Roofed Quinoxaline Cavitands for the Supramolecular Detection of BTEX in Air. *Chem. - A Eur. J.* **22**, 3312–3319 (2016).

13. Trzcinski, W. J. *et al.* In Search of the Ultimate Benzene Sensor: The EtQxBox Solution. *ACS Sensors* **2**, 590–598 (2017).

14. Moran, J. R. *et al.* Vases and Kites as Cavitands. *J. Am. Chem. Soc.* **113**, 5707–5714 (1991).

15. Berryman, O. B., Sather, A. C. & Rebek, J. A deep cavitand with a fluorescent wall functions as an ion sensor. *Org. Lett.* **13**, 5232–5235 (2011).

16. Krieger, E. & Vriend, G. Increasing the Precision of Comparative Models with YASARA NOVA — a Self-Parameterizing Force Field. *PROTEINS Struct. Funct. Genet.* **47**, 393–402 (2002).

17. Tan, K. P., Varadarajan, R. & Madhusudhan, M. S. DEPTH : a web server to compute depth and predict small-molecule binding cavities in proteins. *Nucleic Acids Res.* **39**, 242–248 (2011).

18. Chovancova, E. *et al.* CAVER 3.0 : A Tool for the Analysis of Transport Pathways in Dynamic Protein Structures. *PLOS Comput. Biol.* **8**, 23–30 (2012).

19. Skinner, P. J., Cheetham, A. G., Beeby, A., Gramlich, V. & Diederich, F. Conformational switching of resorcin[4]arene cavitands by protonation: Preliminary communication. *Helv. Chim. Acta* **84**, 2146–2153 (2001).

20. Moran, J. R. *et al.* Vases and Kites as Cavitands. *J. Am. Chem. Soc.* **113**, 5707–5714 (1991).

21. Torelli, M. *et al.* Mechanically-Driven Vase – Kite Conformational Switch in Cavitand Cross-Linked Polyurethanes. *ChemistryOpen* **9**, 261–268 (2020).

22. Yean-Woong, Y. Sensitive Detection of 2-MIB and Geosmin in Drinking Water. *Agil. Technol.* (2012).

23. Jia, Y. *et al.* Organogel Coupled with Microstructured Electrospun Polymeric Nonwovens for the Effective Cleaning of Sensitive Surfaces.

Appl. Mater. Interfaces **12**, 39620–39629 (2020).

24. Pagnotta, G. *et al.* Materials Science & Engineering C Nanodecoration of electrospun polymeric fibers with nanostructured silver coatings by ionized jet deposition for antibacterial tissues. *Mater. Sci. Eng. C* **113**, 1–18 (2020).

25. Cipitria, A., Skelton, A., Dargaville, T. R., Dalton, P. D. & Hutmacher, D. W. Design, fabrication and characterization of PCL electrospun scaffolds—a review. *J. Mater. Chem.* **21**, 9419–9453 (2011).

26. Zhang, C., Li, Y., Wang, P. & Zhang, H. Electrospinning of nanofibers : Potentials and perspectives for active food packaging. *Compr. Rev.* **19**, 479–502 (2020).

27. *SADABS Bruker AXS; Madison, Wisconsin, USA, 2004; SAINT, Software Users Guide, Version 6.0; Bruker Analytical X-ray Systems, Madison, WI (1999). Sheldrick, G. M. SADABS v2.03: Area-Detector Absorption Correction. University of Göttingen, Germany, 1999.* (1999).

28. Altomare, A. *et al.* SIR 97 : a new tool for crystal structure determination and refinement. *J. Appl. Chrystallography* **32**, 115–119 (1999).

29. Sheldrick, G. M. A short history of SHELX. *Acta Crystallogr. Sect. A* **A64**, 112–122 (2008).

30. Farrugia, L. J. WinGX and ORTEP for Windows : an update. *J. Appl. Crystallography* **45**, 849–854 (2012).

31. Beaulieu, F. *et al.* Synthesis and biological evaluation of 4-amino derivatives of benzimidazoquinoxaline, benzimidazoquinoline, and benzopyrazoloquinazoline as potent IKK inhibitors. *Bioorganic Med. Chem. Lett.* **17**, 1233–1237 (2007).

32. Abis, L., Dalcanale, E., Du Vossel, A. & Spera, S. Structurally New Macrocycles from the Resorcinol-Aldehyde Condensation. Configurational and Conformational Analyses by Means of Dynamic NMR, NOE, and T1 Experiments. *J. Org. Chem.* **53**, 6046–6050 (1988).

CHAPTER 3

SURFACE ACTIVATION OF 3D-PRINTED MEMBRANES

3.1 - Introduction

The world is thirsty. Using these words during the celebrations for the 2017 World Water Day, FAO general director Helena Semedo warned the world about the relevant and transversal issue concerning the increase of water shortage worldwide. UN estimated almost 2 billion of people are living in water stressed countries.[1] Demographic growth occurred in last decades combined with an aggressive urbanization, uncontrolled pollutant spilling, and the incoming climate changing negatively affected the availability of good quality waters. This issue reached critical levels in several area of the planet, pushing many university and research centers to develop a series of new technologies and devices for limiting environmental pollution. Being water an essential element for life, in the last years the researchers started to focus their attention on the quality of waters, and on new strategies to mitigate the pollution of wastewaters. This new trend is driven by the concomitant increase of social sensibility towards environmental topics and actions to stop the climate changing, boosting the development of new performant technologies and devices for an effective water pollutants removal.[2]

The water chemical pollutants can be divided in two main groups: macropollutants, usually found in concentration of mg/L, and the wide class of micropollutants present only in traces.[3] Micropollutants are a wide category of chemicals characterized by a huge structural and functional variability, usually found in water in concentrations below ppm or ppb levels. Their high toxicity, even at low concentrations, is related to their high stability and low bio-degradability and the deriving bio-accumulation effects.[4] Micropollutants structural and functional variability, combined with low concentrations, lead to a wide range of interactions with the environment and human life, making more difficult their complete removal. This leads to the necessity of multidisciplinary approach to tackle the issue.

Present treatments used to remove water pollutants are based on chemical, physical and biological methods. The choice of the purifying treatment is strongly related to the pollutant class and consequently to its chemical nature.[2] The kind of water quality and its final application or discharge are additional relevant parameters for the choice of the proper purification treatment.

The most applied technologies to remove pollutants from water are ozonation[5,6], advanced oxidation[7], membrane adsorption and membrane filtration processes[8]. Very often these techniques are used in combination to maximize the effect or to remove altogether different pollutant classes[9]. Between all of them, the most promising and most effective techniques in the water pollution removal are ozonation and advanced oxidation. High stability and low bio-degradability pollutants are easily removed using these techniques. A remarkable disadvantage affecting these techniques is the formation of more-toxic by-products, when there is no a strict control on the ozonation or oxidation processes.[10]

This limitation can be overcome through the application of water purifying treatments based on adsorption mechanism, an effective method characterized by several advantages such as low prices, ease of development, the opportunity to treat high concentration of pollutants and high efficiency. The most used absorbing materials are the activated carbons (ACs), widely used as performing systems in the pollutant removal.[11] ACs are easily integrated in wastewater treatment plants, and they are characterized by low prices and high purifying efficiency. The removal mechanism is based on a physisorption process over the membrane. The dark sides of the activated carbons are the high regeneration prices, the low rate purifying processes and the partial regeneration of the original removal properties.[12,13]

Besides the AC treatment, we can identify several purifying processes, already used in wastewater treatment plants and based on adsorption mechanisms. Microfiltration, nanofiltration and ultrafiltration are a class of adsorbing treatment widely use in the pollutant removal field, and many times combined together to extend the purification effect.[14] Other remarkable techniques are reverse osmosis treatment, membrane reactors systems and reverse electrodialysis.[15,16]

Interactions between the pollutant species and the membrane play a key role in the definition of good performances in the removal process. Fundamental pollutant parameters are the chemical-physical properties such as molecular weight, water solubility, polarity, electrostatic behavior, octanol/water partition coefficient. The presence of structural complementarity between the pollutants and the membrane functional groups is also extremely important. [17]

Pore size and their distribution in the membrane are relevant parameters to control and to improve the inner surface area and consequently to reach a higher contact between the absorbing material and the polluted water.[18]
Metal-organic frameworks, new functional polymers, covalent organic polymers, modified porous silica are widely studied as absorbing agents and their properties were explored in depth.[19–22]
Metal-organic frameworks are able to detect and entrap inside their channels several pollutants present both in water and in the gas phase.
Queen and co-workers synthesized a water stable metal-organic framework/polydopamine composite showing a rapid and selective removal of large amount of heavy metals, such as Pb^{2+} and Hg^{2+}.[23] Using this strategy, they combined the advantages of the high porous structure of the MOF with the metal-coordination ability of the polydopamine (**Figure 3.1**).

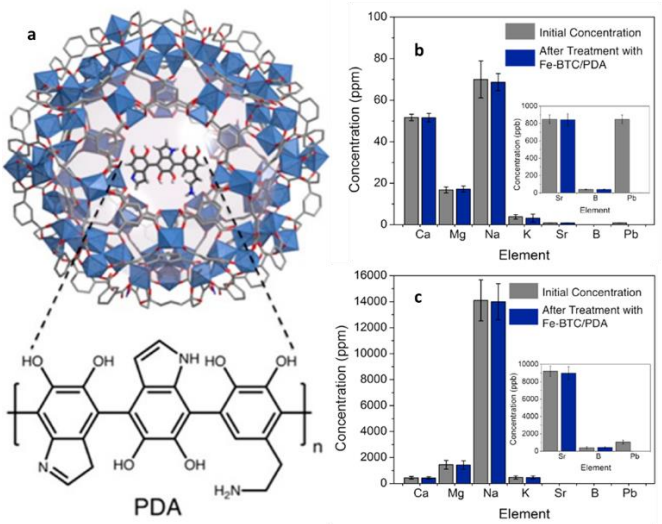

Figure 3.1 *a) Fe-BTC/PDA-19, compositions of the real world samples b) Rhone River water and c) Mediterranean Sea water before and after treatment with Fe-BTC/PDA-19.*[23]

Despite of the high versatility of the MOF materials, their industrial application is limited by the difficulties in the synthesis on a large scale.

Great attention was focused on covalent organic polymers (COP) for their structural versatility. The possibility to develop materials with extremely complex geometry pores and elaborated inner morphology has led to a large diffusion as absorbers.[24]

The development of a new kind of porous polymers called polymers of intrinsic microporosity (PIM) by professor Neil McKeown constitutes a breakthrough in the field.[25,26] McKeown, using a simple aromatic nucleophilic substitution, synthesized a new class of rigid and porous polymers characterized by an extremely high control over pore size and distribution. The PIMs rigid backbone, composed by fused ring sequences stopped by non-planar angular sites, leads to a failure in the chains rearrangement providing to highly contorted shapes and complex organizations.

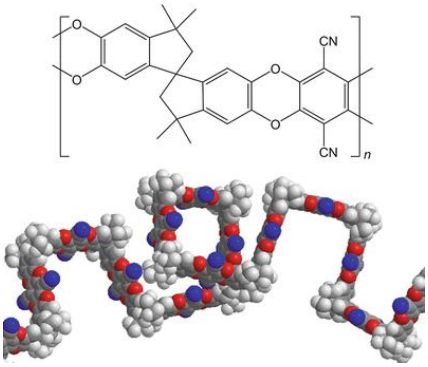

Figure 3.2 *a) McKeown's PIM-1, b) PIM-1 chain-rearrangement and generation of the typical porous internal structure*[26]

The large-scale production of this new class of polymers through a simple reaction has led to a real overtaking of PIM materials over the traditional porous systems such as MOF and COP. After the McKeown's discovery, several researchers started to modify and synthetize new PIM materials characterized by the presence of rigid concave cavities. Dichtel and collaborators developed a new β-cyclodextrin PIM polymer showing interesting properties in the removal in water of naphthalene and Bisphenol-A derivates (**Figure 3.3** *a*).[27] Dichtel and co-workers developed also

a resorcinarene-based PIM system, effective in the removal of chlorinated solvents and dioxane in water (**Figure 3.3** *b*).[28]

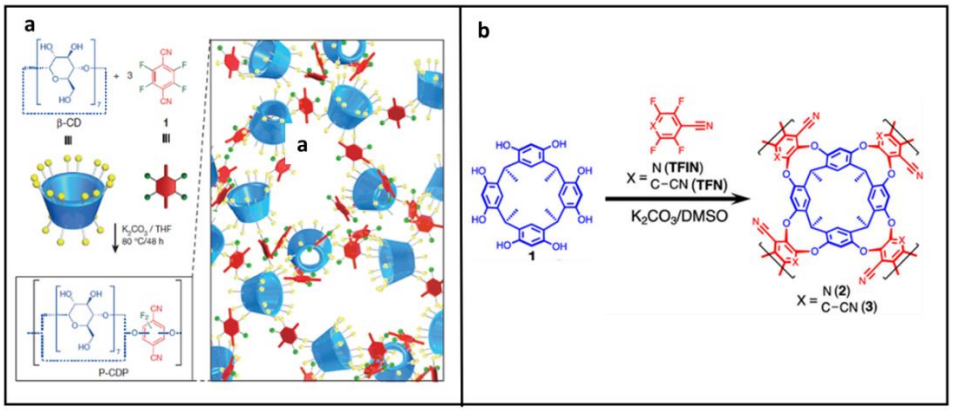

Figure 3.3 *Dichtel's modified PIM a) β-cyclodextrin-based polymer, b) Resorcinarene-based polymer*[27,28]

Trabolsi in the same period used the resorcinarene unit as a monomer to synthetize a new covalent organic polymer useful in the sea-water purification from oil-derivatives pollutants.[29]

Innovations in the advanced-material field were followed by an evolution in the design of new porous materials thanks to the development of new complex systems printed through the 3D printing technology.[30] 3D printing technology is a totally automated addictive manufacturing technique able to create tridimensional objects following a layer-by-layer printing process. The opportunity to create structures with high resolution in the pore design and complex internal morphology has prompted to a rapid diffusion of this technique in the pollutant removal field. Lau et al. using a 3D printer, developed a polydimethylsiloxane porous membrane charged with nanosilica, effective in the removal in water of oil derived pollutant.[31]

An additional advantage of the 3D printing technique is the ability to speed up the technology transfer from laboratory scale to the industrial production, as demonstrated by Sun and collaborator who founded a new start-up moving their idea of purifying membrane from their laboratory to a larger scale production.[32]

During this research project, we decided to develop a new series of polymeric and porous structure printed using the 3D printed stereolithography (SLA) technique,

followed by a covalent surface-functionalization with suitable molecular receptors useful in removal of organic aromatic and chlorinated pollutants, polycyclic aromatic pollutant and heavy metals. The final goal is a multifunctionalized membrane capable of removing all classes of micropollutants in a single treatment.

High-stability and low-biodegradability of permanent organic pollutants (POPs) like aromatic, chlorinated and polycyclic compounds lead to several difficulties during the removal with conventional treatments.[33]

For their uptake, we decided to use two different molecular receptors able to complex and sequestrate inside their cavities pollutant molecules present in water: the quinoxaline cavitand and the benzoquinoxaline cavitand. Their hydrophobic cavities can sequestrate suitable aromatic guest molecules thanks to a series of hydrophobic interactions like π-π and CH-π interactions, leading to the formation of host-guest complexes.[34,35]

For what concern the removal of heavy-metals pollutants, inspired by the Queen's work, we decided to develop a porous 3D printed structure active in the removal of heavy metals in water through a surface functionalization with a dopamine-based methyl methacrylamide.

In order to avoid the physical dispersion of molecular receptors inside the porous printed polymer matrix, this approach allows the reduction of the amount of the active species needed for the purifying processes, maintaining in the same time the advantages of an elaborated and complex porous scaffolds.

3.2 – 3D-Printing technology

Usually, when we talk about 3D-print we refer to a series of new productive techniques, born in the second half of the *XX* century, as a direct consequence of the digital revolution just started in those years. The growing diffusion of PC and highly sophisticated software gradually influenced and changed several productive sectors. The opportunity to introduce the automation in production, and remote control through digital systems has led to a series of new revolutions,

including the 3D-printing technology. The general definition of 3D-printing technology includes all the techniques based on the production of tridimensional objects using digital controlled automated systems.

The official origin of this technology goes back to the 1983, when Charles C. Hull developed a stereolithographic system, patented after three years in 1986.

But the real roots of the technique are to be found ten years before, when in 1977 the German engineers Swainson and Kremer submitted a patent on the first example in history of a project for the creation of 3D systems.[36] This concept model involved the exposure of a reactive monomer under pulse of light radiations with the proper wavelength in order to induce a radical polymerization and the creation of tridimensional objects. Just 4 years after the first idea, Hideo Kodama filed a patent related to a new 3D printing procedural method, described the following year in the paper "automatic method for fabricating a 3D plastic model with photo hardening polymer".[37] Kodame's printer was equipped with a Xenon lamp combined with optical fibers, fixed on a mobile plotter along the x-y plane. This optical system was able to induce the polymerization and curing of photo-hardening monomers mixed with photo initiators and UV-sensitizers. Paradoxically, the 3D-printing technology was attributed to Hull, the first one who, intuiting the relevance and the prospective, highlighted the attention on it, starting the real diffusion and commercialization of this technique.[38] After the first patent, Hull collaborating with the company 3D-System brought on the market the first model of 3D printer.

The Hull's patent was the real sparkle, which ignited the fire. The 90s were crashed by a total boom in the research and development of this new technology, bringing to the introduction of several new processes of addictive manufacturing and a series of technological improvements. The most relevant innovations were the Scott Crump's 3D fused deposition modelling, the Deckard's selective laser sintering printer, the Sachs's inkjet printing and the Feygin's laminated object manufacturing technique.[39–42]

3.2.1 - 3D-Print file

The 3D-printer is a powerful instrument able to move in the reality objects that were living only in a digital world. In order to reach this goal, the first essential step is the use of a computer-aided design software (CAD software) combined with a series of scanning data or in alternative several mathematical equations to create a digital 3D-model of the desired object.[43]
After the development of the 3D-model through a CAD software, the digital data are not directly sent to the printer, but firstly they are converted in a standard tessellation language file (STL).[44]

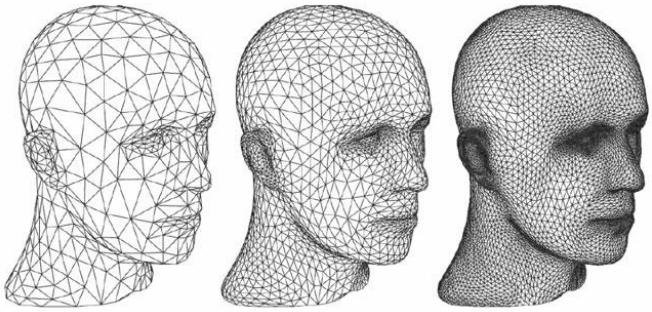

Figure 3.4 *CAD-aided digital tessellation process (with facets) of human face.*[45]

The STL file is obtained by a decomposing process over the digital 3D-objects in small triangles, followed by the conversion of all the triangles vertices (facets) in ASCII language.
Once completed the tessellation process, the following step is played by a slicing software, which starts to slice the 3D-structure in several and thin 2D layers. Every layer is characterized by the same thickness value that is strongly related to the instrument z-axis resolution.
The slicing data of the decomposed 3D shape are sent to the printer that will start with the reverse process of recombination. Paradoxically the printer re-creates and recombines the several 2D layers originated by the slicing software through a moving kart along well-defined positions and pathways. Following this

mechanism, the 3D printer allows the development of tridimensional structures through an accurate and progressive deposition of every layer over the previous one.

3.2.2 - Surface Modification of 3D printed structures

3D printing has been recently used for the fabrication of materials for environmental remediation. The design of 3D objects with a high porosity structure and customizable geometrical shape, followed by surface activation through suitable functionalization, discloses the horizons of this technique for environmental protection. Porosity of the printed material and the chemical composition on the surface are essential to maximize contact and binding interactions between the guest pollutant molecules and the 3D-printed scaffold. Porosity, morphology and the distribution of the pores in 3D-printed objects are just some of the variables to keep in mind in the design of performant filtrating materials. Also relevant are the surface chemical properties, which play a complementary role in the definition of performant filtrating systems. Synergic actions between material porosity and the related surface chemical composition are pivotal to reach appropriate removal properties in the adsorption of the analytes through membranes. The adsorption process can involve both physical factors and chemical interactions between the analytes and the functional groups covering the surface.

In this context, new technologies of chemical and biological functionalization of 3D printed objects are under development.

One of the first examples in literature of a post-functionalization on a printed structure is relatively recent and dates back to 2016. In order to investigate the communication mechanism between neurons, and how the neurons itself send commands to all the body, Su et al. developed a system for the in vivo real-time monitoring of the dynamic fluctuation of extracellular cerebral fluids such as glucose and lactate.[46]

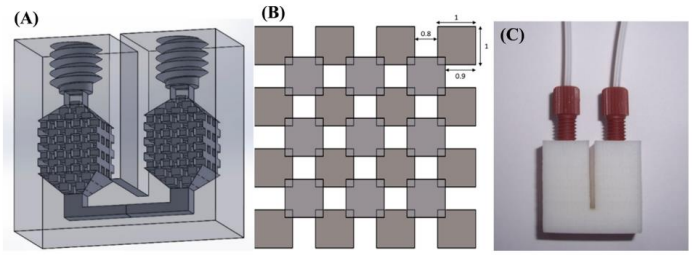

Figure 3.5 *CAD drawings of (A) the flow reactor and (B) a layer of ordered cuboids in the reaction chamber. (C) 3D-printed reactor.*[46]

For that reason, they created a simple and innovative fluxing bioreactor through a 3D-FDM type printer and thermoplastic ABS as printing material (**Figure 3.5**). Using the 3D-printing technology Su was able to design a reactor made by a series of offset ordered and superimposed cubes, reaching an exponential increase in the inner surface area. The innovation relied in the subsequently surface decoration with the glucosidase and lactoxidase enzymes. The first enzyme was covalently bound to the reactor through a previous activation of the surface by glutaraldehyde polymerization. The reaction between amine groups of the glucosidase with the residual aldehyde groups of the glutaraldehyde polymer led to an efficient covalent decoration on the structure (**Figure 3.6**). The second enzyme was bound to the surface by exploiting the hydrophobic interactions with the aromatic rings in the ABS structure.

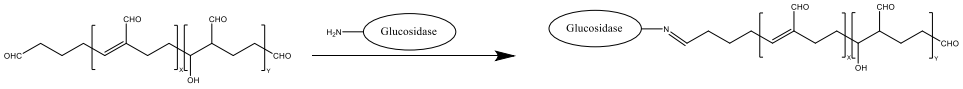

Figure 3.6 *Scheme of the Glucosidase covalent binding over the glutaraldehyde polymer*

MOFs are a class of performing and widely used absorbing materials for pollutant removal. However, the recover and regeneration of these inorganic systems reveals many unsolved issues.
To simplify the recovery process of MOF powders after a pollutant removal step, many researchers started to implement the 3D-printing technology with the MOF concept. The several procedures developed to immobilize MOF powders on

inorganic substrates like silica, alumina e ceramic materials started to be implemented in the 3D-printing.
Wang et al. were able to reach an in situ step-by-step growing of the MOF HKUST-1 on the surface of an ABS polymer structure printed through a FDM printer model. The HKUST-1 is well known for its high surface area, large pores volume and the related ability to remove pollutants in water. It's even known for the catalytic properties, high Lewis acidity and relevant chemical stability.[47] The MOF properties led to optimal performances of the composite system in the removal of methylene blue in water.

3.2.3 - SL technique

Between the several printing techniques developed, the technology selected and used in this research work has been the stereolithography 3D printing system (SL). Stereolithography 3D technique involves the printing of tridimensional structures following a layer-by-layer addition process. The peculiarity of this technique relies in the accurate control in the printing process, reached through a laser-induced photopolymerization of a photoactive liquid resin.
The SL printing technique can be divided in two main macro-areas, in consideration of the technology system involved in the printing process: the direct laser writing (also known as SLA or stereolithographic apparatus) and the digital light processing (DLP) (**Figure 3.7**).[48–51]

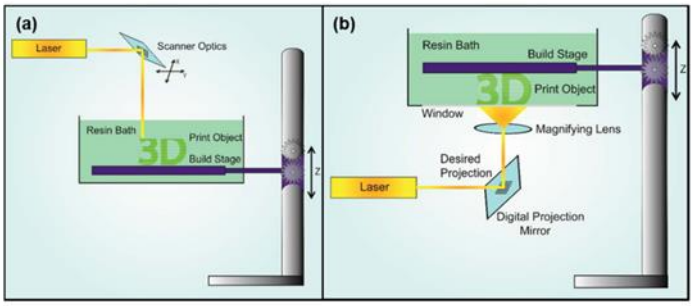

Figure 3.7 *Typology of stereolithography printer: (a) direct laser writing printer, and (b) digital light processing.*[52]

These two different techniques are based on the application of a liquid photo-active resin able to polymerize and cure after the exposition to a radiative source. They are also called vat-polymerization techniques.
SLA technique was the first stereolithographic 3D printing technology introduced and diffused in the market. The apparatus involves mobile platform along the three Cartesian axis, a transparent bottom vat for the resin with a not-sticky internal surface, and a series of galvanometers.[53]
In the printing process using the SLA instrumentation, the first step involves the lowering of the building platform inside the resin vat, to reach the proper immersion depth for the first layer formation.
With the platform in the proper position, the instrument activates the galvanometer mirrors placed under the resin vat. As mirrors, they focalize with extreme precision the laser beam along all the point coordinates that define the starting layer. Photopolymerization and the subsequently photocuring of the material is driven by the beam irradiation in all the STL facets tessellating triangles. Once completed the designing process of the starting layer, the platform rises by a corresponding height to define the following layer along the z-axis. At the same time the vat moves horizontally allowing the cured layer detachment and the flow of fresh resin under the platform. This set of actions define a single productive cycle and allows the generation of a single cured layer. Following an iterative process, the instrument is ready to restart with a series of new cycles in order to build new layers over the previous ones. The direct curing process point-by-point and the assembly of every single layer step-by-step are the

main key features in the 3D SLA printing technology. The instrumentation arrangement reaches a remarkable precision and resolution in the printing process through a user-friendly and fast technique.

An additional advantage of the SLA printing technology over the other 3D printing techniques is the ability to build objects with a final volume greater than the vat one thanks to the gradual rise of the in-printing object over the photoactive resin. This arrangement in the SLA technology allows a more clean and simplified production with the advantage to change the polymerizing materials during the productive process, customizing in real-time the properties of the final product. The combination of all these advantages results in reduced size and cheap equipment.

A limitation in the SLA technique concerns the detachment forces related to the gravity of the in-printing object. These forces build up during the rise of the platform in the resin vat, and they can bring to a complete or partial detachment of the printed structure before the completing of the process. This drawback change with the printable material, implying strong limitations in the final printed volume.

Even if introduced 30 years ago, 3D-SLA technology started to become relevant in chemistry only in the last few years. The necessity to overcome the traditional printable materials improving their properties and extending their applications brought to a major role of the chemistry in this manufacturing field.

The synergic interaction between chemistry and tridimensional manufacturing techniques coincided with the disclosure of new applicative horizons and an exponential economical growing of the 3D printing technology. In the last ten years the market value followed an annual 30% increasing, reaching a final value of 15 billion $ in 2019. Projections are predicting a progressive market exponential growth until a value of 33 billion $ in 2022.[54] This enormous success has been related to the advantages over the traditional manufacturing techniques. The application of 3D printing techniques in multidisciplinary fields like engineering, biotechnology, analytical chemistry, pharmaceutic, robotic, art and food science highlight the versatility and dynamism of this new technology.[55–57]

Remarkable in the 3D printing technology is the opportunity to involve low-price instruments and simple user training. Other advantages are the drastic drop in the waste of raw material and the introduction of a third productive dimension

essential to avoid the traditional productive techniques organized on the assembly of 2D objects. The introduction of a third productive dimension allows the simplification of the fabrication processes and the opportunity to create highly complex structures with a single-body configuration.
A relevant strength is the high rate in the customization of the produced structures, and the application of the "fail fast and often" approach, an essential practice to identify weakness with a low-price process and in a short time.[58]

Isotropy

In addition to the advantages reported above, in the SLA printing technology emerges an extra relevant feature for what concern the mechanical field properties. High isotropic structures can be printed thanks the unique setting and mechanism involved in the SLA process.[59] Isotropy indicates uniformity distribution of the material properties in all the orientations, only achievable with the 3D photo-printing technologies.
The concept of layer-by-layer assembly involved in the conventional 3D printing techniques implied itself the creation of anisotropic objects.
In the FDM printing technology the process involves the fusion and deposition of a soft polymer, followed by the hardening step to define each layer. The assembly mechanism leads to remarkable differences between the forces involved inside every single layer and the forces which bind every layer to each other.[60] The melted material, used in the deposition step, is made by a series of highly twisted and strongly linked polymeric chains. The chains organization inside the single layer provides a greater strength, resistance and rigidity.
However, a strong link in the polymeric chains is not achievable between the previous layer and the following one. The junction's formation between adjacent layers gives good adhesion but poor mechanical properties. In other words, FDM technique utilizes a mechanical adhesion process but not a chemical one, with a decrease in the mechanical performances. Layer's junctions represent the real weakness and anisotropic starting point in those materials, accountable of exfoliation phenomena in the presence of lateral stress. Between every layer, there are several holes and empty spaces in the microscopic range accountable of a not complete final adhesion.

In the photopolymerizing SLA technique, no differences are evaluable both in the chemical interactions inside the individual layer and in the interactions involved in the layer adhesion. The photopolymerization reactions between monomers and oligomers in the resin lead to the formation of a series of covalent bond in the polymeric structure. Particularly relevant is the not-complete polymerization process in every layer that remains in a semi-reactive virgin state. The virgin state is characterized by a greater concentration of active polymerizing sites on the surface than the cured one. The active sites play the role of binding point for the generation of new covalent bonds with the following layers, providing to an effective covalent crosslinking process among them. The assembly of virgin layers in the SLA technique allows a crosslinking propagation along the three Cartesian axes. It guarantees the complete absence of empty spaces or microscopic cracks and the making of a watertight structure.

SLA photo-printable material

The polymeric resins used in the 3D printing stereolithography technology need some essential features such as melting temperature below room temperature or anyway a processability temperature or a glass transition temperature low enough to guarantee a good mobility between the chains in the printing process. This behavior is strongly related to the monomers/oligomers molecular weight and crosslinking level.[61,62]

A viscosity value ranging from 0.25 Pa·s for low molecular weight resins to 10 Pa·s for high molecular weight materials is essential to application in SLA technology.[63,64]

Frequently it's common the use of not-reactive plasticizers mixed with photo-reactive resin to reduce the final viscosity.[65] At the same time, these addictions lead to an increase of the interactions between the reactive functional groups and a subsequently higher hardening rate. Moreover, the low viscosity speeds up the covering rate of the in-printing layer with fresh resin. High viscosity values become disadvantageous both for the increasing of the printing times and to avoid a fast covering process, leading to the rise of many defect in the final structure.[51]

More generally, the resin viscosity is related to the molecular architecture of the polymeric/oligomeric chains and their crosslinking level. Therefore, oligomeric chains with a reduced length, and a lower crosslinked system, will show a lower

viscosity. Moreover, the spherical geometry in the highly crosslinked or hyper-branched polymers leads to a closed morphology able to avoid intramolecular and intermolecular entanglements.[55,66]

Lower viscosity values are obtained using polymeric resins with highly cross-linked or hyper-branched chains. The deriving spherical geometry in the chain conformation leads reduced intermolecular entanglements and a higher chain mobility. 4- and 6-arm star polyisoprenes show lower viscosity values if compared with the linear ones. Polymers with hyper-branched molecular structure show the same behavior, following higher viscosity values for higher branches. [67]

A side effect in the application of hyper-branched or star polymers is the increasing of the suitable active sites for the crosslinking process, and the subsequently enhancement in the curing and gelation rate. At the same time, a higher crosslinking level guarantee better mechanical properties and the limitation of exfoliation mechanism between the layers.[68] All these combined features work to upgrade the mechanical performances in the final structure.

The main used photoreactive functional groups are acrylic and epoxy resins. In more limited cases, cinnamates, coumarins, thiol-ene reactions, and fumarates are used as reactive groups. [69–71]

Altering the end reactive functional groups is an easy trick to influence the photopolymerization kinetics and the related curing and gelation rates. The curing rate in tertiary radical methyl methacrylate species is higher if compared with the rate in a secondary acrylate radical, giving to the rise of a better mechanical behavior.

Printing resolution

The main advantage which boosted the spread of the 3D printing stereolithography technology, is the high printing resolution, not achievable with the conventional 3D technique. The z-layer height is the most relevant parameter to define the printing resolution, usually placed between 25 and 100 µm in the SLA technique.[72] The choice of this setting parameter is relevant for its influence on the printing rate and the quality of the final product.

However, the most emblematic parameter to describe the power in the SLA technology is the printing accuracy along the X-Y plane. The superior resolution is limited by the radiation spot size, in a laser beam extremely small. The laser

radiation of the proper wavelength, hitting the liquid resin induces the photopolymerization and photocuring processes just in the irradiated points. The particular mechanism allows a resolution in a range between 50 and 200 µm. Different photo-printable materials or lasers can remarkably affect the printing resolution. In general, the SLA technology provide a better resolution than other addictive techniques such as the SLS mode (350 µm) or the FDM type (250 – 800 µm).[73]

3.3 - Results and Discussion

We decided to use SLA technique to create a series of new printed and porous structures for the removal of pollutants in water. Trimethylolpropane triacrylate (TMPTA) was used as monomer for the creation of the printed scaffolds. The choice of TMPTA as printing material was guided by a compromise between the necessity of an acceptable wettability grade, essential to work in water, and fast curing rate during the printing process, required to obtain a high pore printing definition.

We focused our attention on the removal of three different class of water pollutant: i) aromatic compounds and chlorinated aromatic compounds, ii) polycyclic aromatic compounds, iii) heavy metals. All of them are constantly monitored by the European Union and several intergovernmental organizations.

The challenge of this research has been the development of new effective purifying systems able to remove an entire class of pollutants in water, and to overcome the development of purely selective system just effective in the removal of a specific analyte.

Three different molecular receptors, equipped with a methyl methacrylate moiety, were covalently anchored over the surface of 3D printed scaffold (**Figure 3.8**).

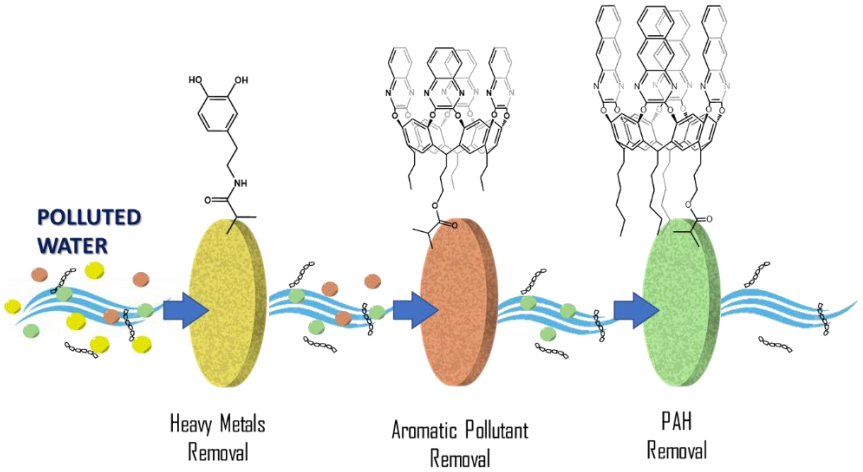

Figure 3.8 *Schematic representation of the molecular receptors used in the activation of 3D-printed membranes*

To remove aromatic organic pollutants and chlorinated aromatic organic pollutants, we employed the tetraquinoxaline cavitand (QxCav), a molecular receptor equipped with a deep and hydrophobic cavity able to complex small aromatic guest through the formation of π- π and CH- π interactions.
To remove polycyclic aromatic compounds (PAH) we used a new resorcinarene-based molecular receptor equipped with four benzoquinoxaline wall at the upper rim (BzQxCav), whose preparation and complexation properties are reported in the *Chapter 2*. The relevant feature is the presence of a deeper and more hydrophobic cavity able to host bulkier aromatic guests.
Both QxCav and BzQxCav receptors were functionalized at the lower rim with a methyl methacrylate moiety, essential for a radical-driven covalent grafting over the scaffold surface.
To develop an effective receptor in the removal of heavy metals in water we were inspired by mussels and their adhesive ability based on their dopamine secretion. The mechanism is driven by the chelating behavior of the dopamine phenolic groups with metal ions. Modifying the amino group and leaving intact the complexing phenolic groups, we developed a dopamine-based receptor equipped with a methyl methacrylamidic moiety. Following the same procedure used for

the previous receptors, the dopamine-based methyl methacrylamide was covalently linked over the surface of a 3D printed porous scaffold.
The functionalized membranes were then tested to evaluate their pollutant removal abilities through GC-MS and optical ICP on polluted waters before and after extracting treatment.
In order to identify new regeneration mechanisms and to restore the scaffold purifying properties, we studied the QxCav conformational switch through fluorescence emission spectrophotometry. Typically, pH or temperature perturbation over quinoxaline cavitands and their derivates lead to conformational switch between a closed *vase* conformation and an open *kite* conformation. The control on the vase-kite equilibrium is proposed to manage the membrane complexing-decomplexing process and consequently the regeneration mechanism for further extracting cycles.

3.3.1 Synthesis of Methyl Methacrylate QxCav 6

For the synthesis of the lower rim functionalized tetraquinoxaline cavitand, we decided to use as scaffold the resorcinarene characterized by the presence of three propyl chains and a OH-ended propyl one. The OH group is the starting point for the introduction of suitable functional moieties.
The most convenient route to synthetize the modified resorcinarene in good yield involves the protection and selective deprotection of the hydroxyl groups in the monoOH footed resorcinarene **1** (**Scheme 3.1**).

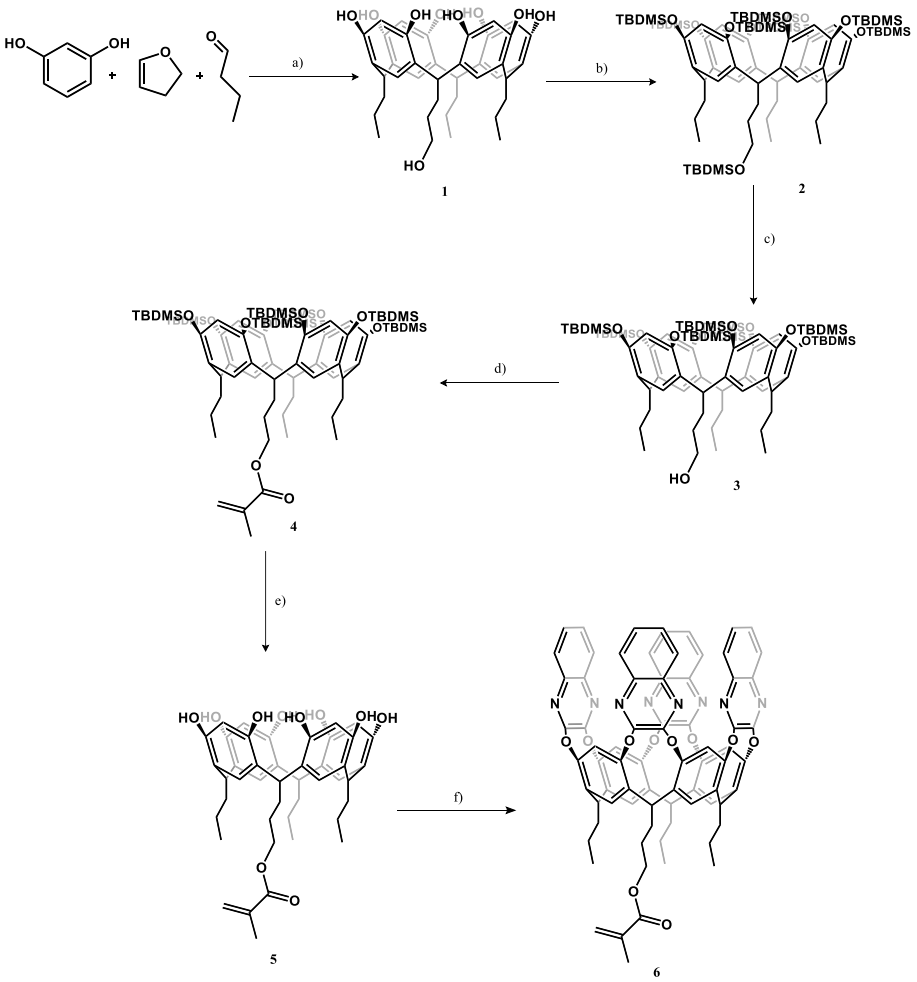

Scheme 3.1 *Synthesis of **6**: a) MeOH, HCl 37%, 50 °C, 7 d; b)Imidazole, tert-Butyldimethylsilyl Chloride, Dimethylformamide, Dichloromethane, 75 °C, 12 h, 25%; c) HF 40%, Acetonitrile, Dichloromethane, r.t., 12 h, 93%; d) Methacryloyl Chloride, Triethylamine, 4-Dimethylaminopiridine, Dichloromethane, 40 °C, 12 h, 76%; e) tert-Butylammonium Fluoride, Glacial Acetic Acid, Tetrahydrofuran, r.t., 12 h, quantitative; f) 2,3-dichloroquinoxaline, Potassium Carbonate, Dimethylformamide, 80 °C, 12 h, 39%.*

MonoOH footed resorcinarene is prepared condensing a 3:1 mixture of butyraldehyde and 2,3-dihydrofuran with resorcinol, under acid conditions. The high polarity of raw material does not allow a simple and effective purification procedure at this step. Therefore, the crude was treated without purification from the other resorcinarenes without OH and with two OH at the lower rim. TBDSM-protected resorcinarene **2** was obtained by reaction of the mixture **1** with tert-butyldimethylsilyl chloride in presence of imidazole and DMF as catalyst. Purification by flash chromatography afforded the TBDMS-protected product **2** in 25% yield. HF treatment led to the selective deprotection of the aliphatic hydroxyl group at the lower rim to give **3** in 93% yield.[74] In the following step, addition of methacryloyl chloride to **3** was performed. Precipitation by methanol afforded the product **4** as a white solid in 76% yield. Once completed the lower rim functionalization, the upper rim protecting groups were removed through TBAF treatment under acidic conditions. Extraction with ethyl acetate led to product **5** in quantitative yield. Finally, the Williamson bridging reaction between **5** and 2,3-dichloroquinoxaline under basic conditions led to methyl methacrylate functionalized quinoxaline cavitand **6**. **6** was purified with flash chromatography and it was obtained in 39% yield. The product was characterized by MALDI-TOF ^{13}C and ^{1}H-NMR.

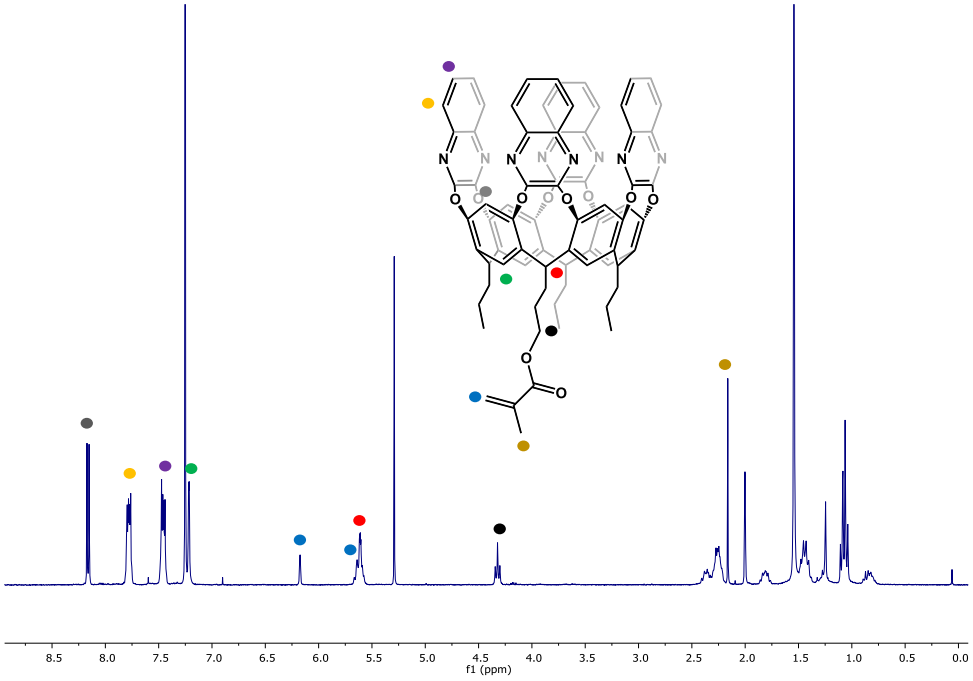

Figure 3.9 *^{1}H-NMR spectrum of **6** in $CDCl_3$.*

The ^{1}H-NMR spectra reported in **Figure 3.9**, shows all the characteristic peaks of the target product. All the low ppm signals are in agreement with the lower rim alkyl chains. The 4.33 ppm triplet signal is associated to the CH_2 next to the O atom at the lower rim, diagnostic of the formation of the ester bond. The resorcinarene scaffold is defined by four singlet signals at 8.18, 8.16, 7.22 and 7.21 ppm. The multiplet signals at 7.79 and 7.46 ppm are associated to the four quinoxaline walls. The methyl methacrylate moiety is defined by the three singlet signals at 6.18, 5.65 ppm and 2.17 ppm. The diagnostic triplets of CH bridge signals at 5.62 ppm confirms the rigid *vase* conformation in $CDCl_3$. The desymmetrization produced by the single substituent at the lower rim is visible in the NMR spectrum only in the splitting of the bridging CH signals and in the resorcinarene ArH signals.

The MALDI-TOF spectrum (**Figure 3.10**) shows the protonated molecular ion as the major peak and the experimental isotopic distribution is in agreement with the calculated one.

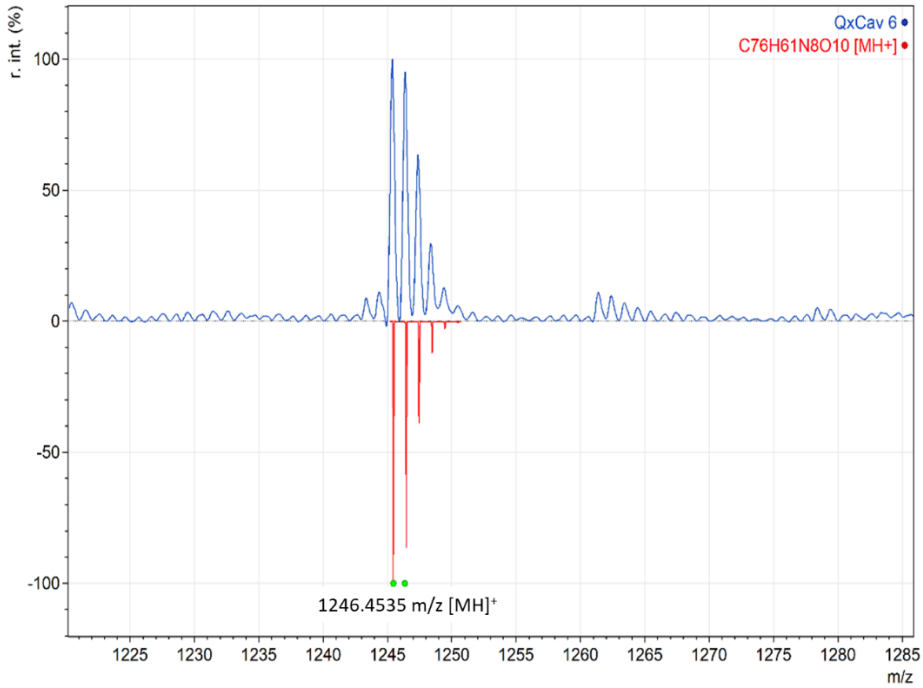

Figure 3.10 *High-resolution MALDI-TOF spectrum of **6**, with experimental (blue profile) versus flipped theoretical (red) isotopic distribution pattern*.

3.3.2 Synthesis of Methyl Methacrylate BzQxCav 12

The synthesis of the highly hydrophobic deep cavitand **12** required the use of the resorcinarene scaffold **7** with the presence of three hexyl alkyl chains to guarantee an optimal solubility of the reaction intermediates and the final product. The remaining OH-ended propyl chain is required for the introduction of a methacrylate unit at lower rim. The synthetic sequence is reported in **Scheme 3.2.**

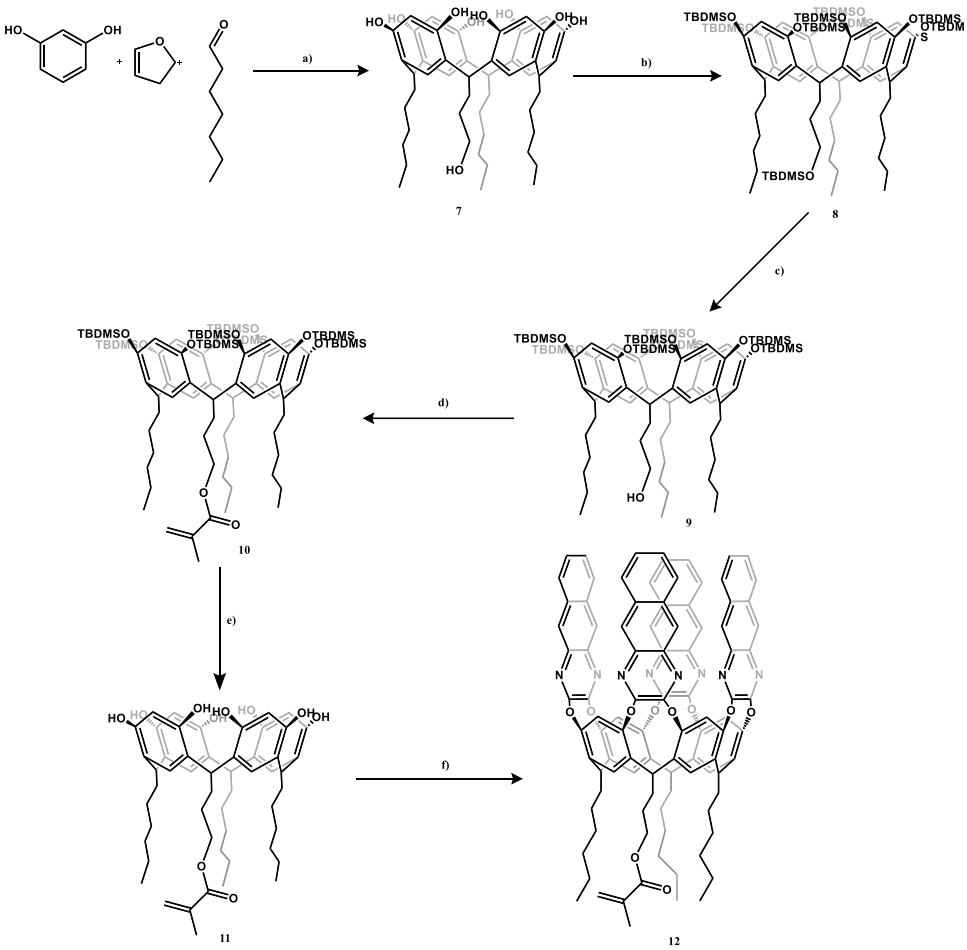

Scheme 3.2 *Synthesis of* ***12****: a) MeOH, HCl 37%, 50 °C, 7 d,; b) Imidazole, tert-Butyldimethylsilyl Chloride, Dimethylformamide, Dichloromethane, 75 °C, 12 h, 24%; c) HF 40%, Acetonitrile, Dichloromethane, r.t., 12 h, quantitative; d) Methacryloyl Chloride, Triethylamine, 4-Dimethylaminopiridine, Dichloromethane, 40 °C, 12 h, 86%; e) tert-Butylammonium Fluoride, Glacial Acetic Acid, Tetrahydrofuran, r.t., 12 h, quantitative; f) 2,3-dichlorobenzoquinoxaline, Potassium Carbonate, Dimethylformamide, 80 °C, 12 h, 28%.*

The condensation a 3:1 mixture of n-heptaldehyde and 2,3-dihydrofuran with resorcinol under acid condition led to the formation of the mono-OH footed resorcinarene **7**. The raw material is directly used without purification as reagent in the following protecting reaction. The TBDMS protection led to a drastic decrease of the molecule polarity, making possible the mixture purification through flash chromatography. The desired product **8** is recovered in 24% yield. The tert-butyldimethylsilyl group linked to hydroxyl group placed at the lower rim is selectively cleaved by HF 40% solution to give **9** in quantitative yield.[74] In the following step, the lower rim aliphatic hydroxyl group is functionalized using methacryloyl chloride, to give **10** in 86% yield. The remaining upper rim protecting groups were removed quantitatively through TBAF treatment under acid condition, obtaining the product **11** as a light red solid. The final reaction was the bridging reaction under basic condition between **11** and **2,3-dichlorobenzoquinoxaline** (see *Experimental Section* in **Chapter 2** for the synthesis of 2,3-dichlorobenzoquinoxaline). Purification of the raw material through flash chromatography afforded the product **12** as a light-yellow solid in 28% yield. The product was characterized by MALDI-TOF and ^{1}H-NMR and ^{13}C-NMR.

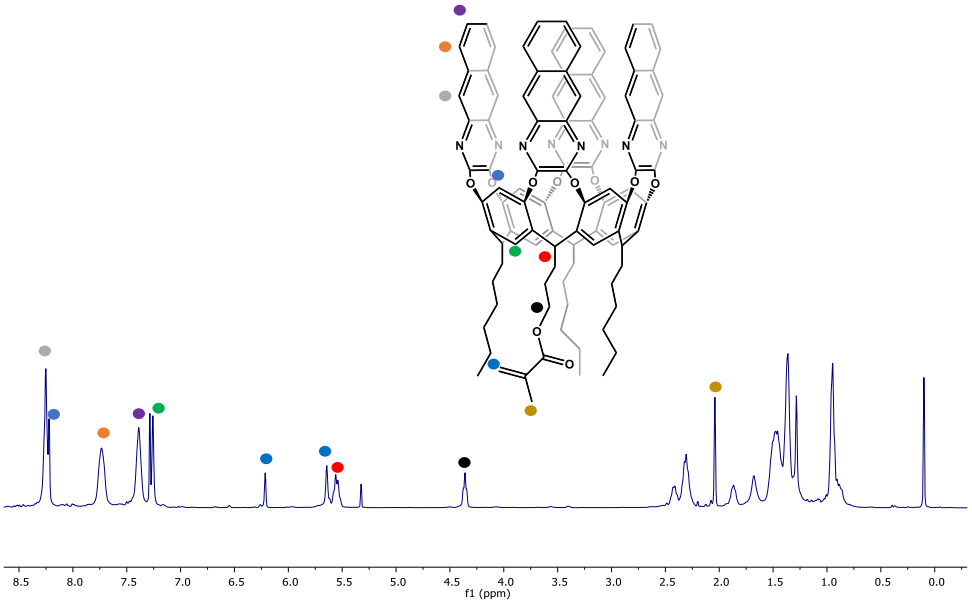

Figure 3.11 ^{1}H-NMR spectrum of **12** in $CDCl_3$.

The ^{1}H-NMR spectrum of **Figure 3.11** features all the characteristic peaks of the final product **12**. All the lower rim alkyl chains are traced by the signals in the upfield range. The 4.33 triplet signal is associated to the CH_2 group linked to the O atom at the lower rim, in agreement with the ester bond formation. The resorcinarene scaffold exhibits by two singlet signals at 8.19 and 7.23 ppm. The four benzoquinoxaline walls are described by a broad singlet at 8.22, and two multiplets at 7.71 and 7.37 ppm. The lower rim methyl methacrylate moiety presents three signals at 6.19, 5.62 ppm and 2.01 ppm respectively. The CH bridge signal at 5.51 ppm is diagnostic of the *vase* conformation of **12** in $CDCl_3$.

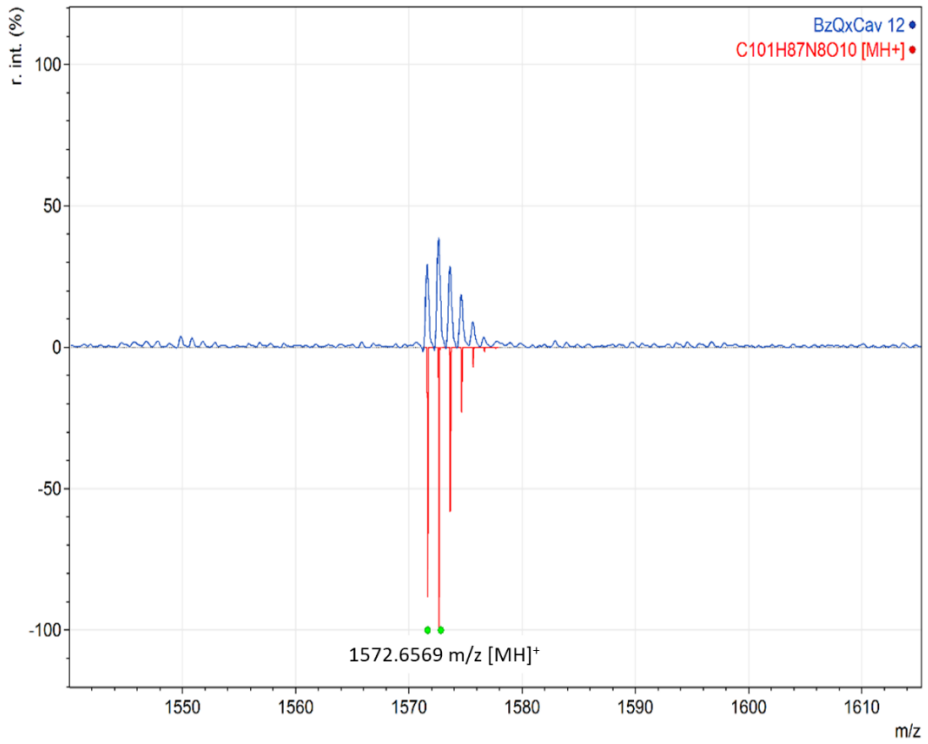

Figure 3.12 *High-resolution MALDI-TOF spectrum of **12**, with experimental (blue profile) versus flipped theoretical (red) isotopic distribution pattern*.

The high-resolution MALDI-TOF spectrum of **Figure 3.12** shows the protonated molecular ion as the major peak and the experimental isotopic distribution is in agreement with the calculated one.

3.3.3 Synthesis of dopamine receptor

The two-step synthesis for the functionalization of the amino group of dopamine with a methyl methacrylate moiety is shown in **Scheme 3.3.**

Given the reactivity of the phenolic OHs toward radicals, the synthetic strategy required the protection of the hydroxyl groups. Unlike the previous receptors reported in the paragraphs above, the deprotecting step to reactivate the hydroxyl binding sites only occurred as last step after the decoration process over the printed structures.

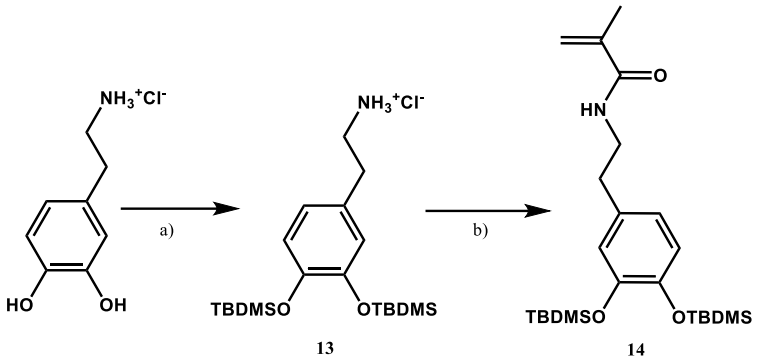

Scheme 3.3 *Synthesis of **14** a) Imidazole, tert-Butyldimethylslyl chloride, Dimethylformamide, Dichloromethane, 75°C, 12h, 65%; b) Methacryloyl Chloride Solution in Dichloromethane 10% w/v, Triethylamine, Dimethylformamide, r.t., 24h, 86%.*

The protection step of the hydroxyl groups was made using TBDMS. Flash chromatography purification afforded the pure product **13** as a yellowish oil in 63% yield. The second step was the introduction of the radical active group through amidation reaction. Reaction between **13** and a 10% w/v solution of methacryloyl chloride at room temperature and subsequently flash chromatography purification led to the oily product **14** in 86% yield. The product **14** was characterized through ^{1}H-NMR, ^{13}C-NMR and ESI-MS analyses.

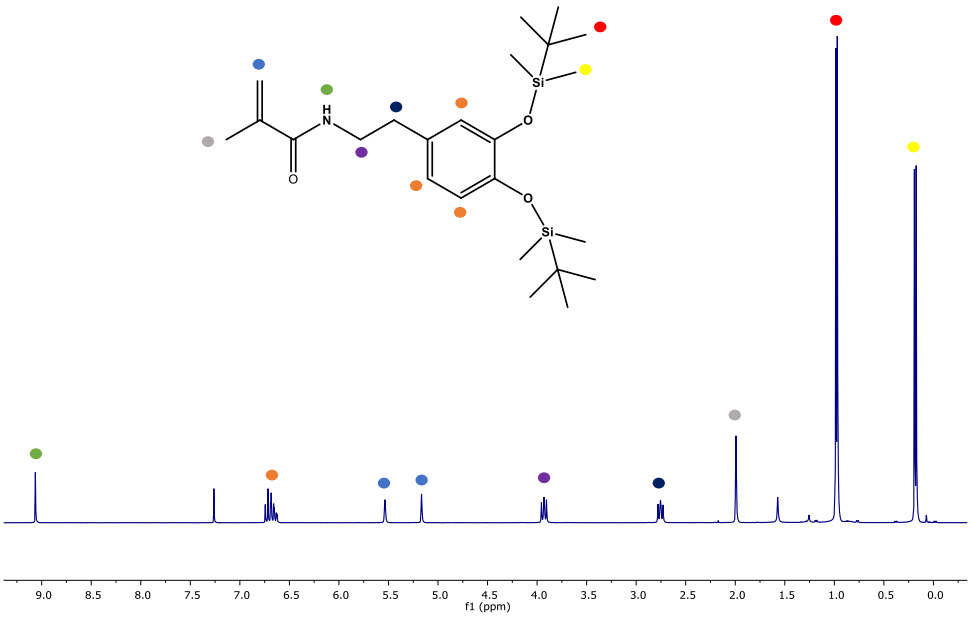

Figure 3.13 ^{1}H-NMR spectrum of **14** in $CDCl_3$.

The ^{1}H-NMR reported above, shows all the characteristic signals of the product **14**. The TBDMS protecting group are identified in the up-field range by four singlet signals at 0.98, 0.97, 0.19 and 0.17 ppm. The multiplet at 3.95 ppm and the triplet signal at 2.72 ppm are associated to the ethylene bridge. The methyl methacrylate moiety is described by three signals at 5.54 ppm and 5.15 ppm for the methylene group, and 2 ppm for the methyl one. Dopamine aromatic protons afforded multiplet signal at 6.71 ppm. The singlet signal at 9.09 ppm belongs to the amide NH.

3.3.4 3D-printed Membrane fabrication

Stereolithography 3D printing was selected as optimal printing technology for the creation of small porous structures. The unique arrangement in the SLA equipment provide high accuracy and precision during the printing process, allowing the creation of complex and elaborated internal porous systems. The opportunity to customize the internal channels geometry and morphology disclose different settings to optimize the following decoration and the final application. To reach the goal we set up a collaboration with the Milanese research group for the 3D printing, conducted using the SLA printer Form 2 model, a new 3D addictive equipment provided by the FormLabs INC (**Figure 3.14** *a*).

We chose methacrylate-based structures (PMMA) in order to reach the good wettability necessary to maximize the contact between the aqueous phase and the extracting membrane. PMMA has a good hydrophilicity, as shown by a contact angle close to 73°.[75]

Trimethylolpropane trimethacrylate monomer (TMPTA) was selected as monomer because its low viscosity (0.1 Pa·s, at 25°C) guarantees fast curing time and ease processing, essential parameters for the development of small size and highly defined internal pores (**Figure 3.14** *c*).

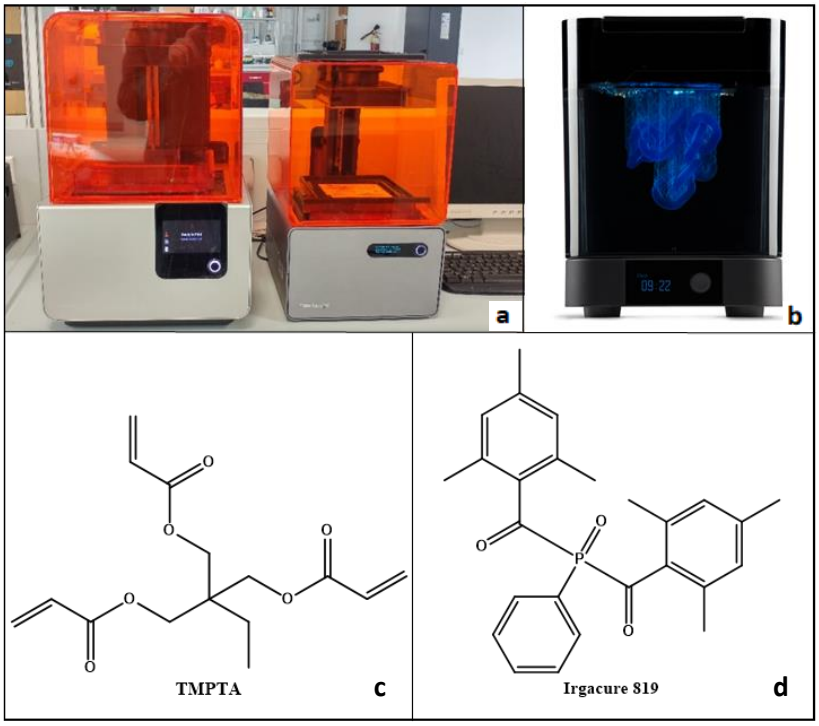

Figure 3.14 *a) SLA printer FORM2 model; b) UV-curing station; c) Trimethylolpropane triacrylate (TMPTA) monomer; d) Photo-radical initiator Irgacure 819*

Using a CAD software, we designed porous structures modelled as cylinders of 1 cm of diameter and 1 cm of height. Every printed layer was equipped with pores of 200 µm each. Additionally, to increase the internal surface area in every subsequent layer, the pore positions were shifted by 100 µm, creating a structure with pores partially closed by the subsequent ones (**Figure 3.15**).

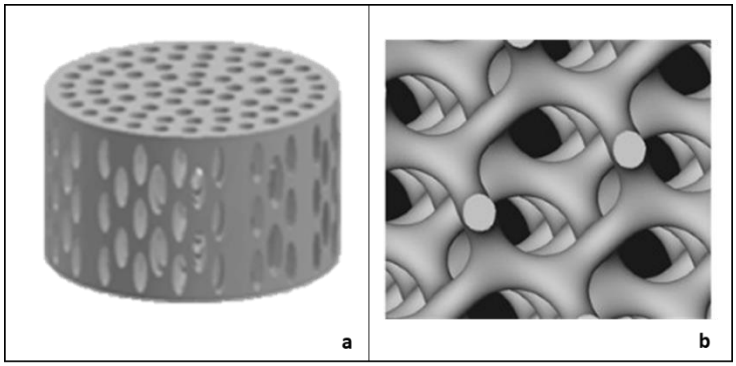

Figure 3.15 *a) CAD porous structure model used to print the scaffolds; b) Overview of the layer-shift involved to reach a pores partial-closure.*

This arrangement led to a more complex internal structure able to increase the contact with the polluted matrix.
The following step has been the printing process using the digital file to guide the laser beam in the layer creation. The instrumentation was equipped with a 405 nm wavelength green laser (power 250 mW) with a beam spot size close to 140 nm. The TMPTA resin was charged with the photo-radical initiator Irgacure 819 (**Figure 3.14** *d*) in 5% w/w concentration and mixed for 12 hours in the dark. The homogenous mixture was transferred in the vat resin in order to start with the printing process. The automated production led to the creation of several and identical cylindric structures adherent to the building platform. The just produced cylinders did not complete the curing and hardening process, remaining in a convenient virgin state characterized by the presence of several methyl methacrylate groups still present for further radical reactions. We took advantage from this still-reactive virgin state in order to obtain a surface decoration with the three receptors described above.
The cylinders were dipped in a dichloromethane solution of the cavitands **6** and **12** (8×10^{-4} M), charged with a 10% w/w of Irgacure 819, and then cured under a *405 nm* UV-curing station (**Figure 3.14** *b*). This operation cycle was repeated 5 times for every cylinder, followed by a sonication in isopropanol and diethyl ether to remove all the unreacted traces and impurities from the printed objects. At the end, the cylinders were dried over vacuum.

Proof of the occurred decoration is the rise of an evident and remarkable fluorescence emission under UV lamp irradiation shown in **Figure 3.16** for cavitand **6** and **Figure 3.17** for cavitand **12**.

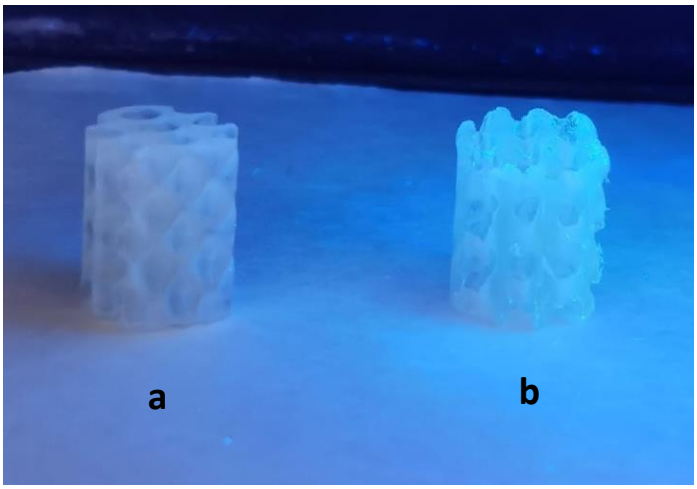

Figure 3.16 *a) Unfunctionalized TMPTA membrane; b) the entire membrane decorated with QxCav **6***

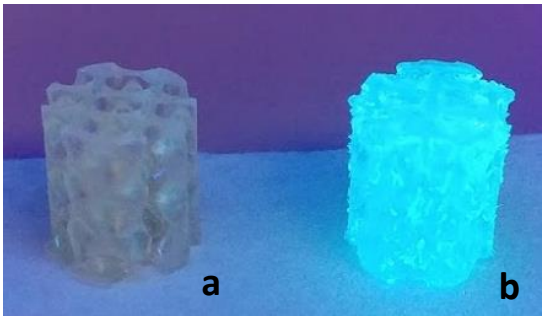

Figure 3.17 *a) Unfunctionalized TMPTA membrane; b) the entire membrane decorated with BzQxCav **12**.*

In the pictures above the relevant difference in the optical behavior between the pristine membranes and the decorated one is evident. The left side

unfunctionalized scaffolds, did not exhibit any fluorescence emission phenomena exposed under UV radiation. Instead, a blue fluorescence emission was observed by the right-side decorated membranes after excitation under a UV lamp. The fluorescence homogeneity and the total absence of non-emitting regions prove the homogeneous surface functionalization reached through the radical grafting mechanism.

Elemental analysis was performed on samples of the decorated membranes in order to quantify the amount of the cavitands **6** and **12**, using nitrogen as diagnostic probe of the presence of cavitands. Despite the optical evidences on the presence of a grafted cavitand layer on the external surface, the elemental analysis did not evidence the presence of nitrogen. The low amount of the macrocyclic receptors grafted on the surface did not reach the instrument minimum detectable level. XPS analyses are ongoing to quantify the cavitand amount on the surface.

The same experimental procedure was applied to the grafting of dopamine monomer **14.** Unlike the optical evidence subsequent the BzQxCav **12** and QxCav **6** decoration, the dopamine **14** grafting did not provide any fluorescence signature in the printed structure. Also, in this case elementary analysis did not detect nitrogen.

Despite the lack of proofs regarding the surface functionalization, the printed cylinders were dipped in a MeOH solution containing the buffer NaH-HF (pH=5), in order to remove the TBDMS protecting groups and to re-activate the complexing binding sites. This particular fluorine buffer was chosen to avoid the tedious work-up associated to the more common deprotecting agents like TBAF. The deprotected cylinders were washed with distilled water until neutral pH was reached.

The surfaces of the functionalized cylinders were characterized before and after the fluorine buffer treatment through IR spectrophotometry in the ATR mode. Monitoring only the surface composition, the IR spectra provided several evidences of the dopamine-based decoration and subsequently deprotection step (**Figure 3.18**).

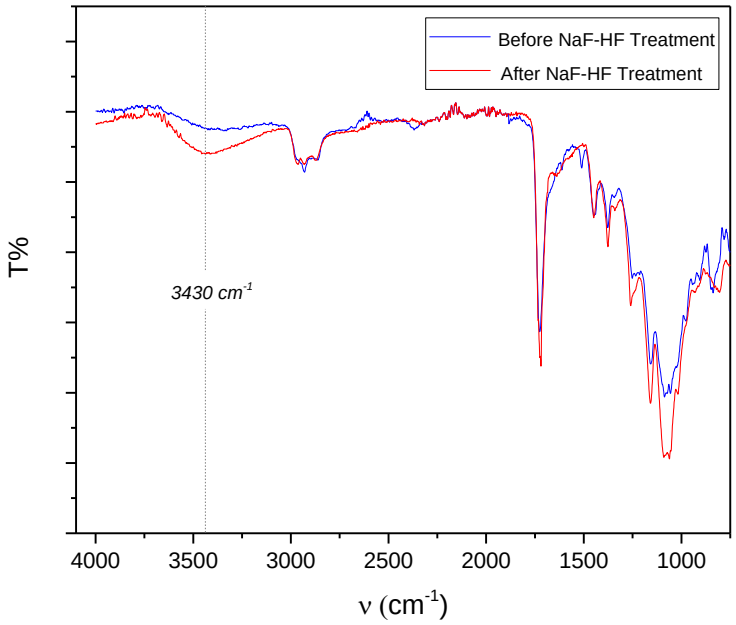

Figure 3.18 *ATR-FTIR spectra of the dopamine-functionalized membrane before and after solid state protective groups cleavage*

The dopamine-based decorating layer over the not-treated membranes was confirmed by the occurrence in the IR spectrum reported above (**Figure 3.18** *blue profile*) of the stretching bands at 1450 cm^{-1} and 1371 cm^{-1}, attributed to the C-N and α-methyl group. An additional evidence of the dopamine decoration was provided by the weak absorption band at 1681 cm^{-1} associated to the amide carboxyl group.
As reported in the IR spectrum (**Figure 3.18** *red profile)*, after the deprotective step OH stretching vibration at 3430 cm^{-1} appeared, not present before the fluorine buffer application. The growth of OH stretching band confirmed the effective TBDMS cleavage and re-activation of the complexing OH groups, essential for ion removal.

3.3.5 Regeneration of the membrane-active sites: the vase-kite equilibrium in the solid state

An interesting feature of the quinoxaline cavitand family is the ability to change its conformation under proper stimulus. Temperature and pH variations are the most common perturbations used to move the cavitand conformation from the closer *vase* structure and the open *kite* one. In solution, this conformational transition is monitored by ^{1}H-NMR, following the upfield shift of the methine bridge triplet signal. This behavior could become extremely interesting in the pollution removal field, in order to regenerate the active receptor, restoring all the original properties. The cavitands do not bind any guest in the open kite form, therefore their inset leads to pollutant release from the cavity. For that reason, we started to study how to induce the vase-kite switch in the solid state. The QxCav conformational shift in the solid state was followed through fluorescence spectrophotometry, following the protocol developed in our group during a previous research.[76] The conformational reversible conversion was induced exposing the QxCav-based membranes to the vapors of a TFA solution monitoring the maximum fluorescence emission shift. Fluorescence emission of the functionalized 3D-scaffold showed a maximum emission peak at *410 nm* and a shoulder at *437 nm (**Figure 3.19**, black profile)*.

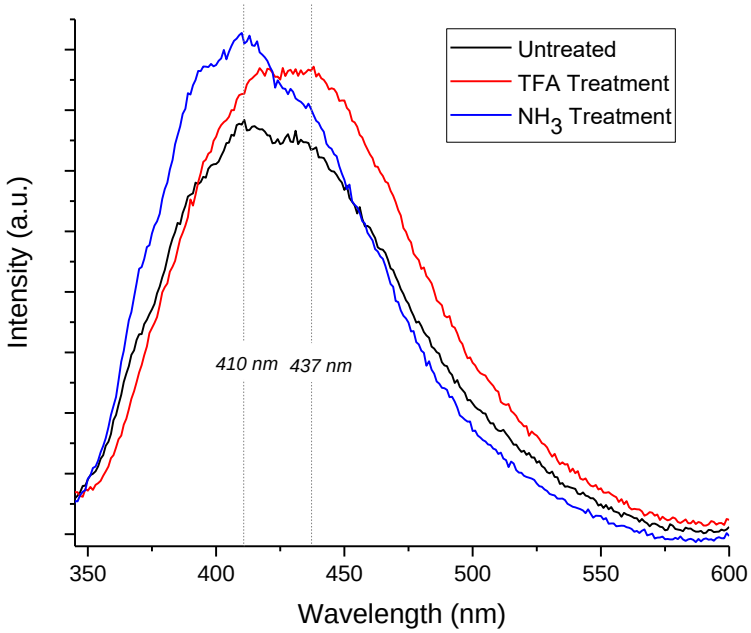

Figure 3.19 *Fluorescence Emission Spectra comparison between the not-treated QxCav-based membrane (black line), after TFA treatment (red line) and after NH_3 treatment (blue line)*

In agreement with the literature data, we associated the *410 nm* peak to the vase conformation emission and the shoulder to the *kite* form. As reported in the spectra, the receptor molecules involved in the surface decoration were mainly in the vase form. Redshift emission at *437 nm* and an increasing in the maximum emission was observed after the exposition to trifluoroacetic acid vapors for 10 minutes (**figure 3.19**, *red profile*). The redshift is associated to the QxCav in the *kite* form. TFA driven protonation of the quinoxaline nitrogen atoms prompted to an electrostatic repulsion between the cavitand walls, inducing conformational *vase* → *kite* conversion.
Treating the porous structures with ammonia vapors, we noticed a new maximum emission shift towards the blue range (**Figure 3.19**, *blue profile*). Basic vapors

deprotonated nitrogen atoms in the quinoxaline walls, removing their repulsive interactions and restoring the original *vase* conformation. This conformational *kite* → *vase* conversion was marked by the maximum emission blue-shift from *437 nm* to *410 nm*.
Fluorescence spectrophotometry gave evidence on the reversibility conformational switch in the solid state, a remarkable useful feature in the breaking of the hydrophobic interactions between the cavity and suitable guest targets. The final vase conformational restoring led to a complete regeneration of the complexing properties, an interesting condition in the prospective for the development of re-usable extracting cycles membranes.

3.3.6 Solid phase extraction of micropollutants with decorated membranes

Analytical measurements were performed to verify the uptake abilities of the functionalized porous 3D-scaffold in the removal of aromatic hydrocarbons in water. Solid phase extraction (SPE) was used following the general procedure reported below, using the QxCav **6** decorated membranes. The printed functionalized cylinders were preliminary washed in Et_2O and subsequently dried under vacuum, in order to remove any trace of solvents or impurities complexed inside the cavity receptor.
In sealed vials, the "activated" membranes were dipped in distilled water contaminated with 1 ppm each of eight aromatic compounds: i) benzene, ii) toluene, iii) ethylbenzene, iv) m,p-xylene, v)o-xylene, vi) chlorobenzene, vii) dichlorobenzene, viii) trichlorobenzene.
The incubation was performed for 30 minutes at room temperature maintaining the vials under gently agitation. To evaluate the membrane sequestering ability, the composition of the contaminated aqueous phase was monitored through GC-MS analyses.

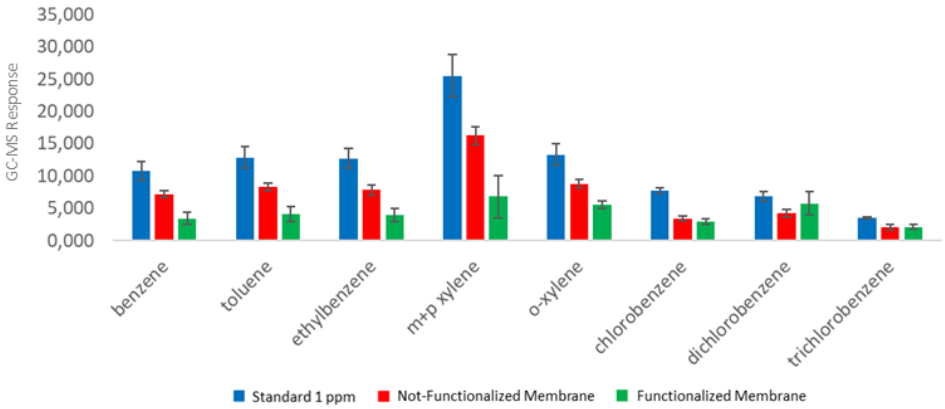

Figure 3.20 *Normalized GC-MS analysis of polluted water after treatment with not-functionalized membrane (red bar) and QxCav functionalized one (green bar)*

The results are reported in the diagram of **Figure 3.20**, with every bar indicating the remaining concentration of the aromatic species in water. Functionalized and not-functionalized membrane are compared in the graph.
The diagram shows the evidence of intrinsic physisorption behavior in pristine membranes with all the evaluated pollutants. An average 20% of every pollutant is removed by the untreated membranes. Higher pristine membrane affinity was observed towards chlorobenzene. Surface functionalization led to a significant increase in the removal ability of all the aromatic chemicals with the only exception of the chlorinated ones. More in details, the activated surfaces compared with the untreated ones, showed the ability to remove an average additional 20% of pollutants. Chlorinated aromatic chemicals have led to a different and unusual trend; the untreated structures provided to a higher or similar removal uptake properties, without gain any remarkable performance after surface decoration. Possibly, the larger size of dichloro and trichlorobenzene compound hinders their inclusion in the cavity of QxCav.

3.3.7 Metal ions uptake with dopamine 14 decorated membrane

Once completed the deprotection and the subsequent activation of the hydroxy groups in the dopamine receptor, we tested the ability of the decorated 3D-printed scaffolds in the removal of metal ions in water.
The dopamine-based porous cylinders were firstly washed with Et_2O and water in order to remove any traces of the NaF-HF buffer and organic solvents, used in the TBDMS cleavage step. Then they were dried under vacuum for 10 hours.
To test their removal ability towards metal ions in water, both pristine and decorated membranes were soaked in a solution of bidistilled water containing Tl^{+}, Hg^{2+}, Cr^{6+} and Pb^{2+}, each present in concentration of 1 ppm. The incubation was performed for 12 hours under stirring. Completed the soaking process, the contaminated waters were filtered on 0.2 µm Nylon filters and then analyzed using the ICP optical emission spectroscopy.
Unfortunately, the ICP analyses did not provide evidence of effective removal abilities in the decorated dopamine-based membrane. Contaminated solutions treated with both pristine and decorated membranes showed the absence of significant differences with the stock solution metal ions concentration.
The use of bi-distilled water as medium did not change the outcome, showing that common water ions such as Na^{+} or Ca^{2+} do not interfere. The absence of significant variations in the concentrations of metal ions in water can be related to the limited amount of **14** grafted on the membrane surface, as highlighted by the negative elementary analyses reported above.

3.4 Conclusions and perspectives

In this Chapter, we reported a new strategy to develop an innovative generation of 3D-printed porous scaffolds useful in the water pollutants removal. In particular, we focused our attention on the removal of aromatic hydrocarbons, polycyclic aromatic hydrocarbons and toxic metal ions such as Cr^{6+}, Tl^{+}, Hg^{2+} and Pb^{2+} from water. In collaboration with the prof. Daniel Milanese at the Parma University we used the 3D-printing stereolithography technology create new acrylate-based porous scaffolds. Through a photocatalytic radical process three

different molecular receptors were covalently linked on the surfaces of post-printed the porous membranes, providing decoration of the polymeric scaffolds with molecular receptors.

The chosen molecular receptors were QxCav **6** selective in the removal of simple aromatic and chlorinated compounds in water, the new BzQxCav **12**, selective for the removal of polycyclic aromatic hydrocarbons, and dopamine **14** as ligand in the complexation of several heavy metals. All the molecular receptors were equipped with an active methyl methacrylate moiety, which was introduced as polymerizable group in order to covalently link the receptors on the membrane surfaces.

The 3D-printed porous scaffold covalently decorated with the receptor **6** was tested in the removal in water of aromatic and chlorinated aromatic pollutants. The GC-MS analyses on the post-treated polluted waters showed the superior removal abilities of the functionalized membrane in the removal of benzene, toluene, ethylbenzene and xylenes over the pristine one.

Additionally, we verified the ability of grafted QxCav **6** to reversibly change its conformation in the solid state, an interesting feature for the regeneration of the membranes. Using the fluorescence emission spectroscopy, we evaluated the ability of the molecular receptor to move from the *vase* close conformation to the *kite* open one and vice versa after exposure to acid and basic vapors.

In order to decorate the porous printed structures with a heavy metal receptor, dopamine was successfully functionalized with the methyl methacrylate moiety and then covalently anchored on the printed porous cylinders. The preparation was completed by activating the dopamine binding sites using a post-decoration silyl cleavage reaction. The porous scaffolds were tested towards the removal in water of Cr^{6+}, Tl^{+}, Hg^{2+} and Pb^{2+}, tested in the concentration of 1 ppm each. Unfortunately, the ICP analyses conducted on the polluted waters treated with the dopamine-covered membranes indicated the absence of removal properties. Tests are now in progress to optimize the decoration process and to improve the amount of dopamine receptor grafted on the printed scaffolds.

So far, the molecular receptor **12** was synthesized and covalently grafted on the printed cylinders. The active 3D-printed membranes have been sent to the prof. Federica Bianchi to test the PAH removal ability in water.

3.5 Acknowledgments

Special thanks to Prof. Daniel Milanese and Dr. Corrado Sciancalepore from the Department of Engineering of Parma University for the design and creation of the 3D-printed and porous scaffold. Thanks to Prof. Federica Bianchi, Dr. Monica Maffini and Dr. Nicolò Riboni of the Department of Chemistry of Parma University for the extraction experiments.

3.6 Experimental Section

Resorcinares **1**, **7**, and cavitands **2**, **3**, **8**, **9** were prepared according to publish procedures by replacement of the n-hexanal with n-butanal and n-heptaldehyde.[77]

Resorcinarene [3C_3H_7, C_3H_6OH; H] (1)[77]

To a solution of resorcinol (10 g, 90.8 mmol,), butanal (6.1 mL, 68.2 mmol) and 2,3-dihydrofuran (1.73 mL, 0.023 mmol) in MeOH (75 mL), a 37% solution of HCl (18 mL) was added dropwise over 30 min at 0°C. After the addition, the reaction mixture was stirred at 55°C for 5 days. The reaction was quenched with water, filtered, dried under vacuum obtaining an orange powder. The crude was used as such and purified in the following synthetic step.

TBDMS-protected resorcinarene (2)[77]

A dry Schlenk tube equipped with a stirring bar was loaded under argon with resorcinarene **1** (2 g), and imidazole (10 g, 146.86 mmol) in dry DMF (30 mL). The resulting mixture was cooled to 0°C. A solution of TBDMS-Cl (9 g, 59.71 mmol) in dry DCM (15 mL) was added dropwise to the cold mixture under inert atmosphere. The solution changed from red to yellow immediately. The reaction mixture was stirred at 75°C for 12 hours. The reaction was quenched removing the solvent under reduced pressure and the crude was purified through flash column chromatography on silica gel (gradient, hexane → Hexane:DCM = 9:1). The product was obtained as a white solid (1.11 g, 0.653 mmol) in 25% yield.

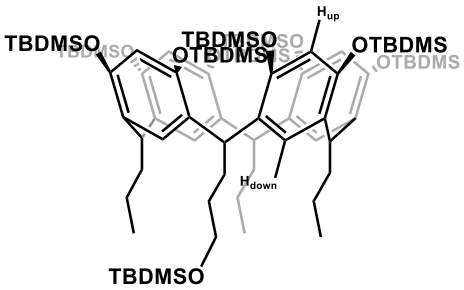

^{1}H NMR ($CDCl_3$, 300 MHz), δ (ppm): 7.11 (s, 1H, **H**$_{up}$), 7.10 (s, 1H, **H**$_{up}$), 6.29 (s, 2H, **H**$_{down}$), 6.21 (s, 1H, **H**$_{up}$), 6.20 (s, 1H, **H**$_{up}$), 6.07 (s, 2H, **H**$_{down}$), 4.38 – 4.30 (m, 4H, ArC**H**), 3.48 (t, *J* = 7.4 Hz, 2H, -$CHCH_2CH_2C$**H_2**OTBDMS), 1.99 – 1.82 (m, 4H, -CHC**H_2**CH_2CH_2OTBDMS + CHC**H_2**CH_2CH_3), 1.73 – 1.57 (m, 4H, -CHC**H_2**CH_2CH_3), 1.34 – 1.11 (m, 8H, -$CHCH_2C$**H_2**CH_3 + $CHCH_2C$**H_2**CH_2OTBDMS), 1.05 (s, 36H, $ArOSi(CH_3)_2C(C$**H_3**$)_3$), 0.95 – 0.87 (m, 9H, $CHCH_2CH_2C$**H_3**), 0.82 (s, 36H, $ArOSi(CH_3)_2C(C$**H_3**$)_3$), 0.81 (s, 9H, -$CH_2OSi(CH_3)_2C(C$**H_3**$)_3$), 0.34 (s, 24H, $ArOSi(C$**H_3**$)_2C(CH_3)_3$), 0.02 (s, 12H, $ArOSi(C$**H_3**$)_2C(CH_3)_3$), -0.05 (s, 6H, $CH_2OSi(C$**H_3**$)_2C(CH_3)_3$), -0.16 (s, 6H, $ArOSi(C$**H_3**$)_2C(CH_3)_3$), -0.18 (s, 6H, $ArOSi(C$**H_3**$)_2C(CH_3)_3$).

MonoOH footed TBDMS resorcinarene (3) [77]

To a solution of **2** (660 mg, 0.39 mmol) in DCM/MeCN 8:3 (55 mL) in a Teflon flask, HF 40% (1 mL, 23 mmol) was slowly added. The resulting mixture was stirred for 12 hours at room temperature. The reaction was quenched with a saturated solution of $CaCO_3$ (7 mL). The mixture was washed with water (4 x 30 mL) and extracted with DCM (4 x 25 mL). The combined organic layers were dried over Na_2SO_4, filtered and concentrated in vacuo, affording the product **3** as a light-yellow solid (574 mg, mmol) in 93% yield.

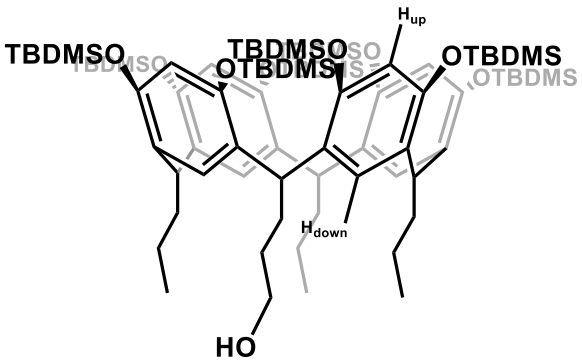

^{1}H NMR ($CDCl_3$, 300 MHz), δ (ppm): 7.11 (s, 1H, **H**$_{up}$), 7.10 (s, 1H, **H**$_{up}$), 6.31 (s, 1H, **H**$_{down}$), 6.30 (s, 1H, **H**$_{down}$), 6.21 (s, 1H, **H**$_{up}$), 6.19 (s, 1H, **H**$_{up}$), 6.09 (s, 1H, **H**$_{down}$), 6.07 (s, 1H, **H**$_{down}$), 4.36 (t, *J* = 13.2 Hz, 4H, ArC**H**), 3.53 (t, *J* = 6.8 Hz, 2H, -$CHCH_2CH_2C\mathbf{H_2}OH$), 1.98 – 1.82 (m, 8H, -$CHC\mathbf{H_2}CH_2CH_3$ + -$CHC\mathbf{H_2}CH_2CH_2OH$), 1.30 – 0.99 (m, 44H, $ArOSi(CH_3)_2C(C\mathbf{H_3})_3$ + $CHCH_2C\mathbf{H_2}CH_3$ + -$CHCH_2C\mathbf{H_2}CH_2OH$), 0.96 – 0.73 (m, 45H, $ArOSi(CH_3)_2C(C\mathbf{H_3})_3$ + $CHCH_2CH_2C\mathbf{H_3}$), 0.34 (s, 24H, $ArOSi(C\mathbf{H_3})_2C(CH_3)_3$), 0.03 (s, 12H, $ArOSi(C\mathbf{H_3})_2C(CH_3)_3$), -0.17 (s, 12H, $ArOSi(C\mathbf{H_3})_2C(CH_3)_3$).

Methyl Methachloride footed TBDMS resorcinarene (4)

A dry Schlenk tube equipped with a stirrer was loaded under argon with **3** (250 mg, 157.54 µmol), DMAP (6.51 mg, 53.3 µmol) and NEt_3 (0.48 mL, 3.44 mmol) in dry DCM (16.6 mL). The resulting mixture was cooled to 0°C and freshly distilled methacryloyl chloride (0.64 mL, 5.77 mmol) was slowly added under inert atmosphere. The reaction mixture is stirred for 12 hours at 40°C. The reaction is quenched by pouring in MeOH (20 mL) and maintaining the stirring for an hour at room temperature. The product, obtained as a white precipitate, is filtered, washed with MeOH and dried over vacuo (198 mg, 119.64 µmol; 76% yield).

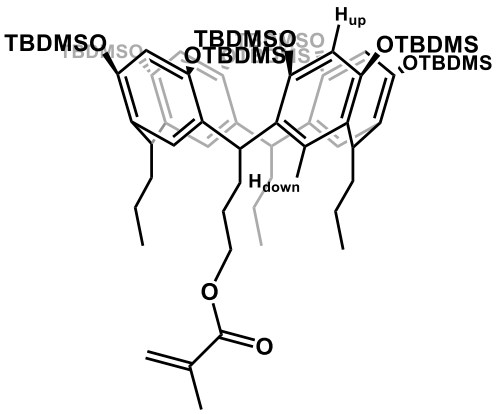

^{1}H NMR ($CDCl_3$, 300 MHz), δ (ppm): 7.12 (s, 1H, **H**$_{up}$), 7.10 (s, 1H, **H**$_{up}$), 6.31 (s, 2H, **H**$_{down}$), 6.22 (s, 1H, **H**$_{up}$), 6.19 (s, 1H, **H**$_{up}$), 6.10 (s, 1H, **H**$_{down}$), 6.08 (s, 1H, **H**$_{down}$), 6.01 (bs, 1H, C=C**H$_2$**$_{trans}$), 5.45 (bs, 1H, C=C**H$_2$**$_{cis}$), 4.45 – 4.29 (m, 4H, ArC**H**), 4.13 – 3.90 (m, 2H, -CHCH$_2$CH$_2$C**H$_2$**OR), 2.01 – 1.83 (m, 7H, -CHC**H$_2$**CH$_2$CH$_2$OR + -CHC**H$_2$**CH$_2$CH$_3$ + OC(O)C(C**H$_3$**)=CH$_2$), 1.72 – 1.58 (m, 4H, -CHC**H$_2$**CH$_2$CH$_3$), 1.31 – 1.12 (m, 8H, -CHCH$_2$C**H$_2$**CH$_3$ + CHCH$_2$C**H$_2$**CH$_2$OR), 1.05 (s, 36H, ArOSi(CH$_3$)$_2$C(C**H$_3$**)$_3$), 0.97 – 0.87 (m, 9H, -CHCH$_2$CH$_2$C**H$_3$**), 0.84 (s, 18H, ArOSi(CH$_3$)$_2$C(C**H$_3$**)$_3$), 0.82 (s, 18H, ArOSi(CH$_3$)$_2$C(C**H$_3$**)$_3$), 0.34 (s, 24H, ArOSi(C**H$_3$**)$_2$C(CH$_3$)$_3$), 0.03 (s, 12H, ArOSi(C**H$_3$**)$_2$C(CH$_3$)$_3$), -0.13 (s, 3H, ArOSi(C**H$_3$**)$_2$C(CH$_3$)$_3$), -0.16 (s, 3H, ArOSi(C**H$_3$**)$_2$C(CH$_3$)$_3$), -0.17 (s, 3H, ArOSi(C**H$_3$**)$_2$C(CH$_3$)$_3$), -0.20 (s, 3H, ArOSi(C**H$_3$**)$_2$C(CH$_3$)$_3$).

DEPTQ ^{13}C NMR (101 MHz, $CDCl_3$) δ 152.53, 152.41, 152.34, 152.28, 150.85, 150.66, 150.63, 150.56, 136.47, 129.22, 129.15, 129.10, 128.89, 128.77, 128.59, 126.20, 126.07, 125.07, 123.83, 123.79, 123.55, 123.12, 110.35, 110.18, 107.40, 65.39, 37.98, 37.85, 37.83, 37.63, 37.55, 37.54, 37.23, 37.11, 31.68, 27.74, 27.63, 26.12, 26.06, 21.98, 18.43, 18.37, 18.26, 14.32, 14.28, 14.18, -3.74, -3.82, -3.91, -3.93, -3.95, -3.99, -4.04, -4.05, -4.07, -4.15.

MALDI-TOF calculated for $C_{92}H_{165}O_{10}Si_8$ $[M+H]^+$ m/z = 1655.0599
found = 1655.1146

Methyl Methacrylate resorcinarene (5)

The reagent **4** (198 mg, 119.64 µmol) was dissolved in THF (23 mL) and the resulting mixture was cooled to 0°C. Glacial acetic acid (165 µL, 2.88 mmol) and TBAF (2.39 mL, 2.39 mmol) were slowly added to the cold mixture, and stirred at room temperature for 12 hours. The reaction was quenched by pouring in water (30 mL). The mixture was washed with a saturated solution of NH_4Cl (4 x 30 mL) and extracted with Acetone/Ethyl Acetate 1:1 (4 x 30 mL). The combined organic layers were dried over Na_2SO_4 and concentrated in vacuo. Product **5** was obtained as a light red solid in a quantitative yield.

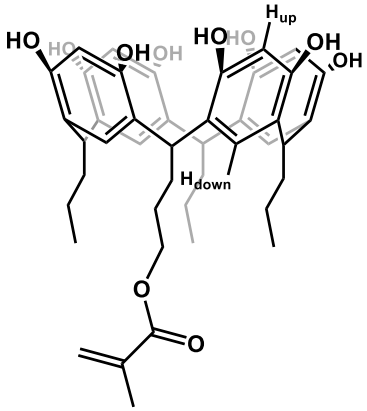

^{1}H NMR ($(CD_3)_2CO$, 300 MHz), δ (ppm): 9.31 (bs, 8H, ArO**H**), 7.45 (s, 2H, $\mathbf{H}_{up}$), 7.41 (s, 2H, $\mathbf{H}_{up}$), 6.64 (bs, 4H, $\mathbf{H}_{down}$), 6.07 (bs, 1H, C=C$\mathbf{H_2}_{trans}$), 5.61 (bs, 1H, C=C$\mathbf{H_2}_{cis}$), 4.32 (t, *J* = 8.0 Hz, 4H, ArC**H**), 4.17 (t, *J* = 6.8 Hz, 2H, -$CHCH_2CH_2C\mathbf{H_2}OR$), 2.42 – 2.30 (m, 2H, -$CHC\mathbf{H_2}CH_2CH_2OR$), 2.29 – 2.15 (m, 6H, -$CHC\mathbf{H_2}CH_2CH_3$), 1.93 (s, 3H, $OC(O)C(C\mathbf{H_3})=CH_2$), 1.37 – 1.19 (m, 8H, -$CHCH_2C\mathbf{H_2}$), 0.92 (t, J = 6.0 Hz, 9H, -$CHCH_2CH_2C\mathbf{H_3}$).

DEPT ^{13}C NMR (101 MHz, Acetone) δ 151.99, 151.83, 136.70, 125.18, 124.63, 124.55, 124.45, 124.29, 124.23, 123.88, 102.76, 64.36, 35.38, 33.20, 32.99, 29.83, 29.40, 29.21, 29.02, 28.82, 27.18, 25.31, 20.94, 19.95, 17.57, 13.44, 13.39.

ESI-MS calculated for $C_{44}H_{53}O_{10}$ $[M+H]^+$ m/z = 741.36,
found = 741.55.

Methyl Methacrylate quinoxaline cavitand (6)

A dry Schlenk tube was loaded under argon with **4** (88 mg, 118.78 µmol), K_2CO_3 (195.7 mg, 1.42 mmol) and 2,3-dichloroquinoxaline (96.3 mg, 483.85 µmol) in dry DMF (4 mL). The reaction mixture was stirred for 12 hours at 80°C. The reaction was quenched by pouring in water (10 mL). The precipitate is filtered and cleaned through flash column chromatography on silica gel (gradient, DCM → DCM:Acetone = 98:2). The product was obtained as a white solid (57 mg, 46.3 µmol) in 39% yield.

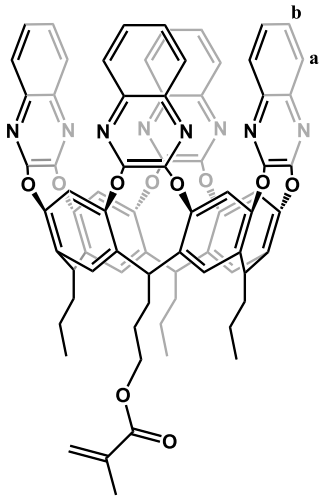

6

^{1}H NMR ($CDCl_3$, 600 MHz), δ (ppm): 8.16 (s, 2H, $\mathbf{H}_{up}$), 8.14 (s, 2H, $\mathbf{H}_{up}$), 7.81 – 7.76 (m, 8H, $\mathbf{H}_{a}$), 7.49 – 7.43 (m, 8H, $\mathbf{H}_{a}$), 7.21 (bs, 4H, $\mathbf{H}_{down}$), 6.17 (bs, 1H, C=C$\mathbf{H}_{2trans}$), 5.64 – 5.55 (m, 5H, C=C$\mathbf{H}_{2cis}$ + ArC**H**), 4.32 (t, *J* = 5.9 Hz, 2H, -$CHCH_2CH_2C\mathbf{H}_2OR$), 2.41 – 2.31 (m, 2H, -$CHC\mathbf{H}_2CH_2CH_2OR$), 2.30 – 2.20 (m, 6H, -$CHC\mathbf{H}_2CH_2CH_3$), 2.00 (s, 3H, $OC(O)C(C\mathbf{H}_3)=CH_2$), 1.84 – 1.77 (m, 2H, -$CHCH_2C\mathbf{H}_2CH_2OR$), 1.48 – 1.40 (m, 6H, -$CHCH_2C\mathbf{H}_2CH_3$), 1.11 – 1.03 (m, 9H, $CHCH_2CH_2C\mathbf{H}_3$).

MALDI-TOF calculated for $C_{76}H_{61}N_8O_{10}$ $[M+H]^+$ m/z = 1246,4535
found = 1246.3236

^{13}C NMR (75 MHz, $CDCl_3$) δ 152.67, 152.52, 152.43, 139.61, 138.47, 136.00, 135.75, 135.59, 135.19, 128.94, 127.73, 123.30, 123.15, 118.92, 118.76, 77.43, 77.01, 76.59, 64.43, 34.37, 34.07, 33.96, 33.88, 21.00, 18.40, 14.07, 14.01.

Resorcinarene [$3C_6H_7$, C_3H_6OH; H] (7) [77]

To a solution of resorcinol (10 g, 90.8 mmol,), heptaldehyde (9.5 mL, 68.2 mmol) and 2,3-dihydrofuran (1.73 mL, 0.023 mmol) in MeOH (75 ml), a 37% solution of HCl (18 mL) was added dropwise over 30 min at 0°C. After the addition, the reaction mixture was stirred at 55°C for 5 days. The reaction was quenched with water, filtered, dried under vacuum obtaining an orange powder. The crude was used as such and purified in the following synthetic step.

TBDMS-protected resorcinarene (8) [77]

A dry Schlenk tube equipped with a stirring bar was loaded under argon with Resorcinarene **7** (1.2 g), and imidazole (5.4 g, 79.6 mmol) in dry DMF (24 mL). The resulting mixture was cooled to 0°C. A solution of TBDMS-Cl (4.6 g, 30.02 mmol) in dry DCM (14 mL) was added dropwise to the cold mixture under inert atmosphere. The solution changed from red to yellow immediately. The reaction mixture was stirred at 75°C for 12 hours. The reaction was quenched removing the solvent under reduced pressure and the crude was purified through flash column chromatography on silica gel (gradient, hexane → Hexane:DCM = 95:5). The product was obtained as a white solid (670 g, 0.36 mmol) in 24% yield.

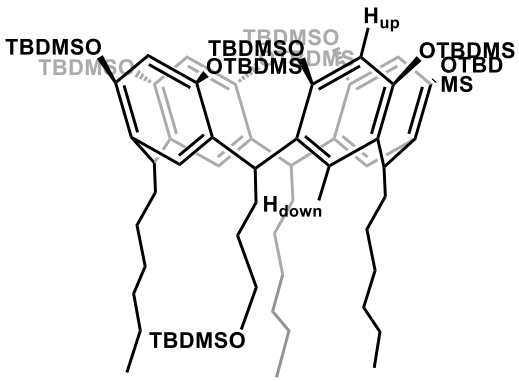

^{1}H NMR ($CDCl_3$, 300 MHz), δ (ppm): 7.12 (s, 1H, **H**$_{up}$), 7.11 (s, 1H, **H**$_{up}$), 6.32 (s, 2H, **H**$_{down}$), 6.24 (s, 1H, **H**$_{up}$), 6.22 (s, 1H, **H**$_{up}$), 6.09 (s, 2H, **H**$_{down}$), 4.43 – 4.29 (m, 4H, -ArC**H**), 3.52 (t, *J* = 7.0 Hz, 2H, -$CHCH_2CH_2C\mathbf{H_2}$OTBDMS), 2.07 – 1.85 (m, 4H, -$CHC\mathbf{H_2}CH_2CH_2CH_2CH_2CH_3$ + -$CHC\mathbf{H_2}CH_2CH_2$OTBDMS), 1.82 – 1.61 (m, 4H, -$CHC\mathbf{H_2}CH_2CH_2CH_2CH_2CH_3$), 1.52 – 1.37 (m, 2H, -$CHCH_2C\mathbf{H_2}CH_2$OTBDMS), 1.26 – 1.12 (m, 24H, -$CHCH_2C\mathbf{H_2}C\mathbf{H_2}C\mathbf{H_2}C\mathbf{H_2}CH_3$), 1.08 (s, 36H, $ArOSi(CH_3)_2C(C\mathbf{H_3})_3$), 0.94 – 0.91 (m, 9H, -$CHCH_2CH_2CH_2CH_2CH_2C\mathbf{H_3}$), 0.85 (s, 36H, $ArOSi(CH_3)_2C(C\mathbf{H_3})_3$), 0.84 (s, 9H, -$CH_2OSi(CH_3)_2C(C\mathbf{H_3})_3$), 0.36 (s, 24H, $ArOSi(C\mathbf{H_3})_2C(CH_3)_3$), 0.05 (s, 12H, $ArOSi(C\mathbf{H_3})_2C(CH_3)_3$), -0.03 (s, 6H, -$CH_2OSi(C\mathbf{H_3})_2C(CH_3)_3$), -0.15 (s, 12H, $ArOSi(C\mathbf{H_3})_2C(CH_3)_3$).

MonoOH footed TBDMS resorcinarene (9) [77]

To a solution of **8** (670 mg, 0.37 mmol) in DCM/MeCN 8:3 (55 mL) in a Teflon flask, HF 40% (0.8 mL, 21 mmol) was slowly added. The resulting mixture was stirred for 12 hours at room temperature. The reaction was quenched with a saturated solution of $CaCO_3$ (6 mL). The mixture was washed with water (4 x 25 mL) and extracted with DCM (4 x 20 mL). The combined organic layers were dried over Na_2SO_4, filtered and concentrated in vacuo, affording the product **9** as a white solid (628 mg, 21 mmol) in quantitative yield.

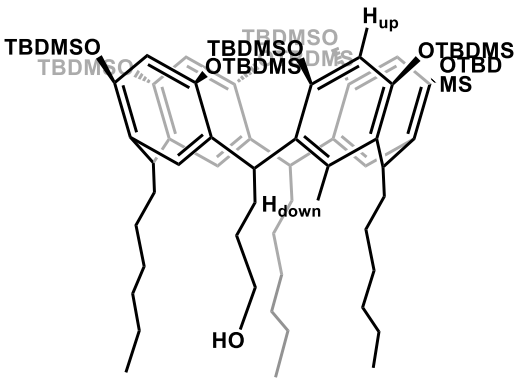

^{1}H NMR ($CDCl_3$, 300 MHz), δ (ppm): 7.10 (bs, 2H, $\mathbf{H}_{up}$), 6.31 (bs, 2H, $\mathbf{H}_{down}$), 6.22 (s, 1H, $\mathbf{H}_{up}$), 6.19 (s, 1H, $\mathbf{H}_{up}$), 6.09 (bs, 2H, $\mathbf{H}_{down}$), 4.44 – 4.29 (m, 4H, ArC**H**), 3.54 (t, *J* = 6.8 Hz, 2H, $CHCH_2CH_2C\mathbf{H_2}OH$), 1.97 – 1.81 (m, 4H, $-CHC\mathbf{H_2}CH_2CH_2CH_2CH_2CH_3$ + $CHC\mathbf{H_2}CH_2CH_2OTBDMS$), 1.80 – 1.61 (m, 4H, $-CHC\mathbf{H_2}CH_2CH_2CH_2CH_2CH_3$), 1.55 – 1.30 (m, 2H, $-CHCH_2C\mathbf{H_2}CH_2OTBDMS$), 1.31 – 1.11 (m, 24H, $-CHCH_2C\mathbf{H_2}C\mathbf{H_2}C\mathbf{H_2}C\mathbf{H_2}CH_3$), 1.06 (s, 36H, $ArOSi(CH_3)_2C(C\mathbf{H_3})_3$), 0.97 – 0.91 (m, 9H, $-CHCH_2CH_2CH_2CH_2CH_2C\mathbf{H_3}$), 0.84 (s, 36H, $ArOSi(CH_3)_2C(C\mathbf{H_3})_3$), 0.35 (s, 24H, $ArOSi(C\mathbf{H_3})_2C(CH_3)_3$), 0.04 (s, 12H, $ArOSi(C\mathbf{H_3})_2C(CH_3)_3$), -0.16 (s, 12H, $ArOSi(C\mathbf{H_3})_2C(CH_3)_3$).

Mehtyl Methacrylate footed resorcinarene (10)

A dry Schlenk tube equipped with a stirrer was loaded under argon with **9** (448 mg, 261.5 µmol), DMAP (10.79 mg, 88.32 µmol) and NEt_3 (0.8 mL, 5.74 mmol) in dry DCM (27 mL). The resulting mixture was cooled to 0°C and freshly distilled metacryloyl chloride (1.06 mL, 9.55 mmol) was slowly added under inert atmosphere. The reaction mixture was stirred for 12 hours at 40°C. The reaction was quenched by pouring in MeOH (20 mL) and maintaining the stirring for an hour at room temperature. The product, obtained as a white precipitate, was filtered, washed with MeOH and dried over vacuo (401 mg, 225.12 µmol; 86% yield).

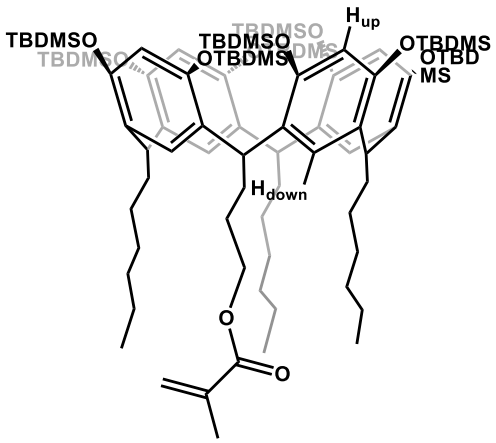

^{1}H NMR ($CDCl_3$, 600 MHz), δ (ppm): 7.09 (bs, 2H, **H_{up}**), 6.29 (s, 2H, **H_{down}**), 6.20 (s, 1H, **H_{up}**), 6.17 (s, 1H, **H_{up}**), 6.08 (s, 1H, **H_{down}**), 6.06 (s, 1H, **H_{down}**), 6.00 (bs, 1H, C=C**H_{2trans}**), 5.43 (bs, 1H, C=C**H_{2cis}**), 4.40 – 4.30 (m, 4H, ArC**H**), 4.06 – 3.97 (m, 2H, -$CHCH_2CH_2C\mathbf{H_2}OR$), 1.98 – 1.88 (m, 2H, -$CHC\mathbf{H_2}CH_2CH_2OR$), 1.86 (s, 3H, $OC(O)C(C\mathbf{H_3})=CH_2$), 1.84 – 1.75 (m, 2H, $CHC\mathbf{H_2}CH_2CH_2CH_2CH_2CH_3$), 1.73 – 1.59 (m, 4H, -$CHC\mathbf{H_2}CH_2CH_2CH_2CH_2CH_3$), 1.23 – 1.07 (m, 26H, -$R_2CHCH_2C\mathbf{H_2}C\mathbf{H_2}C\mathbf{H_2}C\mathbf{H_2}CH_3$ + -$CHCH_2C\mathbf{H_2}CH_2OR$), 1.04 (s, 18H, $ArOSi(CH_3)_2C(C\mathbf{H_3})_3$), 1.037 (s, 18H, $ArOSi(CH_3)_2C(C\mathbf{H_3})_3$), 0.84 – 0.79 (m, 45H, $ArOSi(CH_3)_2C(C\mathbf{H_3})_3$ + -$CHCH_2CH_2CH_2CH_2CH_2C\mathbf{H_3}$), 0.34 – 0.30 (m, 24H, $ArOSi(C\mathbf{H_3})_2C(CH_3)_3$), 0.03 (s, 3H, $ArOSi(C\mathbf{H_3})_2C(CH_3)_3$), 0.02 (s, 3H, $ArOSi(C\mathbf{H_3})_2C(CH_3)_3$), 0.015 (s, 3H, $ArOSi(C\mathbf{H_3})_2C(CH_3)_3$), 0.01 (s, 3H, $ArOSi(C\mathbf{H_3})_2C(CH_3)_3$), -0.15 (s, 3H, $ArOSi(C\mathbf{H_3})_2C(CH_3)_3$), -0.17 (s, 3H, $ArOSi(C\mathbf{H_3})_2C(CH_3)_3$), -0.19 (s, 3H, $ArOSi(C\mathbf{H_3})_2C(CH_3)_3$), -0.21 (s, 3H, $ArOSi(C\mathbf{H_3})_2C(CH_3)_3$).

^{13}C NMR ($CDCl_3$, 101 MHz) δ 129.16, 128.92, 126.25, 126.13, 125.08, 110.28, 110.09, 107.48, 65.42, 37.72, 37.63, 37.56, 37.14, 35.81, 35.77, 35.72, 32.22, 32.18, 31.75, 30.11, 30.06, 29.88, 29.07, 27.65, 22.89, 22.71, 18.37, 14.10, 14.07, -3.68, -3.71, -3.76, -3.87, -3.92, -3.98, -3.99, -4.02, -4.05, -4.10.

MALDI-TOF calculated for $C_{101}H_{183}O_{10}Si_8$ $[M+H]^+$ m/z = 1781.1990,
found = 1781.1532.

Methyl Methacrylate resorcinarene (11)

The reagent **10** (401 mg, 225.12 µmol) was dissolved in THF (43 mL) and the resulting mixture was cooled at 0°C. Acetic acid (309 µL, 8.90 mmol) and TBAF (6.08 mL, 6.08 mmol) were slowly added to the cold mixture, and stirred at room temperature for 12 hours. The reaction was quenched by pouring in water (50 mL). The mixture was washed with a saturated solution of NH_4Cl (4 x 30 mL) and extracted with Acetone/Ethyl Acetate 1:1 (4 x 30 mL). The combined organic layers were dried over Na_2SO_4 and concentrated in vacuo. Product **11** was obtained as a light red solid in a quantitative yield (194 mg, 224.92).

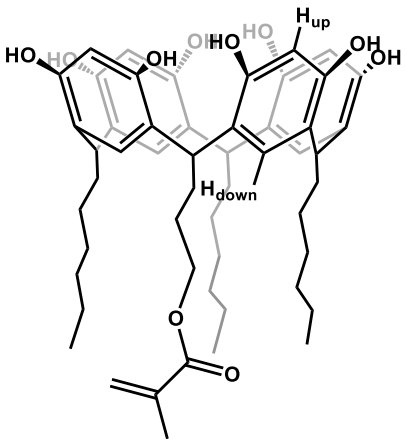

^{1}H NMR ($(CD_3)_2CO$, 600 MHz), δ (ppm): 8.47 (bs, 8H, ArO**H**), 7.53 (s, 2H, $\mathbf{H}_{up}$), 7.51 (s, 2H, $\mathbf{H}_{down}$), 6.23 (s, 2H, $\mathbf{H}_{up}$), 6.22 (s, 2H, $\mathbf{H}_{down}$), 6.05 (bs, 1H, C=C$\mathbf{H_2}_{trans}$), 5.59 (bs, 1H, C=C$\mathbf{H_2}_{cis}$), 4.33 (t, *J* = 8.0 Hz, 1H, ArC**H**$CH_2CH_2CH_2OR$), 4.28 (t, *J* = 8.0 Hz, 3H, ArC**H**CH_2CH_2), 4.14 (t, *J* = 6.9 Hz, 2H, -$CHCH_2CH_2C\mathbf{H_2}OR$), 2.41 – 2.35 (m, 2H, -$CHC\mathbf{H_2}CH_2CH_2OR$), 2.30 – 2.22 (m, 6H, $CHC\mathbf{H_2}CH_2CH_2CH_2CH_2CH_3$), 1.91 (s, 3H, $OC(O)C(C\mathbf{H_3})=CH_2$), 1.69 – 1.62 (m, 2H, $CHCH_2C\mathbf{H_2}CH_2OR$), 1.31 – 1.19 (m, 24H, -$CHCH_2C\mathbf{H_2}C\mathbf{H_2}C\mathbf{H_2}C\mathbf{H_2}CH_3$), 0.88 – 0.82 (m, 9H, $CHCH_2CH_2CH_2CH_2CH_2C\mathbf{H_3}$).

^{13}C NMR (101 MHz, Acetone-d6) δ 167.50, 152.87, 152.71, 137.56, 132.14, 131.60, 129.96, 129.29, 125.42, 125.40, 125.37, 125.30, 125.21, 125.13, 124.74, 103.69, 65.26, 60.54, 34.35, 34.29, 34.08, 32.78, 30.49, 30.17, 30.10, 28.99, 23.39, 23.35, 18.48, 14.35.

ESI-MS calculated for $C_{53}H_{71}O_{10}$ $[M+H]^+$ m/z = 868.51,

found = 868.89.

Methyl Methacrylate BenzoQuinoxaline Cavitand (12)

A dry shlenk tube was loaded under argon with **11** (194 mg, 224 µmol), K_2CO_3 (371.5 mg, 2.69 mmol) and 2,3-dichlorobenzoquinoxaline (234.1 mg, 940 µmol) in dry DMF (5 mL). The reaction mixture was stirred for 48 hours at 80°C. The reaction was quenched by pouring in water (15 mL). The precipitate was filtered and cleaned through flash column chromatography on silica gel (gradient, DCM → DCM:Acetone = 98:2). The product was obtained as a bright yellow solid (98 mg, 62.7 µmol) in 28% yield.

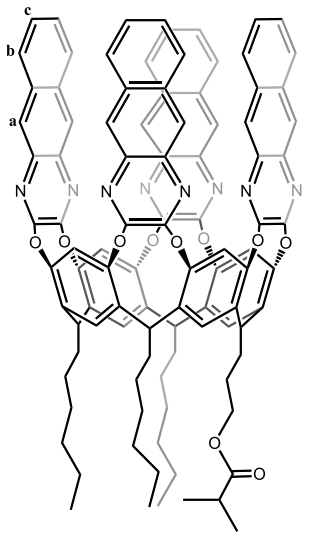

^{1}H NMR ($CDCl_3$, 400 MHz), δ (ppm): 8.25 (bs, 8H, $\mathbf{H}_a$), 8.22 (s, 8H, $\mathbf{H}_{up}$), 7.78–7.68 (m, 8H, $\mathbf{H}_b$), 7.4 –7.35 (m, 8H, $\mathbf{H}_c$), 7.25 (s, 4H, $\mathbf{H}_{down}$), 6.21 (s, 1H, C=C$\mathbf{H_2}_{trans}$), 5.66–5.49 (m, 5H, C=C$\mathbf{H_2}_{cis}$+ArC**H**), 4.35 (t, *J* = 6.6 Hz, 2H, $CHCH_2CH_2C\mathbf{H_2}OR$), 2.46–2.37 (m, 2H, $CHC\mathbf{H_2}CH_2CH_2OR$), 2.36–2.22 (m, 6H, $CHC\mathbf{H_2}CH_2CH_2CH_2CH_2CH_3$), 2.04 (s, 3H, $OC(O)C(C\mathbf{H_3})=CH_2$), 1.91–1.81 (m, 2H, $CHCH_2C\mathbf{H_2}CH_2OR$), 1.54–1.32 (m, 24H, $CHCH_2C\mathbf{H_2}C\mathbf{H_2}C\mathbf{H_2}C\mathbf{H_2}CH_3$), 0.98–0.91 (m, 9H, $(CH_2)_5C\mathbf{H_3}$).

MALDI-TOF calculated for $C_{101}H_{87}N_8O_{10}$ $[M+H]^+$ m/z = 1572.6569,
found = 1572.6113

^{13}C NMR (101 MHz, $CDCl_3$) δ 152.42, 136.60, 135.82, 135.51, 135.36, 134.98, 133.02, 127.94, 126.47, 125.89, 123.27, 123.10, 118.77, 118.60, 77.33, 77.01, 76.69, 64.41, 64.41, 34.59, 34.48, 32.32, 31.88, 29.69, 29.41, 29.30, 28.83, 27.90, 27.18, 22.68, 22.64, 18.39, 18.26, 14.05.

Synthesis of 2-(3,4-bis((tert-butyldimethylsilyl)oxy)phenyl)ethan-1-aminium chloride (13)[78]

A dry Schlenk tube equipped with a stirring bar was loaded under argon with dopamine hydrochloride (500 mg, 3.26 mmol), and imidazole (1.11 g, 16.3 mmol) in dry DMF (15 mL). The resulting mixture was cooled to 0°C. A solution of TBDMS-Cl (1.97 g, 13.04 mmol) in dry DCM (10 mL) was added dropwise to the cold mixture under inert atmosphere. The solution color changed to yellow immediately. The reaction mixture was stirred at 75°C for 12 hours. The reaction was quenched removing the solvent under reduced pressure and the crude was purified through flash column chromatography on silica gel (DCM:MeOH = 95:5). The product was obtained as a yellow oil (809 mg, 2.12 mmol) in 65% yield.

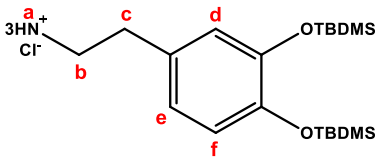

^{1}H NMR ($CDCl_3$, 300 MHz), δ (ppm): 6.76 (d, *J* = 7.8 Hz, 1H, 3H, $\mathbf{H_e}$), 6.69-6.56 (m, 2H, $\mathbf{H_d}$ + $\mathbf{H_f}$), 5.54 (bs, 2H, $\mathbf{H_a}$); 3.51 (q, *J* = 6.5 Hz, 2H, $\mathbf{H_b}$), 2.69 (t, *J* =6.8 Hz, 2H, $\mathbf{H_c}$) 0.975 (s, 9H, $Si(CH_3)_2\mathbf{(CH_3)_3}$); 0.97 (s, 9H, $Si(CH_3)_2\mathbf{(CH_3)_3}$); 0.18 (s, 6H, $Si\mathbf{(CH_3)_2}(CH_3)_3$), 0.17 (s, 6H, $Si\mathbf{(CH_3)_2}(CH_3)_3$).

ESI-MS calculated for $C_{20}H_{39}NO_2Si_2$ $[M+H]^+$ m/z = 382.25,
found = 382.55.

Synthesis of N-(3,4-bis((*tert*-butyldimethylsilyl)oxy)phenethyl)methacrylamide (14)

A double-neck round flask was loaded under argon with **13** (809 mg, 2.12 mmol), dry triethylamine (0.591 mL, 4.24 mmol) in dry DMF (5mL). The resulting mixture was cooled to 0°C and a 10% w/v DCM solution of freshly distilled metacryloyl chloride (3.6 mL, 3.18 mmol) was slowly added under inert atmosphere. The reaction mixture was stirred for 24 hours at room temperature. The reaction was quenched by pouring in MeOH (20 mL) and maintaining the stirring for an hour at room temperature. Solvents were removed over reduced pressure and the pink solid material recovered, was then purified through flash column chromatography through flash column chromatography on silica gel (DCM). The product was obtained as a yellowish oil (832.6 mg, 1.83 mmol) in 86% yield.

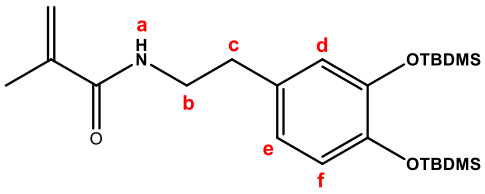

^{1}H NMR (CDCl3, 300 MHz), δ(ppm): 9.06 (s, 1H, **H_a**), 6.83-6.53 (m, 3H, **H_d** + **H_e** + **H_f**); 5.53 (s, 1H, C=C**H_{2trans}**); 5.16 (s, 1H, C=C**H_{2cis}**); 4.03-3.83 (m, 2H, **H_b**); 2.75 (t, J=7.6 Hz, 2H, **H_c**); 1.99 (s, 3H, NC(O)C(C**H_3**)=CH_2); 0.98 (s, 9H, Si$(CH_3)_2$**$(CH_3)_3$**); 0.97 (s, 9H, Si$(CH_3)_2$**$(CH_3)_3$**), 0.19 (s, 6H, Si**$(CH_3)_2$**$(CH_3)_3$), 0.17 (s, 6H, Si**$(CH_3)_2$**$(CH_3)_3$).

^{13}C NMR (75 MHz, $CDCl_3$) δ 163.73, 122.10, 121.83, 121.80, 120.92, 41.13, 33.08, 25.96, 19.97, -4.10.

ESI-MS calculated for $C_{24}H_{43}NO_3Si_2$ $[M+H]^+$ m/z = 450.28,
found = 450.38.

General procedure for the preparation of the printable resin

A HDPE bottle is loaded with 100 g of TMPTA resin and 5 g of Irgacure 819. The mixture was vigorously stirred for 12 hours under dark condition at room temperature. The resin was printed in 3D-porous scaffold using the SLA 3D-Printer Form2.

QxCav receptor 6 membrane decoration

A dip-coater was used to dip the virgin porous membranes in a DCM solution (10 mL) of the QxCav receptor **6** (10 mg, 0.008 mmol) and Irgacure 819 (1 mg, 0.002 mmol) with a dip rate of 10 cm/min. The cylinders were left immersed in the solution for 60 seconds. After the extraction, they were cured under a *405 nm* UV lamp for 10 minutes. This dipping-curing cycle was repeated 5 times. Once completed the surface functionalization the membranes were washed in isopropanol and diethyl ether for 10 minutes each.

BzQxCav receptor 12 membrane decoration

A dip-coater was used to dip the virgin porous membranes in a DCM solution (10 mL) of the BzQxCav receptor **12** (10 mg, 0.006 mmol) and Irgacure 819 (1 mg, 0.002 mmol) with a dip rate of 10 cm/min. The cylinders were left immersed in the solution for 60 seconds. After the extraction they were cured under a *405 nm* UV lamp for 10 minutes. This dipping-curing cycle was repeated 5 times. Once completed the surface functionalization the membranes were washed in isopropanol and diethyl ether for 10 minutes each.

Dopamine Based receptor 14 membrane decoration

A dip-coater was used to dip the virgin porous membranes in a MeOH solution (10 mL) of the dopamine-based receptor **12** (5 mg, 0.01 mmol) and Irgacure 819 (0.5 mg, 0.001 mmol) with a dip rate of 10 cm/min. The cylinders were left immersed in the solution for 5 minutes. After the extraction they were cured under a *405 nm* UV lamp for 10 minutes. This dipping-curing cycle was repeated

5 times. Once completed the surface functionalization the membranes were washed in isopropanol and diethyl ether for 10 minutes each.

Solid State TBDMS cleavage

In a one-neck round Teflon flask, a dopamine-based membrane was dipped in MeOH (10 mL). The system was cooled to 0°C and a pH=5 NaF-HF buffer (1.2 mL) was slowly added. The mixture was stirred for 12 hours at room temperature. The reaction was quenched with distilled water (30 mL) and stirred for 30 minutes. The membrane was washed with an additional amount of water.

Aromatic and chlorinated aromatic pollutant removal - GC-MS Analysis

Extraction in Headspace: a gas mixture of aromatic pollutants in µg/m^3 range was sampled at room temperature for 30 minutes.

GC-MS analysis

Gas-chromatograph HP 6890 Series Plus, Agilent Technologies (Milan, Italy):
- Column: MND-5S (l=30 m, i.d.=0.25 mm, d.f.=0.25 µm) (Supelco);
- Carrier gas: helium
- Carrier gas flux: 1 mL/min
- Carrier gas pressure: 70 KPa.
- Injector Temp: 300°C
- Injection mode: splitless
-Temperature program: 40°C for 5.5 minutes (10°C/min until 80°C) and then 30°C/min until 200°C.

Mass Spectrometer MSD 5973, Agilent Technologies:
- Source Temperature: 200°C;
- Transfer Line temperature: 200°C;
- Ionization: E.I. (70 eV);
-Voltage: 2200 V;
-Acquisition modality: Time scheduled monitoring;
-Solvent delay: 0.5 minutes;
-Dwell time: 30 ms;

-Monitored ions: Range from 40 to 150 m/z

The Mass Spectrometer was tuned using perfluorotributylamine and the analytes were identified by comparison with the retention time of standard solution and with the MS spectra reported in NIST Library (National Institute of Standards and Technology).

Inductively Coupled Plasma Atomic Emission Spectroscopy (ICP-AES) analysis:

Dopamine-decorated 3D-printed membranes were soaked for 12 hours in 10 mL of a bidistilled water solution containing Cr^{6+}, Tl^{+}, Hg^{2+} and Pb^{2+} in concentration of 1 ppm each. Water solutions were filtered over 0.2 µm and analyzed by using an emission spectrometer JY 2501 with coupled plasma induction in radial configuration HORIBA Jobin Yvon (Kyoto, Japan), ULTIMA2 model.
Instrumental features: monochromator Model JY 2501; focal length 1 m; resolution 5 pm; nitrogen flow 2 l/min. ICP source: nebulizer Meinhard, cyclonic spraying chamber; argon flow 12 L/min; wavelengths range 160-785 nm; optical bench temperature 32 °C.
The wavelength used for quantitative analysis was chosen by examining the emission line with greater relative intensity, ensuring that there was no spectral interference with the Argon emission lines.
Data acquisitions and processing were performed using the ICP JY v 5.2 software (Jobin Yvon). Measurements were performed in triplicate.

3.7 References

1. UNESCO. *The United Nations World Water Development Report 2019: Leaving no one behind. UNESCO Digital Library* (2019).
2. Sholl, D. S. & Lively, R. P. Comment. *Nature* **532**, 6–9 (2016).
3. Schwarzenbach, R. P., Egli, T., Hofstetter, T. B., Von Gunten, U. & Wehrli, B. Global water pollution and human health. *Annu. Rev. Environ. Resour.* **35**, 109–136 (2010).
4. Margot, J., Rossi, L., Barry, D. A. & Holliger, C. A review of the fate of micropollutants in wastewater treatment plants. *Wiley Interdiscip. Rev. Water* **2**, 457–487 (2015).
5. Reungoat, J. *et al.* Removal of micropollutants and reduction of biological activity in a full scale reclamation plant using ozonation and activated carbon filtration. *Water Res.* **44**, 625–637 (2010).
6. Hollender, J., Zimmerman, G. S., Koepke, S., Krauss, M. & Mcardell, C. S. Elimination of Organic Micropollutants in a Municipal Wastewater Treatment Plant Upgraded with a Full-Scale Post-Ozonation Followed by Sand Filtration. *Enviromental Sci. Technol.* **43**, 7862–7869 (2009).
7. Klamerth, N., Rizzo, L., Malato, S., Maldonado, M. I. & Ferna, A. R. Degradation of fifteen emerging contaminants at m g L L 1 initial concentrations by mild solar photo-Fenton in MWTP effluents. *Water Res.* **44**, 545–554 (2010).
8. Rodriguez-narvaez, O. M., Peralta-hernandez, J. M., Goonetilleke, A. & Bandala, E. R. Treatment technologies for emerging contaminants in water: A review. *Chem. Eng. J.* **323**, 361–380 (2017).
9. Elorm, O. E. & Sudesh, R. Membrane Technologies in Wastewater Treatment : *Membranes (Basel).* **10**, (2020).
10. Oller, I., Malato, S. & Sánchez-pérez, J. A. Science of the Total Environment Combination of Advanced Oxidation Processes and biological treatments for wastewater decontamination — A review. *Sci. Total Environ.* **409**, 4141–4166 (2011).

11. Stein, B. A., Wang, Z. & Fierke, M. A. Functionalization of Porous Carbon Materials with Designed Pore Architecture. *Adv. Mater.* 265–293 (2009).

12. Órfão, J. J. M. *et al.* Adsorption of a reactive dye on chemically modified activated carbons — Influence of pH. *J. Colloid Interface Sci.* **296**, 480–489 (2006).

13. Pan, B. *et al.* Development of polymeric and polymer-based hybrid adsorbents for pollutants removal from waters. *Chemical Engineering Journal* **151** 19–29 (2009).

14. Snyder, S. A. *et al.* Role of membranes and activated carbon in the removal of endocrine disruptors and pharmaceuticals. *Desalination* **202**, 156–181 (2007).

15. Mohammadi, T., Kazemimoghadam, M. & Saadabadi, M. Modeling of membrane fouling and flux decline in reverse osmosis during separation of oil in water emulsions. *Desalination* **157**, 369–375 (2003).

16. Angelo, A. D., Galia, A. & Scialdone, O. Cathodic abatement of Cr (VI) in water by microbial reverse-electrodialysis cells. *J. Electroanal. Chem.* **748**, 40–46 (2015).

17. Coday, B. D., Almaraz, N. & Cath, T. Y. Forward osmosis desalination of oil and gas wastewater: Impacts of membrane selection and operating conditions on process performance. *J. Memb. Sci.* **488**, 40–55 (2015).

18. Tagliavini, M. & Schaefer, A. I. Removal of steroid micropollutants by polymer-based spherical activated carbon (PBSAC) assisted membrane filtration. *J. Hazard. Mater.* (2018).

19. Amador, R. N., Carboni, M. & Meyer, D. Sorption and photodegradation under visible light irradiation of an organic pollutant by a heterogeneous UiO-67 – Ru – Ti MOF obtained by post-synthetic exchange. *RSC Adv.* **125**, 195–200 (2017).

20. Wang, B. *et al.* Highly Stable Zr(IV)-Based Metal − Organic Frameworks for the Detection and Removal of Antibiotics and Organic Explosives in Water. *J. Am. Chem. Soc.* 6204–6216 (2016).

21. Teng, W. *et al.* Rapid and E ffi cient Removal of Microcystins by Ordered Mesoporous Silica. *Enviromental Sci. Technol.* **47**, 8633–8641 (2013).

22. Shi, B. *et al.* A pillar[5]arene-based 3D network polymer for rapid removal of organic micropollutants from water. *J. Mater. Chem. A* **5**, 24217–24222 (2017).

23. Sun, D. T. *et al.* Rapid, Selective Heavy Metal Removal from Water by a Metal-Organic Framework/Polydopamine Composite. *ACS Cent. Sci.* **4**, 349–356 (2018).

24. Song, P. *et al.* An ionic covalent organic polymer toward highly selective removal of anionic organic dyes in aqueous solution. *New J. Chem.* **44**, 8572–8577 (2020).

25. McKeown, N. B. Polymers of Intrinsic Microporosity. *ISRN Mater. Sci.* **2012**, 1–16 (2012).

26. Budd, P. M. *et al.* Polymers of intrinsic microporosity (PIMs): robust, solution-processable, organic nanoporous materials. *Chem. Commun.* 230–231 (2004).

27. Xiao, L. *et al.* Rapid removal of organic micropollutants from water by a porous β-cyclodextrin polymer. *Nature* **529**, 190–194 (2015).

28. Skala, L. P., Yang, A., Klemes, M. J., Xiao, L. & Dichtel, W. R. Resorcinarene Cavitand Polymers for the Remediation of Halomethanes and 1,4-Dioxane. *J. Am. Chem. Soc.* **141**, 13315–13319 (2019).

29. Raya, J. *et al.* An ultra-absorbent alkyne-rich porous covalent polycalix[4]arene for water purification. *J. Mater. Chem. A* **5**, 62–66 (2016).

30. Wang, X., Jiang, M., Zhou, Z., Gou, J. & Hui, D. 3D printing of polymer matrix composites: A review and prospective. *Compos. Part B Eng.* **110**, 442–458 (2017).

31. Lv, J. *et al.* 3D printing of a mechanically durable superhydrophobic porous membrane for oil–water separation. *J. Mater. Chem. A* **5**, 12435–12444 (2017).

32. Atkinson, S. Nano Sun sets up Singapore's first 3D-printing plant for water filtration membranes. *Membr. Technol.* **2018**, 10–11 (2018).

33. Ashraf, M. A. Persistent organic pollutants (POPs): a global issue, a global challenge. *Environ. Sci. Pollut. Res.* **24**, 4223–4227 (2017).

34. Bianchi, F. *et al.* Cavitands as superior sorbents for benzene detection at trace level. *New J. Chem.* **27**, 502–509 (2003).

35. Trzcinski, W. J. *et al.* In Search of the Ultimate Benzene Sensor: The EtQxBox Solution. *ACS Sensors* **2**, 590–598 (2017).

36. Swainson, W. K. & Data, R. U. S. A. United States Patent (19). (1977).

37. Kodama, H. Automatic method for fabricating a three- dimensional plastic model with photo- hardening polymer. *Rev. Sci. Instrum.* **1770**, 2–6 (1981).

38. Gabriel, S. & Hull, C. W. United States Patent (19). (1984).

39. Crump, S. S. United States Patent (19). (1992).

40. Deckard, C. R., Rock, R., Joseph, J. & Data, R. U. S. A. United States Patent (19). (1992).

41. Haggerty, S., Michael, J., Williams, P. A. & Lawrence, P. E. United States Patent (19). (1993).

42. Shkolnik, A., Angeles, L., Diamond, M. N., Dvorskiy, E. & Angeles, L. United States Patent (19). (1998).

43. Gri, K. M., Cataldo, R. De & Fogarty, K. H. Do-It-Yourself: 3D Models of Hydrogenic Orbitals through 3D Printing. *J. Chem. Educ.* **93**, 1586–1590 (2016).

44. Dolenc, A. Slicing procedures for layered manufacturing techniques. *Comput. Des.* **26**, 119–126 (1994).

45. Tatarchuk, N. Real-Time Tessellation on GPU. in *Eurographics 2007* (2007).

46. Su, C. K., Yen, S. C., Li, T. W. & Sun, Y. C. Enzyme-Immobilized 3D-Printed Reactors for Online Monitoring of Rat Brain Extracellular Glucose and Lactate. *Anal. Chem.* **88**, 6265–6273 (2016).

47. Wang, Z., Wang, J., Li, M., Sun, K. & Liu, C. J. Three-dimensional printed acrylonitrile butadiene styrene framework coated with Cu-BTC metal-organic frameworks for the removal of methylene blue. *Sci. Rep.* **4**, 4–10 (2014).

48. Cooke, M. N., Fisher, J. P., Dean, D., Rimnac, C. & Mikos, A. G. Use of Stereolithography to Manufacture Critical-Sized 3D Biodegradable

Scaffolds for Bone Ingrowth. *Stereolithographic Polym. Biodegrad. scaffolds* 65–69 (2002).

49. Kwon, I. K. & Ã, T. M. Photo-polymerized microarchitectural constructs prepared by microstereolithography (mSL) using liquid acrylate-end-capped trimethylene carbonate-based prepolymers. *Biomaterials* **26**, 1675–1684 (2005).

50. Lee, J. W., Lan, P. X., Kim, B., Lim, G. & Cho, D. 3D scaffold fabrication with PPF/DEF using micro-stereolithography. *Microelectron. Eng.* **84**, 1702–1705 (2007).

51. Lee, K. *et al.* Poly (propylene fumarate) Bone Tissue Engineering Scaffold Fabrication Using Stereolithography : Effects of Resin Formulations and Laser Parameters. *Biomacromolecules* 0–7 (2007).

52. Gupta, V., Nesterenko, P. & Paull, B. 3D Printing in Chemical Sciences. *Royal Society of Chemistry* (2019).

53. Formlabs Inc. The Ultimate Guide to Stereolithography (SLA) 3D Printing. 1–23 (2017).

54. Oskui, S. M. *et al.* Assessing and Reducing the Toxicity of 3D-Printed Parts. *Enviromental Sci. Technol. Lett.* **3**, 1–6 (2016).

55. Peltola, S. M. *et al.* Annals of Medicine A review of rapid prototyping techniques for tissue engineering purposes. *Ann. Med.* **40**, 268–280 (2008).

56. Murphy, S. V & Atala, A. 3D bioprinting of tissues and organs. *Nat. Biotechnol.* **32**, 773–785 (2014).

57. Bartlett, N. *et al.* A 3D-printed, functionally graded soft robot powered by combustion. *Science (80).* **349**, 161–166 (2015).

58. Rogers, C. I. *et al.* 3D printed microfluidic devices with integrated valves. *Biomicrofluidics* **9**, 1–9 (2015).

59. Garcia, E. A., Ayranci, C. & Qureshi, A. J. Material Property-Manufacturing Process Optimization for Form 2 Vat-Photo Polymerization 3D Printers. *J. Manuf. Mater. Process.* **4**, 1–12 (2020).

60. Szykiedans, K. & Credo, W. Mechanical properties of FDM and SLA low-

cost 3-D prints. *Procedia Eng.* **136**, 257–262 (2016).

61. Gupta, P., Elkins, C., Long, T. E. & Wilkes, G. L. Electrospinning of linear homopolymers of poly (methyl methacrylate): exploring relationships between fiber formation , viscosity , molecular weight and concentration in a good solvent. *Polymer.* **46**, 4799–4810 (2005).

62. Mckee, M. G., Wilkes, G. L., Colby, R. H. & Long, T. E. Correlations of Solution Rheology with Electrospun Fiber Formation of Linear and Branched Polyesters. *Macromolecules* **37**, 1760–1767 (2004).

63. Teixeira, S. M., Feijen, J., Grijpma, D. W., Sch, S. & Poot, A. Flexible and Elastic Scaffolds for Cartilage Tissue Engineering Prepared by Stereolithography Using Poly (trimethylene carbonate)-Based Resins. *Macromol. Biosci.* **13**, 1711–1719 (2013).

64. Hinczewski, C., Corbel, S. & Chartie, T. Ceramic Suspensions Suitable for Stereolithogiaphy. *J. Eur. Ceram. Soc.* **18**, 583–590 (1998).

65. Yuan, H., Richards, R. G. & Eglin, D. Poly (trimethylene carbonate) and nano-hydroxyapatite porous scaffolds manufactured by stereolithography. *Polym. Adv. Technol.* **28**, 1219–1225 (2017).

66. Melchels, F. P. W., Feijen, J. & Grijpma, D. W. Biomaterials A poly (D, L-lactide) resin for the preparation of tissue engineering scaffolds by stereolithography. *Biomaterials* **30**, 3801–3809 (2009).

67. Hadjichristidis, N. & Roovers, J. E. L. Synthesis and Solution Properties of Linear , Four-Branched , and Six-Branched Star Polyisoprenes. *J. Polym. Sci.* **12**, 2521–2533 (1974).

68. Hakala, R. A., Korhonen, H., Meretoja, V. V & Sepp, J. V. Photo-Cross-Linked Biodegradable Poly (Ester Anhydride) Networks Prepared from Alkenylsuccinic Anhydride Functionalized Poly (ε-caprolactone) Precursors. *Biomacromolecules* **12**, 2806–2814 (2011).

69. Chem, P., Morozowich, N. L., Nichol, J. L., Mondschein, R. J. & Allcock, H. R. Polymer Chemistry Design and examination of an antioxidant-containing polyphosphazene. *Polym. Chem.* **3**, 778–786 (2012).

70. Huyck, R. H., Trenor, S. R., Love, B. J. & Long, T. E. Photodimerization of coumarin functionalized poly(alkyl acrylate) and poly(alkyl methacrylate)

random copolymers: Influence of copolymer composition on photocrosslinking. *J. Macromol. Sci. Part A Pure Appl. Chem.* **45**, 9–15 (2008).

71. Childers, E. P., Wang, M. O., Becker, M. L., Fisher, J. P. & Dean, D. 3D printing of resorbable poly (propylene fumarate) tissue engineering scaffolds. *MRS Bull.* **40**, 119–126 (2015).

72. Melchels, F. P. W., Feijen, J. & Grijpma, D. W. A review on stereolithography and its applications in biomedical engineering. *Biomaterials* **31**, 6121–6130 (2010).

73. Moore, J. L., Mccuiston, A., Mittendorf, I., Ottway, R. & Johnson, R. D. Behavior of capillary valves in centrifugal microfluidic devices prepared by three-dimensional printing. *Microfluid Nanofluid* **10**, 877–888 (2011).

74. Collington, E. W., Finch, H. & Smith, I. J. SELECTIVE DEPROTECTION OF ALCOHOLIC AND PHENOLIC SILYL ETHERS. *Tetrahedron Lett.* **26**, 681–684 (1985).

75. Schäfer, A. I., Akanyeti, I. & Semião, A. J. C. Micropollutant sorption to membrane polymers: A review of mechanisms for estrogens. *Adv. Colloid Interface Sci.* **164**, 100–117 (2011).

76. Torelli, M. *et al.* pH-Driven Conformational Switching of Quinoxaline Cavitands in Polymer Matrices. *Synlett* 2503–2508 (2018).

77. Hauke, F., Myles, A. J. & Rebek, J. Lower rim mono-functionalization of resorcinarenes. *Chem. Commun.* **40**, 4164–4166 (2005).

78. Dizon, G. V. *et al.* Bio-inert interfaces via biomimetic anchoring of a zwitterionic copolymer on versatile substrates. *J. Colloid Interface Sci.* **529**, 77–89 (2018).

Chapter 4

Tetraphosphonate cavitand as receptor in QCM sensors

4.1 Introduction

World drug report published by the United Nations Office on Drugs and Crime (UNODC) has warned that the world-wide consumption of amphetamine type stimulants (ATS) have an impressive impact over the society in terms of security and human health.[1] In the last years, many countries observed a fast replacement of "traditional" illicit drugs, such as cocaine and heroin, with amphetamine-based drugs, leading to a capillary diffusion and exponential growth of the ATS market.
The conventional methods developed for the detection in water of ATS illicit drugs rely on gas chromatography or high-performance liquid chromatography coupled with mass spectroscopy, UV absorption, fluorescence and chemiluminescence, able to push the LOD in the ppb range.[2–10] However, all these methods are highly time-consuming and based on expensive equipment. Moreover, these techniques are not amenable for direct on-field analyses, requiring on-site sampling followed by pre-treatments and laboratory tests conducted by specialized operators. On-site detection of ATS drugs using portable devices able to guarantee sensitivity, selectivity and fast response are on demand.
An additional challenge relies in the detection of the so called "designer-drugs", drug derivatives obtained through small modifications to the structure of illicit substances maintaining unaltered the psychoactive part.[11,12] These structure modifications move these compounds in a legal grey area, where the laws become unclear and ineffective.[13] The expansion opportunity given to the illegal market by designer drugs prompted several efforts in the modifications of ATS structures, leading to the rise of a wide class of new psychoactive amphetamines free of any law supervision. Cocaine and many ATS drugs have the methyl ammonium group ($^{+}$N-CH_3 red labelled in **Figure 4.1**) as psychoactive site that are in common with other illicit drugs.

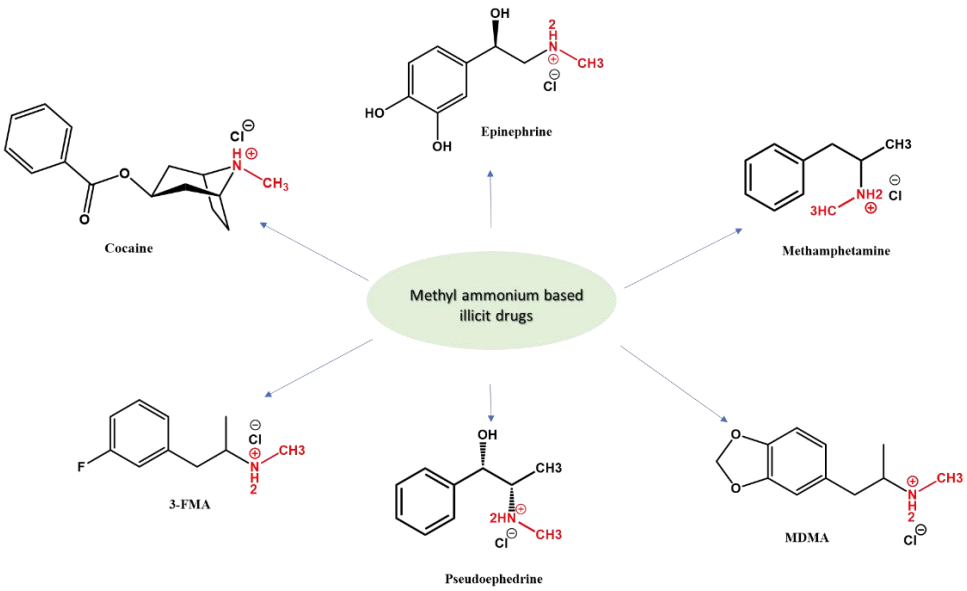

Figure 4.1 *Chemical structures of the most common methyl ammonium based illicit drugs.*

The availability of technologies optimized just to detect a specific drug over the entire class, such as ELISA tests, represents a relevant limitation for the identification of emerging substances. In order to overcome this drawback, supramolecular chemistry can provide new receptors for the detection of a broad set of drugs. In particular, tetraphosphonate cavitand (Tiiii) represents one of the most performant systems in the sensing of Illicit drugs and their derivatives in water.[14] As discussed in *Chapter 1*, the cavity of this macrocyclic receptor is designed to selectively interact with methyl ammonium moieties through the synergic combination of three non-covalent interactions: hydrogen bonds, cation-dipole interaction, cation-π interactions.[15–17] The ability of the tetraphosphonate cavitand in the formation of host-guest complexes with drugs and N-methylated amino acids has been widely explored in the solid state and in solution.[14,16,18]
Taking advantages by the superior recognition properties of the Tiiii cavitand towards molecules bearing methyl ammonium functionalities, our research group fabricated an innovative nanomechanical probe based on the cantilever technology for the detection in water of ATS and other drugs (**Figure 4.2**).[14]

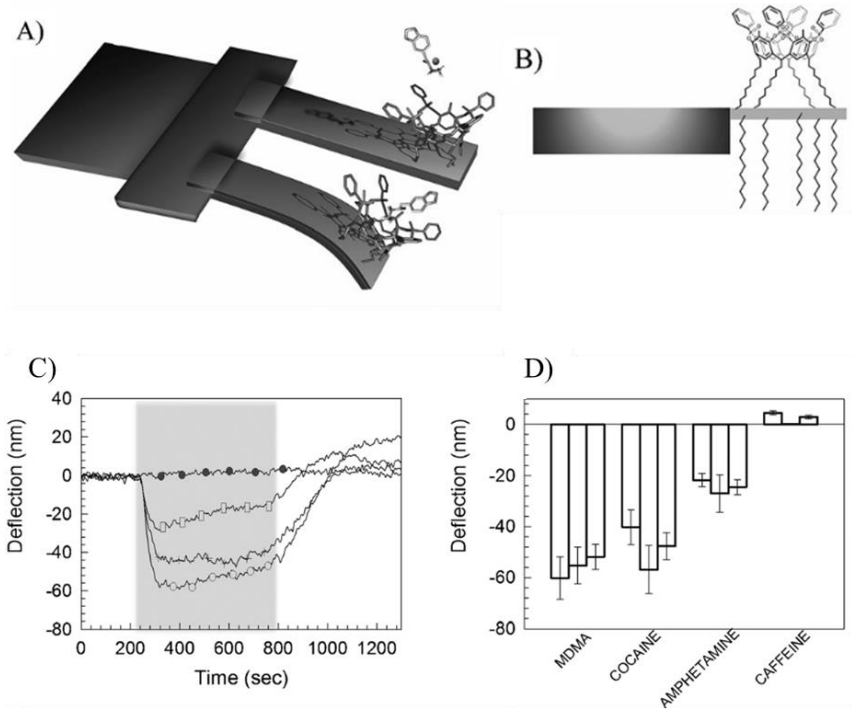

Figure 4.2 *A) Schematic representation of Tiiii-Si-MC; Top face of the probe activated with Tiiii cavitand; C) Absolute deflection curves of the probe after injection of drugs (○ MDMA, + cocaine, □ amphetamine, ● caffeine); D) Mean absolute equilibrium deflections of Tiiii-Si-MCs over subsequent replicates.*[14]

Silicon microcantilevers bearing photochemical grafted Tiiii receptor (Tiiii-Si-MC) was exploited to convert cavitand molecular recognition on surface into a high-fidelity, robust and reproducible nanomechanical response. This particular set-up provided superior performances in the detection of ppm levels of methamphetamine salts and cocaine in water (LOD = 10 ppm).

In recent years increasing attention was focused over the introduction of supramolecular receptors in electrochemical, gravimetric and optical sensors to reach real-time signal transduction.[19,20] In particular, gravimetric devices based on molecular recognition are appealing, thanks to simple operation conditions, equipment miniaturization, sensitivity, fast response, low cost and high

portability. These sensors are widely used in different fields like food safety, pollutant detection and biological analysis.[21,22]

Among available gravimetric devices, quartz crystal microbalances (QCMs) play a major role as transducers. The working mechanism of QCM sensors relies in the piezoelectric behavior of the quartz crystal, which experiences variations of its oscillation frequency that are proportional to mass change on its surface. Application of a voltage in the AC field with a specific frequency leads to resonance of the piezoelectric quartz crystal with a vibrational frequency related to thickness and shear modulus of the device. The correlation between frequency change and mass variation is described by the Sauerbrey equation [23]:

$$\Delta F = \frac{-2 f_0^2 \Delta m}{A\sqrt{\mu_q \rho_q}} \qquad \textit{eq. 1}$$

ΔF: Normalized frequency change (Hz);
f_0: Resonant frequency of the fundamental mode (Hz);
A: Electrodes area (cm^2);
μ_q: Shear modulus;
ρ_q: Quartz crystal density;
Δm: Mass change (g).

Equation 1 shows a negative correlation between mass variations occurring onto the electrodes surface and the changing in the nominal resonant frequency: Changes in the resonant frequency of modified QCM crystals become a powerful instrument in the monitor of extremely low mass changing (ng/cm^2).[24]

In the particular situation of QCM devices working in Newtonian liquids, typically in water, the changing of the resonant frequency is described by the modified Kanazawa and Gordon equation[25]:

$$\Delta F = -f_0^{3/2} \sqrt{\frac{\rho_L \eta_L}{\pi \mu_q \rho_q}} \qquad \textit{eq. 2}$$

ΔF: normalized frequency change (Hz);
f_0: Resonant frequency of the fundamental mode (Hz);
μ_q: Shear modulus;

ρ_q: Quartz crystal density;
ρ_L: Liquid density (g);
η_L: Liquid viscosity.

Despite low prices and high portability of the piezoelectric devices, their spread has been limited by the low selectivity towards target analytes.[26] To overcome the selectivity issue, research focused its attention on the deposition of molecular receptors over quartz crystals. Receptor deposition can be achieved through the application of physical coating techniques, such as spin-coating, spraying coating or LB covering, or *via* electropolymerization (EQCM). In this latter technique, molecular receptors functionalized with proper electroactive monomers are electropolymerized over EQCM gold electrodes achieving a high controlled deposition of the conductive polymer layers.
The electropolymerization process frequently involves the electrochemical oxidation of several aromatic heterocyclic molecules such as pyrrole, thiophene, furan, indole, thianaphthene and carbazole.[27,28] Moreover, additional conducting polymers were synthesized by electropolymerization of benzenoid and nonbenzenoid hydrocarbons as azulene, fluorene, fluoranthene, triphenylene and pyrene.[29–32] In the last years the research in the electrochemistry field focused its attention on 2,2'-bithiophene, an interesting compound made by two thiophene units linked together in the positions 2 and 2'. The popularity of this molecule is related to its superior electroactivity, pushed by the mesomeric effect that induces mutual activation of the two thiophene rings. In fact, the drastic drop in the electroactivity of a modified thiophenes having electron withdrawing groups is frequently overcome by using the more active 2,2'-bithiophene species. The direct oxidation of these monomers is commonly achieved in a three-electrode cell equipped with counter, reference and working electrodes by application of galvanostatic, potentiostatic or potentiodynamic conditions. The driving-force of the process is the monomer electrooxidation induced by the application of an anodic potential over the electrode surface. The electrooxidation of a molecule R into its radical cation $R^{+\cdot}$ at the electrode surface prompts to several follow-up reactions involving monomers, oligomers or electrooxidized species. The proceeding of these reactions leads to the formation and deposition of a polymeric film over the electrode surface that are followed by the real-time monitoring of the frequency drop.

EQCM devices are frequently used in combination with cyclic voltammetry, in order to grow conductive polymers under potentiodynamic conditions. The total charge involved in the process is widely used as control parameter in cyclic voltammetry to evaluate the amount of deposited polymer. A rigorous control of the coating process and layer reproducibility is achieved through simultaneous acquisition of voltammograms and frequencygrams during the deposition of the sensing material.

Recently, our research group developed a EQCM sensor coated with a cavitand-decorated polybithiophene layer for the detection of aromatic pollutants in water.[33] The sensor was prepared by the electropolymerization of a tetraquinoxaline cavitand (QxCav) functionalized at the upper rim with a 2,2'-bithiophene unit. The polymer was directly grown on the gold electrode of a EQCM system in potentiodynamic conditions and the resulting frequencymetric sensor was applied for the detection in water of aromatic, chlorinated aromatic and chlorinated aliphatic pollutants. For the effective complexation of aromatic analytes in the QxCav cavity, this piezoelectric device exhibited high sensitivity and reproducibility of the responses towards chlorinated and not chlorinated aromatic hydrocarbons.

In this Chapter, the development of a new EQCM sensor for the detection of ATS and related designer drugs in water based on polybithiophene functionalized with tetraphosphonate cavitands is presented.

4.2 Results and discussion

Polymerization is essential to convert tetraphosphonate cavitands into a reliable sensing layer. In particular, electropolymerization technique was chosen to precisely control the thickness and morphology of the deposited layer directly on a QCM transducer. To reach this purpose, we decided to synthetize a new tetraphosphonate cavitand functionalized with a 2,2'-bithiophene electroactive functionality. In the design of this new receptor, two possible synthetic pathways can be followed targeting the derivatization of the cavitand upper and lower rim, respectively. The latter approach is more straightforward as it benefits from the availability of monofunctionalized resorcinarenes. Moreover, the choice of a proper linker between the resorcinarene scaffold and the bithiophene unit revealed to be essential to preserve the electroactivity of the final cavitand monomer. In this context, we synthesized the two model tetramethylene cavitands **8** and **10** bearing two different spacer units at the lower rim, a triazole ring and a 4-ethynylbenzoate group, respectively (**Figure 4.3**). Even if they do not impart complexation abilities, the four methylene bridging groups at the upper rim were chosen to ensure an increased synthetic accessibility and chemical stability for these cavitands.

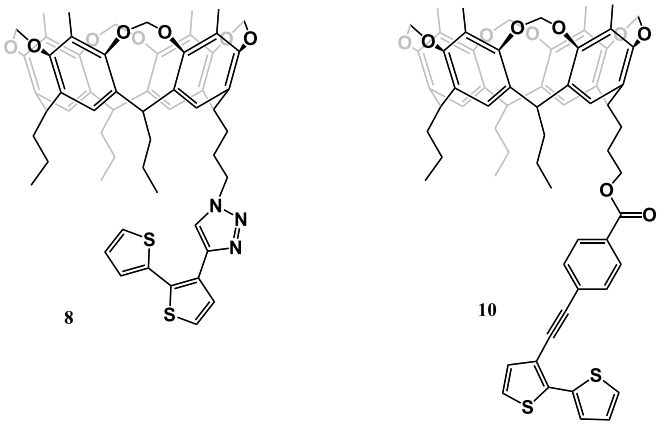

Figure 4.3 *Model cavitand monomers: methylene-bridged cavitands having the triazole (**8**) and the ethynyl benzoate spacer (**10**)*

4.2.1 Synthesis of 3-ethynyl-2,2'-bithiophene (3)

The common electroactive moiety **3** was synthesized in three steps and 15% overall yield (**Scheme 4.1**), following a literature procedure.[33]

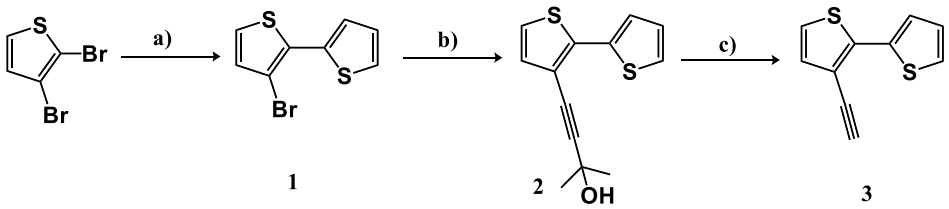

Scheme 4.1 *Synthesis of **3** a) 2-Thienylboronic acid, 2M sodium carbonate solution, 1,4-dioxane, $Pd(PPh_3)_4$, 100 °C, 4 h, 43% yield; b) 2-Methylbut-3-yn-2-ol, diisopropylamine, $Pd(dppf)Cl_2 \cdot CH_2Cl_2$, 85 °C, 24 h, 78% yield; c) Potassium hydroxide, toluene, methanol, 110 °C, 5 h, 63% yield.*

The multistep synthesis started with the Suzuki cross-coupling between the 2,3-dibromothiophene and 2-thienyl boronic acid catalyzed by palladium tetrakis(triphenylphosphine), obtaining the 3-bromo-2,2'-bithiophene **1** in 43% yield.[34] In order to functionalize the halogenated bithiophene with an ethynyl linker as 2-(2-hydroxypropyl) protected derivative, a Sonogashira reaction was performed between **1** and 2-methylbyt-3-yn-2-ol using copper iodide and 1,1'-bis(diphenylphosphino)ferrocene] palladium(II)dichloride ($Pd(dppf)Cl_2$) as catalysts. Product **2** was recovered as a colorless oil in 78% yield. The cleavage of the protecting group from the ethynyl linker was reached by treatment with potassium hydroxide. Flash chromatography purification of the crude material afforded product **3** as a colorless oil in 63% yield. Product **3** was characterized by ^{1}H NMR and ESI-MS.

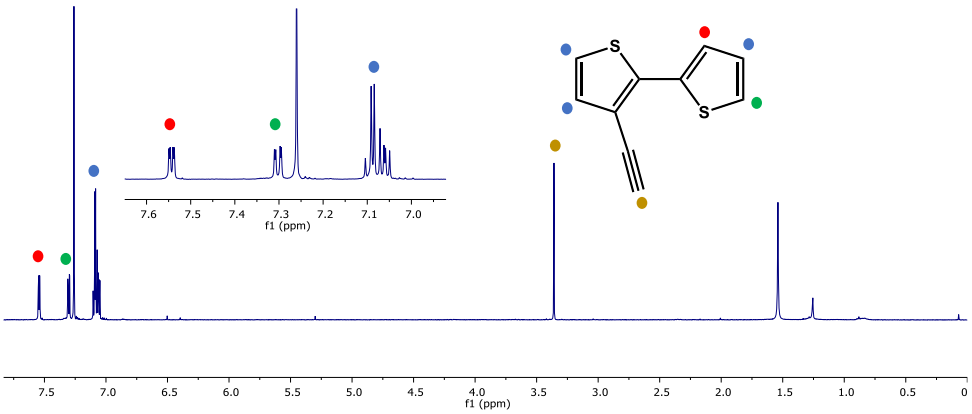

Figure 4.4 *^{1}H NMR spectrum of **3** in $CDCl_3$, aromatic region magnification in the inset.*

The ^{1}H NMR spectrum of 3-ethynyl-2,2'-thiophene is reported in **Figure 4.4**. The singlet signal at 3.36 ppm (*gold* spot) is associated to the terminal proton of the alkyne group. The two doublet of doublet signals at 7.55 and 7.31 ppm are related to the $H_{3'}$ and $H_{5'}$ protons (*red* and *green* spots), meanwhile the multiplet at 7.06 ppm is generated by the H_4, H_5 and $H_{4'}$ protons (*blue* spots).

4.2.2 Control cavitands synthesis and electroactivity evaluation

The first tested spacer between the resorcinarene lower rim and the bithiophene unit was the triazole ring. For this purpose, the methylene-bridged cavitand **8** was synthesized by click-reaction between the azide footed cavitand **7** and bithiophene **3** (**Scheme 4.2**).

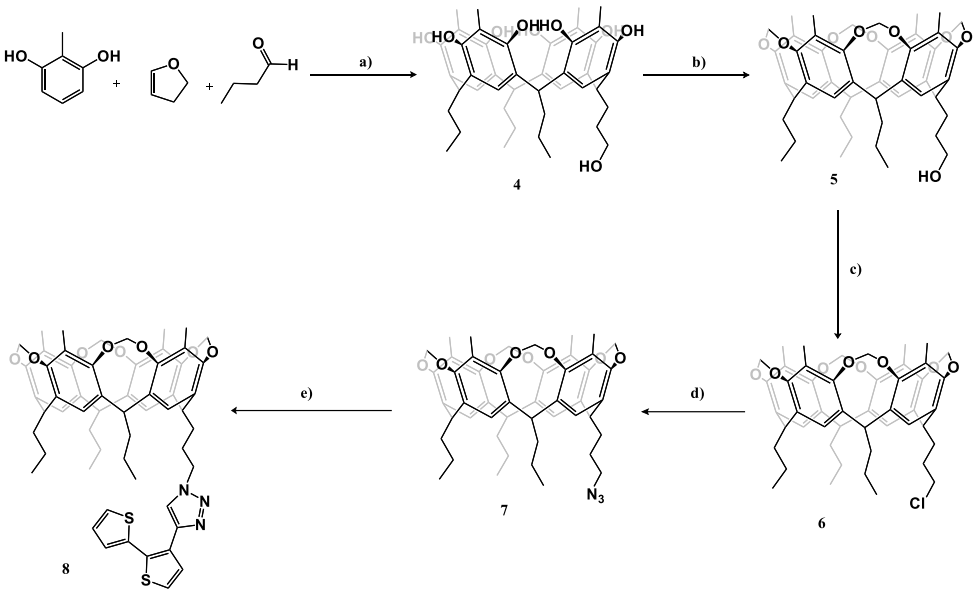

Scheme 4.2 *Synthesis of **8**: a) HCl 37%, methanol, 55 °C, 5 d; b) Bromochloromethane, potassium carbonate, DMF, 80 °C, 16 h, 29% yield (over two steps); c) Thionyl chloride, DMF, toluene, 55 °C, 16 h, 80% yield; d) Sodium azide, DMF, 80 °C, 16 h, 62% yield; e) 3-Ethynyl-2,2'-bithiophene, sodium ascorbate, $CuSO_4 \cdot 5H_2O$, water, DMSO, MW assisted, 80 °C, 150 W, 1 h, 48% yield.*

The functionalization of the cavitand lower rim was achieved using mono OH-footed resorcinarene **4** as macrocyclic precursor. Resorcinarene **4** was prepared by condensation reaction between a 3:1 mixture of butyraldehyde and 2,3-dihydrofuran and 2-methylresorcinol under acidic conditions. The reaction afforded a crude mixture of differently substituted resorcinarenes, characterized by the presence at the lower rim of none, one or two OH groups. Due the high polarity of these macrocycles and to avoid tedious purification processes, the obtained crude was used in the subsequent reaction without any purification. Cavitand **5** was obtained by bridging the phenolic OH groups with bromochloromethane under basic conditions; product **5** was isolated in 29% yield after flash chromatography purification. Chlorination of aliphatic hydroxyl group at the lower rim was achieved by reaction with thionyl chloride with DMF as

catalyst. Cavitand **6** was recovered as a light orange solid in 80% yield. In the next step the nucleophilic substitution of the chlorine atom with an azide group, using sodium azide, afforded product **7** in 62% yield.
The target cavitand **8** was synthesized through a micro-wave assisted Copper(I)-catalyzed cycloaddition between the azide-footed cavitand **7** and the ethynyl-bithiophene **3**, in the presence of $CuSO_4 \cdot 5H_2O$ and sodium ascorbate. Ascorbate-driven reduction of copper sulfate into Cu(I) species is pivotal for the generation of the sole 1,4 regioisomer. Cavitand **8** was isolated after purification *via* flash chromatography in 48% yield and characterized by ESI-MS and NMR.

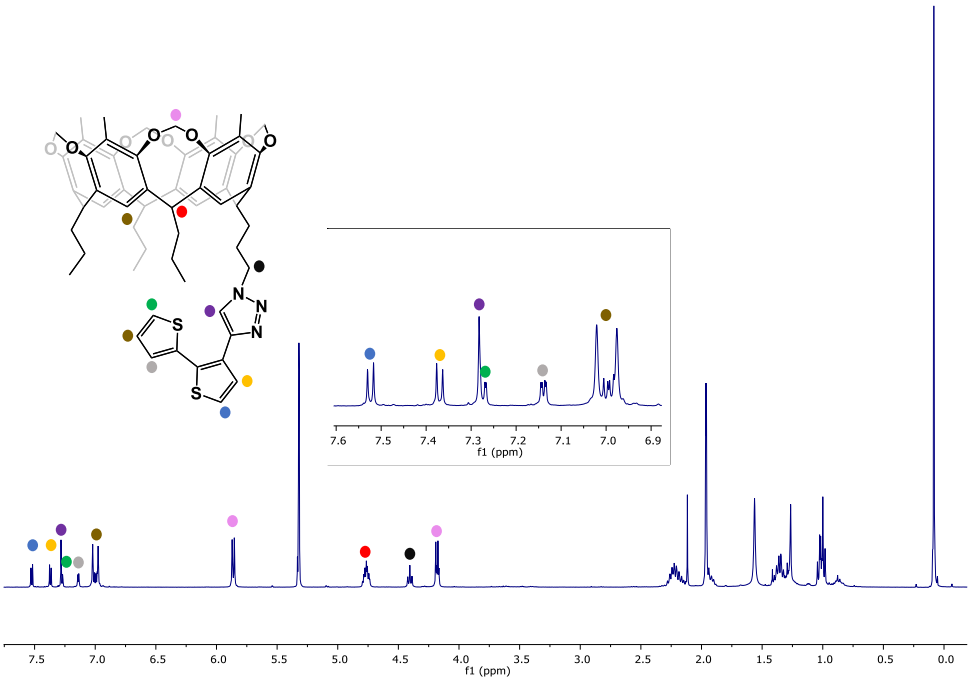

Figure 4.5 ^{1}H NMR spectrum of **8** in CD_2Cl_2 (400 MHz).

The ^{1}H NMR spectrum reported in **Figure 4.5** shows all the characteristics peaks of cavitand **8**. Looking in the low field range, the two doublet signals at 7.53 ppm and 7.38 ppm are related to the protons H_4 and H_5 (*yellow* and *blue* spots) of the bithiophene moiety. The multiplet at 7.27 ppm is composed by the doublet signal of the bithiophene proton $H_{5'}$ (*green* spot) superimposed with the singlet signal

of the proton in the triazole ring (*purple* spot). The doublet signal at 7.14 ppm is related to the bithiophene proton $H_{3'}$ (*grey* spot), meanwhile the multiplet signal at 7.0 ppm is made by the contribution of $H_{4'}$ and Ar*H* protons of the resorcinarene scaffold (*brown* spots).
The methylene bridges are identified by the two multiplet signals at 5.87 and 4.17 ppm associated respectively to the protons inward and outward the macrocyclic cavity (*pink* spots). The multiplet at 4.76 ppm is ascribed to the characteristic C*H* bridging groups (*red* spot) meanwhile the methyl apical species are associated to the singlet signal at 1.96 ppm. The triplet signal at 4.41 ppm is defined by the lower rim CH_2 vicinal group to the triazole ring (*black* spot). All the signals at lower ppm are in agreement with the lower rim alkyl chains.

To investigate the effect of the triazole linker on the electro-activity of the 2,2'-bithiophene unit, cavitand **8** was electropolymerized trough cyclic voltammetry in potentiodynamic conditions, monitoring the formation of polymeric films over the gold electrodes of a QCM device. A piezoelectric quartz crystal covered by a gold lamina was used as a working electrode, meanwhile a silver-silver chloride pseudoreference and a platinum rod were used respectively as reference and counter electrodes.
Electropolymerization tests were performed using a $5 \cdot 10^{-4}$ M solution of cavitand **8** in dry dichloromethane:acetonitrile mixture (1:5 v/v). The binary mixture was chosen to solubilize the monomer and to induce the precipitation and subsequent deposition of the thiophene oligomers over the gold electrodes. Tetrabutylammonium hexafluorophospate (TBAHFP) was used as supporting electrolyte (10^{-1} M). Voltammograms and frequencygrams were simultaneously acquired during the deposition of the sensing material (**Figure 4.6**).

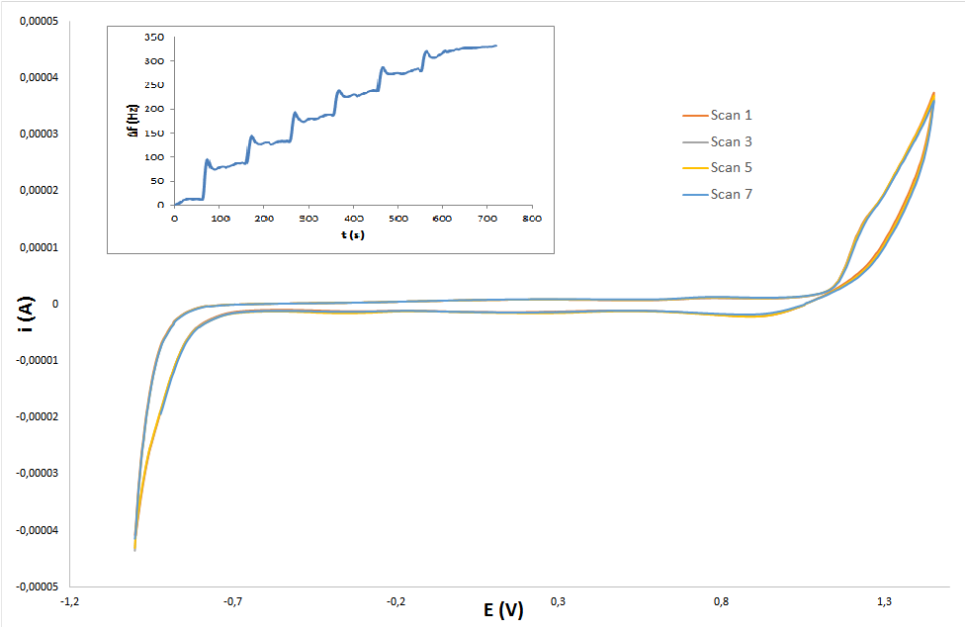

Figure 4.6 *CV-scans and frequencygram (inset) collected during the electropolymerization trial of the cavitand **8** over the QCM gold electrodes.*

The recorded voltammogram shows the same profile for every single scan, demonstrating the total absence of electro-activity of compound **8** and no polymer deposition over the QCM device. Moreover, progressive increment in the frequencygram highlights a mass loss related to the leaching of the gold surfaces. The deactivation of the 2,2'-bithiophene group by the triazole ring prompted us to test the 4-ethynylbenzoate group as spacer between the cavitand lower rim and the bithiophene unit, in order to preserve the electroactivity of the latter. For this purpose, cavitand **10** was synthesized in two-steps, following the synthetic pathway reported in **Scheme 4.3**.

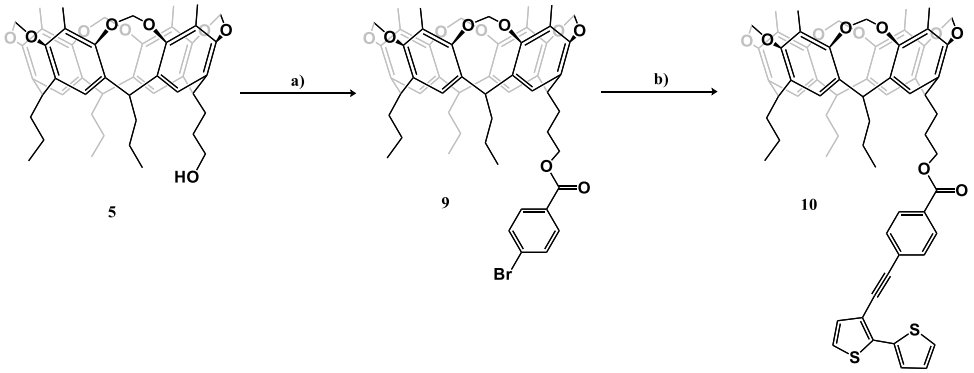

Scheme 4.3 *Synthesis of **10**: a) p-Bromobenzoic acid, 4-dimethylaminopyridine, N,N'-diciclohexylcarbodiimide, dichloromethane, r.t., 72 h, 56% yield; b) 3-ethynyl-2,2'-bithiophene (**8**), diisopropylamine, $Pd(PPh_3)_4$, CuI, toluene, 110 °C, 16 h, 10% yield.*

In the first step, the aliphatic hydroxyl group of cavitand **5** was esterified with p-bromobenzoic acid. The reaction was performed under mild conditions, using N,N'-diciclohexylcarbodiimide as coupling agent and 4-dimethylaminopyridine as catalyst (Steglich esterification). After flash chromatography purification, product **9** was recovered as a yellow solid in 78% yield. In the last step, a Sonogashira cross-coupling reaction between cavitand **9** and 3-ethynyl-2,2'-bithiophene **3** was performed using tetrakis(triphenylphosphine)palladium(0) and copper iodide as catalysts and diisopropylamine as base. Purification by flash chromatography afforded product **10** as a yellow solid in 10% yield.

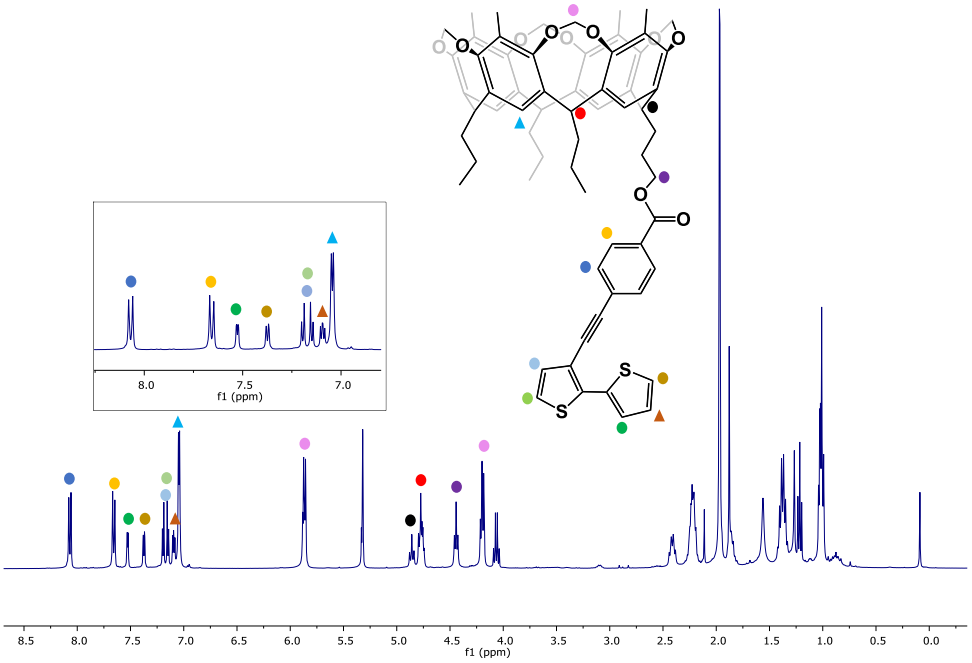

Figure 4.7 *^{1}H NMR spectrum of **10** in CD_2Cl_2 (400 MHz).*

The ^{1}H NMR spectrum, reported in **Figure 4.7**, shows all the characteristic peaks of the product **10**. All the signals in the high-field range are in agreement with the aliphatic protons of the lower rim alkyl chains. The multiplet signals at 4.19 and 5.87 ppm are ascribed to the methylene-bridge protons inward and outward the cavity. The triplet signal at 4.44 ppm (*purple* spot) is associated to CH_2 in α to the oxygen atom of the ester group. The characteristic CH methine bridges are identified by the two triplet signals at 4.89 and 4.77 ppm (*black* and *red* spots), showing a clear discrimination between the methine group linked to the functionalized alkyl chain and the remaining CH groups. The lower rim functionalization led to a differentiation of resorcinarene aromatic protons, which are defined by two singlet signals at 7.05 and 7.03 ppm (*blue* triangle). The bithiophene moiety is identified by the set of signals between 7.09 and 7.53 ppm, while the protons of the benzoate ring by the two doublets at 7.65 and 8.07 ppm (*blue* and *yellow* spots).

Cavitand **10** electropolymerization ability was tested using cyclic voltammetry, acquiring voltammograms and frequencygrams simultaneously. The electropolymerization was performed over the gold electrodes of a QCM device using potentiodynamic conditions. As for the previous experiments, a $5 \cdot 10^{-4}$ M solution in DCM:ACN (1:5 v/v) of **10** was used in combination with a 10^{-1} M solution of TBAHFP as supporting electrolyte.

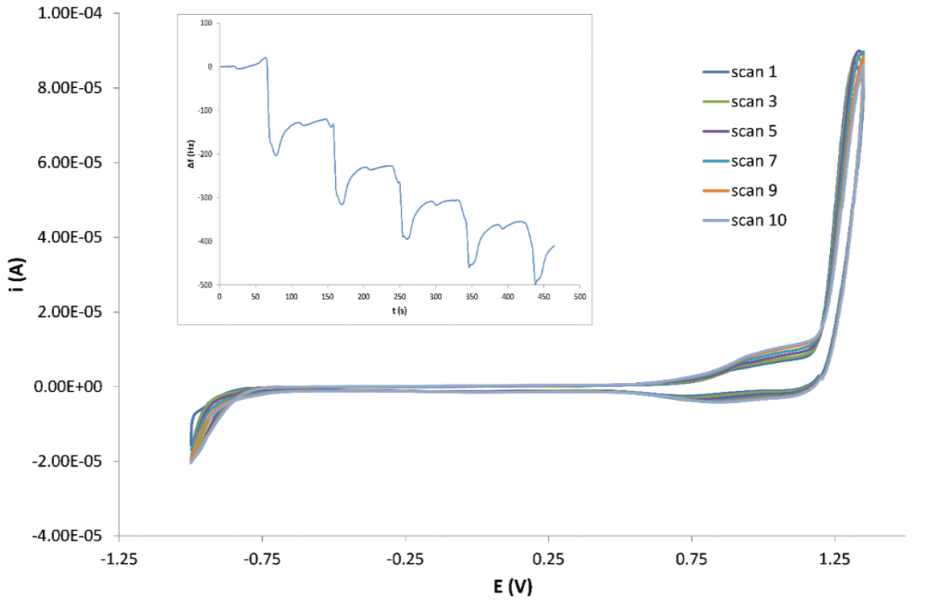

Figure 4.8 *CV-scans and frequencygram (inset) collected during the electropolymerization trial of the cavitand **10** over the QCM gold electrodes.*

Monomer **10** reactivity during the electropolymerization process and the regularity in the polymer growth onto the electrode surfaces are highlighted by the voltammogram and the frequencygram reported in **Figure 4.8**. Voltammogram showed a progressive increase of the current related to the deposition of the electroactive coating, meanwhile the frequencygram reported a gradual decrease in the resonant frequency of the QCM quartz crystal. The formation of a layer onto the surface of the EQCM device is visible by naked eye as reported in **Figure 4.9**.

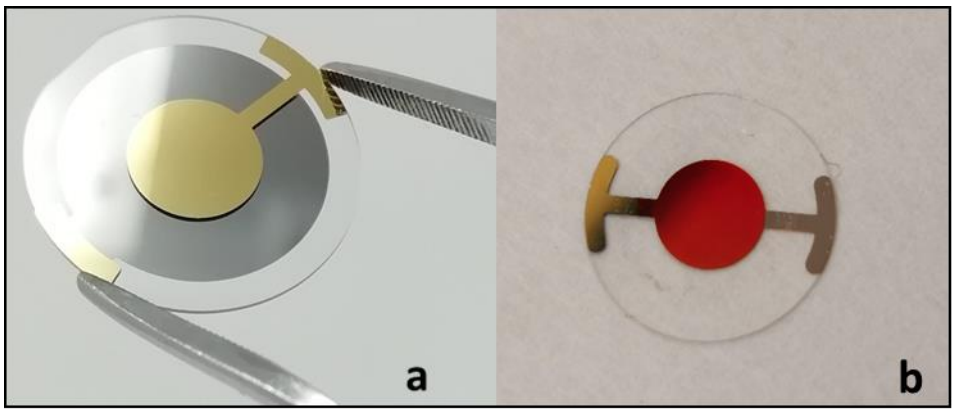

Figure 4.9 *EQCM crystal a) before and b) after electropolymerization of the cavitand **10** (the gold electrode is covered by a red polymeric film).*

This result highlighted the suitability of the benzoic ester as spacing group between the cavitand and the 2,2'-bithiophene polymerizable unit. Consequently, we decided to synthetize the target electroactive tetraphosphonate cavitand functionalized at the lower rim with a 4-([2,2'-bithiophen]-3-ylethynyl) benzoate group.

4.2.3 Synthesis and electroactivity evaluation of Cavitand 14

The synthetic pathway followed to synthetize the new electroactive cavitand is reported in the scheme below (**Scheme 4.4**). The key steps of the synthesis were (i) the stereospecific introduction of four inward phosphate bridges at the upper rim and (ii) the insertion of the electroactive 4-([2,2'-bithiophen]-3-ylethynyl) benzoate moiety at the lower rim.

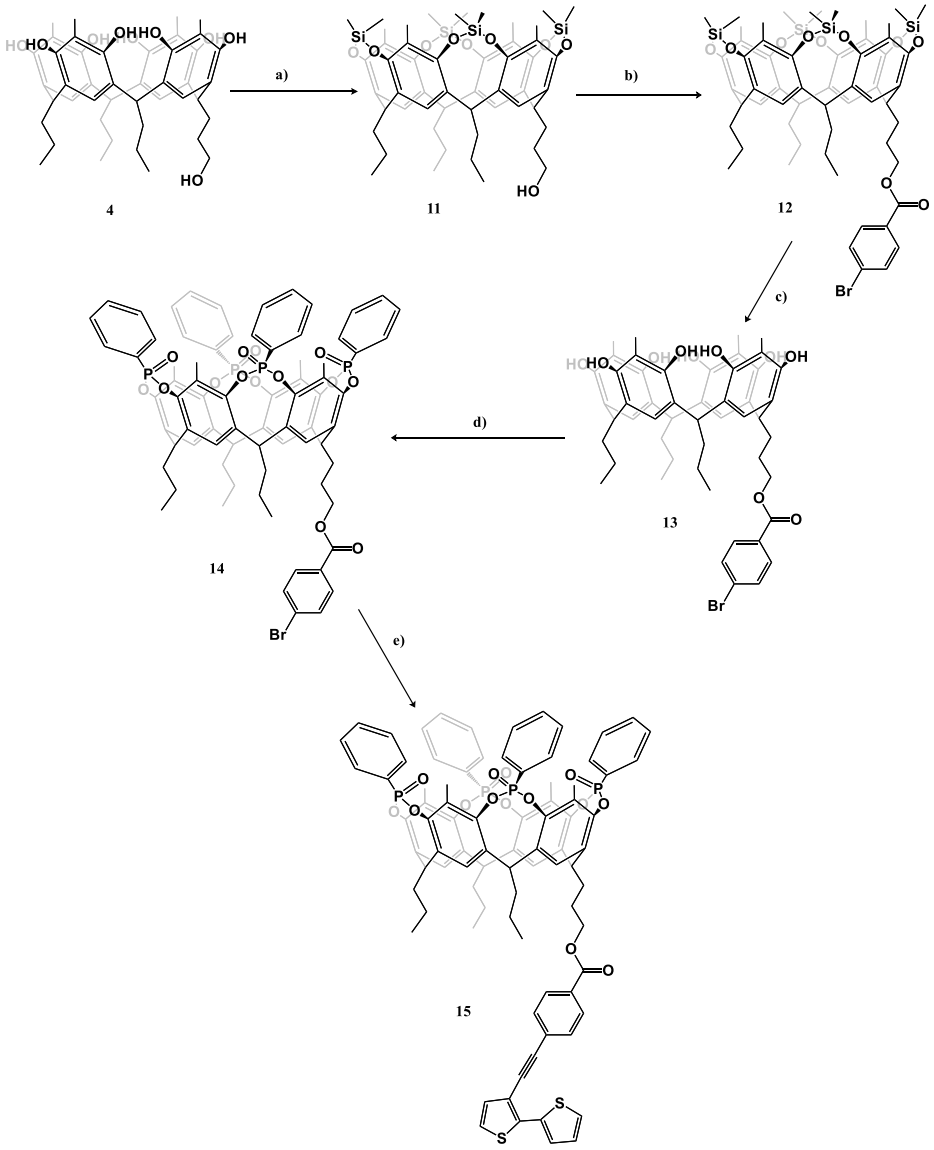

Scheme 4.4 *Synthesis of **15** a) dimethyldichlorosilane, pyridine, 55 °C, 18 h, 35% yield; b) p-bromobenzoic acid, 4-dimethylaminopyridine, N,N'-diciclohexylcarbodiimide, dichloromethane, DMF , r.t., 12 h, 85% yield; c) HF 40% v/v, DMF, chloroform, r.t. 12 h, quantitative yield; d) 1- dichlorophenylphosphine,*

pyridine, 80 °C, 4 h; 2- H_2O_2 35% m/v, 0 °C, 1 h, 61% yield; e)TBAF, $PdCl_2(PPh_3)_2$, THF dry, r.t., dark condition, 48 h, 10% yield.

As reported above for the synthesis of **5**, in order to avoid tricky purification, the raw mixture containing resorcinarene **4** was used as reagent in the first step. Dimethyl silyl groups were used as protecting agents for the phenolic OH groups at the upper rim of the resorcinarene scaffold. Product **11** was obtained as a white solid in 35% yield after flash chromatography purification. In consideration of the relative stability of the silyl protecting groups, Steglich esterification under mild conditions was performed to functionalized the lower rim OH group with *p*-bromobenzoic acid. The reaction was conducted using N,N'-diciclohexylcarbodiimide to activate the carboxylic acid and 4-dimethylamminopyridine as catalyst. Product **12**, purified through flash chromatography, was recovered as a white solid in 85% yield. In the following step the silyl protecting groups were cleaved using a 40% HF solution, restoring the phenolic groups at the upper rim. After the quenching of the reaction, resorcinarene **13** was recovered as a white precipitate in quantitative yield.

The synthesis of target cavitand **14** proceeded through the bridging reaction of the phenolic OHs of **13** with dichlorophenylphosphine in pyridine as solvent, followed by the *in-situ* oxidation of the intermediate tetraphosphonito cavitand with hydrogen peroxide. This procedure allows to obtain the sole stereoisomer Tiiii having all the four P=O groups pointing inward the cavity. Cavitand **14** was obtained after precipitation in water as a white solid in 61% yield.
Sonogashira cross-coupling reaction was performed in order to link the tetraphosphonate receptor **14** to the 3-ethynyl-2,2'-bithiophene **3**. The reaction was conducted at 110°C for 24 hours using $Pd(PPh_3)_4$ and CuI as catalysts, and DIPA as base in toluene dry.
The reaction was monitored through TLC, showing the disappearance of the reagent spot and the presence of a new fluorescent species having a slightly lower polarity respect to cavitand **14**. Although the different polarity and the fluorescent character, ^{1}H-NMR analysis revealed that the fluorescent species was the unreacted reagent **14**, as highlighted by the overlapped NMRs in **Figure 4.10**.

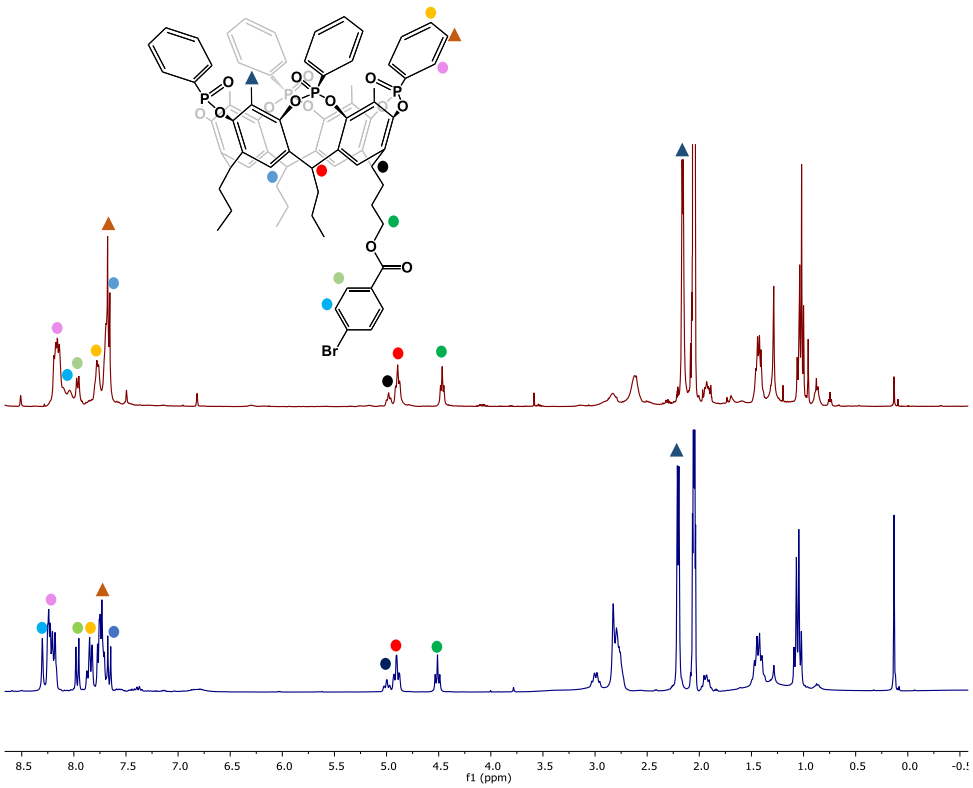

Figure 4.10 *^{1}H-NMR spectrum of **14** before (red trace) and after (blue trace) the Sonogashira coupling in acetone-d^{6} (400 MHz).*

The comparison of the ^{1}H-NMR spectra before (*red trace*) and after (*blue trace*) the Sonogashira coupling, highlighted the presence of all the characteristic signals of the protons of cavitand **14**. The differences affecting the signal distribution in the aromatic region and the slight shift of the signal related to the methyl apical groups, suggested the occurrence of a variation in the cavity occupancy induced by the cross-coupling reaction.

MALDI-TOF analysis of the unreacted cavitand **14** showed, besides the typical mono-charged adducts derived by the complexation of H^+, NH_4^+, Na^+, K^+ ions by the cavitand, the presence of other two mono-charged complexes due to the formation of $[cavitand+Cu]^+$ and $[cavitand+K+Cu]^+$ complexes (**Figure 4.11**). Formation of the mono-charged adduct between cavitand **14** and the two monovalent ions Cu and K is the result of reductive processes due to the presence of several electrons in the gas phase, generated by the laser ionization.[35,36]

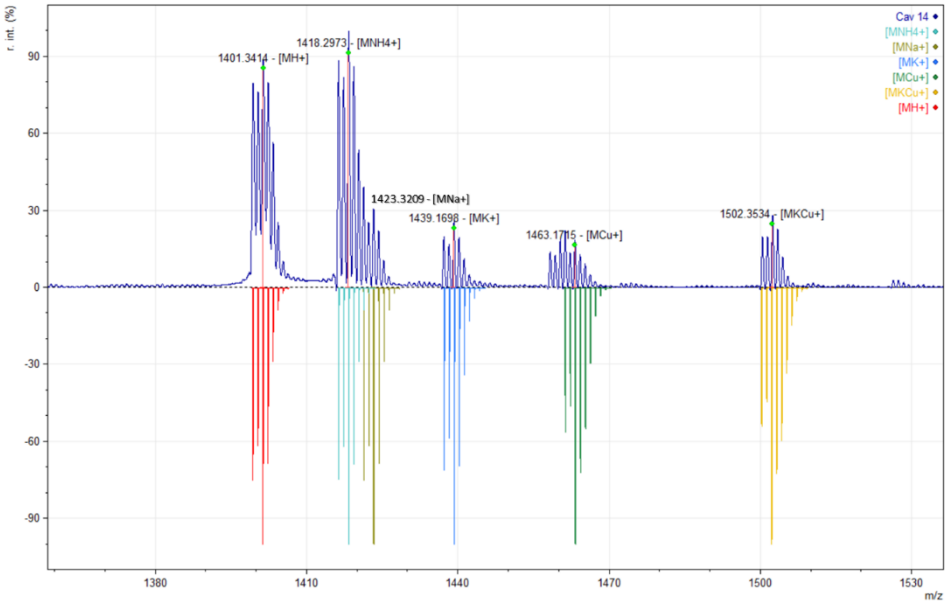

Figure 4.11 *MALDI-TOF spectrum of **14** after the Sonogashira coupling.*

Moreover, it is worth noting that the Glaser homocoupling compound, a typical diacetylene by-product of the Sonogashira reactions related to the presence of copper, was totally absent in the reaction mixture.

The ^{1}H NMR and MALDI results combined with the anomalous absence of the copper-induced Glaser by-product, suggested that probably **14** complexes and thus removes the copper ions from the reaction, hence hampering the Sonogashira coupling and consequently the formation of the target compound **15**.

For this reason, we decided to use a copper-free Sonogashira coupling, in order to finally synthetize the final product **15**.[37] The copper-free reaction was performed between the recovered cavitand **14** and the 3-ethynyl-2,2'-bithiophene **3** in dark conditions at room temperature for 48 hours using $PdCl_2(PPh_3)_2$ as catalyst, and TBAF as base and co-catalyst, in dry THF. Product **15** was recovered after a tricky flash chromatography purification as a yellow solid in 10% yield. The product was characterized by NMR and MALDI-TOF analysis.

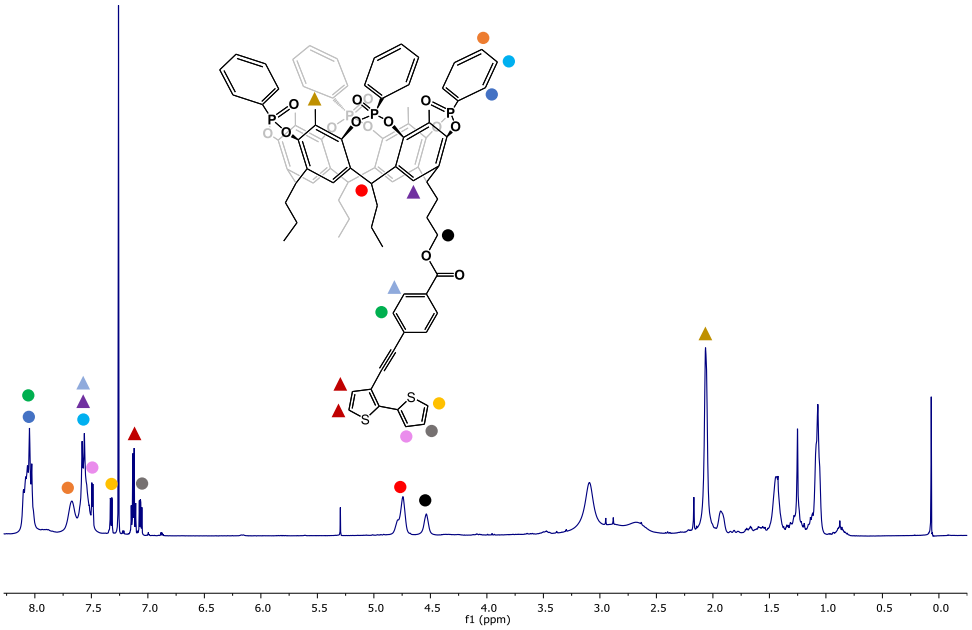

Figure 4.12 *^{1}H-NMR spectrum of **15** in $CDCl_3$ (400 MHz).*

In the ^{1}H-NMR spectrum reported above (**Figure 4.12**), all the diagnostic peaks of product **15** can be identified. The high field peaks are in agreement with the aliphatic lower rim alkyl chains. The broad signals at 4.55 and 4.75 ppm are associated to the CH_2 group close to the ester group (*black* spot), and to the methine bridges of the resorcinarene scaffold (*red* spot), respectively. In the aromatic region we can identify all the signals related to the aromatic phosphonate protons, the linker, and the protons of the bithiophene moiety. In particular, the signals related to the bithiophene unit are the doublets at 7.49 and 7.33 ppm (*pink* and *yellow* spots) and the multiplets at 7.12 and 7.07 (*dark-red* triangle and *grey* spot). With regards to the benzoic ester spacer, the two diagnostic peaks are the multiplets at 8.07 ppm (*green* spot) and at 7.60 ppm (*cyan* spot). As for the phenyl group attached to the phosphorous, we can find at 8.07 ppm the multiplet associated to the *ortho* protons (*blue* spot), the broad signal at 7.67 ppm (*orange* spot) related to the protons in *para* position and finally, the multiplet at 7.60 ppm due to the *meta* protons.

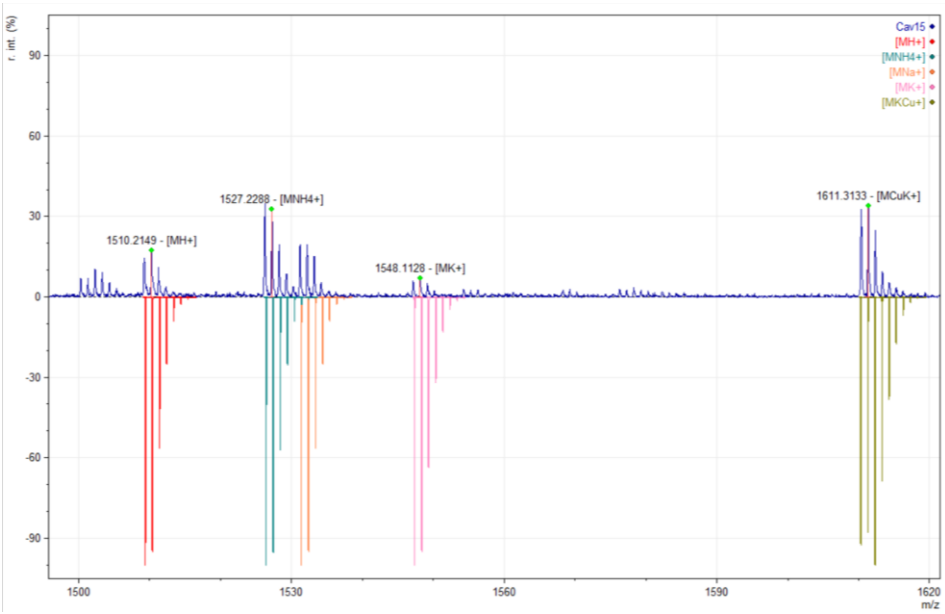

Figure 4.13 *MALDI-TOF of cavitand **15**.*

MALDI-TOF analysis (**Figure 4.13**) confirmed the molecular weight of the target product **15**, showing the typical adducts with the most common metal ions.
Interesting to note in the mass profile, the occurrence of the unusual monocharged ionic adduct of product **15** complexed with Cu and K ions (1611,3133 m/z). The Cu ion derived from the starting cavitand **14**, since we were not able to remove it from the cavity. Cavitand **15** was then employed in the subsequent electropolymerization tests, in order to optimize and standardize the polymerization conditions.

The electrosynthesis of cavitand-based polymer was conducted on a QCM device following the same protocol reported above for product **10**.
The polymerization was performed in potentiondynamic conditions through cyclic voltammetry technique on a $5 \cdot 10^{-3}$M solution of cavitand **15** in DCM:ACN (1:5 v/v). TBAHFP solution (0.1 M DCM:ACN 1:5 v/v) was used as support electrolyte.

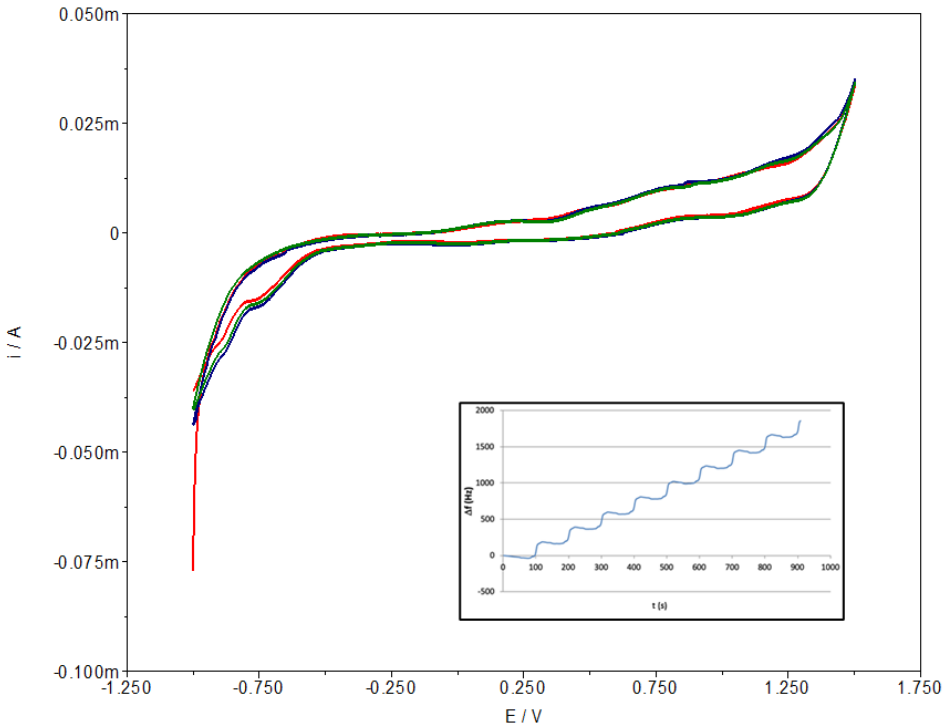

Figure 4.14 *CV-scans and frequencygram (inset) collected during the electropolymerization trial of the cavitand **15** over the QCM gold electrodes.*

Voltammogram and frequencygram showed the total absence of electroactivity of cavitand **15** in the applied conditions (**Figure 4.14**).

The same profile recorded for every CV scan during the acquisition of the voltammogram highlighted the inhibition of the electropolymerization, while the progressive increment in the frequencygram provided evidences of a systematic mass loss on the crystal surface related to the leaching of the gold electrodes instead of the deposition of the polymer layer.
To foster the electropolymerization of the cavitand, several parameters such as concentration, supporting electrolyte, potential were changed during the electrosynthesis, but unfortunately without success. These results compared to the one obtained in the case of the electropolymerization of cavitand **10**, can be

explained by the fact that the presence of the four outward-directed phenyl groups at the upper rim of **15** makes the cavitand head too large to allow the formation of the polymer, creating steric hindrance.
Another explanation can be that the presence of copper ions complexed in the macrocyclic cavity could affect the electropolymerization process, leading to uncontrolled side-reactions.
To overcome the first problem, further attempt will be made co-polymerizing cavitand **15** in presence of a bithiophene unit as co-monomer to dilute the number of neighbors cavitand molecules in the polymer chain. In case the polymerization will fail again, a new synthetic pathway will be designed in order to avoid the use of copper in presence of the cavitand.

4.3 Conclusions

In this chapter, we reported the synthesis of a tetraphosphonate cavitand equipped at the lower rim with an electroactive bithiophene unit suitable for electropolymerization to develop a new QCM sensor for the detection of N-methyl ammonium species in water. As first step, we evaluated the best linker to be used to attach the electroactive species to the lower rim of the cavitand. To this purpose, we used a tetramethylene bridged cavitand as tetraphosphonate cavitand proxy. The two linkers used in the tests were a triazole ring and a 4-ethynylbenzoate group, obtaining cavitand **8** and **10**, respectively. Electropolymerization trials in potentiodynamic conditions conducted using cavitand **8** highlighted an inhibition of the bithiophene electroactivity induced by the triazole ring. The introduction of a 4-ethynylbenzoate spacer as linker between the macrocyclic scaffold and the bithiophene moiety (cavitand **10**) led to the formation of a polymer during electropolymerization in potentiodynamic conditions. 4-ethynylbenzoate group was so selected as suitable linker to attach the electroactive bithiophene unit to our target tetraphosphonate cavitand via copper-free Sonogashira cross coupling. Unfortunately, the synthesized cavitand **15** resulted inactive during the electopolymerization, as highlighted by the recorded frequencygram and voltammograms. The absence of activity in the target cavitand **15** is probably related to the steric hindrance exerted by the

presence of four bulky phenyl groups at the upper rim of the cavitand, which inhibited the polymer formation onto the QCM electrodes.

4.4 Acknowledgments

Special thanks to Prof. Marco Giannetto from Parma University for the electrochemical tests.

4.5 Experimental Section

Synthesis of 3-Bromo-2,2'-dithiophene (1)[39]

A Schlenk reactor was loaded with 2,3-dibromothiophene (0.5 mL, 4.4 mmol), 2-thienylboronic acid (625 mg, 4.9 mmol) and a 2M Na_2CO_3 solution (8 mL) in 1,4-dioxane (50 mL). After degassing, $Pd(PPh_3)_4$ (213 mg, 0.18 mmol) was added to the system. The mixture was stirred for 4 hours at 100 °C. The reaction was quenched by pouring in water (250 mL) and extracted with diethyl ether. The organic solvent was removed under reduced pressure. The raw material was purified through flash chromatography column on silica gel using ciclohexane as eluent, affording product **1** as a yellow oil in 43% yield.

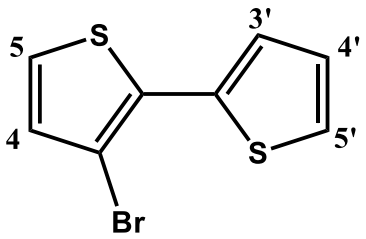

^{1}H NMR (300 MHz $CDCl_3$): δ = 7.44 (dd, 1H, J= 3.6 Hz, 1.2 Hz, Ar**H$_{3'}$**); 7.38 (dd, 1H, J= 5.1 Hz, J=1.2 Hz, Ar**H$_{5'}$**); 7.22 (d, 1 H, J=5.4 Hz, Ar**H$_5$**); 7.11 (dd, 1H, J= 3.6 Hz, J= 5.1 Hz, Ar**H$_{4'}$**); 7.04 (d, 1H, J=5.4 Hz, Ar**H$_4$**).

Synthesis of 4-([2,2'-bithiophen]-3-yl)-2-methylbut-3-yn-2-ol (2)[40]

A Schlenk reactor was loaded with **1** (510 mg, 2.08 mmol) and 2-methylbut-3-yn-2-ol (192 mg, 2.29 mmol) in diisopropylamine (12 mL). The solution was degassed (3 x freeze-pump-thaw) and $Pd(dppf)Cl_2 \cdot CH_2Cl_2$ (18 mg, 0.021 mmol) was added followed by CuI (41.2 mg, 0.046 mmol). The mixture was stirred for 24 hours at 85°C. The reaction was quenched by filtration over celite pad. The solvent was removed under vacuum and the crude purified by flash chromatography column

on silica gel (Eluent: hexane/ethyl acetate = 8:2). The product was obtained as white solid in 78% yield (404 mg, 1.62 mmol).

^{1}H NMR (300 MHz $CDCl_3$): δ = 7.44 (dd, 1H, J=3.6 Hz, J=1.1 Hz, Ar**H$_{3'}$**); 7.26 (dd, 1H, J=5.1 Hz, J=1.1 Hz, Ar**H$_{5'}$**); 7.05-6.97 (m, 3H, Ar**H$_4$** + Ar**H$_5$** + Ar**H$_{4'}$**); 2.5 (s, 1H, OH); 1.66 (s, 6H, C(C**H$_3$**)$_2$OH).

Synthesis of 3-ethynyl-2,2'-bithiophene (3)[40]

In a Schlenk reactor, **2** was dissolved in toluene (3 mL) and methanol (3 mL) under argon atmosphere. After degassing through freeze-pump-thaw protocol, potassium hydroxide was added to the system and the mixture was stirred for 5 hours at 110 °C. The reaction was quenched by extraction using DCM and water. The dried organic phase was purified through flash chromatography column on silica gel (eluent: hexane). Product **3** was recovered as colorless oil in 63 % yield (72 mg, 0.38 mmol).

^{1}H NMR (300 MHz $CDCl_3$): δ = 7.56 (dd, 1H, J= 3.6 Hz, J=0.7 Hz, Ar**H$_{5'}$**); 7.31 (dd, 1H, J= 5.1 Hz, J=0.7 Hz, Ar**H$_{3'}$**); 7.12-7.02 (m, 3H, Ar**H$_4$** + Ar**H$_5$** + Ar**H$_{4'}$**); 3.38 (s, 1H, C**H**).

Synthesis of mono OH-footed resorcinarene (4)[41]

To a solution of 2-methylresorcinol (10 g, 80.6 mmol,), butanal (5.5 mL, 60.4 mmol) and 2,3-dihydrofuran (1.51 mL, 20.1 mmol) in MeOH (75 mL), a 37% solution of HCl (9.33 mL) was added dropwise over 30 min at 0°C. After the addition, the reaction mixture was stirred at 55°C for 5 days. The reaction was quenched with water, filtered, dried under vacuum obtaining an orange powder. The crude was used as such and purified in the following synthetic step.

Synthesis of Methyl-bridged mono OH-footed cavitand (5)

A Schlenk reactor was loaded with **4** (1g), potassium carbonate and $BrCH_2Cl$ in dry DMF (20 mL) under argon atmosphere. The resulting mixture was stirred for 16

hours at 80°C. The reaction was quenched in water (50 mL). The obtained suspension was extracted with DCM and purified through flash chromatography column on silica gel (eluent: DCM/AcOEt from 97:3 to 95:5). Product **5** was recovered as a brown solid in 29% yield (310 mg, 0.4 mmol).

^{1}H NMR (300 MHz $CDCl_3$): δ = 7.04 (s, 2H, Ar**H**); 7.00 (s, 2H, Ar**H**); 5.93-5.86 (m, 4H, OC**$H_{2\ out}$**); 4.8 (t, 4H, J=7.9 Hz, ArC**H**); 4.31-4.25 (m, 4H, OC**$H_{2\ in}$**); 3.77 (t, 2H, J=6.3 Hz, $CH_2C\mathbf{H}_2OH$); 2.42-2.30 (m, 2H, $C\mathbf{H}_2CH_2CH_2OH$); 2.29-2.13 (m, 6H, $C\mathbf{H}_2CH_2CH_3$); 1.97 (s, 12H, ArC**H_3**); 1.71-1.60 (m, 2H, $CH_2\mathbf{CH}_2CH_2OH$); 1.46-1.34 (m, 6H, $CH_2C\mathbf{H}_2CH_3$); 1.09-0.98 (m, 9H, $CH_2CH_2C\mathbf{H}_3$).

DEPTQ ^{13}C NMR (101 MHz, $CDCl_3$) δ 153.25, 137.91, 123.61, 117.63, 98.52, 36.58, 32.11, 20.94, 14.17, 10.34, 1.04.

ESI-MS: m/z = calculated for $C_{48}H_{56}O_9K$ = 815.36 $[M+K]^+$
found = 815.48.

Synthesis of Methyl-bridged mono Cl-footed cavitand (6)

Cavitand **5** (310 mg, 0.4 mmol) was dissolved in toluene (7 mL); thionyl chloride (143 mg, 1.2 mmol) and a catalytic amount of DMF were added and the reaction mixture was stirred for 16 hours at 55°C. The solvent was removed under vacuum, and the raw material extracted with DCM/H_2O. The organic phase was dried under reduced pressure and product **6** afforded as a light orange solid in 80% yield (255 mg, 0.32 mmol) without any further purification.

^{1}H NMR (300 MH $CDCl_3$): δ = 7.02 (s, 2H, Ar**H**); 7.01 (s, 2H, Ar**H**); 5.95-5.87 (m, 4H, OC**$H_{2\ out}$**); 4.86- 4.77 (m, 4H, ArC**H**); 4.33-4.25 (m, 4H, OC**$H_{2\ in}$**); 3.68 (t, 2H, J=6.2 Hz, $CH_2C\mathbf{H}_2Cl$); 2.46-2.38 (m, 2H, J= 6.2 Hz, $C\mathbf{H}_2CH_2CH_2Cl$); 2.28-2.15 (m, 6H, $C\mathbf{H}_2CH_2CH_3$); 2.00 (s, 12H, ArC**H_3**); 1.93-1.82 (m, 2H, $CH_2\mathbf{CH}_2CH_2Cl$); 1.49-1.34 (m, 6H, $CH_2C\mathbf{H}_2CH_3$); 1.05 (t, 9H, J= 7.3 Hz, $CH_2CH_2C\mathbf{H}_3$).

DEPTQ ^{13}C NMR (101 MHz, $CDCl_3$) δ 153.26, 152.22, 151.68, 142.14, 138.24, 137.81, 137.27, 136.91, 117.75, 117.64, 117.45, 98.53, 65.26, 65.19, 63.33, 45.18,

36.61, 34.17, 32.12, 29.72, 29.14, 24.93, 24.48, 22.71, 20.99, 14.16, 10.34, 1.56, 1.04.

MALDI-TOF: m/z = calculated for C48H55ClO8 = 795.3664 $[M+H]^+$
found = 795.4302.

Synthesis of Methyl-bridged N_3-footed cavitand (7)

Cavitand **6** (120 mg, 0.15 mmol) was dissolved in dry DMF (15 mL) under inert atmosphere. Sodium azide (30 mg, 0.45 mmol) was added and the reactive system was stirred for 16 hours at 80°C. The reaction was quenched in water (150 mL). The afforded precipitate was recovered through filtration and washed several times with water. Product **7** was obtained as a light brown solid in 62% yield (70 mg, 0.092 mmol) without any further purification.

^{1}H NMR (300 MHz $CDCl_3$): δ = 7.01 (s, 2H, Ar**H**); 6.99 (s, 2H, Ar**H**); 5.96-5.87 (m, 4H, OC**$H_{2\,out}$**); 4.85- 4.77 (m, 4H, ArC**H**); 4.34-4.28 (m, 4H, OC**$H_{2\,in}$**); 3.44 (t, 2H, J=6.6 Hz, $CH_2C\mathbf{H}_2N_3$); 2.38-2.14 (m, 8H, C**H_2**$CH_2CH_2N_3$ + C**H_2**CH_2CH_3); 2.00 (s, 12H, ArC**H_3**); 1.73-1.65 (m, 2H, $CH_2\mathbf{CH}_2CH_2N_3$); 1.47-1.35 (m, 6H, $CH_2C\mathbf{H}_2CH_3$); 1.05 (t, 9H, J= 7.3 Hz, $CH_2CH_2C\mathbf{H}_3$).

DEPTQ ^{13}C NMR (101 MHz, $CDCl_3$) δ 153.44, 153.28, 153.20, 138.26, 137.97, 137.76, 137.25, 123.86, 123.65, 117.62, 117.37, 98.52, 51.46, 36.58, 32.10, 29.72, 27.45, 27.19, 20.97, 20.94, 14.16, 10.35, 1.04.

MALDI-TOF: m/z = calculated for $C_{48}H_{55}N_3O_8$ = 801.3989 $[M+H]^+$
found = 801.553.

Synthesis of Cavitand 8

A microwave tube reactor was loaded with **7** (42 mg, 0.052 mmol) and **3** (20 mg, 0.1 mmol) in DMSO (2 mL) under inert atmosphere. A water solution (0.5

mL) containing sodium ascorbate (3 mg, 0.013 mmol) and $CuSO_4 \cdot 5H_2O$ was added to the DMSO mixture. The reaction was performed in a microwave reactor for an hour at 80°C and 150 W of power. The reaction was quenched in water and the raw material extracted with DCM. DCM was removed under reduced pressure and the crude purified trough preparative TLC (eluent: DCM:Acetone = 98:2). Product **8** was recovered as a yellow powder in 48% yield (24 mg, 0.042 mmol).

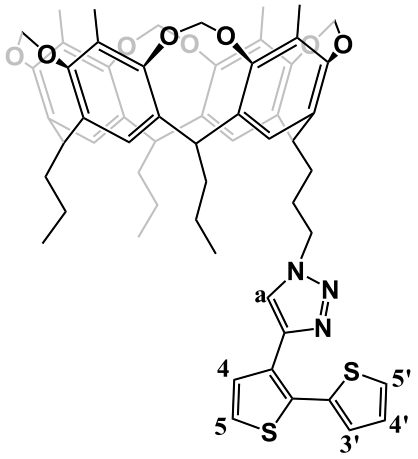

^{1}H NMR (400 MHz CD_2Cl_2): δ = 7.56 (d, 1 H, J=5.3 Hz, Ar**H$_5$**); 7.41 (d, 1H, J=5.3 Hz, Ar**H$_4$**); 7.32-7.29 (m, 2H, Ar**H$_{5'}$** + **H$_a$**); 7.18 (dd, 1H, J= 3.6 Hz, 1.1 Hz, **H$_{3'}$**); 7.07-6.99 (m, 5H, Ar**H$_{4'}$** + Ar**H**); 5.94-5.86 (m, 4H, OC**H$_{2,out}$**); 4.84-4.75 (m, 4H, ArC**H**); 4.44 (t, 2H, J=7.0 Hz, $CH_2C\mathbf{H}_2N$); 4.24-4.16 (m, 4H, OC**H$_{2,in}$**); 2.33-2.15 (m, 8H, C**H$_2$**CH_2CH_2N + C**H$_2$**CH_2CH_3); 2.0 (s, 12H, ArC**H$_3$**); 1.95 (m, 2H, CH_2**CH_2**CH_2N); 1.46-1.35 (m, 6H, $CH_2C\mathbf{H}_2CH_3$); 1.09-1.01 (m, 9H, CH2CH2C**H$_3$**). (Assigned by COSY-NMR).

DEPTQ ^{13}C NMR (101 MHz, CD_2Cl_2) δ 153.42, 153.18, 153.15, 137.91, 137.65, 136.93, 128.69, 128.08, 127.43, 126.92, 125.41, 124.20, 123.92, 120.85, 117.94, 117.61, 98.51, 98.47, 49.87, 36.72, 36.64, 36.39, 32.12, 32.05, 29.69, 28.60, 26.68, 20.96, 20.94, 9.89, 0.76.

ESI-MS: m/z = calculated for $C_{58}H_{62}N_3O_8S_2$ = 992.4 $[M+H]^+$
found = 992.8.

Synthesis of Cavitand 9

A round two-neck flask was loaded with **5** (136 mg, 0.18 mmol), DCC (75 mg, 0.36 mmol), DMAP (25 mg, 0.2 mmol) and p-bromobenzoic acid (72 mg, 0.36 mmol) in dry DCM (25 mL) under a dry atmosphere. The mixture was stirred for 72 hours at room temperature. The reaction was quenched in water and the crude extracted three times with DCM. The organic phase was dried under vacuum and purified through flash chromatography column on silica gel (eluent: DCM:Hexane = 98:2 → DCM). Product **9** was recovered as white solid in 56% yield (97 mg, 0.1 mmol).

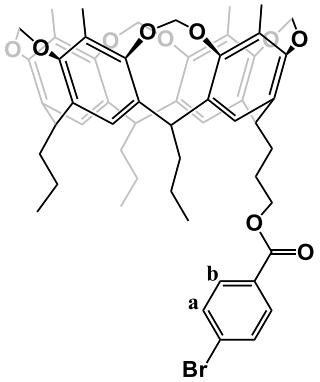

^{1}H NMR (300 MHz $CDCl_3$): δ = 7.96 (d, 2H, J = 8.6 Hz, Ar**H$_a$**); 7.61 (d, 2H, J = 8.5 Hz, Ar**H$_b$**); 7.01 (s, 4H, Ar**H**); 5.95-5.87 (m, 4H, OC**H$_{2\ out}$**); 4.93-4.76 (m, 4H, ArC**H**); 4.47 (t, 2H, J=6.6 Hz, $CH_2C\mathbf{H}_2O$); 4.34-4.24 (m, 4H, OC**H$_{2\ in}$**); 2.45-2.34 (m, 2H, C**H$_2$**CH_2CH_2O); 2.29-2.14 (m, 6H, C**H$_2$**CH_2CH_3); 2.00 (s, 12H, ArC**H$_3$**),1.88 (m, 2H, CH_2**CH$_2$**CH_2O), 1.44 (m, 6H, $CH_2C\mathbf{H}_2CH_3$), 1.04 (m, 9H, $CH_2CH_2C\mathbf{H}_3$).

DEPTQ ^{13}C NMR (101 MHz, $CDCl_3$) δ 153.47, 153.29, 153.27, 153.25, 138.20, 137.97, 137.75, 137.28, 131.71, 131.15, 129.24, 128.06, 123.92, 123.66, 117.60, 117.34, 98.51, 65.19, 36.53, 32.11, 32.08, 27.13, 26.69, 20.94, 14.19, 14.14, 10.35.

ESI-MS: m/z = calculated for $C_{55}H_{59}BrO_{10}Na$ = 981.32 $[M+Na]^+$
found = 981.81.

Synthesis of Cavitand 10

A Schlenk reactor was loaded with **9** (97 mg, 0.1 mmol), **3** (21 mg, 0.11 mmol) and DIPA (0.144 mL, 2 mmol), dissolved in dry toluene under an argon atmosphere. The solution was degassed by freeze-pump-thaw protocol, and $Pd(PPh_3)_4$ (5 mg, 0.004 mmol) and CuI (0.8 mg, 0.004 mmol) were added. The mixture was stirred for 48 hours at 110 °C. The reaction was cooled to room temperature and filtered over celite pad and washed with DCM. The organic phase was dried under reduced pressure and purified through flash chromatography column on silica gel (eluent: Hexane:Ethyl Acetate = 85:15). The product was obtained as yellow solid in 10% yield (12.4 mg, 0.01 mmol).

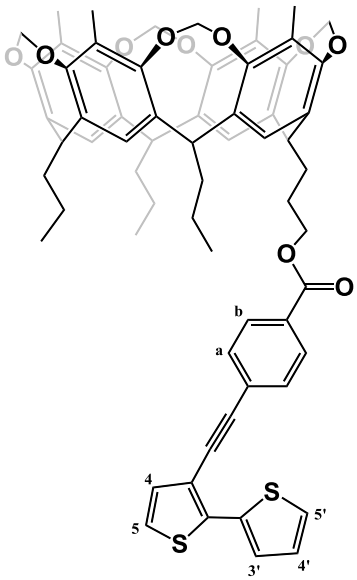

^{1}H NMR (400 MHz CD_2Cl_2): δ = 8.07 (d, 2H, J = 8.3 Hz, Ar**H$_a$**); 7.65 (d, 2 H, J = 8.3 Hz, Ar**H$_b$**); 7.53 (d, 1H, J = 3.6 Hz, Ar**H$_{3'}$**); 7.37 (d, 1H, J =5.2 Hz, Ar**H$_{5'}$**); 7.19 (d, 1 H, J =5.2 Hz, Ar**H$_5$**); 7.15 (d, 1H, J =5.3 Hz, Ar**H$_4$**); 7.09 (dd, 1H, J = 5.0 Hz, J = 3.6 Hz, Ar**H$_{4'}$**); 7.05 (s, 2H, Ar**H**); 7.04 (s, 2H, Ar**H**); 5.93-5.88 (m, 4H, OC**H$_{2out}$**); 4.86 (t, 1H, J=8.1 Hz, ArC**H**); 4.81-4.73 (m, 3H, ArC**H**); 4.44 (t, 2H, J=6.5 Hz, CH_2CH_2O); 4.23-4.16 (m, 4H, OC**H$_{2in}$**); 2.47-2.35 (m, 2H, C**H$_2$**CH_2CH_2O); 2.27-2.17 (m, 6H, C**H$_2$**CH_2CH_3); 2.97 (s, 12H, ArC**H$_3$**); 1.90-1.83 (m, 2H, $CH_2CH_2CH_2O$); 1.47-1.36 (m, 6H, $CH_2CH_2CH_3$); 1.08-0.96 (m, 9H, $CH_2CH_2CH_3$).

^{13}C NMR (75 MHz CD_2Cl_2): δ (ppm) = 165.8, 153.34, 153.18, 38.08, 137.88, 137.73, 137.31, 135.67, 131.16, 131.05, 129.96, 129.49, 127.80, 127.29, 125.97, 125.85, 124.12, 123.90, 123.20, 117.92, 117.72, 116.78, 98.49, 93.11, 88.01, 65.10, 54.13, 53.77, 53.41, 53.05, 52.69, 36.73, 36.67, 32.08, 29.67, 27.13, 26.66, 20.94, 13.92, 9.87.

HR-MS Orbitrap: m/z = calculated for $C_{65}H_{65}O_{10}S_2$ = 1069.4019 $[M+Na]^+$
found = 1069.4001.

Synthesis of Cavitand 11[41]

A Schlenk reactor was loaded with **4** (2 g, 2.7 mmol) dissolved in dry pyridine, under dry atmosphere. The solution was cooled to 0°C and dichlorodimethylsilane (4 mL, 33 mmol) was added to the mixture. The reaction was stirred for 18 hours at 55°C. The solvent was removed under reduced pressure, and the crude was suspended in methanol, sonicated, filtered and washed several times with methanol. The solid was then purified through flash chromatography column on silica gel (eluent, DCM → DCM:Acetone = 95:5), and product **11** recovered as a white solid (905 mg, 0.95 mmol) in 35% yield.

^{1}H NMR (300 MHz $CDCl_3$): δ = 7.20 (s, 2H, Ar**H**); 7.17 (s, 2H, Ar**H**); 4.66-4.54 (m, 4H, ArC**H**); 3.72 (t, 2H, J=6.3 Hz, $CH_2C\mathbf{H}_2OH$); 2.39-2.26 (m, 2H, $C\mathbf{H}_2CH_2CH_2OH$); 2.25-2.09 (m, 6H, $C\mathbf{H}_2CH_2CH_3$); 1.91 (s, 12H, $ArC\mathbf{H}_3$); 1.65-1.52 (m, 2H, $CH_2C\mathbf{H}_2CH_2OH$); 1.38-1.22 (m, 6H, $CH_2C\mathbf{H}_2CH_3$); 0.98 (t, 9H, J=7.3 Hz, $CH_2CH_2C\mathbf{H}_3$); 0.53 (s, 12H, $SiC\mathbf{H}_{3out}$); -0.68 (s, 12H, $SiC\mathbf{H}_{3in}$).

Synthesis of Cavitand 12

In a round double neck flask, Cavitand **11** (470 mg, 0.49 mmol), 4-dimethylaminopyridine (139.3 mg, 1.14 mmol) and *p*-bromobenzoic acid (466 mg, 2.3 mmol) were solubilized in dry DCM (18 mL) and dry DMF (22 mL) under inert atmosphere. The mixture was cooled to 0°C and N,N'-diciclohexylcarbodiimide (357 mg, 1.73 mmol) was added. The reaction was stirred for 12 hours at room temperature. Once completed, the reaction was quenched in water and the crude extracted with DCM. The organic phase was dried under reduced pressure. The

crude was recovered in methanol, filtered and washed with methanol. Product **12** was obtained pure as a white solid in 85% yield (480 mg, 0.42 mmol).

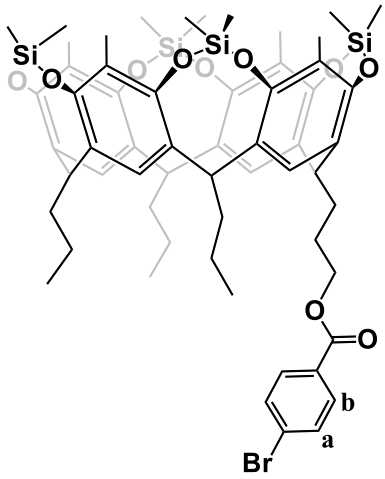

^{1}H NMR (300 MHz $CDCl_3$): δ = 7.91 (d, 2H, J= 8.2 Hz, Ar**H$_a$**); 7.57 (d, 2H, J= 8.2 Hz, Ar**H$_b$**); 7.18 (s, 4H, Ar**H**); 4.75-4.52 (m, 4H, ArC**H**); 4.40 (t, 2H, J=6.6 Hz, $CH_2CH_2C\mathbf{H_2}O$); 2.46-2.26 (m, 2H, $C\mathbf{H_2}CH_2CH_2O$); 2.26-2.09 (m, 6H, $C\mathbf{H_2}CH_2CH_3$); 1.92 (s, 12H, Ar**CH$_3$**); 1.83-1.72 (m, 2H, $CH_2C\mathbf{H_2}CH_2O$); 1.42-1.15 (m, 6H, $CH_2C\mathbf{H_2}CH_3$); 1.05-0.86 (m, 9H, $CH_2CH_2C\mathbf{H_3}$); 0.52 (s, 12H, SiC**H$_{3,in}$**); -0.67 (s, 12H, SiC**H$_{3,out}$**).

^{13}C NMR (101 MHz, $CDCl_3$) δ 148.59, 148.37, 148.34, 131.66, 131.49, 131.25, 131.13, 131.02, 130.54, 129.37, 127.93, 119.87, 119.64, 119.40, 119.18, 105.94, 65.37, 35.25, 35.21, 35.15, 35.13, 29.71, 29.54, 27.40, 14.16, 10.57, -3.07, -6.26.

ESI-MS: m/z = calculated for $C_{59}H_{75}BrO_{10}Si_4Na$ = 1159.35 $[M+Na]^+$
found = 1159.78.

Synthesis of resorcinarene 13

In a Teflon flask, cavitand **12** (210 mg, 0.185 mmol) was dissolved in a mixture of DMF-chloroform (13+13 mL), and a solution of HF 40% v/v (0.3 mL, 6.6 mmol) was added. The mixture was stirred for 12 hours at room temperature. Once completed, the reaction was quenched in water (10 mL) and subsequently the

solvent was removed under reduced pressure. The light-yellow precipitate was washed several times with water and dried. Product **13** was recovered as a white solid in quantitative yield.

^{1}H NMR (400 MHz Acetone-d_6): δ = 8.03 (s, 8H, ArO**H**); 7.97 (d, 2H, J = 8.5Hz, Ar**H$_a$**); 7.73 (d, 2H, J = 8.5 Hz, Ar**H$_b$**); 7.49 (s, 2H, Ar**H**); 7.43 (s, 2H, Ar**H**); 4.52-4.33 (m, 6H, ArC**H** + CH_2CH_2C**H$_2$**O); 2.04 (bs, 12H, Ar**CH$_3$**); 2.52-2.44 (m, 2H, C**H$_2$**CH_2CH_2O); 2.32-2.21 (m, 6H, C**H$_2$**CH_2CH_3); 1.83-1.73 (m, 2H, CH_2C**H$_2$**CH_2O); 1.36-1.24 (m, 6H, CH_2C**H$_2$**CH_3); 0.98-0.88 (m, 9H, CH_2CH_2C**H$_3$**).

^{13}C 135 NMR (101 MHz, Acetone-d_6) δ 166.18, 150.69, 150.47, 132.79, 132.12, 130.64, 128.33, 125.89, 125.65, 125.27, 122.38, 112.32, 112.13, 66.09, 36.69, 36.23, 35.22, 35.02, 30.93, 28.20, 21.94, 14.44, 14.41, 9.90, 1.49.

ESI-MS: m/z = calculated for $C_{51}H_{60}BrO_{10}$ = 911.93 $[M+H]^+$
found = 911.42.

Synthesis of Cavitand 14

In a Schlenk tube, resorcinarene **13** (175 mg, 0.19 mmol) was dissolved in pyridine (5 mL) under argon atmosphere. Maintaining the system under stirring, dichlorophenylphosphine (0.117 mL, 0.86 mmol) was added to the mixture. The reaction was stirred for 4 hours at 80°C. A 35% v/v solution of H_2O_2 (5 mL, 49 mmol) was added to the mixture cooled at 0°C. The reaction was stirred at low temperature for an additional hour. The mixture was quenched in water. The obtained precipitate was recovered by filtration and washed with water. Product **14** was collected as a white powder in 61% yield (163 mg, 0.12 mmol).

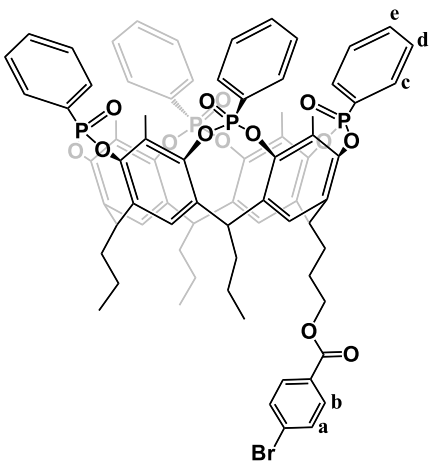

^{1}H NMR (400 MHz $CDCl_3$): δ =8.13 (m, 8H, P(O)Ar**H$_c$**,); 7.90 (d, 2H, J= 8.2 Hz, Ar**H$_a$**); 7.70-7.60 (m, 4H, P(O)Ar**H$_e$**,); 7.56 (m, 10H, P(O)Ar**H$_d$**+Ar**H$_b$**); 7.16 (s, 4H, Ar**H**); 4.94-4.79 (m, 4H, ArC**H**); 4.50 (t, 2H, J=6.5 Hz, $CH_2CH_2C\mathbf{H_2}O$); 2.49 (m, 2H, $C\mathbf{H_2}CH_2CH_2O$); 2.39-2.24 (m, 18H, $C\mathbf{H_2}CH_2CH_3$+Ar$C\mathbf{H_3}$); 1.91 (m, 2H, $CH_2C\mathbf{H_2}CH_2O$); 1.45-1.44 (m, 6H, $CH_2C\mathbf{H_2}CH_3$); 1.14-1.00 (m, 9H, $CH_2CH_2C\mathbf{H_3}$).

^{13}C NMR (101 MHz, $CDCl_3$) δ 166.01, 144.84, 144.56, 133.87, 133.80, 133.76, 131.67, 131.53, 131.42, 131.32, 131.28, 131.17, 129.04, 128.88, 65.10, 37.54, 36.99, 36.83, 33.17, 32.28, 32.13, 31.94, 30.97, 29.72, 29.68, 27.17, 21.04, 13.92, 13.80, 11.50.

^{31}P{1H} NMR (162 MHz $CDCl_3$)**:** δ = 6.12 (s, 1P, P=O); 5.98 (s, 3P, P=O).

ESI-MS: m/z = calculated for $C_{75}H_{71}BrO_{14}P_4$ = 1423.29 $[M+H]^+$
found = 1422.63.

Synthesis of Cavitand 15

Under argon atmosphere, in a Schlenk tube, cavitand **14**@Cu (50 mg, 0.036 mmol) was dissolved in dry THF (3 mL), and 3-ethynyl-2,2'-bithiophene **3** (8.15 mg, 0.043 mmol) and TBAF (33 mg, 0.013 mmol) were added. The mixture was degassed (3 x freeze-pump-thaw) and $PdCl_2(PPh_3)_2$ (0.9 mg, 0.0013 mmol) was added. The mixture was stirred in dark conditions for 48 hours at room temperature.

The suspension was filtered over celite and the solvent dried under vacuum. The raw material was purified trough flash chromatography column on silica gel (DCM:Acetone = 1:1) and the obtained product further crystallized in Acetone:Hexane = 1:9. Cavitand **15** was recovered as a yellow solid in 10% yield (6 mg, 0.0036 mmol).

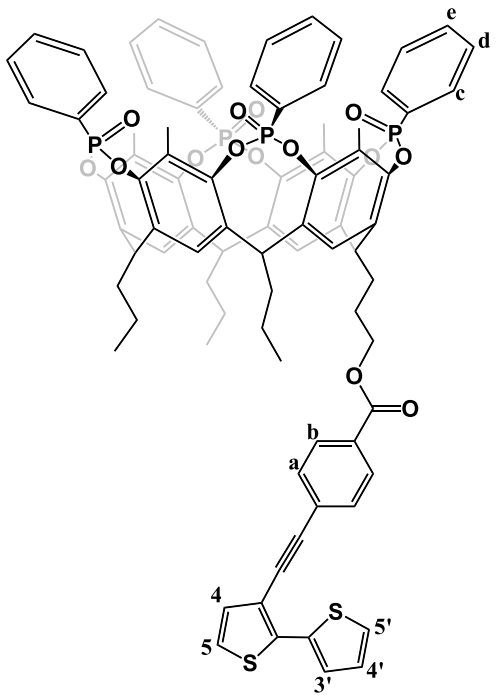

^{1}H NMR (400 MHz $CDCl_3$): δ 8.16 – 7.95 (m, 10H, $\mathbf{H_c}$ + $\mathbf{H_a}$), 7.78 – 7.66 (m, 4H, $\mathbf{H_e}$), 7.66 – 7.52 (m, 14H, $\mathbf{H_d}$ + $\mathbf{H_b}$ + Ar**H**), 7.49 (dd, *J* = 3.6, 1.2 Hz, 1H, $\mathbf{H_{3'}}$), 7.33 (dd, *J* = 5.1, 1.2 Hz, 1H, $\mathbf{H_{5'}}$), 7.18 – 7.08 (m, 2H, $\mathbf{H_4}$+ $\mathbf{H_5}$), 7.07 (dd, *J* = 5.1, 3.7 Hz, 1H, $\mathbf{H_{4'}}$), 4.83 – 4.65 (m, 4H, ArC**H**), 4.60 – 4.49 (m, 2H, $CH_2CH_2C\mathbf{H_2}O$), 3.07 – 2.88 (m, 8H, $C\mathbf{H_2}CH_2CH_2O$ + $C\mathbf{H_2}CH_2CH_3$), 2.06 (s, 12H, Ar$\mathbf{CH_3}$), 1.97 – 1.90 (m, 2H, $CH_2C\mathbf{H_2}CH_2O$), 1.50 – 1.41 (m, 6H, $CH_2C\mathbf{H_2}CH_3$), 1.12 – 1.03 (m, 9H, $CH_2CH_2C\mathbf{H_3}$).

^{1}H-^{13}C HSQC NMR (600 MHz $CDCl_3$):

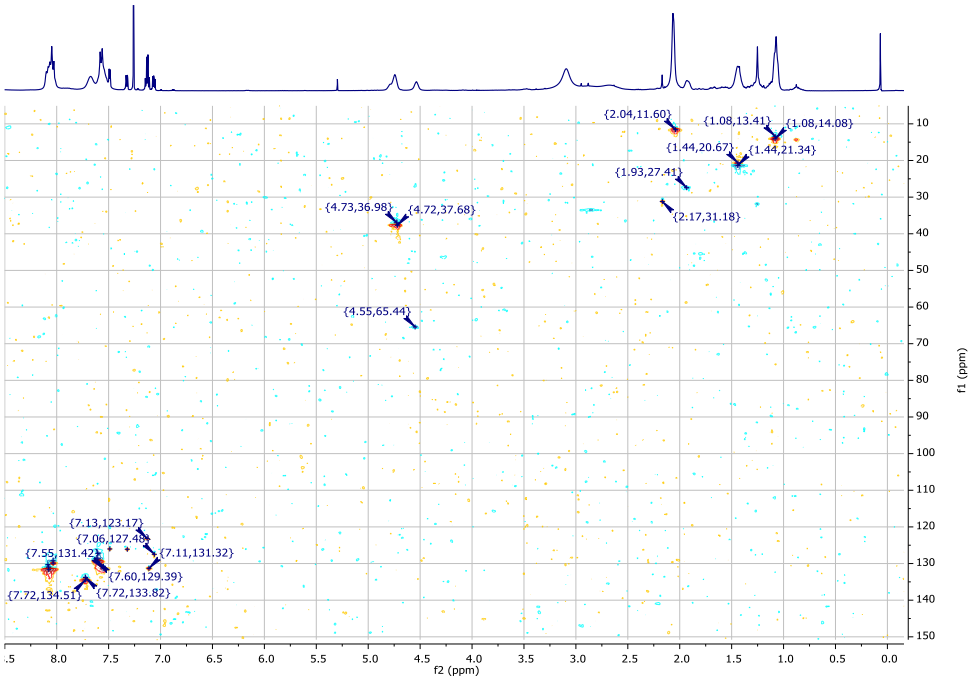

^{31}P{1H} NMR (162 MHz)**:** δ = 11.49 (s, 1P, P=O); 10.58 (s, 3P, P=O).

MALDI-TOF: m/z = calculated for $C_{85}H_{76}O_{14}P_4S_2$ = 1510.3665 $[M+H]^+$
found = 1510.2149.

Electropolymerization

Preparation of the polymeric coatings was performed using a computerized Autolab PGSTAT 20 potentiostat (Ecochemie, Utrecht, Netherlands) controlled by Ecochemie GPES 4.9 software. The polymer layers were growth under potentiodynamic conditions (cyclic voltammetry) in a Teflon cell (5 mL) using the QCM device as working electrode, a silver-silver chloride pseudoreference as reference electrode and a platinum rod as counter electrode. QCM units having 10 MHz AT-cut piezoelectric quartz crystals chips with gold electrodes on both sides were exploited. More in details, the QCM used have 13.9 mm diameter and 160 µm and thickness, with the gold electrode diameter of 6 mm.

4.6 References

1. Nations, U. *World Drug Report 2020*. (United Nations, 2020).
2. Pellegrini, M. *et al.* Rapid screening method for determination of Ecstasy and amphetamines in urine samples using gas chromatography – chemical ionisation mass spectrometry. *J. Chromatogr. B* **769**, 243–251 (2002).
3. Marquet, P., Lacassie, E., Battu, C., Faubert, H. & Lachatre, G. Simultaneous determination of amphetamine and its analogs in human whole blood by gas chromatography-mass spectrometry. *J. Chromatogr. B* **700**, 77–82 (1997).
4. Ortuno, J. *et al.* Quantification of 3 , 4-methylenedioxymetamphetamine and its metabolites in plasma and urine by gas chromatography with nitrogen-phosphorus detection. *J. Chromatogr. B* **723**, 221–232 (1999).
5. Herraez-Hernandez, R., Campins-Falco, P. & Verdù-Andrès, J. Sensitive determination of methylenedioxylated amphetamines by liquid chromatography. *Analyst* **126**, 581–586 (2001).
6. Sadeghipour, F. & Veuthey, J.-L. Sensitive and selective determination of methylenedioxylated amphetamines by high-performance liquid chromatography with fluorimetric detection. *J. Chromatogr. A* **787**, 137–143 (1997).
7. Sadeghipour, F., Giroud, C., Rivier, L. & Veuthey, J. L. Rapid determination of amphetamines by high-performance liquid chromatography with UV detection. *J. Chromatogr. A* **761**, 71–78 (1997).
8. Hayakawa, K., Hasegawa, K., Imaizumi, N., Wong, O. S. & Miyazaki, M. Determination of amphetamine-related compounds by HPLC with chemiluminescence and fluorescence detections. *J. Chromatogr.* **464**, 343–352 (1989).
9. Hupka, Y. *et al.* HPLC with laser-induced native fluorescence detection for morphine and morphine glucuronides from blood after immunoaffinity extraction. *Int. J. Legal Med.* **119**, 121–128 (2005).
10. Butler, D., Pravda, M. & Guilbault, G. G. Development of a disposable

amperometric immunosensor for the detection of ecstasy and its analogues using screen-printed electrodes. *Anal. Chim. Acta* **556**, 333–339 (2006).

11. Pourmand, A., Mazer-Amirshahi, M., Chistov, S., Li, A. & Park, M. Designer drugs: Review and implications for emergency management. *Human and Experimental Toxicology* vol. 37 94–101 (2018).

12. Luethi, D. & Liechti, M. E. Designer drugs: mechanism of action and adverse effects. *Archives of Toxicology* vol. 94 1085–1133 (2020).

13. Christophersen, A. S. Amphetamine designer drugs - An overview and epidemiology. in *Toxicology Letters* vols 112–113 127–131 (2000).

14. Biavardi, E. *et al.* Cavitand-Grafted Silicon Microcantilevers as a Universal Probe for Illicit and Designer Drugs in Water. *Angew. Chemie - Int. Ed.* **53**, 9183–9188 (2014).

15. Pinalli, R. & Dalcanale, E. Supramolecular Sensing with Phosphonate Cavitands. *Acc. Chem. Res.* **46**, 399–411 (2013).

16. Biavardi, E. *et al.* Molecular Recognition on a Cavitand-Functionalized Silicon Surface. *J. Am. Chem. Soc.* **131**, 7447–7455 (2009).

17. Dionisio, M. *et al.* Cavitand-Functionalized SWCNTs for N-Methylammonium Detection. *J. Am. Chem. Soc.* **134**, 5–8 (2012).

18. Biavardi, E. *et al.* Fully reversible guest exchange in tetraphosphonate cavitand complexes probed by fluorescence spectroscopy. *Chem. Commun.* 1638–1640 (2008).

19. Bell, T. W. & Hext, N. M. Supramolecular optical chemosensors for organic analytes. *Chem. Soc. Rev.* **33**, 589–598 (2004).

20. Temel, F. Real-time and selective recognition of erythromycin by self-assembly of calix[4]arene on QCM sensor. *J. Mol. Liq.* **297**, 111818 (2020).

21. Zheng, F. *et al.* Simultaneous and Ultrasensitive Detection of Foodborne Bacteria by Gold Nanoparticles-Amplified Microcantilever Array Biosensor. *Front. Chem.* **7**, 232 (2019).

22. Bearzotti, A., Macagnano, A., Papa, P., Venditti, I. & Zampetti, E. A study of a QCM sensor based on pentacene for the detection of BTX vapors in air.

Sensors Actuators B. Chem. **240**, 1160–1164 (2017).

23. Pinalli, R., Pedrini, A. & Dalcanale, E. Environmental gas sensing with cavitands. *Chem. - A Eur. J.* **24**, 1010–1019 (2018).

24. Giannetto, M. *et al.* Sensing of halogenated aromatic hydrocarbons in water with a cavitand coated piezoelectric device. *Sensors Actuators B. Chem.* **276**, 340–348 (2018).

25. Zhou, M. & Heinze, J. Electropolymerization of pyrrole and electrochemical study of polypyrrole: 1. Evidence for structural diversity of polypyrrole. *Electrochim. Acta* **44**, 1733–1748 (1999).

26. Gu, H. *et al.* Synthesis and Electropolymerization of Furan End−capped Dibenzothiophene/Dibenzofuran and Electrochromic Properties of Their Polymers. *Int. J. Electrochem. Sci.* **12**, 5000–5011 (2017).

27. Cappellari, M. V., Marzari, G., Ferna, L., Hernandez, L. & Fungo, F. Improving the Electropolymerization Properties of Fluorene-Bridged Dicarbazole Monomers through Polyfluoroalkyl Side Chains. *Langmuir* **35**, 8732–8740 (2019).

28. Bachman, J. C. *et al.* Electrochemical polymerization of pyrene derivatives on functionalized carbon nanotubes for pseudocapacitive electrodes. *Nat. Commun.* **6**, 3–4 (2015).

29. He, N., Gyurcsányi, R. E. & Lindfors, T. Electropolymerized hydrophobic polyazulene as solid-contacts in potassium-selective electrodes. *Analyst* **141**, 2990–2997 (2016).

30. Hao, Q. *et al.* Electrochemical Polymerization and Properties of Poly (triphenylene), an Excellent Blue-Green-Light Emitter. *J. Phys. Chem.* **114**, 9608–9617 (2010).

31. Sauerbrey, G. Verwendung von Schwingquarzen zur Wagung dunner Schichten und zur Mikrowagung. *Zeitschrift fiir Phys.* **222**, 206–22 (1959).

32. Ding, Y. *et al.* Quartz crystal microbalances (QCM) are suitable for real-time dosimetry in nanotoxicological studies using VITROCELL ® Cloud cell exposure systems. *Part. Fibre Toxicol.* **17**, 1–20 (2020).

33. Kanazawa, K. K. & Gordon II, J. G. Frequency of a Quartz Microbalance in

Contact with Liquid. *Anal. Chem.* **57**, 1770–1771 (1985).

34. Scheuble, M. *et al.* Polythiophenes with Thiophene Side Chain Extensions: Convergent Syntheses and Investigation of Mesoscopic Order. *Macromolecules* **48**, 7049–7059 (2015).

35. Karas, M., Gluckmann, M. & Schafer, J. Ionization in matrix-assisted laser desorption/ionization: singly charged molecular ions are the lucky survivors. *J. Mass Spectrosc.* **12**, 1–12 (2000).

36. Zhang, J., Frankevich, V., Knochenmuss, R., Friess, S. D. & Zenobi, R. Reduction of Cu (II) in Matrix-Assisted Laser Desorption/Ionization Mass Spectrometry. *J. Am. Soc. Mass Spectrosc.* **14**, 42–50 (2003).

37. Liang, Y., Xie, Y. & Li, J. Modified Palladium-Catalyzed Sonogashira Cross-Coupling Reactions under Copper-, Amine-, and Solvent-Free Conditions. *J. Org. Chem.* 379–381 (2006).

39. Scheuble, M. *et al.* Polythiophenes with Thiophene Side Chain Extensions: Convergent Syntheses and Investigation of Mesoscopic Order. *Macromolecules* **48**, 7049–7059 (2015).

40. Giannetto, M. *et al.* Sensing of halogenated aromatic hydrocarbons in water with a cavitand coated piezoelectric device. *Sensors Actuators B. Chem.* **276**, 340–348 (2018).

41. Yebeutchou, R. M. *et al.* Host-Guest Driven Self-Assembly of Linear and Star Supramolecular Polymers. *Angew. Chem. Int. Ed.* **47**, 4504–4508 (2008).

Chapter 5

Cavitand-based Polythiophenes for Impedance sensors*

*This work has been carried out in the group of Prof. Timothy M. Swager at Massachusetts Institute of Technology (MIT), Cambridge (USA).

5.1 Introduction

The design of new sensors featuring at the same time portability, ease of usage, chemical stability, high selectivity and sensitivity remains a challenge for both researchers and industries.

Among the several technologies available to reach this purpose, the electrochemical sensors are versatile in the detection of traces of analytes. The common working principle of electrochemical sensors is the evaluation of a single or multiple electric property of the sample such as resistance, conductance or the capacitance after the application of external stimulus.

In the majority of the electrochemical techniques, these information are achieved by applying strong perturbations able to move the system far from the equilibrium condition. An alternative approach is the application of small external perturbations in order to collect several kinetics data, maintaining in the same time the device near the steady-state.[1] These small perturbation experiments are conducted exploiting the electrochemical impedance spectroscopy (EIS), a non-destructive steady-state technique for the evaluation of several relaxation phenomena characterizing the electroactive systems. All the relaxation phenomena are traced by the impedance changes in the electrochemical sample. EIS experiments are performed by applying small voltage perturbations V_a in a wide range of frequencies f (10^{-4} – 10^6 Hz) in the AC field across interdigitated electrodes (IDEs) in close contact with an electroactive sample.[2] The voltage input is expressed as a function of time t:

$$V(t) = V_a \sin(2\pi f t)$$

The current response to a sinusoidal voltage perturbation is a shifted sinusoid profile having the same frequency:

$$I(t) = I_a \sin(2\pi f t + \varphi)$$

The complex impedance provided by the experiments can be defined as the ratio between the input sinusoidal perturbation and the output response:

$$Z^* = \frac{V_a \sin(2\pi f t)}{I_a \sin(2\pi f t + \varphi)} = Z_a \frac{\sin(2\pi f t)}{\sin(2\pi f t + \varphi)}$$

Applying the Euler's relationship, the complex impedance can be represented as a combination of a real "in-phase" term and the imaginary "out-of-phase" part

$$Z^* = Z_a e^{i\varphi} = Z_a(\cos\varphi + i\sin\varphi) = Z_{Real} + Z_{im}$$

The complex representation of the impedance becomes extremely convenient for the extrapolation of additional information of the electrochemical sample such as the resistivity from the real term Z_{real} and its dielectric behavior described by the imaginary part Z_{im}. More in details, the dielectric information enclosed in the impedance imaginary component monitors the system permittivity and how it changes in the presence of perturbations.
Permittivity describes the ability of an electroactive material to interact with a frequency-variable electromagnetic fields, and just like the impedance even the permittivity can be expressed as complex parameter:

$$\varepsilon_s = \varepsilon'(2\pi f) - i\varepsilon''(2\pi f)$$

Real and imaginary terms of the permittivity detail respectively how the system will store energy and how the same system will dissipate the energy as heat.[2]
The permittivity components, play a key role in the interpretation of the relaxation phenomena influenced by frequency-variable electromagnetic fields.
As shown in **Figure 5.1**, the real and imaginary terms of the permittivity plotted in relationship with the frequency of the external electromagnetic field, provide insight about ionic processes such as charge transfers, molecular flipping or twisting mechanisms induced by the electric dipole of the sample, molecular vibrations and electronic phenomena such as UV-absorption or light scattering.[3]
Impedance spectroscopy correlates the dielectric behavior of a material with a wide range of phenomena, opening the way for the development of new electrochemical devices.

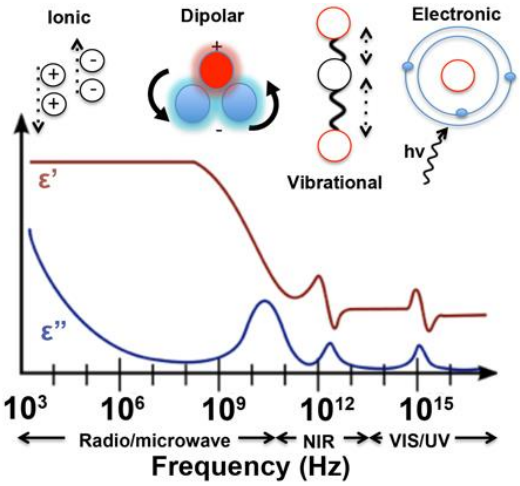

Figure 5.1 *Relaxation processes in electrochemical systems*[3]

The relevance of this strong relationship relies in the opportunity to follow interface phenomena such as charge transfers or analytes absorption through changes in the dielectric properties of the electroactive surface.

The possibility to gain a large amount of information and the ability to discriminate electric contributions from the dielectric responses in an electroactive sample make the impedance spectroscopy one of the most powerful and complete electrochemical technique. These advantages combined with the working mechanism based on the application of small external perturbations allow the development of a new generation of electrochemical impedance sensors.

Moreover an additional feature of the EIS in the electrochemical sensor relies in the opportunity to use several parameters as output response, making this technique extremely versatile.[4]

In this prospective, in the last decade several researches were focused on the development of new impedance sensors for the detection of analytes in the gas phase through the deposition of electroactive materials over interdigitated electrodes.[5,6]

In a recent work, Sridhar et al. exploited the impedance spectroscopy to fabricate a new sensor for the detection of H_2S in the gas phase.[7] Interdigitated alumina electrodes were coated with a composite material made by reduced graphene oxide (rGO) incorporated in nano-zinc oxide (ZnO) (**Figure 5.2** *a*). In dry conditions,

oxygen molecules were physisorbed and chemisorbed on the highly active surface of ZnO/rGO. The depletion of oxygen species induced by interacting H_2S molecules provide a change in the complex resistance of the composite material.

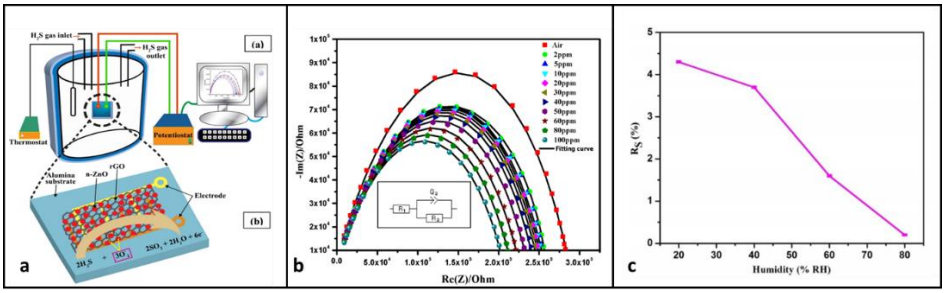

Figure 5.2 *a) Scheme of the experimental setup; b) Nyquist impedance plot of ZnO/rGO composite exposed to air and different concentrations of H_2S gas at 90°C; c) Decrease in the sensor response with the increasing of the relative humidity.*[7]

The sensor was exposed to several H_2S concentration ranging from 2 to 100 ppm at 90°C. The Nyquist plot reported in **Figure 5.2** *b,* shows the increasing in the diameter of the semicircles with decreasing H_2S gas concentration. This trend highlighted the existence of a significant influence of the H_2S on the resistance of the sensing material.

However, like most of the available impedance sensors, even the sensing properties of the composite ZnO/rGO were negatively affected by moisture and more in general water molecules. Given its high dielectric constant, water altered the impedance values, leading to a rapid drop in the sensor response (**Figure 5.2** *c*).

The emergence of the impedance spectroscopy as superior electrochemical technique boosted the search of reliable strategies to overcome the water interference. One of the most promising routes involved the introduction of molecular recognition in the development of new electroactive surfaces for impedance sensors. The water interfering effect can be reduced by the introduction of supramolecular interactions on the sensor surface, leading to a strong and selective recognition towards suitable analytes.

Moving in this direction, Chen at al. developed a new supramolecular impedimetric sensor selective for the detection in water of 3-phenylpropylamine (3-PPA) and potentially the entire class of the ATS drugs.[8]
The supramolecular electroactive surface is composed by aggregates of cucurbit[7]uril (CB[7]) coated gold nano particles (AuNPs) immobilized on the gold electrode surface, thus allowing the generation of an impedance system (**Figure 5.3** *a*).
The occurrence of impedance variations as consequence of selective supramolecular complexation of CB[7] towards 3-PPA were exploited by Chen as useful tools in the detecting process.

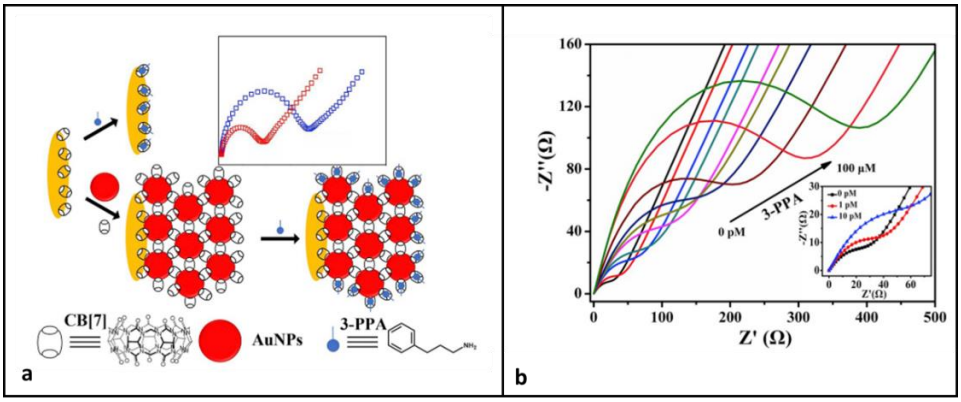

Figure 5.3 *a) Scheme of the experimental setup; b) Nyquist Plot of the AuNPs@CB[7] sensor incubated with different 3-PPA concentrations*[8]

The wide range of analyte concentrations (from 1 pM to 100 μM) explored during the impedimetric experiments showed the extreme sensitivity of the electrochemical device even at traces levels.

The progressive increasing in the diameter of the semicircles (Nyquist plot reported in **Figure 5.3** *b*), is indicative of the increase of the impedance-related to the concentration of the target analyte.
Recently the introduction of conducting polymers as electroactive interface for sensor application has boosted the EIS field. Conducting polymers such as polypyrrole, polythiophene, polyaniline have been widely studied to enhance

sensitivity, selectivity and detection limit of electrochemical sensors.[9] An additional feature of this attractive class of material is their mixed ionic/electronic conductivity, essential to guarantee a fast conversion of the ionic response in an electrical signal.

Here we combine molecular recognition and conductive polymers as electroactive coating on gold interdigitated electrodes (IDEs) for the detection in water of suitable guests.

Taking advantage of the superior performances of conducting polymers, two different synthetic pathways were followed to synthetize modified polythiophenes functionalized with resorcinarene-based cavitands: a polymer functionalized with the tetraquinoxaline cavitand (QxCav) selective in the detection of aromatic species and a polymer equipped with the tetraphosphonate cavitand (Tiiii) for the detection of methyl ammonium and pyridinium groups (**Figure 5.4**).

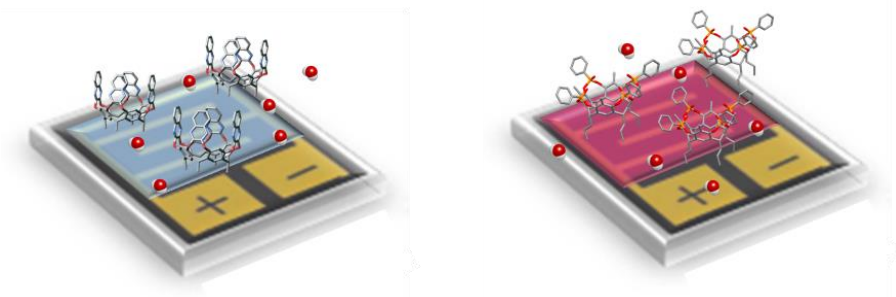

Figure 5.4 *Schematic representation of the IDEs set-up covered with the polythiophenes functionalized with a) the tetraquinoxaline cavitand and b) the tetraphosphonate Tiiii cavitand*

The deep and hydrophobic cavity in the QxCav is effective in the complexation of suitable aromatic molecules in water through a combination of π-π and CH-π hydrophobic interactions (*see Chapter 1 for the related literature*).[10,11]

Likewise, the synergic combination in the Tiiii cavitand of non-covalent interactions such as hydrogen bonds, cation-dipole interaction and CH_3-π interactions provided to the selective recognition of the cavitand towards methyl ammonium and methyl pyridinium moieties. [12,13]

5.2 Results and Discussion

5.2.1 Synthesis of the QxCav-based thiophene polymer 6

The synthetic strategy exploited to synthetize a new thiophene-based conductive polymer functionalized with the tetraquinoxaline cavitand (QxCav) is divided in two main parts: the synthesis of tetraquinoxaline cavitand functionalized at the upper rim with a 2,2'-bithiophene moiety, and afterwards its $FeCl_3$-driven heterogeneous oxidative polymerization.

The bithiophene cavitand monomer **5** was prepared following the same convergent synthetic approach developed in a previous work by our research group (**Scheme 5.1**).[14]

For the preparation of cavitand **5**, resorcinarene **1** with hexyl feet was chosen as macrocyclic scaffold.

To functionalize the upper rim of the tetraquinoxaline cavitand with the bithiophene moiety, the synthetic pathway chosen required the preparation of a triquinoxaline-bridged resorcinarene **3**, afterwards bridged with 6-bromo-2,3-dichloroquinoxaline wall (**Scheme 5.1**).

The most convenient route for the preparation of **3** is the selective excision of a quinoxaline wall from the parent tetraquinoxaline cavitand **2** (QxCav).[15]

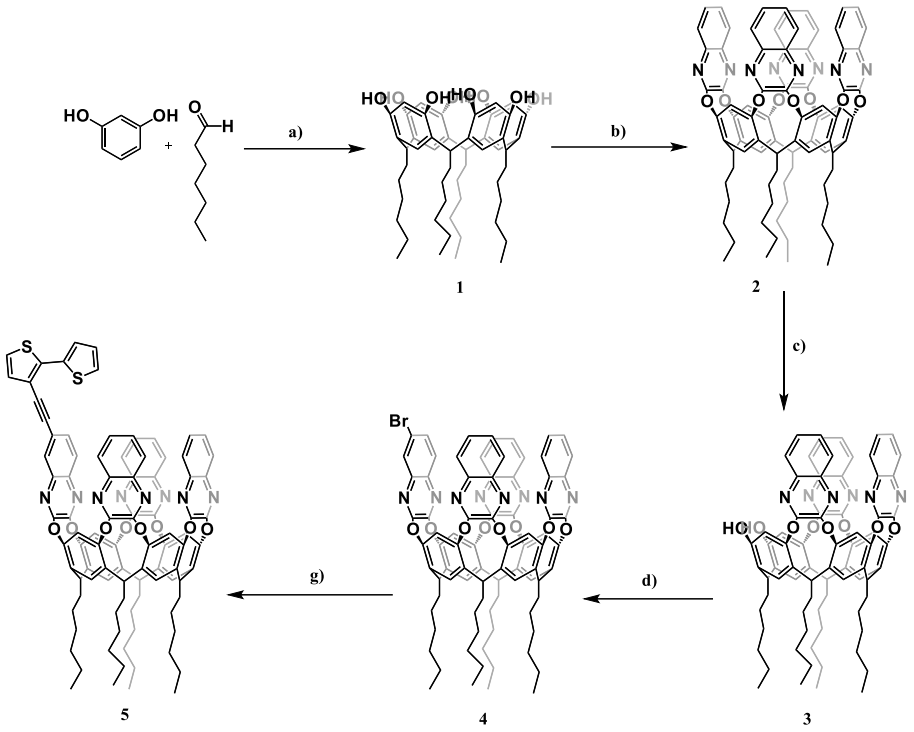

Scheme 5.1 *a) MeOH, HCl 37%, 55°C, 7d, 65%; b) 2,3-dichloroquinoxaline, K_2CO_3, DMF, 110°C, 1.5h, MW (150W), 54%; c) CsF, Catechol, DMF, 1h, 69%; d) 6-bromo-2,3-dichloroquinoxaline, K_2CO_3, DMF, 110°C, 1.5h, MW (150W), 81%; g) $Pd(PPh_3)_4$, CuI, Toluene, 110°C, 47%.*

In the first synthetic step the bridging reaction between the resorcinarene and the 2,3-dichlorobenzoquinoxaline was performed in order to obtain the tetraquinoxaline cavitand **2**. The macrocyclic receptor **2** was purified through crystallization and isolated in 54% yield. In the following step, the selective removal of a single quinoxaline wall was performed in basic condition by reaction of **2** using catechol and cesium fluoride. Product **3** was purified by flash chromatography column and recovered as a white solid in 69%. The bridging reaction between **3** and 6-bromo-2,3-quinoxaline was performed in presence of potassium carbonate in DMF as solvent. Purification by flash chromatography afforded the product **4** in 81% yield. In the following step, a Sonogashira cross-

coupling reaction was exploited in order to functionalized the cavitand **4** upper rim with the 3-ethynyl-2,2'-bithiophene group. Product **5** was isolated after chromatography purification in 47% yield. The ^{1}H-NMR and ^{1}H-^{1}H COSY NMR of the spectrum of product **5**, in agreement with the previous characterization reported in literature, confirmed the product structure.

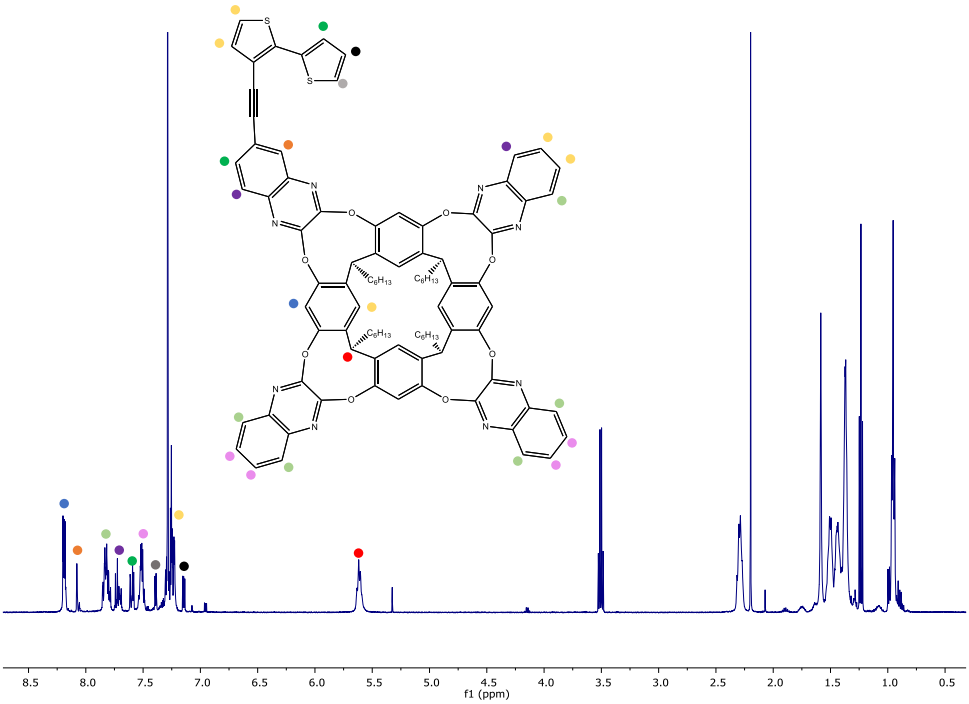

Figure 5.5 ^{1}H-NMR spectrum of monomer **5** in $CDCl_3$ (500 MHz).

The ^{1}H-NMR spectra reported in **Figure 5.5**, shows all the characteristic peaks of the target product. All the low ppm signals are in agreement with the lower rim alkyl chains. The 5.60 ppm multiplet is associated to the bridging CH signals, a clear evidence on the *vase* conformation of the cavitand in $CDCl_3$. The introduction of a brominated quinoxaline wall reduces the symmetry of the molecule and leads to a complex splitting of the signals associated to the quinoxaline protons and the resorcinarene ArH signals. The unsubstituted

quinoxaline walls are defined by the multiplet signals at 7.78, 7.68, 7.47 and 7.24 ppm. The functionalized wall is described by the doublet at 8.03 ppm, the multiplet at 7.56 ppm and the doublet signal overlapped over the previous multiplet at 7.68. Even the bithiophene group is associated to the doublet of doublet signals overlapped in the previous reported multiplets at 7.56 and 7.24 ppm. Additional characteristic peaks defined by the bithiophene group are the 7.35 and 7.11 doublet of doublet signals.

The corresponding polythiophene functionalized with the tetraquinoxaline cavitand, was obtained via heterogenous oxidative polymerization of monomer **5** with $FeCl_3$ in dry DCM under strictly dry conditions (**Scheme 5.2**).

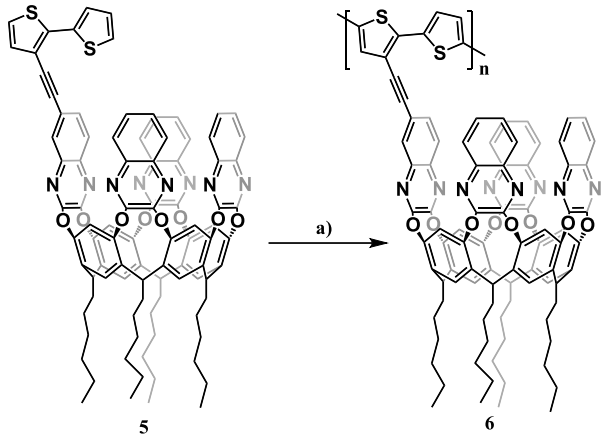

Scheme 5.2 a) $FeCl_3$, DCM, r.t

The oxidative $FeCl_3$-driven polymerization was chosen as cheap and easy method for the production of polymers under mild conditions (**Figure 5.6**). An additional advantage of this method relies in the easy scale up.

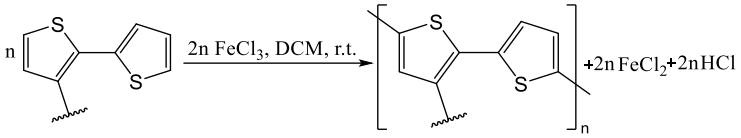

Figure 5.6 *General $FeCl_3$-driven polymerization of 2,2'-bithiophene*

Two different oxidative polymerizations were performed using different concentrations (0.01 and 0.0165 M) and different reaction time (12 and 24 h) as reported in **Table 5.1** below. In both cases, the polymeric products were obtained as a dark red powder in 80% average yield. The polymers were characterized by ^{1}H-NMR and GPC analysis.

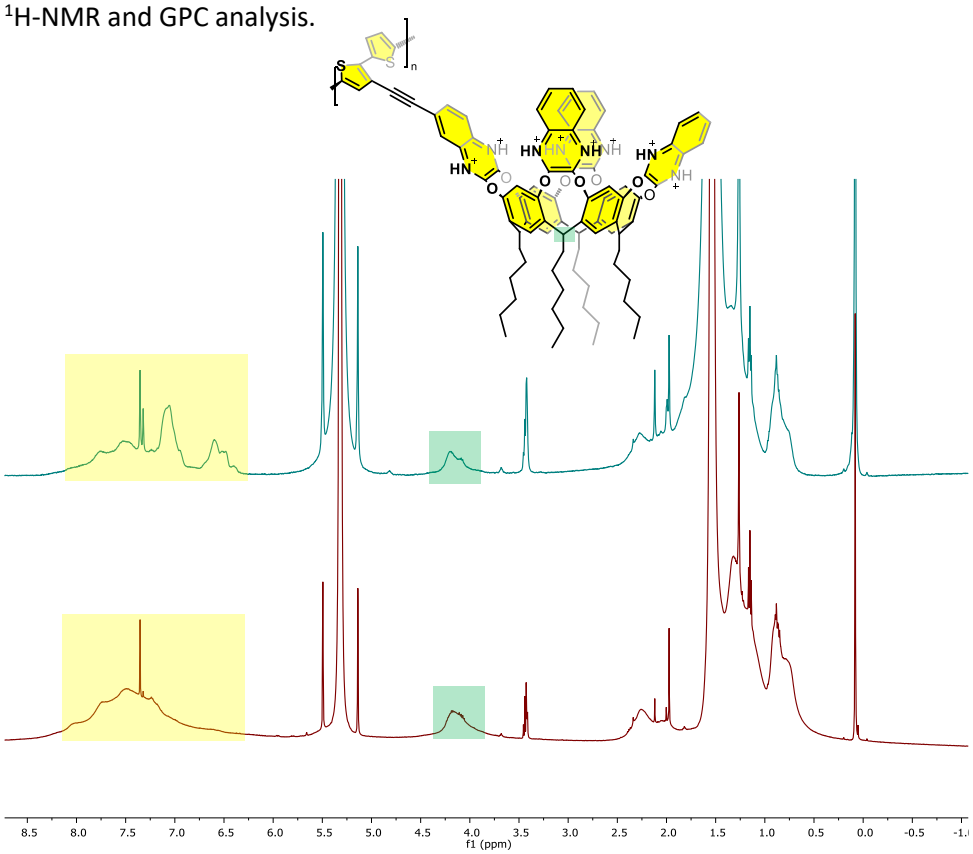

Figure 5.7 *Overlapped ^{1}H-NMR spectrum of polymers A (green trace) and B (red trace) in CD_2Cl_2 (500 MHz).*

The overlapped ^{1}H-NMR spectrum of the two polymers is reported above in **Figure 5.7**. Both ^{1}H-NMR spectrum of polymer **A** and polymer **B** (**Figure 5.7**) shows the presence of the diagnostic broad peak of CH bridge signal at 4.19 ppm, a clear evidence of the *kite* conformation of the tetraquinoxaline cavitands in the polymer. Protonation of the quinoxaline nitrogen atoms induced by the acidic conditions in the polymerization reaction switched the cavitand conformation

from the *vase* form of the monomer **5** to the *kite* one of the polymers. Comparing the ^{1}H-NMR spectrum of polymer **A** and polymer **B**, it is evident the occurrence of slight differences of signals both in the aromatic and aliphatic regions of the polymers.
A more defined spectrum in the *green profile* of polymer **A** and the presence of additional aromatic and aliphatic signals than the spectrum of polymer **B** (*red profile*).
These variations in the definition of the two spectrum and in the distribution of the signals are attributed to the differences in molecular weight of the two polymers (**Table 5.1**).

Entry	n° eq $FeCl_3$	Solvent	C	Time	M_w (g/mol)	D
A	10	DCM dry	0,01 M	12 h	7K	2,32
B	10	DCM dry	0,0165 M	24 h	25K	5,75

Table 5.1 *Experimental conditions followed in the preparation of polymers **A** and **B** and corresponding GPC analysis*

The GPC analyses performed at room temperature in THF determined a M_w of 7K g/mol and a polydispersity index (D) of 2.32 for the polymer **A**, and a M_w of 25K g/mol and polydispersity index (D) of 5.75 for polymer **B** (see *Experimental Part*).

Polymers **A** and **B** were furtherly characterized by UV-Vis absorption and Fluorescence emission spectroscopy.
The UV-absorption spectra of **A** and **B** were recorded at room temperature in THF as solvent (**Figure 5.8**).

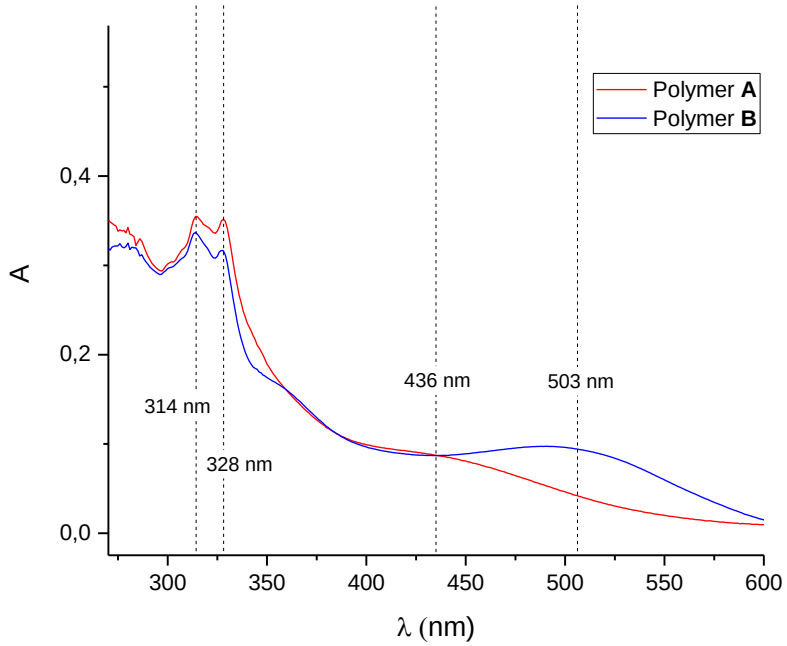

Figure 5.8 *UV-Vis absorption spectrum of polymers **A** ([**A**] = 4·10^{-6} M) and **B** ([**B**] = 2·10^{-6} M) in THF. T = 298K.*

In both UV-Vis absorption spectra two different macroregions were identified: a low wavelength region associated to the tetraquinoxaline cavitands in the polymeric structure, and a high wavelength region in the visible range correlated to the π-π* bands of the polythiophene backbone.

More in details, the *kite* conformation of the tetraquinoxaline cavitands in polymer **A** was described in the UV-Vis spectrum by two absorption peaks at *314 nm* (ε = 85000 M^{-1}·cm^{-1}) and *328 nm* (ε = 84000 M^{-1}·cm^{-1}), in agreement with literature data.[16]

Kite conformation of the tetraquinoxaline cavitands in polymer **B** was confirmed by the occurrence of the same profile trend in the low wavelength range. Despite the presence of the same contour in both profiles, the higher molecular weight of **B** induced a remarkable increasing in the polymer molar extinction coefficient in the visible region (Polymer **B** ε_{314} = 167500 M^{-1}·cm^{-1}; ε_{328} = 159000 M^{-1}·cm^{-1}).

The occurrence of a bathochromic shift from 436 nm (ε = 21600 $M^{-1}\cdot cm^{-1}$) in polymer **A** to 503 nm (ε = 47500 $M^{-1}\cdot cm^{-1}$) in polymer **B**, is a commonly observed in association with the increase of the polymer molecular weight.[17]
Fluorescence emission characterization of the two polymers highlighted the occurrence of a similar red-shift phenomenon, as observed in the UV-Vis absorption spectrum reported above (**Figure 5.9**).

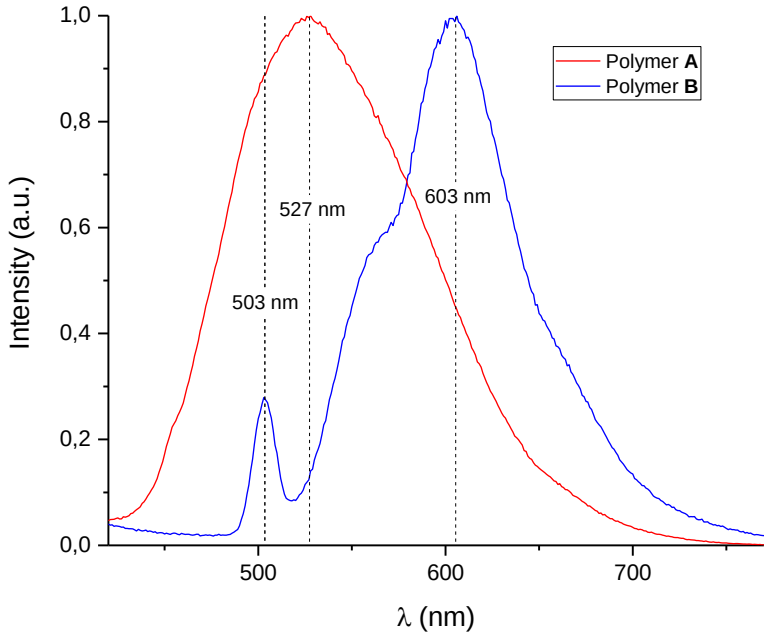

Figure 5.9 *Fluorescence emission spectrum of polymers **A** ([**A**] = 4·10^{-6} M) and **B** ([**B**] = 2·10^{-6} M) in THF. T = 298K.*

The emission spectrum, collected in THF at room temperature ([**A**] = 4·10^{-6} M; [**B**] = 2·10^{-5} M), showed the presence of a peak at 527 nm with polymer **A** (M_w = 7K g/mol) which shifted to 603 nm in the polymer **B** profile (M_w = 25K g/mol). In consideration of the high polydispersity index observed in polymer **B,** the additional peak at 503 nm in the blue profile emission spectrum indicated the presence of a significant amount of low weight oligomers.

5.2.2 Synthesis of the Tiiii-based thiophene polymer 19

In order to synthetize a thiophene-based conductive polymer functionalized with a tetraphosphonate cavitand, the synthetic strategy was divided in two main parts: the preparation of a modified bithiophene **12** as electroactive group, and the synthesis of the Tiiii-based polythiophene **19,** followed by Stille cross-coupling polymerization of the lower rim functionalized cavitand **18**. Cavitand monomer **18** was prepared in mild condition by Steglich esterification of the mono OH footed Tiiii cavitand **17** with the modified bithiophene **12**.

- *Synthesis of the modified bithiophene **12***

Modified bithiophene **12** was synthesized following the multistep convergent synthetic approach reported in **Scheme 5.3.**

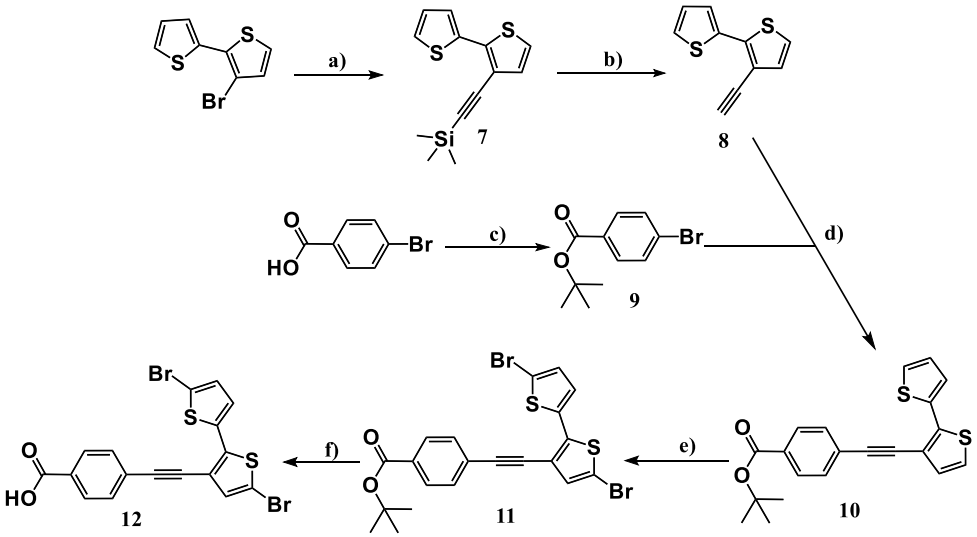

Scheme 5.3 *a) Trimethylsilyl acetylene, $Pd(PPh_3)_2Cl_2$, PPh_3, CuI, DIPA, 95°C, 24h, 77% yield; b) K_2CO_3, MeOH/THF, r.t., 3h, quantitative yield; c) CDI, tert-ButOK, THF,r.t., 5h, 73% yield; d) $Pd(Ph_3)_2Cl_2$, PPh_3, CuI, Toluene, 110°C, 24h, 64% yield; e) NBS, DCM, from 0°C to r.t., dark conditions, 38%; f) KOH, THF, 60°C, 12h, quantitative yield.*

In the first step, the bithiophene **7** was obtained by Sonogashira cross coupling reaction of **3-bromo-2,2'-bithiophene** (see *Experimental Section* of Chapter 4 for the synthesis of **3-bromo-2,2'-bithiophene**) with trimethylsilyl acetylene. Product **7** was isolated in 77% yield after flash chromatography purification as colorless oil. The cleavage of the TMS protecting group was performed by reaction of **7** with K_2CO_3, and product **8** was recovered as colorless oil in quantitative yield.

An esterification reaction was performed under mild conditions between potassium *tert*-butoxide and p-bromobenzoic acid, using carbonyldiimidazole (CDI) as activating reagent. The product *tert*-butyl 4-bromobenzoate **9** was isolated after flash chromatography purification as colorless oil in 73% yield. In the following step, product **10** was prepared performing a Sonogashira cross-coupling between the bromobenzoate ester **9** and bithiophene **8**. Purification by flash chromatography afforded product **10** as yellowish oil in 64% yield. In the next step, **10** was brominated in 5 and 5' positions. Despite the high selectivity of the NBS brominating reaction, product **11** was isolated after flash chromatography purification just in 38% yield. The electronic withdrawal effect of the ethynyl chain linked in position *3* in the bithiophene structure induced to the formation of several mono-brominated by-products, which negatively affected the final yield.

In the last step, the *tert*-butoxide protecting group of the bithiophene **11** was removed by reaction with KOH. Purification of the crude material afforded product **12** as a yellow precipitate in quantitative yield. Modified bithiophene **12** was characterized by NMR and ESI-MS spectrometry.

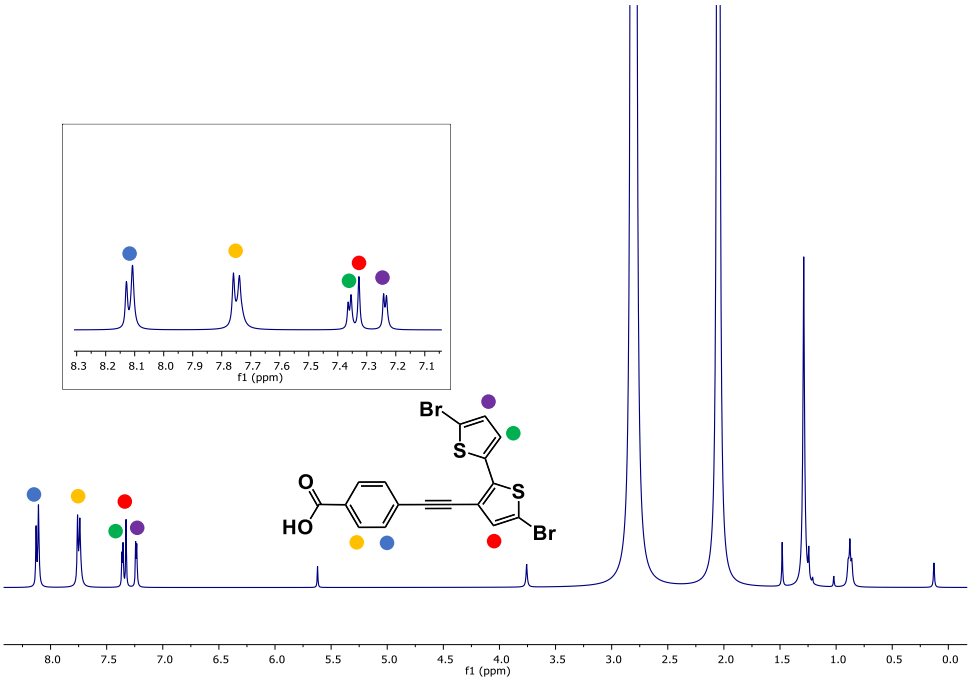

Figure 5.10 *^{1}H-NMR of **12** in Acetone-d^{6} (500 MHz). Aromatic region magnification in the inset.*

The ^{1}H-NMR spectrum of compound **12** reported in **Figure 5.10** shows all the characteristic peaks of the target molecule. The two doublet signals at 8.12 and 7.75 ppm are associated to the protons of the benzoic acid aromatic ring. The bithiophene group is defined by the doublet signals at 7.36 and 7.23 ppm and a singlet at 7.33 ppm.
Moreover, ESI-MS analysis highlighted the occurrence of a peak at 466.91 m/z in the negative field, totally in agreement with the calculated deprotonated ionic species (**Figure 5.11**).

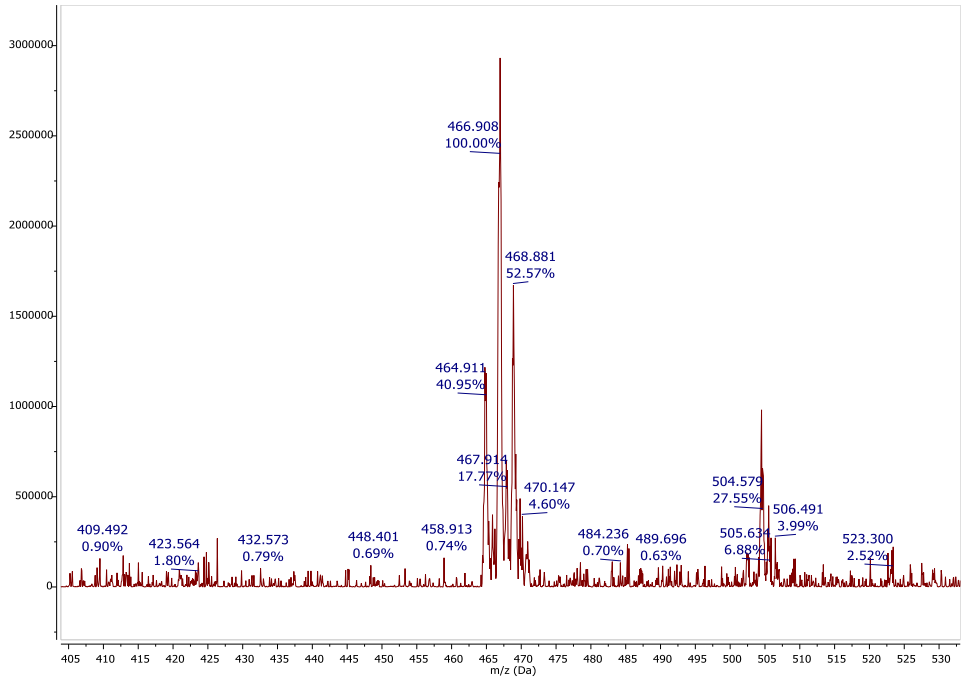

Figure 5.11 ESI-MS analysis of **12**

- *Synthesis of the Tiiii based thiophene polymer **19***

Once completed the preparation of **12**, thiophene-based conductive polymer **19** functionalized with a tetraphosphonate cavitand was synthesized following the convergent synthetic approach reported in **Scheme 5.4.**

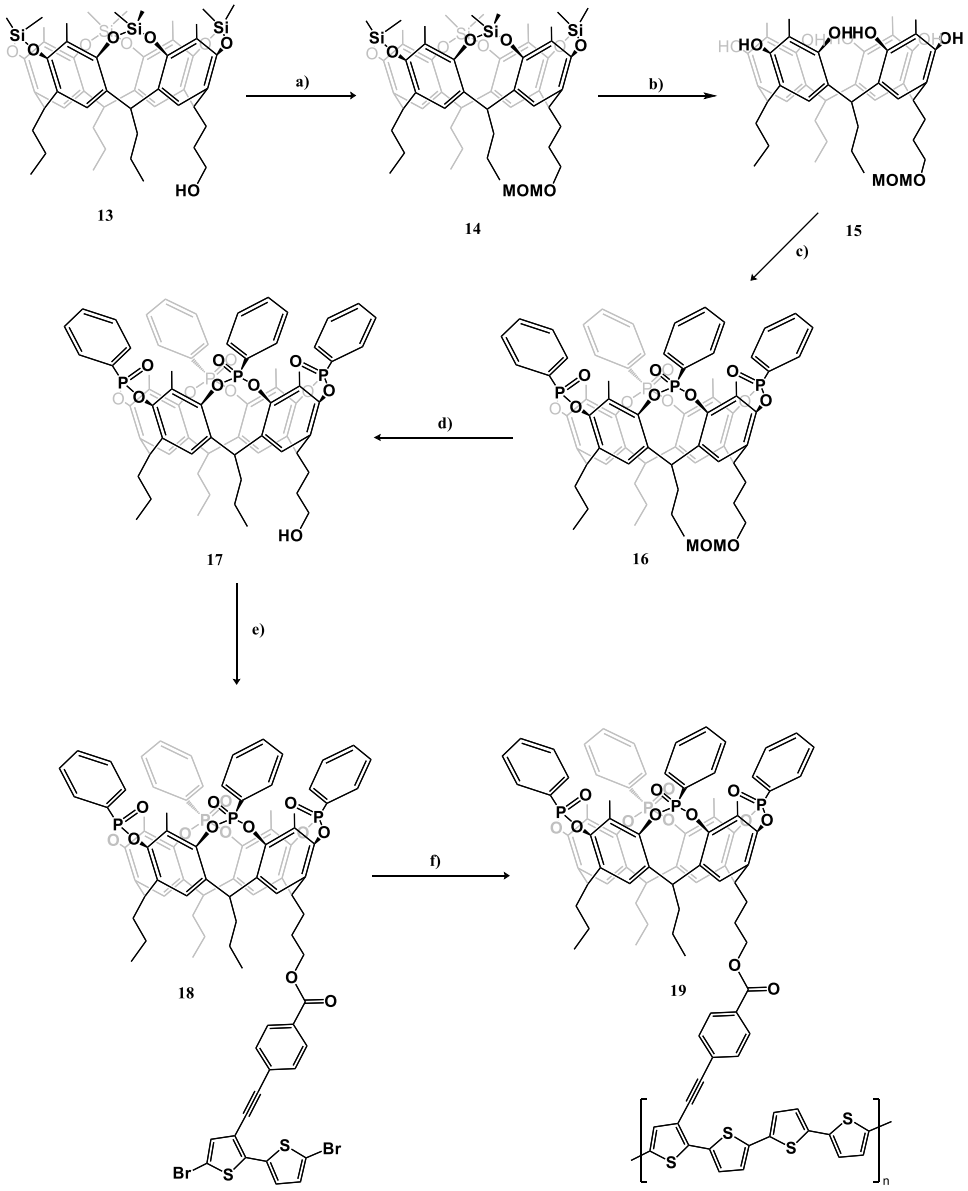

Scheme 5.4 *a) MOMCl, DIPEA, DMF, 50°C, 12h, 74% yield; b) TBAF, THF, r.t., 1h, quantitative yield; c) 1 - $PhPCl_2$, Pyridine, 80°C, 4h, 2 – H_2O_2, 0°C, 1h, 94%; d) HCl 37%, MeOH, $CHCl_3$, 93%; e)* ***12****, DCC, DMAP, DMF, DCM, r.t., 12h, 50% f) 5,5'-Bis(trimethylstannyl)-2,2'-bithiophene, $Pd(PPh_3)_4$, Toluene, DMF, 110°C, 24h.*

Cavitand **14** was prepared by reaction of the mono OH footed cavitand **13** (for the synthesis of cavitand **13** see the *Experimental Section* of Chapter 4) with chloromethyl methyl ether in DMF as solvent. The product was isolated after flash chromatography purification as a white solid in 74% yield. TBAF treatment led to the removal of the dimethylsilyl protecting groups at the upper rim to give **15** in quantitative yield.

In the following step, tetraphosphonate cavitand **16** was prepared by reaction of the phenolic OH groups of **15** with dichlorophenylphosphine in pyridine as solvent, followed by in situ oxidation of the intermediate tetraphosphonito cavitand with hydrogen peroxide. This particular procedure guaranteed only the formation of the Tiiii stereoisomer, featured by four P=O groups pointing inward the cavity. Purification by precipitation afforded the cavitand **16** in 94% yield.

Then, lower rim MOM protecting group was cleaved by treatment with HCl 37% and cavitand **17** was recovered as yellow solid in 93% yield.

A mild condition Steglich esterification was performed in order to link the Tiiii cavitand **17** with the electroactive group **12.** The reaction proceeded using N,N'-diciclohexylcarbodiimide to activate **12** and 4-dimethylamminopyridine as catalyst. Product **18** was isolated after flash chromatography purification as a yellow solid in 50% yield. Monomer **18** was characterized by NMR, ESI-MS and MALDI-TOF.

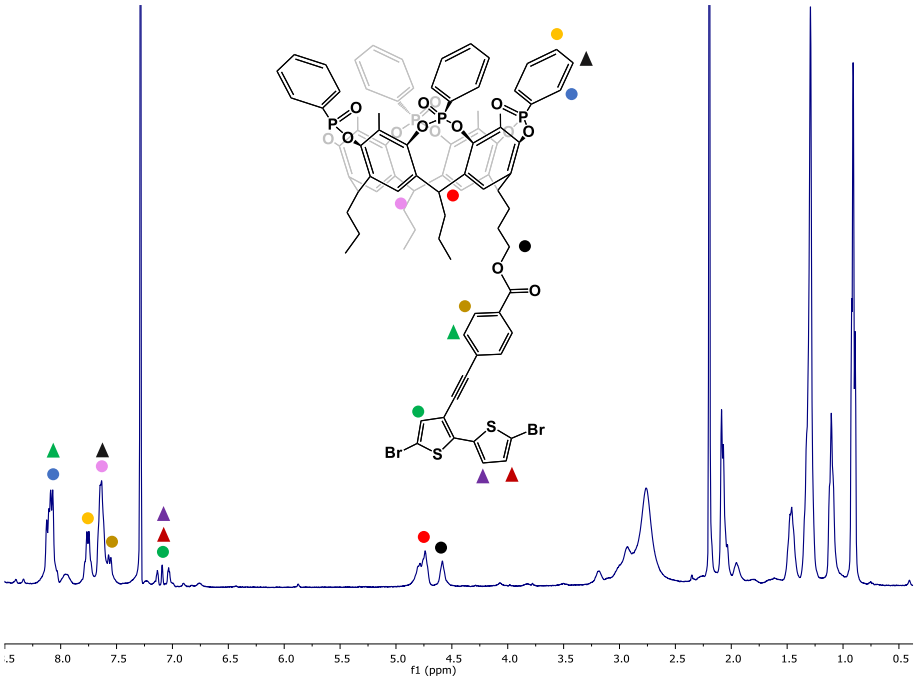

Figure 5.12 ^{1}H-NMR of cavitand **18** in $CDCl_3$ (400 MHz).

The ^{1}H-NMR spectrum of compound **18** reported in **Figure 5.12** shows all the characteristic peaks of the target molecule. All the low ppm signals are in agreement with the lower rim alkyl chains. The 4.58 ppm broad signal associated to the CH_2 next to the O atom at the lower rim (*black* spot), an evidence of the formation of the ester bond. The disymmetrization introduced by the single substituent at the lower rim gives the splitting of the bridging CH signals. More in details, the multiplet signal at 4.74 ppm (*red* spot) is generated by the overlapping of the diagnostic triplets of the CH groups. Multiplet signals at 8.09 and 7.64 ppm, and doublet signal at 7.56 ppm are associated to the lower rim benzene ring (*gold* spot and *green* triangle), the resorcinarene scaffold (*pink* spot) and to the protons in *ortho* and *meta* positions in the phosphonate groups (*blue* spot and *black* triangle). The remaining *meta*-proton of the phosphonate aromatic rings is defined by a multiplet at 7.73 ppm (*yellow* spot). The bithiophene unit is defined

by the broad signals at 7.11, 7.06 and 7.01 ppm (*green* spot, *red* and *purple* triangles)

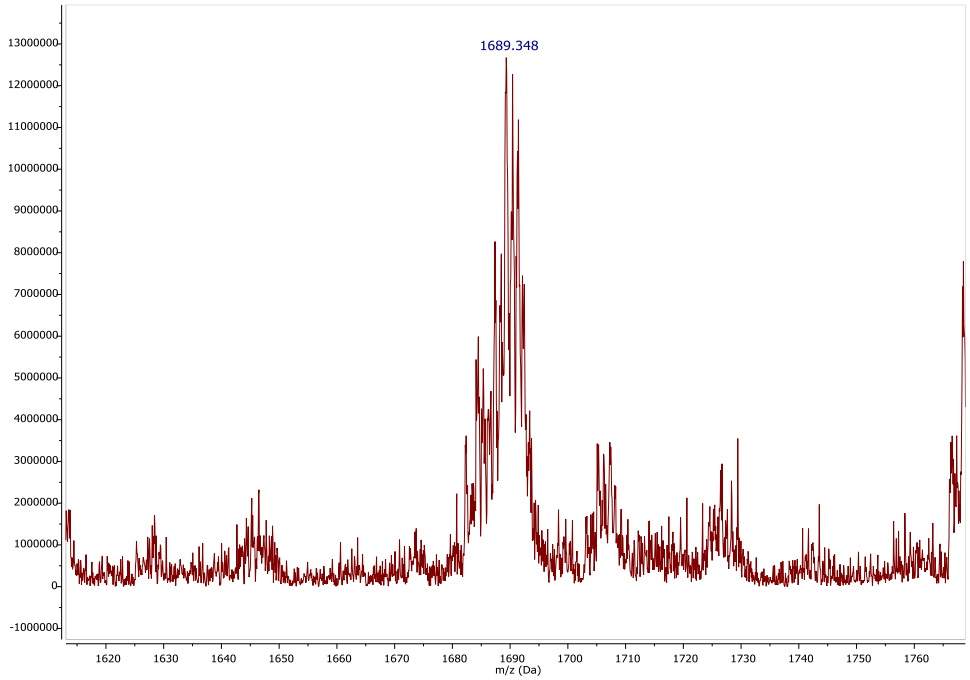

Figure 5.13 ESI-MS analysis of cavitand **18**.

The ESI-MS profile (**Figure 5.13**) shows the molecular ion sodium-complex as the major peak at 1689.35 m/z, in agreement with the calculated one.

MALDI-TOF analysis confirmed the molecular weight of the cavitand monomer **18**, showing the typical protonated adduct (**Figure 5.14**).

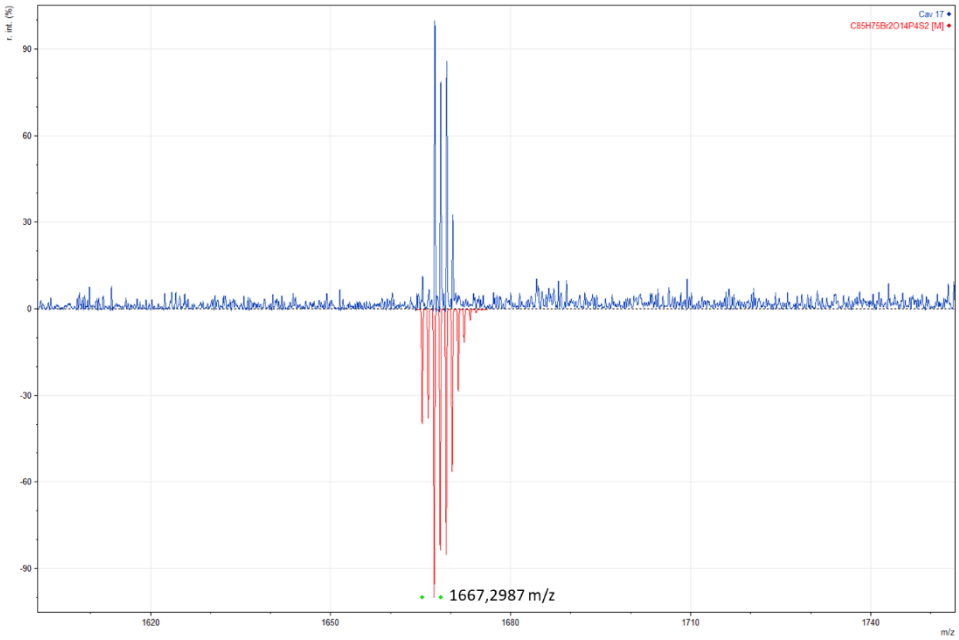

Figure 5.14. *MALDI-TOF spectrum of **18,** with experimental (blue profile) versus flipped theoretical (red) isotopic distribution pattern*.

Once completed the preparation of the cavitand monomer **18**, a Stille cross-coupling reaction was performed in order to co-polymerize monomer **18** with commercially available 5,5'-Bis(trimethylstannyl)-2,2'-bithiophene (**Scheme 5.4** *f*). The reaction was conducted at 110°C for 24 hours in strictly oxygen-free conditions using $Pd(PPh_3)_4$ as catalyst in a mixture of dry DMF/Toluene. Unfortunately, the dark powder recovered by purification of the crude material did not provide evidences of the polymer formation. Despite the occurrence of an orange fluorescence in THF solution, ^{1}H-NMR spectrum of the recovered material did not exhibit several characteristic peaks of the starting monomer **18**.

5.3 Conclusions

In this chapter, we explored two different synthetic approaches for the preparation of thiophene based conductive polymers functionalized with the tetraquinoxaline cavitand (QxCav) and the tetraphosphonate one (Tiiii).

The QxCav-based polythiophene was obtained through $FeCl_3$-driven oxidative polymerization of the tetraquinoxaline cavitand **5** functionalized at the upper rim with a 3-ethynyl-2,2'-bithiophene electroactive group. Monomer **5** was synthesized following the procedure reported in a previous work by our research group.[14] Polymerization of the cavitand **5** was conducted in two different conditions leading to the formation of polymeric materials featured by different molecular weights and polydispersity indexes. The acidic condition of the polymerization reaction, and the subsequent protonation of the quinoxaline walls of **5**, induced a change in the cavitand conformation. ^{1}H-NMR characterization of the two polymers highlighted the conformational transition of the QxCavs from the monomer *vase* form to the *kite* one in the polymer. QxCav-based polymers were furtherly characterized by UV-Vis and fluorescence spectroscopy. Both UV-Vis spectra confirmed the open conformation of the cavitands in the polymers. Moreover, a red-shift of the π-π* bands associated to the polythiophene backbone was observed with the increasing of the molecular weight of the polymer. Fluorescence spectroscopy analysis of the polymeric materials highlighted the occurrence of a M_w-dependent bathochromic effect in the emission peaks and the occurrence of a mixture of low and high molecular weight polymers, as determined via GPC. In the prospective to develop impedance sensors for the selective detection in water of aromatic species, the switch of the cavitand units to the vase form in the polymers is ongoing.

A Stille cross-coupling reaction was performed between the cavitand monomer **18** and 5,5'-Bis(trimethylstannyl)-2,2'-bithiophene to synthetize Tiiii-based polythiophene, overcoming the steric hindrance issues reported in *Chapter 4*. The monomer **18** was synthesized in mild condition by Steglich esterification of the mono OH footed tetraphosphonate cavitand **17** and the modified bithiophene **12**. Despite the success in the preparation of monomer **18,** the preliminary tests in the Stille-coupling polymerization did not lead to the formation of the target

polymer **19**. Additional tests are now in progress to find the best polymerization conditions for the preparation of the Tiiii-based polythiophene **19**.

5.4 Acknowledgments

Special thanks to Prof. Timothy M. Swager from Department of Chemistry, Massachusetts Institute of Technology, Cambridge (USA).

5.5 Experimental Section

Synthesis of Cavitand 5

The synthesis of cavitand **5** is reported in the paper "Sensing of halogenated aromatic hydrocarbons in water with a cavitand coated piezoelectric device" – Giannetto, M., Pedrini, A., Fortunati, S., Brando, D., Milano, S., Massera, C., Tatti, R., Verrucchi, R., Careri, M., Dalcanale, E. & Pinalli, R. (2018). *Sens. Actuators B Chem.* **276**, 340-348.

Synthesis of Polymer 6 Procedure A

Cavitand **5** (10 mg, 0.0066 mmol) was dissolved in dry DCM (3.5 mL) under argon atmosphere, maintaining a gently stirring. The system was cooled at 0°C and a suspension of $FeCl_3$ (10 mg, 0.066 mmol) in dry DCM (3 mL) was slowly dropwise added to the solution. The mixture was stirred for 1h at 0°C and for 12 hours at room temperature. The reaction was quenched by pouring the solution in MeOH. The red solid precipitate was recovered by filtration and washed several times with MeOH and H_2O. The polymer was obtained as dark red powder in 85% yield (8.6 mg).

^{1}H NMR (500 MHz, Methylene Chloride-d_2) δ 8.20 – 6.86 (m, 31H), 6.75 – 6.34 (m, 7H), 4.41 – 3.88 (m, 4H), 3.51 – 3.34 (m, 2H), 2.55 – 1.69 (m, 10H), 1.32 – 0.64 (m, 36H).

GPC analysis: M_w = 7k g/mol; D = 2.32.

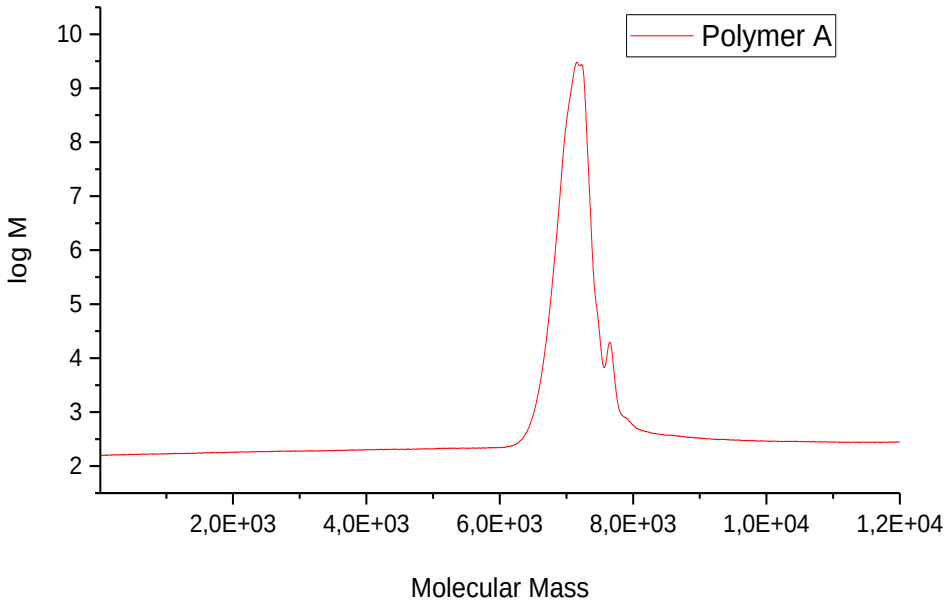

Figure 5.14 GPC trace of polymer **A** collected in THF at 298K. [C] = 0.5 mg/ml

Synthesis of Polymer 6 Procedure B

The differences between this procedure and the previous one are the longer reaction time and the higher monomer concentration.

Cavitand **5** (10 mg, 0.0066 mmol) was dissolved in dry DCM (2 mL) under argon atmosphere, maintaining a gently stirring. The system was cooled at 0°C and a suspension of $FeCl_3$ (10 mg, 0.066 mmol) in dry DCM (2 mL) was slowly dropwise added to the solution. The mixture was stirred for 1h at 0°C and for 12 hours at room temperature. The reaction was quenched by pouring the solution in MeOH. The red solid precipitate was recovered by filtration and washed several times with MeOH and H_2O. The polymer was obtained as dark red powder in 85% yield (7.4 mg).

^{1}H NMR (500 MHz, Methylene Chloride-d_2) δ 8.20 – 6.86 (m, 31H), 6.75 – 6.34 (m, 7H), 4.41 – 3.88 (m, 4H), 3.51 – 3.34 (m, 2H), 2.55 – 1.69 (m, 10H), 1.32 – 0.64 (m, 36H).

GPC analysis: M_w = 25k g/mol; D = 5.75

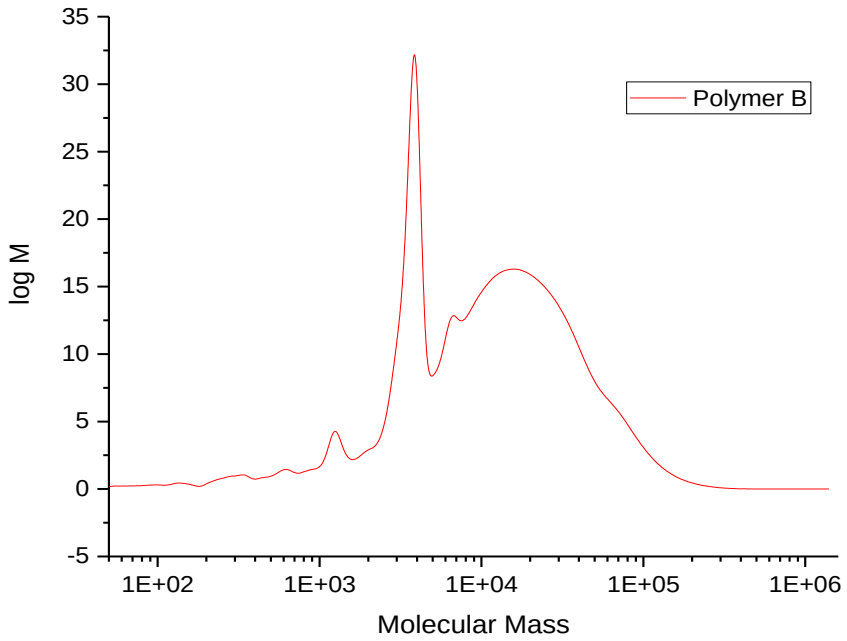

Figure 5.15 GPC trace of polymer **B** collected in THF at 298K. [C] = 0.5 mg/ml

Synthesis of ([2,2'-bithiophen]-3-ylethynyl)trimethylsilane (7)

A Schlenk tube reactor was loaded with 3-bromo-2,2'-bithiophene (180 mg, 0.734 mmol) and ethynyltrimethylsilane (0.131 mL, 1.1 mmol) in dry diisopropylamine (6 mL) under argon atmosphere. The solution was degassed with three freeze-pump-thaw cycles. $PdCl_2(PPh_3)_2$ (15.46 mg, 0.022 mmol), PPh_3 (11.54 mg, 0.044 mmol) and CuI (8.39 mg, 0.044 mmol) were added and the mixture was stirred at 95°C for 24 hours. The crude mixture was filtered over celite and the organic phase was dried under reduced pressure. The raw material was purified through

flash chromatography column (Hexane). The product was recovered as a colorless oil in 66% yield (128 mg, 0.487 mmol).

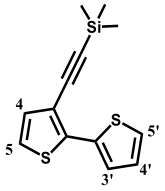

^{1}H NMR (400 MHz, $CDCl_3$) δ 7.53 (dd, *J* = 3.7, 1.2 Hz, 1H, **$H_{3'}$**), 7.30 (dd, *J* = 5.1, 1.2 Hz, 1H, **$H_{5'}$**), 7.07 – 7.02 (m, 3H, **H_4** + **H_5** + **$H_{4'}$**), 0.29 (s, 9H, Si**$(CH_3)_3$**).

ESI-MS: m/z = calculated for $C_{13}H_{15}S_2Si$ = 263.04 $[M+H]^+$
found = 263.18.

Synthesis of 3-ethynyl-2,2'-bithiophene (8)[14]

A Schlenk tube reactor was loaded with **7** (128 mg, 0.487 mmol) in a mixture 1:1 of dry MeOH and dry THF (6 mL) under argon atmosphere. The solution was degassed with three freeze-pump-thaw cycles. K_2CO_3 (740 mg, 5.36 mmol) was added and the mixture was stirred for 12 hours at room temperature in dark conditions. The solvents were removed under reduced pressure. The crude material was extracted three times with DCM/H_2O. The product was recovered as a colorless oil in quantitative yield (92 mg, 0.487 mmol).

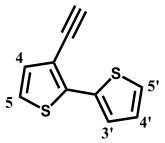

^{1}H NMR (400 MHz $CDCl_3$): δ = 7.56 (dd, 1H, J= 3.6 Hz, J=0.7 Hz, Ar**$H_{3'}$**); 7.31 (dd, 1H, J= 5.1 Hz, J=0.7 Hz, Ar**$H_{5'}$**); 7.12-7.02 (m, 3H, Ar**H_4** + Ar**H_5** + Ar**$H_{4'}$**); 3.38 (s, 1H, C**H**).

Synthesis of tert-butyl 4-bromobenzoate (9)[18]

p-Bromobenzoic acid (500 mg, 2.49 mmol) and CDI (645.95 mg, 3.98 mmol) were dissolved in dry THF (7 mL) under argon atmosphere and stirred at room temperature. The system changed rapidly from a white suspension to an orange solution. After 3 hours of stirring, a solution in dry THF (7 mL) of potassium tert-butoxide (1.12 g, 9.96 mmol) was added dropwise to the mixture. The system was stirred for 12 hours at room temperature and the solvent removed under vacuum. The crude material was extracted three times with EtOAc/H_2O and the content of the organic phase recovered. Impurities were removed by precipitation in DCM:Hexane (1:5). The precipitate was removed by filtration and the purified organic phase was dried under vacuum. The product was obtained as colorless oil in 74% yield (470 mg, 1.84 mmol).

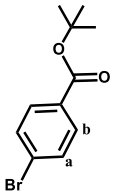

^{1}H NMR (500 MHz, $CDCl_3$) δ 7.87 (d, *J* = 8.7 Hz, 2H, **H_a**), 7.57 (d, *J* = 8.9 Hz, 2H, **H_b**), 1.61 (s, 9H, C**$(CH_3)_3$**).

ESI-MS: m/z = calculated for $C_{11}H_{14}BrO_2$ = 258.14 $[M+H]^+$
found = 258.02.

Synthesis of tert-butyl 4-(([2,2'-bithiophen]-3-yl)ethynyl)benzoate (10)

A Schlenk tube reactor was loaded with **8** (92 mg, 0.487 mmol), **9** (137 mg, 0.536 mmol) and diisopropylamine (1,46 mL, 10.4 mmol) in dry toluene (15 mL) under argon atmosphere. The solution was degassed with three freeze-pump-thaw cycles. $PdCl_2(PPh_3)_2$ (10.9 mg, 0.156 mmol), PPh_3 (8.2 mg, 0.0312 mmol) and CuI (2.97 mg, 0.0156 mmol) were added and the mixture was stirred at 110°C for 24 hours. The reaction was filtered over celite and the organic phase was dried under reduced pressure. The crude material was purified through flash chromatography

column (Hexane → Hexane:DCM = 8:2). The product was recovered as a yellowish oil in 67% yield (120 mg, 0.326 mmol).

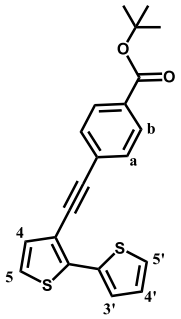

^{1}H NMR (500 MHz, $CDCl_3$) δ 7.99 (d, *J* = 8.4 Hz, 2H, **H_a**), 7.60 (d, *J* = 8.4 Hz, 2H, **H_b**), 7.51 (dd, *J* = 3.7, 1.2 Hz, 1H, **$H_{3'}$**), 7.34 (dd, *J* = 5.1, 1.2 Hz, 1H, **$H_{5'}$**), 7.16 – 7.11 (m, 2H, **H_4** + **H_5**), 7.08 (dd, *J* = 5.1, 3.7 Hz, 1H, **$H_{4'}$**), 1.61 (s, 9H, C**$(CH_3)_3$**).

^{13}C NMR (101 MHz, $CDCl_3$) δ 131.11, 129.43, 127.25, 125.88, 125.80, 122.95, 118.39, 30.96, 30.81, 29.72, 28.21, 1.04.

ESI-MS: m/z = calculated for $C_{21}H_{19}O_2S_2$ = 367.50 $[M+H]^+$
found = 367.21

Synthesis of tert-butyl 4-((5,5'-dibromo-[2,2'-bithiophen]-3-yl)ethynyl)benzoate (11)

To a solution of **10** (60 mg, 0.164 mmol) in dry DMF (2 mL) under argon atmosphere and cooled at 0°C, a dry DMF solution (2 mL) of N-bromosuccinimide (67 mg, 0.376 mmol) was slowly added dropwise. The mixture was stirred at room temperature for 3 days in dark conditions. The solvent was removed by evaporation under reduced pressure. The crude mixture was extracted with DCM/H_2O and the organic phase was purified through flash chromatography column (DCM:Hexane = 2:8). The product was recovered as a yellowish oil in 47% yield (41 mg, 0.078 mmol).

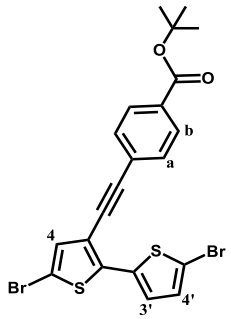

^{1}H NMR (500 MHz, $CDCl_3$) δ 8.00 (d, *J* = 8.5 Hz, 2H, **H_a**), 7.58 (d, *J* = 8.5 Hz, 2H, **H_b**), 7.11 (d, *J* = 4.0 Hz, 1H, **$H_{3'}$**), 7.08 (s, 1H, **H_4**), 7.02 (d, *J* = 3.9 Hz, 1H, **$H_{4'}$**), 1.61 (s, 9H, C**$(CH_3)_3$**).

^{13}C NMR (126 MHz, $CDCl_3$) δ 133.12, 131.17, 130.01, 129.51, 29.71, 28.20, 22.71, 14.13.

ESI-MS: m/z = calculated for $C_{21}H_{17}Br_2O_2S_2$ = 525.31 $[M+H]^+$
found = 525.02

Synthesis of 4-((5,5'-dibromo-[2,2'-bithiophen]-3-yl)ethynyl)benzoic acid 12

To a solution of **5** (41 mg, 0.078 mmol) in dry THF (5 mL) under inert atmosphere finely ground KOH (160 mg, 2.9 mg) was added and the mixture was stirred at 60°C for 12 hours. The solvent was removed by evaporation under reduced pressure. The crude material was extracted with EtOAc and H_2O. The organic phase was washed with HCl 1N and dried. The product was recovered as a yellow solid in quantitative yield (36 mg, 0.078 mmol).

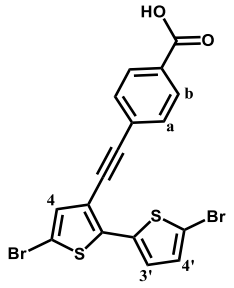

^{1}H NMR (400 MHz, Acetone-d_6) δ 8.12 (d, *J* = 8.4 Hz, 2H, **H_a**), 7.75 (d, *J* = 8.3 Hz, 2H, **H_b**), 7.36 (d, *J* = 4.1 Hz, 1H, **$H_{3'}$**), 7.33 (s, 1H, **H_4**), 7.24 (d, *J* = 4.1 Hz, 1H, **$H_{4'}$**).

^{13}C NMR (126 MHz, Acetone) = 151.49, 131.38, 130.84, 129.90, 124.62.

ESI-MS: m/z = calculated for $C_{17}H_7Br_2O_2S_2$ = 466.91 $[M-H]^-$
found = 467.10

Synthesis of Cavitand 13
For the synthesis of cavitand **13** see *Experimental part* of **Chapter 4**

Synthesis of Cavitand 14[19]

A Schlenk tube reactor was loaded with cavitand **13** (850 mg, 0.891 mmol), dry DIPEA (0.702 mL, 4.011 mmol) in dry DMF (8 mL) under argon atmosphere and the system was cooled at 0°C. Chloromethyl methyl ether (0.203 mL, 2.67 mmol) was slowly added under inert atmosphere and the dispersion was stirred at 50°C for 48 hours. The solvent was removed under reduced pressure; the crude material was washed with H_2O and purified through flash chromatography column (Hexane:EtOAc = 9:1). The product was recovered as white solid in 72% yield (632 mg, 0.633 mmol).

^{1}H NMR (500 MHz, $CDCl_3$) δ 7.19 (s, 2H, Ar**H**), 7.17 (s, 2H, Ar**H**), 4.65 (s, 2H, OC**H_2**OCH_3), 4.61 (t, *J* = 8.8 Hz, 4H, ArC**H**), 3.61 (t, *J* = 6.3 Hz, 2H, CH_2CH_2C**H_2**O), 3.39 (s, 3H, OCH_2OC**H_3**), 2.30 (q, *J* = 8.0 Hz, 2H, C**H_2**CH_2CH_2O), 2.18 (q, *J* = 7.0, 6.1 Hz, 6H, C**H_2**CH_2CH_3), 1.92 (s, 6H, ArC**H_3**), 1.90 (s, 6H, ArC**H_3**), 1.63 – 1.56 (m, 2H,

$CH_2C\mathbf{H_2}CH_2O$), 1.36 – 1.26 (m, 6H, $CH_2C\mathbf{H_2}CH_3$), 1.01 – 0.95 (m, 9H, $CH_2CH_2C\mathbf{H_3}$), 0.51 (s, 12H, $SiC\mathbf{H_{3,in}}$), -0.69 (s, 12H, $SiC\mathbf{H_{3,out}}$).

ESI-MS: m/z = calculated for $C_{54}H_{77}O_{10}Si_4$ = 998.46 $[M+H]^+$
found = 998.62

Synthesis of resorcinarene 15[19]

A round bottom flask was loaded with cavitand **14** (632 mg, 0.633 mmol), glacial Acetic Acid (0.305 mL, 5.33 mmol) in THF (16 mL) and then was cooled at 0°C. 1M TBAF solution in THF (1.54 mL, 5.33 mmol) was slowly added and the solution was stirred at room temperature for an hour. The reaction was quenched by pouring the solution in NH_4Cl saturated solution (10 ml). The mixture was extracted with EtOAc/H_2O. Organic phase was dried under reduced pressure and product **15** was recovered as a yellowish solid in quantitative yield (490 mg, 0.633 mmol).

^{1}H NMR (400 MHz, Acetone-d_6) δ 7.45 (s, 2H, Ar**H**), 7.43 (s, 2H, Ar**H**), 4.57 (s, 2H, $OC\mathbf{H_2}OCH_3$), 4.39 (t, *J* = 7.0 Hz, 4H, ArC**H**), 3.53 (t, *J* = 6.6 Hz, 2H, $CH_2CH_2C\mathbf{H_2}O$), 3.30 (s, 3H, $OCH_2OC\mathbf{H_3}$), 2.42 – 2.22 (m, 8H, $C\mathbf{H_2}CH_2CH_2O$ + $C\mathbf{H_2}CH_2CH_3$), 2.03 (s, 12H, $ArC\mathbf{H_3}$), 1.62 – 1.48 (m, 2H, $CH_2C\mathbf{H_2}CH_2O$), 1.39 – 1.23 (m, 6H, $CH_2C\mathbf{H_2}CH_3$), 0.93 (t, *J* = 7.4 Hz, 9H, $CH_2CH_2C\mathbf{H_3}$).

ESI-MS: m/z = calculated for $C_{46}H_{60}O_{10}Na$ = 795.97 $[M+Na]^+$
found = 795.51

Synthesis of Cavitand 16[19]

A Schlenk reactor tube was loaded with resorcinarene **15** (490 mg, 0.633 mmol) and dichlorophenylphosphine (0.387 mL, 2.85 mmol) in freshly distilled pyridine (13 mL) under argon atmosphere. The mixture was stirred at 80°C for 3 hours. After 3 hours the solution was cooled down at 0°C and 6 mL of aqueous 40% H_2O_2 was added. The resulting mixture was stirred at 0°C for an hour. The solvent was removed by evaporation under reduced pressure, and the crude material was purified by precipitation in DCM:Hexane (3:7). The product was recovered as a white precipitate in 96% yield (767 mg, 0.608 mmol).

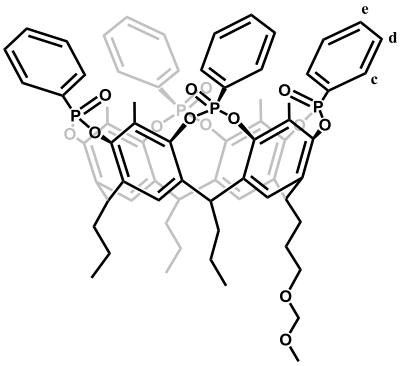

^{1}H NMR (400 MHz, $CDCl_3$) δ 8.07 (dd, *J* = 14.3, 7.6 Hz, 8H, **H_c**), 7.80 – 7.68 (m, 4H, **H_e**), 7.67 – 7.53 (m, 12H, **H_d** + Ar**H**), 4.82 – 4.62 (m, 6H, ArC**H** + OC**H_2**OCH_3), 3.74 (t, *J* = 6.6 Hz, 2H, CH_2CH_2C**H_2**O), 3.37 (s, 3H, OCH_2OC**H_3**), 2.88 – 2.74 (m, 8H, C**H_2**CH_2CH_2O + C**H_2**CH_2CH_3), 2.06 (s, 12H, ArC**H_3**), 1.79 – 1.63 (m, 2H, CH_2C**H_2**CH_2O), 1.52 – 1.33 (m, 6H, CH_2C**H_2**CH_3), 1.14 – 0.98 (m, 9H, CH_2CH_2C**H_3**).

^{31}P{1H} NMR (162 MHz $CDCl_3$)**:** δ = 11.58 (s, 1P, P=O); 11.47 (s, 3P, P=O) (cavitand complexed with Na^+).
ESI-MS: m/z = calculated for $C_{70}H_{72}O_{14}P_4Na$ = 1284.22 $[M+Na]^+$
found = 1284.38

Synthesis of Cavitand 17[19]

Cavitand **16** was solubilized in a mixture 1:1 of $CHCl_3$ and MeOH (28 mL). The solution was cooled down at 0°C and aqueous 37% HCl solution (0.369 mL, 12.16 mmol) was slowly added. The solution was stirred at 50°C for 12 hours. The solvent was removed by evaporation under reduced pressure and the crude material was extracted with DCM/H_2O. The organic phase was dried under reduced pressure and the product **17** was recovered as a yellow solid in 93% yield (688 mg, 0.565 mmol).

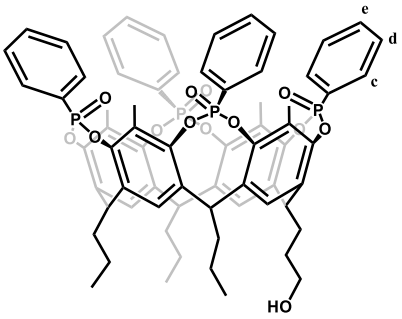

^{1}H NMR (400 MHz, $CDCl_3$) δ 8.23 – 8.06 (m, 8H, **H_c**), 7.71 – 7.63 (m, 4H, **H_e**), 7.63 – 7.51 (m, 12H, **H_d** + Ar**H**), 4.92 – 4.79 (m, 4H, ArC**H**), 3.84 (t, *J* = 6.0 Hz, 2H, $CH_2CH_2C\mathbf{H_2}O$), 2.62 – 2.34 (m, 8H, $C\mathbf{H_2}CH_2CH_2O$ + $C\mathbf{H_2}CH_2CH_3$), 2.30 (s, 12H, Ar$C\mathbf{H_3}$), 1.73 – 1.65 (m, 2H, $CH_2C\mathbf{H_2}CH_2O$), 1.54 – 1.39 (m, 6H, $CH_2C\mathbf{H_2}CH_3$), 1.16 – 1.02 (m, 9H, $CH_2CH_2C\mathbf{H_3}$).

^{31}P{1H} NMR (162 MHz $CDCl_3$)**:** δ = 6.21 (s, 1P, P=O); 6.01 (s, 3P, P=O).

MALDI-TOF: m/z = calculated for $C_{68}H_{69}O_{13}P_4$ = 1218.3871 $[M+H]^+$
found = 1218.5639.

Synthesis of cavitand 18

Cavitand **17** (24 mg, 0.019 mmol), bithiophene **12** (36 mg, 0.077 mmol) and 4-dimethylaminopyridine (5.3 mg, 0.044 mmol) were dissolved in a 1:1 mixture of dry DMF (0.5 mL) and dry DCM (0.5 mL) under argon atmosphere. The solution was cooled down at 0°C and N,N'-Dicyclohexylcarbodiimide (14.2 mg, 0.069 mmol) was added. The mixture was stirred at room temperature for 12 hours. The solvents were removed under reduced pressure and the crude material was purified through flash chromatography column on silica (DCM:MeOH = 9:1). The product was recovered as a yellow solid in 50% yield (16 mg, 0.095 mmol).

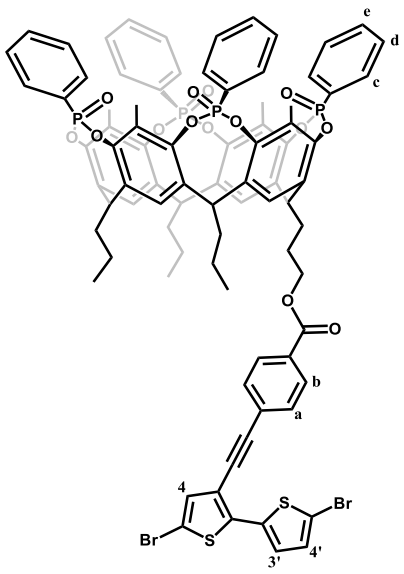

^{1}H NMR (400 MHz, $CDCl_3$) δ 8.16 – 7.99 (m, 10H, $\mathbf{H_c}$ + $\mathbf{H_a}$), 7.73 (q, *J* = 7.7, 7.2 Hz, 4H, $\mathbf{H_e}$), 7.68 – 7.56 (m, 12H, $\mathbf{H_d}$ + Ar**H**), 7.53 (d, *J* = 8.3 Hz, 2H, $\mathbf{H_b}$), 7.11 (bs, 1H, $\mathbf{H_{3'}}$), 7.06 (s, 1H, $\mathbf{H_4}$), 7.01 (bs, 1H, $\mathbf{H_{4'}}$), 4.86 – 4.62 (m, 4H, ArC**H**), 4.56 (t, 2H, $CH_2CH_2C\mathbf{H_2}O$), 2.74 – 2.68 (m, 8H, $C\mathbf{H_2}CH_2CH_2O$ + $C\mathbf{H_2}CH_2CH_3$), 2.06 (s, 6H, ArC$\mathbf{H_3}$), 2.04 (s, 6H, ArC$\mathbf{H_3}$), 1.97 – 1.86 (m, 2H, $CH_2C\mathbf{H_2}CH_2O$), 1.54 – 1.35 (m, 6H, $CH_2C\mathbf{H_2}CH_3$), 1.15 – 0.99 (m, 9H, $CH_2CH_2C\mathbf{H_3}$).

^{1}H-^{13}C HSQC NMR (151 MHz, $CDCl_3$)

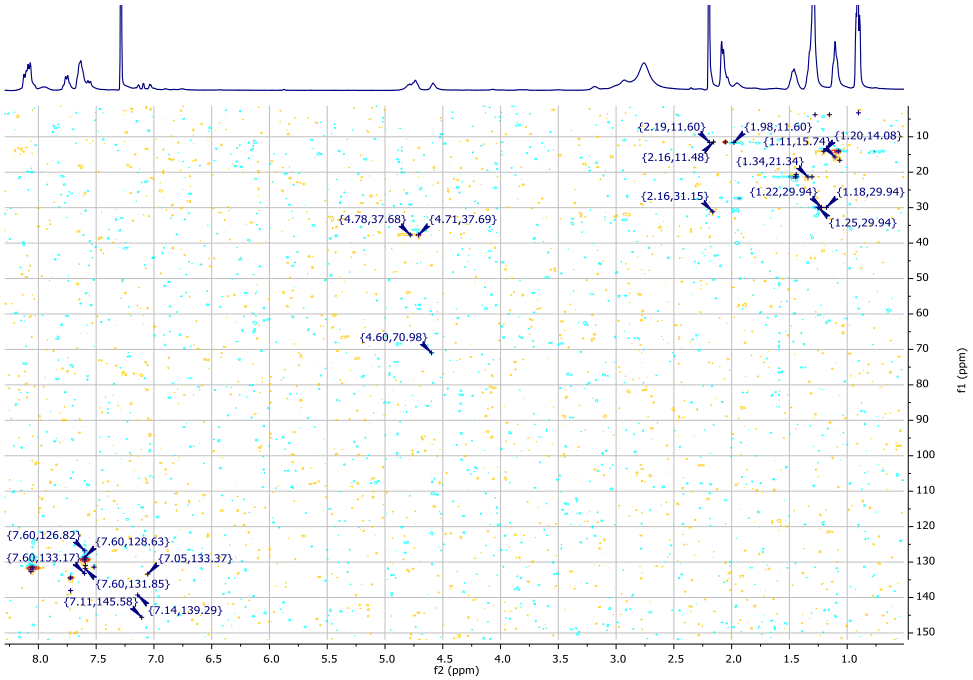

^{31}P{1H} NMR (162 MHz $CDCl_3$)**:** δ = 11.65 (s, 1P, P=O); 11.49 (s, 3P, P=O) (cavitand complexed with Na^+)

ESI-MS: m/z = calculated for $C_{85}H_{74}Br_2O_{14}P_4S_2Na$ = 1690.33 $[M+Na]^+$
found = 1690.35

MALDI-TOF: m/z = calculated for $C_{85}H_{75}Br_2O_{14}P_4S_2$ = 1667.2987 $[M+H]^+$
found = 1667.1911

5.6 References

1. Pejcic, B. & Marco, R. De. Impedance spectroscopy : Over 35 years of electrochemical sensor optimization. *Electrochim. Acta* **51**, 6217–6229 (2006).
2. Fields, E. & Fields, S. E. *Electric and Magnetic Fields Bioeffects*. (2014).
3. Hau, E. Von. Impedance Spectroscopy for Emerging Photovoltaics Published as part of The Journal of Physical Chemistry virtual special issue " Young Scientists " . *J. Phys. Chem. C* **123**, 11-329–11346 (2019).
4. Montes-garcía, V. *et al.* Harnessing Selectivity and Sensitivity in Ion Sensing via Supramolecular Recognition : A 3D Hybrid Gold Nanoparticle Network Chemiresistor. *Adv. Funct. Mater.* **2008554**, 1–11 (2020).
5. Bindra, P. & Hazra, A. Capacitive gas and vapor sensors using nanomaterials. *J. Mater. Sci. Mater. Electron.* **29**, 6129–6148 (2018).
6. Balasubramani, V. *et al.* Recent Advances in Electrochemical Impedance Spectroscopy Based Toxic Gas Sensors Using Semiconducting Metal Oxides Review — Recent Advances in Electrochemical Impedance Spectroscopy Based Toxic Gas Sensors Using Semiconducting Metal Oxides. *J. Electrochem. Soc.* **167**, (2020).
7. Balasubramani, V., Sureshkumar, S., Rao, T. S. & Sridhar, T. M. Impedance Spectroscopy-Based Reduced Graphene Oxide- Incorporated ZnO Composite Sensor for H_2S Investigations. *ACS Omega* **4**, 9976–9982 (2019).
8. Li, H., Hu, X., Zhao, J., Koh, K. & Chen, H. A label-free impedimetric sensor for the detection of an amphetamine-type derivative based on cucurbit [7] uril-mediated three-dimensional AuNPs. *Electrochem. commun.* **100**, 126–133 (2019).
9. Chandrasekhar, P. *Conducting Polymers, Fundamentals and Applications* (1999).
10. Bianchi, F. *et al.* Cavitands as superior sorbents for benzene detection at trace level. *New J. Chem.* **27**, 502–509 (2003).
11. Trzcinski, W. J. *et al.* In Search of the Ultimate Benzene Sensor: The

EtQxBox Solution. *ACS Sensors* **2**, 590–598 (2017).

12. Pinalli, R. & Dalcanale, E. Supramolecular Sensing with Phosphonate Cavitands. *Acc. Chem. Res.* **46**, 399–411 (2013).

13. Biavardi, E. *et al.* Molecular Recognition on a Cavitand-Functionalized Silicon Surface. *J. Am. Chem. Soc.* **131**, 7447–7455 (2009).

14. Giannetto, M. *et al.* Sensing of halogenated aromatic hydrocarbons in water with a cavitand coated piezoelectric device. *Sensors Actuators B. Chem.* **276**, 340–348 (2018).

15. Castro, P. P., Zhao, G., Masangkay, G. A., Hernandez, C. & Gutierrez-tunstad, L. M. Quinoxaline Excision : A Novel Approach to Tri- and Diquinoxaline Cavitands. *Org. Lett.* **6**, 333–336 (2004).

16. Cram, D. J., Choi, H. J., Bryant, J. A. & Knobler, C. B. Solvophobic and Entropic Driving Forces for Forming Velcraplexes, Which Are Four-Fold, Lock-Key Dimers in Organic Media. *J. Am. Chem. Soc.* **114**, 7748–7765 (1992).

17. Hayashi, S., Yamamoto, S. & Koizumi, T. Effects of molecular weight on the optical and electrochemical properties of EDOT-based π-onjugated polymers. *Sci. Rep.* **7**, 1–8 (2017).

18. Galanti, A. *et al.* A New Class of Rigid Multi(azobenzene) Switches Featuring Electronic Decoupling: Unravelling the Isomerization in Individual Photochromes. *J. Am. Chem. Soc.* **141**, 9273–9283 (2019).

19. Tancini, F. *et al.* Hierarchical Self-Assembly on Silicon. *J. Am. Chem. Soc.* **132**, 4781–4789 (2010).